Ice and Gas

Linking Infrared and Millimetric Observations towards young Solar-type Stars

Giulia Perotti

Dissertation submitted for the degree of

PHILOSOPHIÆ DOCTOR

Niels Bohr Institute & Centre for Star and Planet Formation
Faculty of Science
University of Copenhagen

April 7^{th} 2021

This thesis has been submitted to the PhD School of The Faculty of Science,
University of Copenhagen

Title	Ice and Gas, Linking Infrared and Millimetric Observations toward
Author	Giulia Perotti
Department	Niels Bohr Institute and Centre for Star and Planet Formation, Faculty of Science, University of Copenhagen
Academic Advisor	Assoc. Prof. Jes K. Jørgensen
Assessment Committee	Prof. Anja C. Andersen (chair) Dr. Sergio Ioppolo Dr. Izaskun Jiménez-Serra

Typeset using LaTeX and the `memoir` documentclass.
Layout and typography inspired by Friedrich Wiemer's thesis
using the class `classicthesis` developed by André Miede.

A mamma e papá

Abstract

The interaction between interstellar dust, ice and gas plays a major role for the chemistry in regions where star and planets form. Different reactions occur in the gas and on the ice mantles of dust grains in these regions, and consequently the mutual exchange of matter between the two phases is what regulates the chemical evolution of newborn stars and planets. Methanol (CH_3OH) is a key molecule in this process, as it predominantly forms through the sequential addition of hydrogen atoms to condensed CO molecules. Once present on the ice mantles, it is considered a fundamental precursor of more complex interstellar species.

To determine the importance of the various chemical processes governing this interplay, I conduct multi-wavelength observational studies and obtain relative abundances of solid- and gas-phase molecules, particularly of methanol. This methodology allows to calculate gas-to-ice ratios and directly access the efficiencies of condensation and desorption processes. The selected targets are the cold protostellar envelopes of low-mass stars belonging to three nearby star-forming regions, with distinct physical conditions and histories. By comparing these it is possible to test the dependencies of the chemical evolution of protostars on the large-scale environment from which they form.

The calculated CH_3OH gas-to-ice ratios of the order of $\sim 10^{-3} - 10^{-4}$ validate previous experimental and theoretical predictions, consistent with a considerably efficient non-thermal desorption mechanism in cold envelopes. Similarities in the gas-to-ice ratios in different nearby star-forming regions suggest that the CH_3OH-mediated chemistry in the outer protostellar envelopes is relatively independent on variations of the physical conditions. This might explain the ubiquitous presence of methanol in a variety of interstellar and circumstellar environments. The combination of millimetric and infrared observations presented in this thesis has proven to be an essential tool to cast light onto the small-scale variations in the ice chemistry and its relation to the physics on large scales in star-forming regions. Thereby, these studies serve as a critical pathfinder for future work with the *James Webb Space Telescope* and the *Atacama Large Millimeter/submillimeter Array* to constrain further the routes to the formation of complex molecules during the embedded stages of star formation.

Dansk resumé

Vekselvirkningerne mellem støv, is og gas spiller en yderst vigtig rolle for kemien i de områder hvor stjerner og planeter bliver dannet. Forskellige kemiske reaktioner foregår i iskapperne på støvkorn og i gas og som konsekvens regulerer balancen mellem disse to faser den kemiske udvikling af nydannede stjerner og planeter. Methanol (CH_3OH) er et fundamentalt molekyle i disse processer eftersom det dannes når hydrogen atomer tilføjes til CO molekyler i isen på støvkornene. Dets videre kemiske udvikling gør det til en vigtig byggesten for mere komplekse molekyler i den interstellare gas.

For at belyse naturen af de kemiske processer der styrer balancen mellem isen og gassen har jeg foretaget målinger af molekyler tilstede i disse to faser gennem astronomiske observationer ved forskellige bølgelængder. Ved hjælp af disse metoder bestemmer jeg den relative forekomst af molekylerne i isen og gassen og derigennem hvor effektivt de henholdsvis fryser ud og fordamper fra iskapperne af støvkornene. Specifikt har jeg studeret de kolde skyer omkring unge stjerner i tre nære stjerne-dannende områder, hver med deres egne karakteristiske fysiske egenskaber og historier. Ved at sammenligne disse områder er det muligt at bestemme hvordan protostjerners kemiske udvikling afhænger af området hvori de dannes.

De beregnede CH_3OH gas-til-is forhold af størrelsesordener $\sim 10^{-3}-10^{-4}$ understøtter tidligere eksperimentelle og teoretiske forudsigelser og er konsistente med at der er en effektiv ikke-termisk fordamning af CH_3OH i de kolde skyer omkring de unge stjerner. Henover de tre områder viser gas-til-is forholdene forholdsvis små variationer, hvilket er en indikation af at CH_3OH kemien er mindre afhængig af de specifikke fysiske betingelserne i områderne. Dette kan muligvis forklare hvorfor methanol er tilstede generelt i interstellare og cirkumstellare områder. Kombinationen af observationer ved millimeter og infrarøde bølgelængder præsenteret i denne afhandling er et vigtigt redskab for at studere detaljerne i is-kemien og dens relation til de fysiske variationer på store skalaer i de stjerne-dannende områder. Dermed vil disse studier også virke som et vigtigt første skridt for fremtidige observationer med *James Webb Space Telescope* og *Atacama Large Millimeter/submillimeter Array* med henblik på at fastlægge de kemiske reaktioner der fører til dannelsen af komplekse organiske molekyler i løbet af de tidligste stadier i livet af unge stjerner.

Acknowledgments

"Traveller, there is no road;
you make your own path as you walk."
–Antonio Machado

As Antonio Machado writes "el camino se hace al andar", "you make your own path as you walk". I started "walking" (or better cycling?!) in Denmark about five years ago and it is now time to thank those who have accompanied me throughout this metaphoric ride. I would like to express my deep gratitude towards my supervisor, Jes Jørgensen, for his excellent guidance during the past years, which allowed me to grow professionally. Your supervision made me a better scientist. Thank you for giving me the possibility to select the main research topic of my Ph.D. and for always being available whenever I needed your help. Also, thanks for sharing your vast knowledge in observational astronomy and for allowing me to go observing on Mauna Kea, Hawaii - an experience I will surely never forget. Similarly, I want to thank Lars Kristensen for his immense support throughout these years, for assisting during interferometric data reduction, and providing crucial feedback on observational and research proposals. I often happen to think what a great opportunity it has been to join the Submillimeter group. Thank you Lars and Jes for your competence and dedication, for transmitting me your passion for astrochemistry, and for being role models to look up to.

I also want to acknowledge my collaborators, in particular Will Rocha, for spending a significant amount of his time guiding me through the spectral decomposition of the infrared data, and Tue Hassenkam for his advice in developing the analysis of the Murchison meteorite as an additional project besides my Ph.D. I also want to say grazie to Piero Ugliengo for introducing me to the field of astrochemistry in the first place.

StarPlan has been a nice and stimulating working environment which I will undoubtedly miss. I want to thank all my colleagues, in particular Catarina Fernandes, Philipp Weber, Elizabeth Artur de la Villarmois, Laura Bouvier, Kasia Dutkowska, Manar El Akel, Charl van der Walt, Sigurd Jensen, Mafalda Costa, Mirek Groen, Elishevah van Kooten, Nikitha Saji, Rajita Kuruwita, Georgy Makhatadze, Sébastien Manigand, Niina Jensen, Siw Egdalen, Ke Zhu, Lu Pan, Zhengbing Deng, Jean Bollard, Lene Bentzen, Sylvia Blaaw and Marianne Bentsen. Tusind tak to all of you, for the epic conversations during lunches and Friday bars: your daily support made the work a lot of fun!

Walking this path would not have been as pleasant without the company of all my friends, who helped me face difficult times and celebrated my accomplishments. Many thanks to my flatmates in Fuglebakkevej 87, Eleonora, Marilena, Niina and Emil: it has been great to share my daily routine with cheerful friends like you. Moreover, I am glad to be part of a joyful group of lindy hoppers, thanks for the uncountable laughs and good dances. I also want to thank my friends in Italy - although we have been living in two

different countries for many years now, when we meet up during Carnival it feels as if I have never left. A big thank also goes to Hannah, Joana, Joachim, Pau, Lea and Alejandra who have become dear friends in an incredibly short amount of time.

Finally, I want to thank my extraordinary family, for the unconditional love and support. Dankeschön Regina and Helmut, for hosting Michael and me during the first lockdown and for caring so much about me. I will never forget the laughs during my $28^{'h}$ birthday when we opened the frozen champagne! I want to say thank you to my grandparents for nurturing my passion for nature, and therefore for letting me play and experiment in the garden all the day long. Zio Gulbert, for being the cheerful uncle he is and for always being present. Your curiosity in studying and preserving this world surely inspired me to become a researcher. Se ho deciso di intraprendere lo studio delle stelle, di sicuro c'é anche il tuo zampino! I want to thank my sister Elisabetta for leading the way in many occasions when we were kids and for always being able to clear my mind when I have to take an important decision. Non ci sono parole per descrivere il nostro legame - davvero non ci sono - e la cosa non sai quanto mi rende felice. I want to thank my parents Daniela and Graziano, for giving me the freedom to walk my own path and not narrowing my horizons. You have taught me to appreciate cultural diversity and to be curious: two skills that made me quickly feel at home in a foreign country. Grazie per il vostro supporto e per i vostri insegnamenti. Last, but not least, I want to thank Michael, for caring so much about our relationship, committing to it and frequently travelling back and forth between Heidelberg and Copenhagen during these past years. Thank you for your incredible support throughout the thesis writing, particularly during the LaTeX breakdowns, and for your love. I am very "prudente" of our relationship.

Contents

ABSTRACT v

DANSK RESUMÉ vii

ACKNOWLEDGEMENTS ix

CONTENTS xii

1 INTRODUCTION 1
1.1 The formation and evolution of a low-mass star . . . 3
1.1.1 The earliest protostellar classes: Class 0 and Class I . . 6
1.2 Chemical processes in star-forming regions . . . 8
1.2.1 Gas-phase chemistry . . . 8
1.2.2 Grain-surface and ice chemistry . . . 11
1.2.3 Desorption processes . . . 13
1.3 The gas and ice interplay in protostellar envelopes . . . 14
1.4 The astrochemical relevance of methanol . . . 17

2 METHODS 19
2.1 Molecular spectroscopy . . . 19
2.2 Observing molecules at infrared wavelengths . . . 21
2.2.1 Decomposition of infrared spectra . . . 23
2.3 Observing molecules at millimeter wavelengths . . . 25
2.3.1 Single-dish versus interferometric observations . . . 25
2.3.2 Two-antenna interferometer . . . 27
2.3.3 Interferometric data calibration and imaging . . . 30
2.3.4 Combination of interferometric and single-dish data . 33

3 THE STAR-FORMING REGIONS 39
3.1 The Serpens Molecular Cloud Complex . . . 39
3.2 The Orion Molecular Cloud Complex . . . 41
3.3 The Corona Australis Molecular Cloud Complex . . . 42

4 THIS THESIS 45
4.1 Research context and description . . . 45
4.2 Publications . . . 47
4.2.1 Article I: Linking ice and gas in the Serpens low-mass star-forming region . . . 48
4.2.2 Article II: Linking ice and gas in the λ Orionis Barnard 35A cloud . . . 48
4.2.3 Article III: Linking ice and gas in the Coronet cluster in Corona Australis . . . 49
4.3 Overall conclusions and outlook . . . 50
4.4 Own contributions versus contributions of collaborators . . . 52

5 LINKING ICE AND GAS IN THE SERPENS LOW-MASS STAR-FORMING REGION 55
5.1 Introduction . . . 56
5.2 Observations and archival data . . . 59
5.2.1 SMA and APEX observations . . . 59

5.2.2 VLT observations . . . 61
5.3 Results . . . 62
5.3.1 Ice column densities . . . 62
5.3.2 Gas column densities . . . 70
5.4 Analysis . . . 71
5.4.1 H_2 column density and physical structure of the region 71
5.4.2 Combined gas-ice maps . . . 73
5.4.3 Gas and ice variations . . . 76
5.5 Discussion . . . 78
5.6 Conclusions . . . 79

APPENDICES 83
5.A Fitting of ice data . . . 83
5.A.1 Continuum determination . . . 83
5.A.2 Optical depth fitting . . . 84
5.A.3 Derivation of H_2O and CH_3OH ice column density . . 89
5.A.4 Derivation of CO ice column density . . . 89
5.B Producing gas-phase maps . . . 91
5.B.1 Combination of interferometric and single-dish data . 91
5.B.2 CO isotopologue optical depth . . . 91
5.C Producing an H_2 column density map . . . 97

6 LINKING ICE AND GAS IN THE λ ORIONIS BARNARD 35A CLOUD 99
6.1 Introduction . . . 100
6.2 Observations and archival data . . . 103
6.2.1 SMA and APEX observations . . . 103
6.2.2 JCMT/SCUBA-2, Spitzer IRAC, 2MASS, IRAM 30 m and AKARI data . . . 105
6.3 Results . . . 105
6.3.1 Gas-phase species . . . 105
6.3.2 Ice column densities . . . 110
6.3.3 H_2 column densities . . . 111
6.4 Analysis . . . 113
6.4.1 Gas-ice maps . . . 113
6.4.2 Gas and ice variations . . . 114
6.4.3 Comparison with previous gas-ice maps of B35A . . 117
6.5 Discussion . . . 119
6.5.1 Sputtering of CH_3OH in B35A . . . 120
6.5.2 Gas-to-ice ratios . . . 121
6.6 Conclusions . . . 123

APPENDICES 125
6.A Production of gas-phase maps . . . 125
6.A.1 Interferometric and single-dish data combination . . 125
6.A.2 Optical depth of the CO isotopologues . . . 125
6.A.3 Channel maps and spectra of individual transitions . 126
6.A.4 Derivation of gas-phase column densities . . . 127
6.B H_2 column density from visual extinction . . . 132

7 LINKING ICE AND GAS IN THE CORONET CLUSTER IN CORONA AUSTRALIS 135
7.1 Introduction . . . 136
7.2 Observations and archival data . . . 139
7.2.1 SMA observations . . . 139

7.2.2 Ancillary data 140
7.3 Results 140
7.3.1 Gas-phase detections 140
7.4 Analysis 147
7.4.1 H_2 column densities 147
7.4.2 Gas and ice variations in the Coronet 148
7.4.3 IRS7A and IRS7B 150
7.5 Discussion 150
7.6 Conclusions 153

APPENDICES 155
7.A Non-detections 155

BIBLIOGRAPHY 157

1

Introduction

"It is difficult to admit the existence of molecules in interstellar space because when once a molecule becomes dissociated there seems no chance of the atoms joining up again."
—Sir Arthur Eddington

Life on Earth arose at least 3.7 billion years ago, when our planet was approximately 700 Myr old (Mojzsis *et al.*, 1996; Hassenkam *et al.*, 2017). This time estimate comes from biogenic carbon inclusions found in the oldest known terrestrial rocks, the Isua rocks in West Greenland. Although upper limits on *when* life appeared are available, it is still very uncertain *how* life emerged in the Universe, and in particular what were the exact physical conditions triggering the transition from chemistry to biology. In this context, astronomical observations of young solar-type stars can yield valuable insights onto the environment and reactions at play during the birth of planetary systems akin to our Solar System. Comparisons between the molecular species detected around young stars and found in pristine meteorites, comets and asteroids, provide important clues on the chemical evolution leading to the origin of life in the early Solar System and potentially elsewhere in the Universe.

What we currently know about life is that it appeared as the product of complex chemical reactions leading to stable biomolecules assembling into cells and, ultimately, multicellular organisms (Ehrenfreund and Charnley, 2000). A logical key step consists of tracing what are the ingredients required for the synthesis of biomolecules when solar-type stars are born. From astronomical observations and theoretical models, we can ascertain that gas-phase and solid-state chemistries are intertwined and promote chemical complexity during the assembly of a planetary system (e.g., Herbst and van Dishoeck, 2009; Jørgensen *et al.*, 2020; Öberg and Bergin, 2021). The subtle interplay between these two phases of matter is involved in the formation of diatomic molecules such as molecular hydrogen (H_2), to the production of the building blocks of life in planetary systems. The study of this interplay is fundamental to unveil the intricate chemical steps that brought simple molecules to give rise to larger biomolecules and, ultimately, to the primordial metabolism on early Earth.

The work presented in this thesis investigates the solid-gas interplay in protostellar envelopes surrounding low-mass protostars. The main aim is to test how different physical conditions impact the balance between gas-phase and solid-state chemistries, and in a broader context, how this affects the composition of the material incorporated into forming-planets. To accomplish this goal, this thesis is driven by comparative studies of gas and solid interstellar molecules at millimeter and infrared wavelengths, respectively.

The main focus of this is methanol (CH_3OH). Methanol is a prime test-case as according to models and laboratory experiments, it predominantly forms as a consequence of the solid-gas interplay (hydrogenation of condensed CO molecules onto the grain surfaces) and it is associated with the production of more complex molecules. To explore how the environment influences the balance between gas and solid-state chemistries, observational constraints on the gas-to-ice ratios of CH_3OH are calculated in nearby star-forming regions located in three different giant molecular clouds.

This thesis is structured as follows. Chapter 1 gives an introduction to the present view of the star-formation process, based on recent astronomical observations, theoretical predictions and simulations. In particular, it provides an overview of the evolutionary stages of the formation of a low-mass star, focusing on the solid and gas-phase composition of the material involved in this journey. The remainder of the chapter describes our current knowledge of the gas-phase and solid-state chemistries at work in pre- and protostellar environments, setting the initial conditions for planet formation.

Chapter 2 outlines the methods adopted in this thesis. It begins with a summary of molecular spectroscopy, focusing on the dominant transitions characterizing molecular spectra of star-forming regions. It continues with a description of astronomical observations of solid-state and gas-phase interstellar molecules at infrared and millimeter wavelengths. The chapter ends with an introduction to the basic principles of radio-interferometry, and to the combination of single-dish and interferometric data.

Chapter 3 presents the three low-mass star-forming regions selected as testbeds for the presented research: the Serpens cloud core, the Orion Barnard 35A cloud and the Coronet cluster in Corona Australis. It starts with a presentation of the giant molecular cloud complexes and it continues with a brief, more detailed characterization of the physical structure of the star-forming clusters.

Chapter 4 summarizes the articles forming an integral part of this thesis. It discusses their contribution to the field of astrochemistry and proposes some avenues for future work. The articles themselves are presented in Chapters 5, 6 and 7.

1.1 THE FORMATION AND EVOLUTION OF A LOW-MASS STAR

The journey of the solid-state and gas-phase material leading to the formation of a low-mass star starts in dense regions of the InterStellar Medium (ISM), called *Giant Molecular Clouds* (GMCs). These are large asymmetric structures with sizes on the order of ≈100 pc and masses ≈ $10^5 M_\odot$ (Herbst and van Dishoeck, 2009; Heyer and Dame, 2015). Table 1.1 summarizes the typical densities and temperatures of these environments. The vast majority of their mass is in the form of molecular gas, although a smaller fraction (approximately 1 % of the total mass) is locked in micrometer-size dust grains mostly composed of silicates and refractory carbon-bearing compounds (Draine, 2003; Henning, 2010).

Inside giant molecular clouds reside higher density regions with sizes of ≈0.1 pc, called *dense cores*. The average dense core density is a few 10^4 cm^{-3} and the temperature is ≈10 K (Myers *et al.*, 1983; Benson and Myers, 1989; Bergin and Tafalla, 2007). Dense cores tend to form along filamentary structures (e.g., Schneider and Elmegreen, 1979; Myers, 2009; André *et al.*, 2010; Könyves *et al.*, 2015) which originate as a consequence of the cloud turbulent activity compressing the molecular gas (Padoan and Nordlund, 2002; Mac Low and Klessen, 2004; André *et al.*, 2014). Figure 1.1 shows one of the most notable examples of filamentary networks, observed in the Polaris flare cloud.

Pre-stellar cores can undergo gravitational collapse, initiating a cascade of processes leading to the formation of a star, and eventually of a planetary system. In the classical description of star formation, the core is approximated as an isothermal sphere of gas with a density profile following the power-law $\rho \propto r^{-2}$ at larger radii and flattening at small radii. The maximum mass the core can have to be gravitationally bounded is referred to as the mass of a *Bonnor-Ebert sphere* ($M_{\rm BE}$) (Ebert, 1955; Bonnor, 1956):

$$M_{\rm BE} = \frac{C_{\rm BE} c_{\rm s}^4}{\sqrt{P_0 G^3}} \tag{1.1}$$

where the constant $C_{\rm BE}$ is ~1.8, $c_{\rm s}$ represents the isothermal sound speed, P_0 is the pressure of the gas and G is the gravitational constant. When the mass of the core exceeds the critical mass of the Bonnor-Ebert sphere, the core begins to collapse in free-fall from the central regions, characterized

TABLE 1.1: Comparison between densities and temperatures in interstellar, circumstellar and planetary environments. The density is expressed as hydrogen nuclei per cm^{-3}.

Environment	n(cm^{-3})	T(K)	Object
Giant Molecular Cloud	100	15	Orion
Dark Cloud	500	10	Taurus-Auriga
Dense Core	10^4	10	TMC-1
Disk midplane*	$10^6 - 10^{11}$	10 – 150	T-Tauri
Planet	†10^{19}	300	Earth

Note: Adapted from Stahler and Palla (2004). * from Williams and Best (2014). † molecules per cm^{-3}.

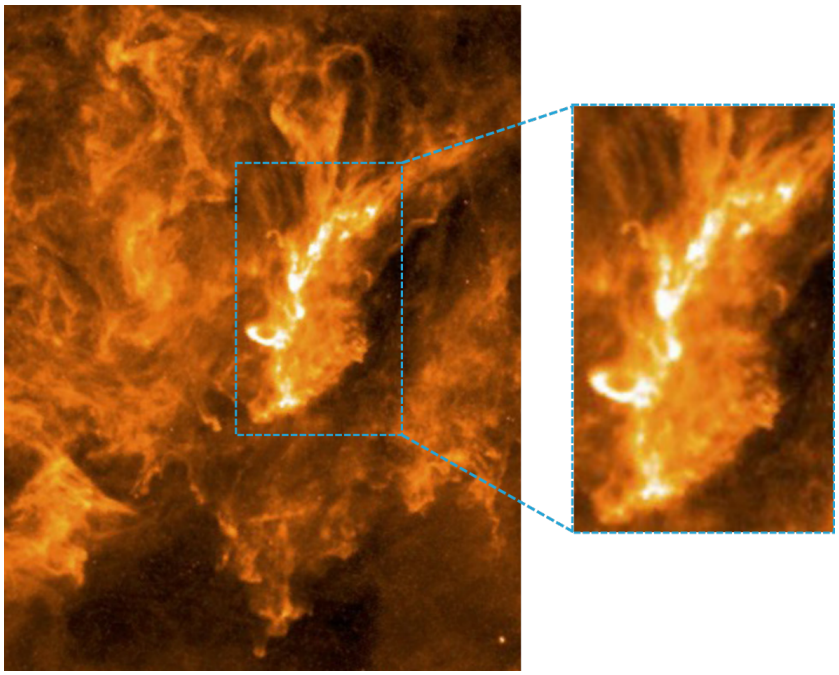

FIGURE 1.1: *Herschel*/SPIRE 250 μm image capturing the filamentary structure of the Polaris flare cloud. The zoom-in displays the brightest filament which harbours multiple non-spherical dense cores. Adapted from André (2017).

by the highest densities. The density profile within the collapse radius, corresponding to the free-falling inner *protostellar envelope* regions, follows the power-law $\rho \propto r^{-1.5}$. This inflow region expands radially at the sound speed until the accretion front reaches the external layers of the core. Since the expansion occurs from the inner to the outer layers of the cloud core, this model is called the *inside-out collapse* (Shu, 1977).

In general, the inside-out collapse provides a good conceptual understanding of the low-mass star-formation process, but it does not necessarily account for the full physical picture. For instance, modern-day high resolution observations (e.g., Lin *et al.*, 2017; Zhang *et al.*, 2020) and detailed numerical simulations (Kuffmeier *et al.*, 2017; Bate, 2018) have shown that cores are not spherical as assumed by classical calculations (Jeans, 1902), but inherit more complex structures from the large-scale environment as can be seen in Figure 1.1. Additionally, stars often form in clusters (Duquennoy and Mayor, 1991; Tobin *et al.*, 2015; Murillo *et al.*, 2016), as it is the case for the protostars studied in Chapters 5, 6 and 7.

The sequence of events implicated in the formation and evolution of a protostar entails multiple physical processes, many of which are only partially understood and challenged by observations and computational simulations. Figure 1.2 displays a simplified illustration of such processes. After the collapse has begun, more and more material accreates towards the center of the core. When the material reaches densities and temperatures sufficiently high ($T \approx 10^6$ K) for deuterium fusion reactions to ignite, a protostar forms at the center. The infalling material carries the angular momentum of the parental core. Due to the conservation of angular momentum, a portion of material settles into a *circumstellar disk* around the protostar (Tscharnuter, 1975; Terebey *et al.*, 1984). The presence of a large-scale

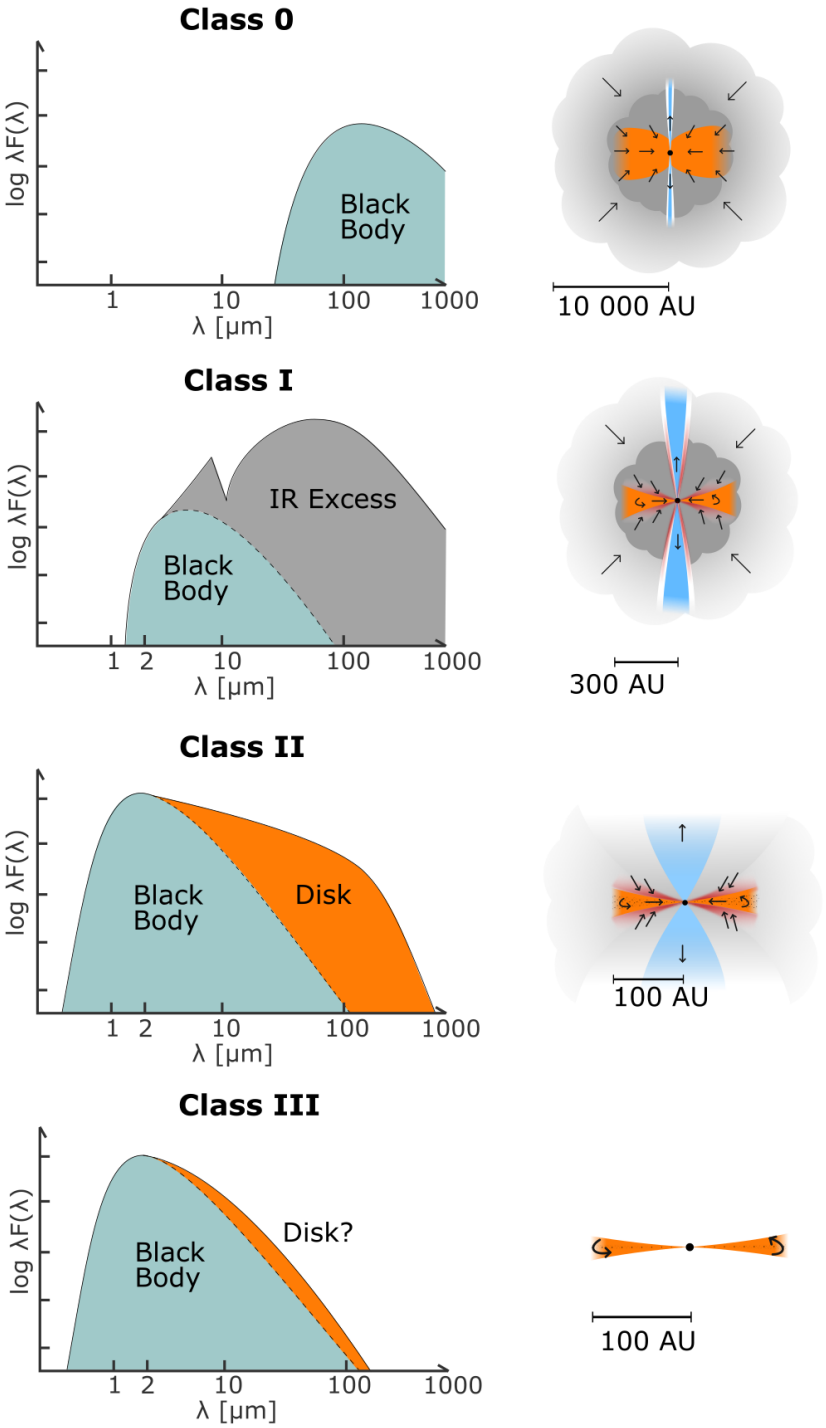

FIGURE 1.2: Evolutionary stages of low-mass young stellar objects. *Left:* Spectral energy distributions (SEDs). *Right:* Cartoon representing each protostellar stage. Credit: M. V. Persson.

magnetic field regulates the rotation of the disk (Pudritz and Ray, 2019). It can remove angular momentum from the protostar-disk system through powerful outflows such as jets and winds (Blandford and Payne, 1982) and via a process called magnetic braking (Lüst and Schlüter, 1955; Mestel, 1968).

The circumstellar disk is commonly referred to as *protoplanetary disk*, to indicate that it is the birthplace of planets. Disks lifetimes are typically on

TABLE 1.2: Physical quantities used to classify young stellar objects.

Class	SED slope (α_{IR})	Bolometric temperature (T_{bol})	Luminosity ratio (L_{submm}/L_{bol})
0	-	$T_{bol} \leq 70$ K	> 0.5 %
I	$\alpha_{IR} > 0.3$	70 K $< T_{bol} \leq 650$ K	< 0.5 %
II	-1.6 $< \alpha_{IR} <$ -0.3	650 K $< T_{bol} \leq 2800$ K	-
III	$\alpha_{IR} < 1.6$	$T_{bol} > 2800$ K	-

Note: Adapted from Williams and Cieza (2011). The values for the bolometric temperature and L_{submm}/L_{bol} are taken from Chen *et al.* (1995) and Dunham *et al.* (2014), respectively.

the order of 1 – 10 Myrs (Mamajek, 2009; Williams and Cieza, 2011). In this period of time, the aggregation of dust grains in the disk interior forms pebbles of bigger and bigger sizes which ultimately lead to the assembly of planetary embryos, and eventually planets (Brauer *et al.*, 2008; Blum and Wurm, 2008). It is still not completely clear when exactly planet formation occurs, but recent high-resolution observations of young disks suggest that planets start to assemble earlier than previously thought, possibly already during the embedded (Class 0/I) stages of the young stellar object (ALMA Partnership *et al.*, 2015; Andrews *et al.*, 2018; Harsono *et al.*, 2018; Alves *et al.*, 2020).

1.1.1 *The earliest protostellar classes: Class 0 and Class I*

The evolution of young stellar objects have traditionally been captured through classification of them based on their *spectral energy distributions* (SEDs). Figure 1.2 displays the SEDs and the illustration of the corresponding protostellar class. Initially, the young protostars were catalogued into three classes, Class I-III, according to the slope of their spectral energy distributions at near- and mid-infrared wavelengths (Lada, 1987)). A decade later, a second classification was introduced which, compared to the previous grouping, added an earlier class, the "Class 0" (Andre *et al.*, 1993). When moving from Class 0 to Class III, the spectral energy distribution curve is shifted to shorter wavelengths (Fig. 1.2), reflecting the dispersal of the protostellar envelope and, later in the evolution, of the circumstellar disk.

Young stellar objects are classified according to:

- their *infrared spectral index* $(\alpha_{IR}) = \frac{d\ \log(\lambda F_\lambda)}{d\ \log(\lambda)}$, which represents the slope of the SED in logarithmic scale in the spectral range between 2.2 and 20 μm (Lada, 1987);
- their *bolometric temperature* (T_{bol}), i.e., the temperature of a black body with the same mean frequency as the observed continuum spectrum (Myers and Ladd, 1993);
- the ratio between the luminosity at submillimeter wavelengths ($\lambda \geq 350$ μm) and the bolometric luminosity L_{submm}/L_{bol} (Dunham *et al.*, 2014). This identifier was introduced to discriminate between Class 0 and Class I sources.

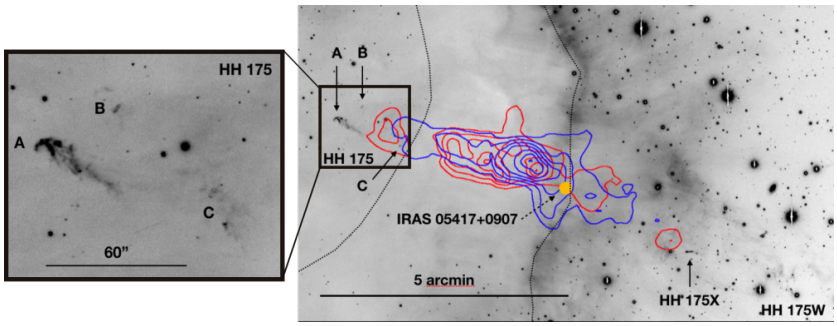

FIGURE 1.3: The molecular outflow driven by IRAS05417+0907 overlaid on a [SII] optical image. The bright clumps of the Herbig-Haro 175 can be observed towards the end of the eastern lobe of the outflow, to the left of the image. Credit: Reipurth and Friberg (2021).

Table 1.2 delineates the conventional values adopted to classify young stellar objects. In general, this classification provides a broad picture of the nature of the individual sources. However, it is important to remark that the classes do not directly reflect the physical stage of an object (Robitaille *et al.*, 2006), as shown by synthetic observations based on MHD simulations of collapsing giant molecular clouds (Frimann *et al.*, 2016) and actual observations of the earliest stellar stages (e.g., Tobin *et al.*, 2012; Tobin *et al.*, 2015).

Class 0

In a physical description, Class 0 protostars are surrounded by a massive protostellar envelope constituting at least 50% of the total mass of the protostar-envelope system. Such envelopes have typical sizes of 10^4 AU and might harbour a thick protodisk. The spectral energy distribution of Class 0 sources peaks at submillimeter wavelengths - tracing the presence of cold material in their infalling envelope - and it is characterized by the lack of emission in the near-infrared (Andre *et al.*, 1993; Table 1.2). Typical bolometric temperatures for this class are $\leq$ 70 K (Chen *et al.*, 1995) and the submillimeter-to-bolometric luminosity ratio $L_{\rm submm}/L_{\rm bol}$ is $>$ 0.5 % (Dunham *et al.*, 2014).

The estimated life-time of the Class 0 stage is $\approx$50 000 yrs (Kristensen and Dunham, 2018) and it is characterized by the ejection of material through the launch of outflows and jets sometimes associated with Herbig-Haro objects (Herbig, 1950; Haro, 1952). These are small nebulae typically extending for 20−30″ and detected from peculiar bright clumps of gas located along the outflow direction (Reipurth and Bally, 2001). They are indicators of the powerful mass-loss from newly born stars. Figure 1.3 depicts an example of Herbig-Haro objects within the giant molecular outflow launched by the multi-protostellar system IRAS05417+0907 (Reipurth and Friberg, 2021). How outflows affect the chemical structure of the protostellar envelope and in particular the exact balance of molecules in the gas- and solid-state is one of the topics of Chapters 5, 6 and 7.

Class I

From a physical point of view, Class I protostars also exhibit an envelope - although less massive than the Class 0 one - and they are surrounded by a disk with a radius in the range $\approx$25−500 AU (Williams and Cieza, 2011).

The emission of Class I sources is a composite of the envelope and of the disk contributions. The spectral energy distribution of Class I sources peaks in the mid-/far-infrared (Figure 1.2) and it is characterized by the 9.7 μm absorption band of dust silicates (Henning, 2010; Henning and Meeus, 2011). The spectral index is > 0.3 (Table 1.2) and the bolometric temperature is in the range 650 K < $T_{\rm bol}$ ≤ 2800 K (Chen *et al.*, 1995). The submillimeter-to-bolometric luminosity ratio $L_{\rm submm}/L_{\rm bol}$ is < 0.5 % (Dunham *et al.*, 2014). As for Class 0 sources, also Class I protostars manifest powerful outflows and Herbig-Haro objects, responsible for carving a cavity in Class I envelopes. However, these flows are typically less energetic compared to the earliest class (e.g., Mottram *et al.*, 2017).

The Atacama Large Millimeter/Submillimeter Array (ALMA) and other interferometers, revealed the presence of disks surrounding multiple Class I sources (e.g., Harsono *et al.*, 2014; Artur de la Villarmois *et al.*, 2019) and a number of Class 0 objects (e.g., Tobin *et al.*, 2012; Segura-Cox *et al.*, 2018). Since protoplanetary disks form already at these early stages, the study of Class 0 and I sources provides important clues on the initial physical and chemical conditions for planet formation.

1.2 CHEMICAL PROCESSES IN STAR-FORMING REGIONS

After describing the formation of low-mass stars, and introducing the earliest protostellar stages, the remainder of this chapter will focus on the chemical evolution of the material involved in the star-formation process. Before outlining the changes registered in the composition of the material throughout this journey, the following two sections will provide a summary overview of the chemical processes in star-forming environments. These can be divided into two groups, depending on the state of matter in which they occur: the gas-phase chemistry and the solid-state chemistry. The latter takes place on the dust grain surfaces which are covered with ice mantles, composed by water and other volatile species. These two chemistries are highly intertwined and specific types of reactions take place exclusively in one of the two phases, leading to different products. Since gas-phase molecules can condense on the ice mantles and, in turn, solid-state molecules on the grain surfaces can be released to the gas-phase, the balance between the gas-phase chemistry and the solid-state chemistry is crucial for the chemical evolution of interstellar material. One of the most obvious example of the gas and ice interplay is the methanol-mediated chemistry. Methanol can be produced on the grain surfaces upon hydrogenation of condensed CO molecules (e.g., Watanabe and Kouchi, 2002; Fuchs *et al.*, 2009), and it is involved in the formation of more complex molecules (e.g., Garrod *et al.*, 2008). Consequently, the gas and ice interplay plays a major role in setting the initial chemical conditions for planet formation (van Dishoeck and Bergin, 2020).

1.2.1 *Gas-phase chemistry*

The chemistries of star-forming regions and those of planets differ because these environments are characterized by different physical conditions. Table 1.1 shows that the density of star-forming sites is significantly lower

compared to planetary atmospheres. This inhibits three-body reactions in the gas-phase, i.e., $A + B + C \rightarrow ABC^* \rightarrow AB + C$, which are common on Earth. Additionally, the typical temperatures of bulk material in regions of star and planet formation are far too low for reactions with activation energy barriers to occur (Herbst and Klemperer, 1973; Watson, 1973), except in regions in the vicinity of the newly formed protostar. Consequently, the reactions governing the chemistry of stellar nurseries are exothermic, that is they are barrierless and release energy in the form of heat (Herbst and Klemperer, 1973). The principal gas-phase reaction mechanisms occurring under the physical conditions outlined in Table 1.1 can be divided into three groups (Figure 1.4): bond formation, bond destruction and bond rearrangement.

Bond formation

Among the gas-phase bond formation reactions, the most effective pathway is *radiative association* (Herbst and Klemperer, 1973):

$$A + B \rightarrow AB^* \rightarrow AB + h\nu \tag{1.2}$$

during which the collision of two gas-phase species A and B leads to the formation of an unstable complex AB^*. This complex is stabilized by the formation of a bond between A and B, and through the emission of a photon. Since this mechanism requires gas-phase densities high enough for collisions to manifest, it implies that the principal reactant is the most abundant element in star-forming regions, i.e. atomic or molecular hydrogen (Herbst and Klemperer, 1973).

Bond destruction

The dominating bond destruction channel in regions subjected to UV radiation, e.g., circumstellar environments, photon-dominated regions (PDRs), is *photodissociation* (Hollenbach and Tielens, 1999):

$$AB + h\nu \rightarrow A + B. \tag{1.3}$$

This destruction pathway can be direct, indirect or spontaneous. Most of the interstellar molecules undergo direct photodissociation, where a molecule is excited into a dissociative electronic state upon absorption of a photon. The energy of the incident photon needs to be above the bond dissociation energy for the dissociation to occur.

In the indirect channel, the molecule is excited to a bound electronic state, and then falls into a dissociative state, i.e., *predissociation* (van Dishoeck and Black, 1988; van Dishoeck, 1988). Alternatively, from the bound electronic state, the excited molecule can decay by spontaneously emitting a photon, i.e., *spontaneous radiative association* (van Dishoeck and Black, 1988; Lee *et al.*, 1996). In the absence of UV irradiation, chemical bonds can be destroyed via collisions with electrons and cosmic rays in a process called *dissociative recombination*:

$$AB + e^- \rightarrow A + B. \tag{1.4}$$

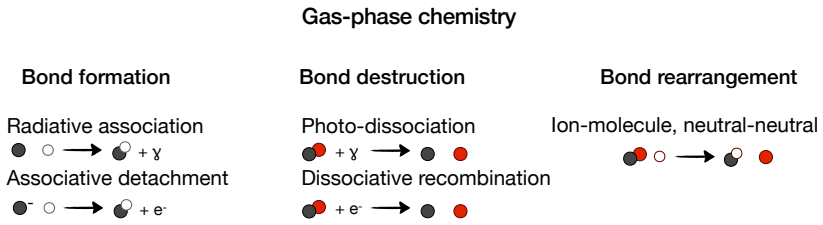

FIGURE 1.4: Schematic representation of the most common gas-phase chemical reactions in star-forming regions. Credit: Öberg and Bergin (2021).

Bond rearrangement

A particularly important group of reactions in the gas-phase of the interstellar medium is the one where the bonds in a molecule are rearranged:

$$AB + C \rightarrow A + BC \tag{1.5}$$

where the reactants are ions and molecules or neutral species only, i.e, *ion-molecule reactions* or *neutral-neutral reactions*. Ion-molecule reactions consists of the ion-capture by a molecule due to the long-range charge attractions between the two reactants, creating an induced dipole moment (Langevin, 1905). These reactions are crucial in gas-phase chemistry and are for example responsible for the formation of the second most abundant molecule in the Universe, CO:

$$C^+ + OH \rightarrow CO^+ + H \tag{1.6}$$

$$CO^+ + H_2 \rightarrow HCO^+ + H \tag{1.7}$$

followed by a dissociative recombination of HCO^+ to form CO + H (van Dishoeck and Black, 1986).

The gas-phase chemistry in dense molecular clouds - especially ion-molecule reactions - is powered by the activity of the simplest polyatomic molecule, protonated molecular hydrogen (H_3^+) (Herbst and Leung, 1989; Dalgarno, 1994; Oka, 2006). H_3^+ is the product of the ionization of H_2 by cosmic-rays or X-rays and its successive protonation (Stecher and Williams, 1969; Stevenson and Schissler, 1958). It is abundantly synthesised in molecular clouds and it has a high chemical reactivity. Being a strong acid, it can donate its "extra" proton to neighboring molecules triggering a large number of ion-molecule reactions.

Neutral-neutral reactions are slower compared to ion-molecule reactions because the reactants are non-charged species and the reactions might have activation energy barriers. Therefore, they typically occur at higher temperatures relative to ion-molecule reactions. For instance, they account for the synthesis of fundamental astrochemical species such as hydroxyl radical (OH) and H_2O in hot gas ($T > 400$ K; e.g., Wagner and Graff, 1987):

$$O + H_2 \rightarrow OH + H \tag{1.8}$$

$$OH + H_2 \rightarrow H_2O + H. \tag{1.9}$$

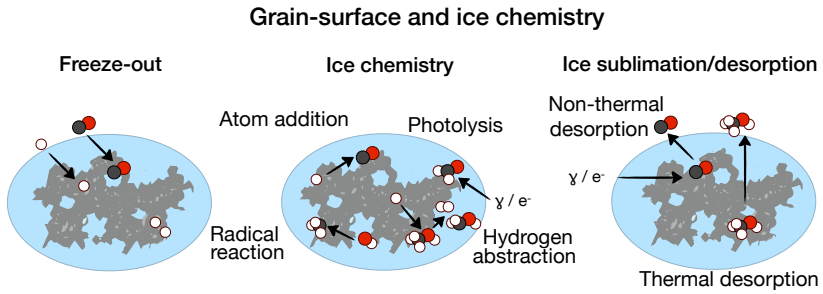

FIGURE 1.5: Schematic representation of the most common grain-surface and ice chemistry reactions in star-forming regions. Credit: Öberg and Bergin (2021).

Recent studies have proved the importance of neutral-neutral reactions not only in high-temperature regions, e.g., hot cores. For instance, it has been shown that they play a key role in the formation of organic molecules akin methoxy (CH_3O), dimethyl ether (CH_3OCH_3) and methyl formate ($HCOOCH_3$) in cold gas (Balucani *et al.*, 2015). This particular synthesis is a good example of interplay between gas and ice chemistry. In fact, the chain of neutral-neutral reactions leading to the three molecules initiates upon the release of methanol (CH_3OH) from the ice mantles (see Sect. 1.2.2).

The efficiency of complex molecule formation via gas-phase pathways compared to solid-state chemistry reactions is not well constrained at present (Sect. 1.2.2). Currently, quantum chemistry models are exploring a number of feasible chemical routes in cold regions. The reactants are typically CH_3OH (Shannon *et al.*, 2013; Antiñolo *et al.*, 2016) or CH_3CH_2OH (Skouteris *et al.*, 2018). The increasing detections of prebiotic molecule precursors are motivating the need for computational studies on the formation and reactivity of such large molecules in the gas phase (e.g., Redondo *et al.*, 2017a; Redondo *et al.*, 2017b).

1.2.2 *Grain-surface and ice chemistry*

The presence of dust grains transforms the chemistry of star-forming environments, expanding the types of chemical processes available and enhancing chemical complexity (Figure 1.5). In fact, although dust grains represent a minor fraction of the total mass of stellar nurseries ($\approx$ 1%; Sect. 1.1), their role as catalysts has a profound impact on the overall interstellar chemistry (Hasegawa *et al.*, 1992; Hasegawa and Herbst, 1993).

In the coldest regions of dense clouds ($T \approx 10$ K) gas-phase species colliding with the surfaces of dust grains are adsorbed in a process called *freeze-out*. This occurs to most interstellar species except for He and H_2, which sublimate at these low temperatures (Hollenbach and Salpeter, 1971). Freeze-out is responsible for the build-up of layers onto the grain surfaces, commonly referred to as ice mantles (Pickles and Williams, 1977; Hasegawa *et al.*, 1992; Ruffle and Herbst, 2001a). Molecules and atoms accreting onto ice mantles, i.e., adsorbates, are either chemically bounded to the surface of the grain, i.e., *chemisorption*, or adsorbed via van der Waals forces, i.e., *physisorption*. Van der Waals forces are weaker compared to molecular bonds implying that physisorbed species require less energy to be released to the gas-phase with respect to chemisorbed species, e.g., Buch and Czerminski

(1991), Bolina and Brown (2005), and Shimonishi *et al.* (2018).

In general, surface reactions are believed to proceed via one of the following mechanisms: *Langmuir-Hinshelwood*, *Eley-Rideal* and *Kasemo-Harris* also referred to as *hot atom*. In the Langmuir-Hinshelwood mechanism, both reactants are mobile and diffuse between binding sites on the grain surface either by tunneling across the potential energy barrier or via thermal hopping until they meet and react (Langmuir, 1922; Hinshelwood, 1940). Alternatively, in the *Eley-Rideal* mechanism, the gas-phase species reacts with a stationary adsorbate (Eley and Rideal, 1940). Finally, in the hot atom mechanism, a gas-phase species collides with the grain and has sufficient kinetic energy to move on the surface until it encounters an adsorbate to react with (Harris and Kasemo, 1981). Among the three mechanisms the Langmuir-Hinshelwood is the most studied and included in astrochemical models (Kolasinski, 2002), whereas the hot atom pathway is thought not to prevail as the hot atom is typically thermalized before encountering a reactant (Cuppen *et al.*, 2017).

The molecules residing onto ice layers can undergo the set of reactions illustrated in Figure 1.5. One of the dominant reactions is H atom addition, i.e. *hydrogenation*, as H atoms due to their small sizes diffuse on grain surfaces via tunneling (Hasegawa *et al.*, 1992). Atom addition reactions lead to the formation of H_2, the most abundant molecule in space (Gould and Salpeter, 1963; Hollenbach and Salpeter, 1971; Watson and Salpeter, 1972; Wakelam *et al.*, 2017). When H atoms react sequentially with heavier elements such as oxygen atoms or O_2 and O_3, the most abundant ice species is formed, H_2O (Tielens and Hagen, 1982; Cuppen and Herbst, 2007; Ioppolo *et al.*, 2008; Miyauchi *et al.*, 2008). This process involves a number of reactions in which H atoms are added and abstracted. Similarly, H atom additions produce ammonia (NH_3) and methane (CH_4) onto ice mantles (van de Hulst, 1946; Qasim *et al.*, 2020). When CO freezes out, a number of chemical routes open up. Most importantly, carbon dioxide (CO_2) is produced (Ruffle and Herbst, 2001b; Ioppolo *et al.*, 2007; Ioppolo *et al.*, 2009) and simultaneously, the sequential hydrogenation of CO initiates the formation of complex organic molecules (COMs) such as methanol (Charnley *et al.*, 1997; Watanabe and Kouchi, 2002; Ioppolo *et al.*, 2007; Fuchs *et al.*, 2009):

$$\mathrm{CO} \longrightarrow \mathrm{HCO^{\bullet}} \longrightarrow \mathrm{H_2CO} \longrightarrow \mathrm{CH_3O^{\bullet}/^{\bullet}CH_2OH} \longrightarrow \mathrm{CH_3OH} \qquad (1.10)$$

where the pathway via $CH_3O^{\bullet}$ is the energetically favourable one, and hence, the prevalent (Song and Kästner, 2017). The implications of the formation of CH_3OH in star-forming regions will be discussed in Sect. 1.4.

In general, the reactions leading to complex molecules involve, besides atoms and molecules, radicals (e.g., Garrod *et al.*, 2008; Öberg *et al.*, 2009b; Chuang *et al.*, 2017), as can be seen in the reaction above. Radicals are typically produced during H addition and abstraction reactions or via photolysis and dissociative recombination. Reactions involving radical additions are considered fundamental to explain the high abundances of complex molecules in embedded young protostars (Garrod *et al.*, 2008; see Sect. 1.3).

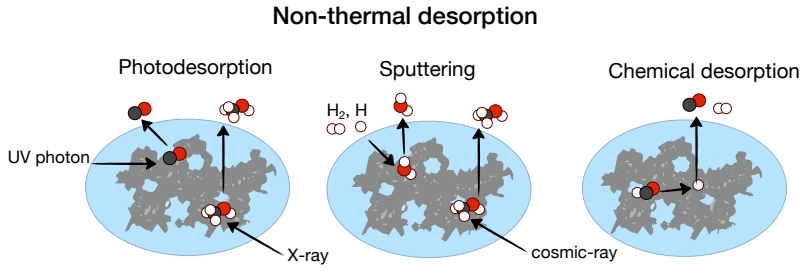

FIGURE 1.6: Schematic representation of the most common non-thermal desorption mechanisms in star-forming regions. Adapted from Öberg and Bergin (2021).

1.2.3 *Desorption processes*

Molecules and atoms residing onto ice mantles can be released to the gas-phase through *desorption* reactions (Figure 1.5). These, jointly with the freeze-out process, govern the interplay between solid-state and gas-phase in star-forming regions, enhancing the chemical complexity of protostars. Desorption reactions are grouped into two categories: thermal and non-thermal.

Thermal desorption

Thermal desorption is triggered upon global heating of the grain which leads to the sublimation of the ice mantles. This chemical process occurs when the dust temperature is higher than the sublimation temperature of a chemical species. It is the most studied desorption reaction, both theoretically (e.g., Penteado *et al.*, 2017; Das *et al.*, 2018; Ferrero *et al.*, 2020) and experimentally, through temperature programmed desorption (TPD) experiments (e.g., Fraser *et al.*, 2001; Collings *et al.*, 2004; Öberg *et al.*, 2005; Bisschop *et al.*, 2006). TPD experiments revealed that thermal desorption is more complex than initially thought as it is sensitive to multiple parameters, most importantly the ice morphology and composition (e.g., Fayolle *et al.*, 2016). Thermal desorption reactions are particularly crucial in protoplanetary disks, because the radii at which they occur determine the so-called *snowlines* (or icelines) which have important consequences on the chemical composition of forming planets (Öberg *et al.*, 2011b; Eistrup *et al.*, 2016; van 't Hoff *et al.*, 2017; Grassi *et al.*, 2020).

Non-thermal desorption

Non-thermal desorption is a consequence of local heating of the grain, followed by a partial sublimation of the ice mantles (Figure 1.6). The factors leading to non-thermal desorption processes are several and they are thought to occur in the cold regions of protostellar envelopes. For instance, the most investigated one is *photodesorption*, when the local heating is caused by impinging UV photons on the grain surface (Westley *et al.*, 1995; Öberg *et al.*, 2009a; Öberg *et al.*, 2009b; Fayolle *et al.*, 2011). This process is not as straightforward because it can lead to the photodissociation of the interested species, a channel that has been explored with molecular dynamics simulations (Andersson *et al.*, 2006; Andersson and van Dishoeck, 2008), and in the laboratory (e.g., Bertin *et al.*, 2016; Cruz-Diaz *et al.*, 2016; Martín-Doménech *et al.*, 2016) especially for H_2O and CH_3OH.

Non-thermal desorption can also be triggered by *sputtering* when atoms and neutral species collide with the grain surfaces and have sufficient kinetic energy to eject ice molecules into the gas-phase. This is considered as the dominant non-thermal desorption process in shocked regions (e.g., Jørgensen *et al.*, 2004; Jiménez-Serra *et al.*, 2008; Kristensen *et al.*, 2010; Suutarinen *et al.*, 2014; Allen *et al.*, 2020). *Cosmic-ray induced sputtering* is also a viable route, and the efficiency of this process has been constrained in the laboratory for pure H_2O, CO_2:CH_3OH and H_2O:CH_3OH:CH_3COOCH_3 ice analogues (Dartois *et al.*, 2018; Dartois *et al.*, 2019; Dartois *et al.*, 2020). These experiments demonstrated that, compared to photodesorption, a large fraction of species is non-thermally desorbed intact during sputtering by cosmic rays.

More recently, an additional non-thermal desorption mechanisms has been proposed in the literature to explain the abundance of complex organics in UV-shielded and quiescent regions (Garrod *et al.*, 2007). It is referred to as *chemical desorption* or *reactive desorption* (Dulieu *et al.*, 2013; Vasyunin and Herbst, 2013; Minissale *et al.*, 2016b; Cazaux *et al.*, 2016; Vasyunin *et al.*, 2017). The factor triggering this desorption channel is the exothermicity of a reaction taking place on the grain surfaces, which is able to expel the product of the reaction or the neighbouring species. Finally, a novel mechanism has been tested called *X-ray photodesorption*. This process is thought to have an impact on the desorption of ice mantles in protoplanetary disks initiated by X-rays emitted from the central protostar (Andrade *et al.*, 2010; Dupuy *et al.*, 2018; Jiménez-Escobar *et al.*, 2018; Ciaravella *et al.*, 2020; Basalgète *et al.*, 2021a; Basalgète *et al.*, 2021b).

This discussion clearly shows that desorption processes, especially the non-thermal ones, are far from being well understood. Laboratory data exists only for a discrete number of species and many of the above mechanisms are not yet included into astrochemical models. In addition to this, it is a challenging task to distinguish between the various non-thermal desorption mechanisms from an observational point of view. This implies that numerous venues exists for future studies on this topic.

After describing the physical processes during star-formation (Sect. 1.1) and the chemical processes involved in it (Sect. 1.2), the upcoming section "brings together the two worlds" by outlining which type of chemistry and molecular complexity is observed around protostars.

1.3 THE GAS AND ICE INTERPLAY IN PROTOSTELLAR ENVELOPES

The gas and ice interplay is ubiquitous in the Universe, and it is involved in all the stages of star and planetary system formation. It is responsible for changes in the ice and gas composition of the envelope material incorporated into protoplanetary disks and, eventually, planet-forming zones (Öberg and Bergin, 2021; van Dishoeck and Bergin, 2020). In this context, a major unanswered question in astrochemistry is whether the disk material and the proto-planets preserve the chemical fingerprints of the parental molecular cloud, i.e., *inheritance* scenario, or not, due various degrees of thermal processing, i.e., *reset* scenario (Pontoppidan and Blevins, 2014). At present, neither of the two hypotheses can be discarded, as the material of pristine

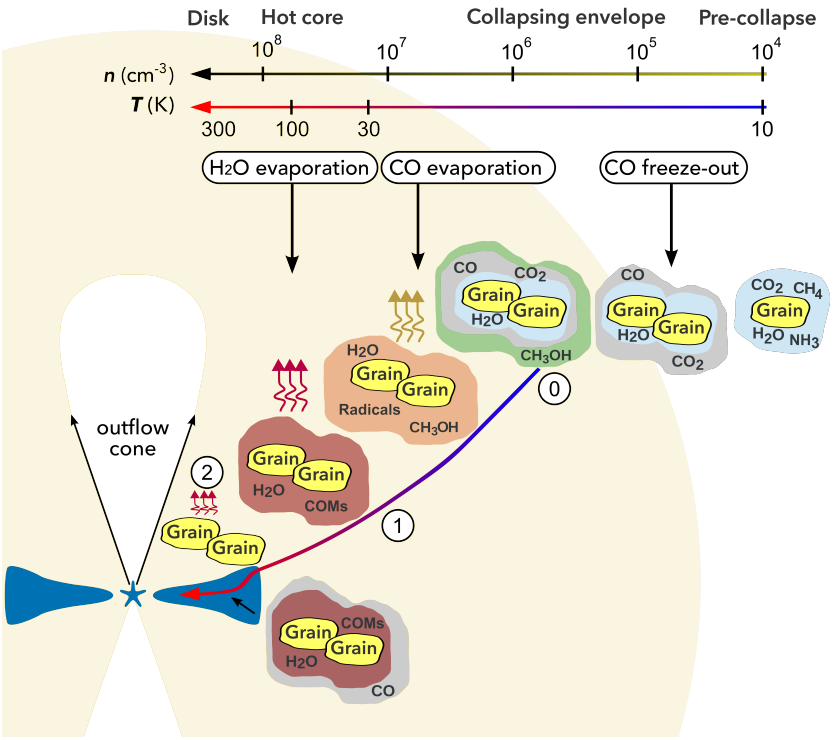

FIGURE 1.7: Illustration of the chemical evolution of the material during the formation of a low-mass star, from the pre-stellar core to the protoplanetary disk. The material experiences an increase in chemical complexity in the protostellar envelope. The numbers 0, 1, and 2 refer to the formation of the 0th-, 1st-, and 2nd-generation of organic molecules on the ice mantles. The grains are not to scale and the acronym COMs stands for Complex Organic Molecules (COMs). Adapted figures from Herbst and van Dishoeck (2009) and Boogert *et al.* (2015).

Solar System objects, e.g., comets, share similarities with the protostellar material. (Drozdovskaya *et al.*, 2019). In contrast, the organic matter found in carbonaceous chondrites is often aqueously altered and has a more complex chemical structure (Alexander *et al.*, 2007).

The composition of the protostellar material varies according to its location in the collapsing envelope, and by consequence, on the underlying chemistry (Figure 1.7). This thesis focuses on the chemistry occurring in the outer regions of the envelope ($\approx 10^4$ AU), characterized by low temperatures ($\approx 10-20$ K). The prevalent process under these physical conditions is freeze-out, which leads to the built up of ice layers (see Sect. 1.2.2). The gas-species accreting onto the ice grains (e.g., CO) undergo atom addition/abstraction reactions producing simple molecules (e.g., H_2O, CO_2) and larger organic molecules, e.g. CH_3OH, CH_3CH_2OH sometimes referred to as 0th-generation species (Charnley, 1997). Non-thermal desorption processes prevail during this cold phase (Figure 1.6).

As the material falls inward towards the forming protostar, it warms up. The increase in temperature impacts considerably the ice chemistry compared to the gas-phase chemistry (Herbst and van Dishoeck, 2009). Volatile molecules such as CO, N_2 and CH_4 start to thermally desorb from the ice mantles when the dust temperature is ~20 K (Collings *et al.*, 2004; Bisschop *et al.*, 2006; Acharyya *et al.*, 2007). Concurrently, less volatile species remain on the ice mantles and become more mobile, but yet too

stable to start a rich chemistry. The ice chemistry during the warm-up phase is thought to be dominated by radical-radical addition surface reactions (e.g., $HCO^{\bullet}$ + $CH_3O^{\bullet}$) triggered by a cosmic-ray induced photochemistry (Garrod and Herbst, 2006; Garrod *et al.*, 2008). The radicals are produced during the photo-dissociation of 0^{th}-generation species. The products of the warm-up chemistry are denoted as 1^{st}-generation species. Some examples are saturated species such as formic acid (HCOOH) and methyl formate ($HCOOCH_3$).

When the material reaches the innermost regions of the envelope (< 200 AU; Schöier *et al.*, 2002), the temperatures are above 100 K. Under these conditions, all the ice mantles are thermally desorbed, and by consequence, chemical reactions uniquely take place in the gas (Figure 1.4). This phase, referred to as *hot-corino*, is characterized by a rich-chemistry as the high temperatures (100−300 K) permit the occurrence of endothermic reactions (i.e, routes requiring energy to overcome the potential energy barrier between reactants and products). Ion-molecule and neutral-neutral reactions produce larger complex organic molecules known as as 2^{nd}-generation species. Examples of this class of molecules include formamide (NH_2CHO) and ethylene glycol ($HOCH_2CH_2OH$; Jørgensen *et al.*, 2016).

A fraction of the molecules produced in hot-corinos is inevitably photo-dissociated because they are subjected to the irradiation from the protostar. However, there is some evidence that part of the envelope material can be incorporated into the protoplanetary disk, and hence inherited to the planet and comets forming zones. This is suggested by numerical models by e.g., Visser *et al.* (2009) and Visser *et al.* (2011) which revealed that some of the disk material is heavily processed, whereas some remains pristine. From an observational point of view, Drozdovskaya *et al.* (2019) found a correlation between the relative abundances of CHO-, N-, and S-bearing molecules detected towards the protostellar system IRAS 16293-2422 and the comet 67P/Churyumov-Gerasimenko. This indicates a certain degree of inheritance from the protostellar stages to the locations in the disk where planets and comets are formed. Recent laboratory experiments successfully synthesized glycine, the simplest amino acid, through atom and radical-radical addition, without the need for energetic processing (Ioppolo *et al.*, 2021). This implies that molecules as complex as glycine can plausibly form at much earlier stages in the star-formation process than previously thought, e.g. during the cold phase or earlier. This result and the unambiguous detection of glycine in cometary material (Altwegg *et al.*, 2016) suggests that the coldest regions of disk mid-planes might be favourable for the conservation of material inherited from the molecular cloud or for the production of molecules biologically relevant for life.

The last section of this introduction presents the principal molecule studied in this thesis, methanol (CH_3OH), with a particular focus on the astrochemical implications concerning its presence in star-forming regions.

1.4 THE ASTROCHEMICAL RELEVANCE OF METHANOL

Methanol (or methyl alcohol) is the simplest and most abundant complex organic molecule and it is ubiquitous in stellar nurseries. Its presence has been inferred in the gas-phase of pre-stellar cores (e.g., Bizzocchi *et al.*, 2014), starless cores (e.g., Spezzano *et al.*, 2020) hot-cores and hot-corinos (e.g., Jørgensen *et al.*, 2020), protoplanetary disks (Walsh *et al.*, 2016; van 't Hoff *et al.*, 2018) and cometary material (e.g., Hoban *et al.*, 1993; Bockelee-Morvan *et al.*, 1994; Mumma and Charnley, 2011; Le Roy *et al.*, 2015; Rubin *et al.*, 2019). Its solid-state counterpart has also been detected towards a variety of astrophysical environments, for instance in the ice mantles of low- and high-mass protostars (Boogert *et al.*, 2015), pre-stellar and starless cores (Chu *et al.*, 2020; Goto *et al.*, 2020), on the icy surface of the Kuiper belt object Arrokoth (Grundy *et al.*, 2020), and in the Murchison CM2 chondrite (Jungclaus *et al.*, 1976).

Extensive laboratory studies on CH_3OH formation in pre-stellar and protostellar environments have been carried out in the past decades. At higher cloud extinctions ($A_V > 9$) and low temperatures, once the catastrophic CO freeze-out has occurred (Boogert *et al.*, 2011; Chiar *et al.*, 2011), the formation of methanol is dominated by the CO + H reaction (Sect. 1.2.2). This chemical pathway is considered the most relevant source of CH_3OH in star-forming regions (e.g., Watanabe and Kouchi, 2002; Fuchs *et al.*, 2009). An important route to account for the presence of CH_3OH at earlier stages, prior to the heavy CO freeze-out, has been studied experimentally by Qasim *et al.* (2018). At a cloud visual extinction (A_V) of ≈ 3 mag, only a low fraction of gas-phase CO accreates onto the dust grains, due to low gas densities at this extinction (Pontoppidan, 2006). Therefore, the grain surfaces are mostly composed by H_2O-rich ices that contain CH_4, but CH_3OH can nevertheless form via the sequential surface reaction chain (Qasim *et al.*, 2018):

$$CH_4 + {}^{\bullet}OH \longrightarrow {}^{\bullet}CH_3 + H_2O \tag{1.11}$$

where the hydroxyl radical mediates the H abstraction. This is followed by the recombination of the two radicals:

$${}^{\bullet}CH_3 + {}^{\bullet}OH \longrightarrow CH_3OH. \tag{1.12}$$

Apart from being omnipresent in interstellar and circumstellar environments, methanol is regarded as the gateway species for the formation of complex organic molecules in the ISM (Öberg *et al.*, 2009b; Herbst and van Dishoeck, 2009). The experiments by Fedoseev *et al.* (2015) and Chuang *et al.* (2016) reveal that CH_3OH is plausibly a key reactant in the production of complex organics in the cold phase of the star-formation process (Figure 1.7). These studies show that the radicals originating from CH_3OH, i.e., ${}^{\bullet}CH_3$ and ${}^{\bullet}OH$, are able to combine with other species present on the ice analogs, leading to the production of larger organics akin glycerol ($HOCH_2CH(OH)CH_2OH$), an important component of cell membranes (Fedoseev *et al.*, 2017). These chemical routes occur via non-energetic processing, i.e., under low temperatures ($T < 20$ K) and in the absence of UV radiation.

Simultaneously, the production of complex organics from CH_3OH has been studied in the laboratory via energetic processing. Figure 1.8 displays the chemical network triggered upon UV-irradiation of CH_3OH-containing ice analogs (e.g., pure CH_3OH, pure CO and CH_4:CH_3OH ices). The products are a suite of more complex organic species such as ethanol (CH_3CH_2OH), dimethyl ether (CH_3OCH_3) and glycolaldehyde ($HOCH_2CHO$) (e.g., Bennett *et al.*, 2007; Öberg *et al.*, 2009b). These experiments suggest that the formation of methanol is fundamental for the development of molecular complexity in UV-irradiated regions, during the protostellar stage.

The hypothesis above is supported further by UV-irradiation experiments of ice mixtures of different compositions such H_2O:CH_3OH by Meinert *et al.* (2016) and Nuevo *et al.* (2018). These studies have synthesized, among several compounds of biological interests, ribose (Meinert *et al.*, 2016) and 2-deoxyribose, the sugar composing the deoxyribonucleic acid (DNA) (Nuevo *et al.*, 2018). Continuous advances in laboratory experiments (via energetic and non-energetic processing) and models will help accounting for the role of methanol in the ISM and for the molecular complexity observed (e.g., Jiménez-Serra *et al.*, 2020) - and yet to be observed in star-forming regions, and ultimately to link it to the origin of life on Earth.

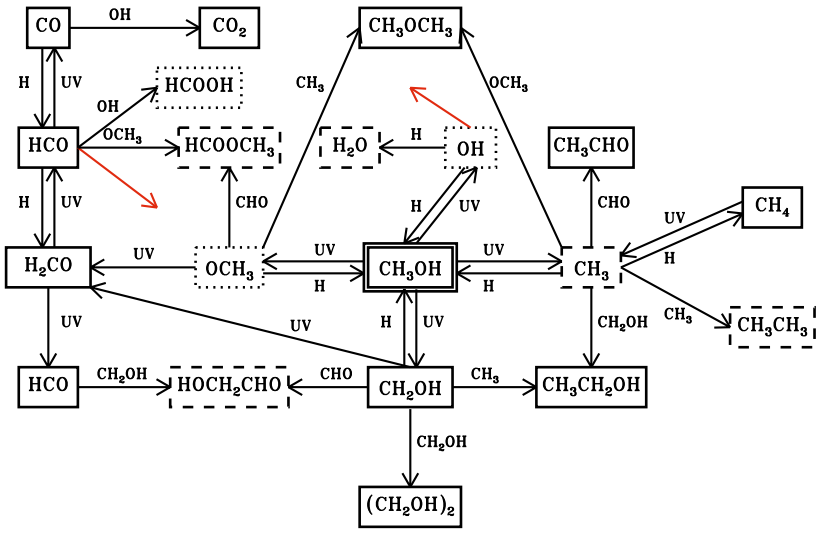

FIGURE 1.8: The CH_3OH reaction network upon UV-irradiation of pure CH_3OH ice (solid boxes), pure CO ice and CH_4:CH_3OH ice analogs (dashed boxes). Credit: Öberg *et al.* (2009b).

The main aim of this thesis is to study the interplay between methanol gas and ice through millimetric and infrared observations of solar-type protostellar envelopes. In particular, to access the dependencies of the methanol gas-to-ice ratio on different physical conditions. This is achieved by obtaining and comparing direct measurements of gas-phase and ice methanol towards protostars located in the three nearby star-forming regions presented in Chapter 3.

2

Methods

The first chapter of this thesis describes our current understanding of the physical and chemical processes active in pre- and proto-stellar environments, which set the initial conditions for the formation of low-mass stars. This chapter dives into the observational methods at the foundation of the present-day picture of the evolution of protostars: astronomical observations of interstellar molecules.

Astronomical observations are the only tools available to directly access the chemistry at play in regions of ongoing star and planet formation. This is because the closest stellar nurseries to the Solar System are situated at best ~100 pc away, thus physically unreachable by current space missions. Observations can be conducted with ground-based telescopes, at well-designated spectral ranges where the Earth's atmosphere is transparent enough. Alternatively, space-based telescopes are used to observe molecules at wavelengths at which Earth's atmosphere is opaque.

A major limitation of astronomical observations is the lack of emissivity of the most abundant interstellar molecule, molecular hydrogen (H_2), at the typical densities and temperatures of stellar and planet formation. Fortunately, spectral features of more than two hundred interstellar species are detectable beyond H_2 (McGuire, 2018), which are excellent diagnostics of the physical and chemical conditions of the earliest stellar stages (Herbst and van Dishoeck, 2009). Strictly speaking, observations of molecular species are feasible at all frequencies from ultraviolet (UV) to radio wavelengths. Practically, most of the observations of molecular species are conducted at infrared (IR), sub-millimeter and millimeter wavelengths.

2.1 MOLECULAR SPECTROSCOPY

Molecular emission and absorption recorded during observational runs can be used as probes of the physico-chemical conditions of a wide range of astronomical objects (Herbst and van Dishoeck, 2009; Jørgensen *et al.*, 2020). This section provides a summary overview of molecular spectroscopy and of the transitions assigned to molecular species in pre- and proto-stellar environments.

Compared to atoms, whose spectra consists of mere electronic transitions, molecules possess further degrees of freedom associated with the rotation and vibration of their atoms. This implies that each molecular electronic

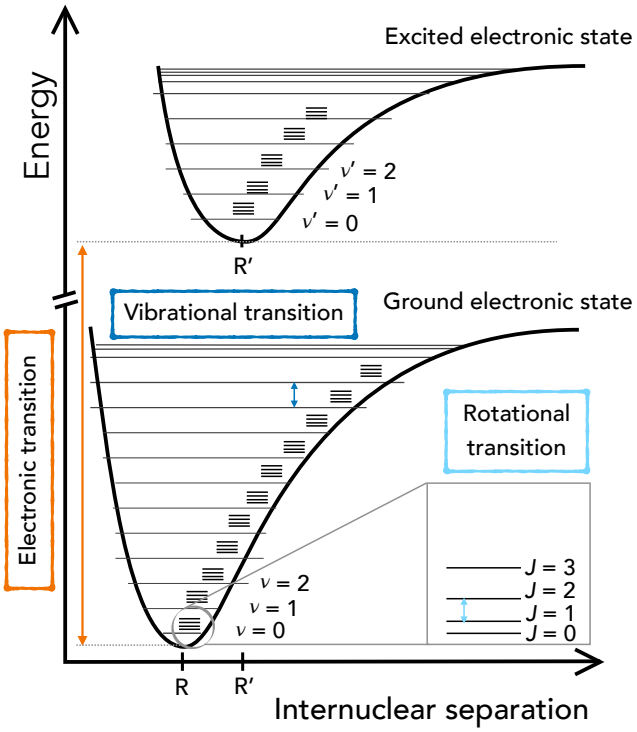

FIGURE 2.1: The electronic, vibrational, and rotational levels of a diatomic molecule. Electronic transitions arise between discrete vibrational and rotational levels in each electronic state.

state is accompanied by a suite of vibrational energy levels. And, in turn, to each vibrational level correspond a set of rotational levels (Figure 2.1). Therefore, the total energy E of a molecule can be described as the sum of its electronic $E_{\rm el}$, vibrational $E_{\rm vib}$ and rotational $E_{\rm rot}$ energies:

$$E = E_{\rm el} + E_{\rm vib} + E_{\rm rot}. \tag{2.1}$$

Molecules undergo rotational, vibrational and electronic transitions, by populating their energy levels upon absorption and emission of photons at discrete energies, i.e. *quanta* (Planck, 1900). For instance, a diatomic linear molecule, e.g. CO, can be considered as a rigid rotor. In this approximation, the energy needed to populate its rotational levels is equal to:

$$E_{\rm rot} = \frac{\hbar^2}{2I} J(J+1) \tag{2.2}$$

where $\hbar$ is the reduced Planck constant, I is the moment of inertia and J is the rotational quantum number. Relatively low energies are required to populate the rotational levels of molecules akin to CO, which correspond to pure rotational transitions at far-infrared, submillimeter and millimeter wavelengths (Sect. 2.3).

Higher energies are needed to populate vibrational levels, which are associated with transitions in the infrared range of the electromagnetic spectrum (Sect. 2.2). In the harmonic oscillator approximation, the vibrational energy of a molecule is defined as:

$$E_{\rm vib} = 2\pi\nu_0\hbar(\nu + \frac{1}{2}) \tag{2.3}$$

where ν_0 is the natural frequency of the oscillation and v is the vibrational quantum number. The vibrational energy is related to the oscillation of the bonds within a molecule, which are referred to as *vibrational modes*. The most common modes are *stretching* and *bending*, during which vibrations change the bond length and the bond angle, respectively. Besides hosting pure vibrational transitions, the infrared spectral range is where *rovibrational* transitions arise, which involve simultaneous transitions between rotational and vibrational levels.

Finally, even higher energies are required for electronic transitions to occur. These often lie in the ultraviolet-visible spectral domains and reflect the promotion of an electron to an higher energy orbital within the same molecule. The electron promotion normally takes place from the highest occupied molecular orbital (HOMO) to the lowest unoccupied molecular orbital (LUMO), following an energetically favourable transition.

The following sections describe how observations of molecular species at infrared wavelengths are carried out. Particular focus is given to the observations of solid-state molecules in absorption and to the spectral decomposition method used in this thesis to study the molecules residing on the ice mantles in the coldest regions of protostellar envelopes.

2.2 OBSERVING MOLECULES AT INFRARED WAVELENGTHS

Molecular vibrations give rise to spectral features in the near- (0.7 – 5 μm), mid- (5 – 30 μm) and far-infrared (30 – 300 μm), which are used to explore the gas-phase and solid-state compositions in a variety of astronomical environments (e.g., van Dishoeck and Blake, 1998; Pontoppidan *et al.*, 2014; Boogert *et al.*, 2015). Most infrared gas-phase compositional studies are carried out in emission and probe warm gas, e.g., in the inner disks (Pontoppidan *et al.*, 2019). In contrast, solid-state molecules are predominantly studied in absorption, which allows to trace the constituents of ice mantles before their sublimation (Boogert *et al.*, 2015).

Infrared observations are performed both from the ground and from

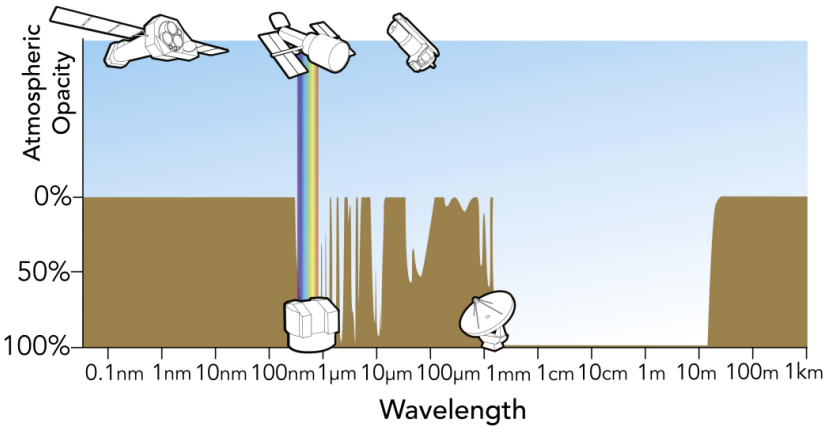

FIGURE 2.2: Electromagnetic transmittance or opacity of the Earth's atmosphere as function of wavelength. Only in a few infrared-wavelength ranges Earth's atmosphere is sufficiently transparent to carry out infrared ground-based observations. Ground-based observations are possible in the radio atmospheric window. Credit: ESA/Hubble/F. Granato.

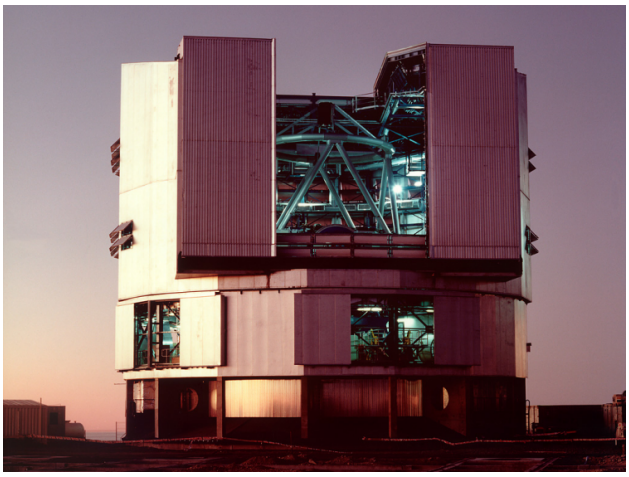

FIGURE 2.3: The ANTU telescope unit of the Very Large Telescope (VLT) - Cerro Paranal, Chile. Credit: ESO.

space, albeit the coverage of the entire infrared spectral domain ($\approx 0.7 - 300$ μm) is exclusively achievable from space. Figure 2.2 illustrates this, by displaying the electromagnetic transmittance or opacity of the Earth's atmosphere as function of wavelength. It can be noted that the majority of the infrared light proceeding from space is absorbed by Earth's atmospheric gases, mainly water vapour and carbon dioxide. Only in a few infrared-wavelength ranges Earth's atmosphere is not opaque and hence the infrared light can be observed with ground-based infrared facilities. Besides telluric absorption, a second obstacle to the feasibility of infrared ground-based observations is the emission of the Earth's atmosphere itself, which radiates at ~ 10 μm, challenging the observations of the infrared objects of interest. An example of infrared ground-based facility is the Very Large Telescope, which is operated by the European Southern Observatory. It composed by four unit telescopes with a mirror of 8.2 m in diameter. Each telescope unit can be operated separately or as an interferometer to reach higher angular resolution. Figure 2.3 displays the ANTU telescope unit of the Very Large Telescope (VLT) used to carry out the near-infrared observations presented in Chapter 5. If near- and mid-infrared observations are feasible from the ground, far-infrared observations are not possible using ground-based telescopes, but can be achieved from space and at altitudes above the water vapour of the Earth's atmosphere with the airborne observatory SOFIA (Stratospheric Observatory for Infrared Astronomy).

Solid-state molecules in ice mantles are identified from *absorption bands* in the near- and mid-infrared, which are associated with vibrational modes of their *functional groups* (Hagen *et al.*, 1980). The latter are specific ensembles of atoms in a molecule, e.g., -OH, -CH_3, showing peculiar chemical properties despite of the molecule they are bonded to. Ice mantles in the ISM are predominantly studied in the $\sim$3$-$16 μm range through the analysis of the stretching, bending and librational modes (Gibb *et al.*, 2004). Table 2.1 lists the vibrational modes of the solid-state molecules studied in this thesis. The detections of interstellar species in absorption is primarily achieved against infrared continuum sources. Typically used background stars are bright infrared giants (Murakawa *et al.*, 2000; Knez *et al.*, 2005; Boogert *et al.*,

TABLE 2.1: Spectral position of the ice absorption bands studied in this thesis.

Wavelength [λ_{center}]	Vibrational mode	Identification
3.0	O-H stretching	H_2O, CH_3OH
3.53	C-H stretching	CH_3OH
4.67	C-O stretching	CO
6.0	bending	H_2O
6.85	bending	NH_4^+?
9.74	C-O stretching	CH_3OH
13.6	libration	H_2O

Note: The values are taken from Boogert *et al.* (2015).

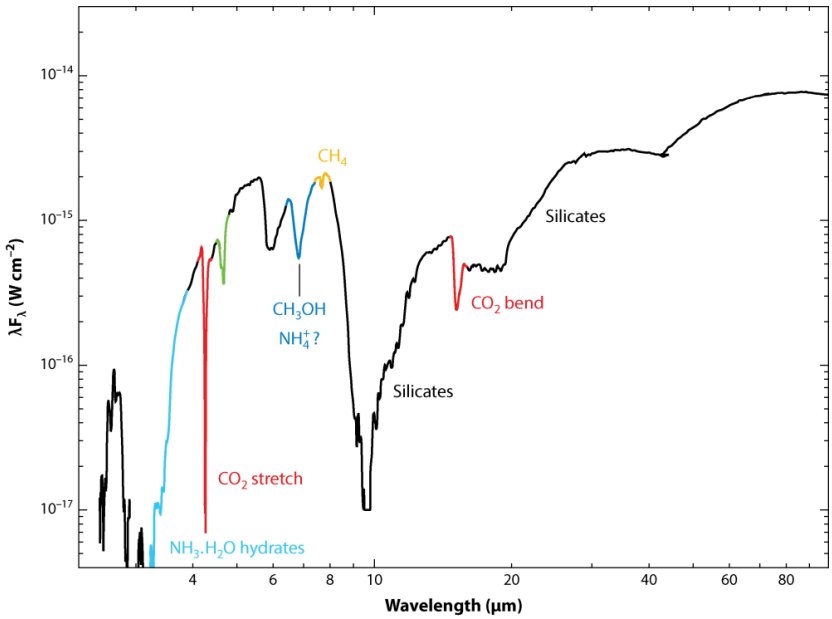

FIGURE 2.4: Near-to-mid infrared spectrum of the massive young stellar object (YSO) AFGL7009 S. The most prominent ice and dust features in this spectral range are indicated. Credit: Boogert *et al.* (2015).

2011; Goto *et al.*, 2020) or Class I young stellar objects (e.g., Pontoppidan *et al.*, 2004; Pontoppidan, 2006; Zasowski *et al.*, 2009; Rocha and Pilling, 2015). Alternatively, the compositions of the ices can be studied in regions where the background emission is enhanced by dust scattering (Pendleton *et al.*, 1990; Honda *et al.*, 2009).

2.2.1 *Decomposition of infrared spectra*

Compared to the ro-vibrational transitions observed in the infrared spectral domain, absorption bands are significantly broader, and therefore not easily attributable to specific functional groups. Figure 2.4 outlines the principal ice and dust features observable at near- and mid-infrared wavelengths, and the molecules primarily responsible for them. Several methods have been developed throughout the years to identify solid-state molecules in infrared spectra. They rely on comparisons with infrared laboratory data. The procedure followed in this thesis to determine to what degree a solid-

state molecule contributes to an observed absorption band consists of initially converting the calibrated infrared spectrum to an optical depth τ scale:

$$\tau = -ln\left(\frac{F_{\rm obs}}{F_{\rm cont}}\right) \tag{2.4}$$

where $F_{\rm obs}$ is the observed flux and $F_{\rm cont}$ is the continuum. This is achieved by following the procedure below:

- **Dust continuum determination**
  To accurately determine the continuum, only in specific wavelength ranges (e.g., $\sim$ 4.5 – 4.9 μm) it is necessary to remove all the ro-vibrational transitions in the observed spectrum. The resulting spectrum has to include only pure absorption features and the dust continuum. The next step consists of determining the continuum to be used in Eq. 2.4, by fitting a low-order polynomial function to the observed flux spectrum, excluding the regions where ice features are present (Gibb *et al.*, 2004; Boogert *et al.*, 2000; Öberg *et al.*, 2011a). A second option involves the use of Kurucz stellar atmosphere models or black body functions (Pontoppidan *et al.*, 2003b; Pontoppidan *et al.*, 2004). Alternatively, photometry points can be used to produce a reddened spectral energy distribution of the field source, which is then adopted as a local continuum (Boogert *et al.*, 2013).

- **Optical depth calculation**
  After determining the continuum ($F_{\rm cont}$), the computation of the ratio in Eq. 2.4 generates the optical depth spectrum.

Once the optical depth spectrum is obtained, the spectral decomposition of the observational data is performed, to investigate which solid-state molecules contribute to the observed ice features, and to what extent. The fitting routine adopted in this thesis to carry out the spectral decomposition of the infrared spectra is the open-source Python library OMNIFIT[1] (Suutarinen, 2015a). This code concurrently fits a set of selected laboratory data and analytical functions to the observed infrared absorption features. The OMNIFIT fitting utility operates as follows:

[1] https://ricemunk.github.io/omnifit/

1. The observed infrared spectrum (on an optical depth scale) and the complex refractive index spectrum are imported. The latter contains information on the laboratory data, and in particular on the real and imaginary parts of the complex refractive index, also referred to as the optical constants n and k, as function of wavenumber $\tilde{\nu}$.

2. The complex refractive index spectrum is corrected for grain shape effects, according to the "Continuous Distribution of Ellipsoids" method (Bohren and Huffman, 1983). This treatment is adopted in OMNIFIT to account for the fact that ice analogs reproduced in the laboratory and interstellar ices have different shapes.

3. The fitting parameters are prepared and the fit is performed. If only one laboratory dataset is selected, the parameter will be an initial guess for the best-fit multiplier. Other fitting parameters can be added,

depending on the number of laboratory datasets imported, and kept at a fixed value or allowed to vary during the fit. Additionally, a maximum and minimum value can be specified for each inserted parameter. In this thesis OMNIFIT performs the non-linear optimization using the Levenberg-Marquardt method (Levenberg, 1944; Marquardt, 1963). This consists of fitting the observed spectrum, via an iterative procedure, by finding the parameters for which the sum of the squares of the deviations is at its minimum.

The above steps summarize the OMNIFIT workflow when only one empirical dataset is selected. However, a large set of empirical and analytical data can be fitted simultaneously to the observed infrared spectrum as it is the case for the study presented in Chapter 5. When analytical functions are included in the fit, the resulting fitting parameters will incorporate initial guesses for the position, height and full width at half maximum of the observed absorption band. One of the caveat of OMNIFIT, common to other fitting algorithms adopted in the spectral decomposition of infrared data, is that it finds a local minimum solution, which does not necessarily represent the global minimum. The outcomes of the fit allow to determine whether and to what extent a solid-state species contributes to the observed ice features.

The next sections draw an overview of observations at millimeter wavelengths, used in this thesis to investigate the gas-phase molecular inventory of cold protostellar envelopes.

2.3 OBSERVING MOLECULES AT MILLIMETER WAVELENGTHS

The vast majority of detections in interstellar and circumstellar environments has been achieved in the submillimeter and millimeter spectral domains, predominantly from pure rotational transitions of molecules in their lowest vibrational level and ground electronic state (Williams and Viti, 2013; McGuire, 2018).

The rotational transitions at these wavelength regimes (300 μm−1cm) enable to probe gas emissions from pre-stellar and proto-stellar environments characterized by temperatures below 20 K to the high temperatures of hot-corino regions ($T > 100$ K). Submillimeter and millimeter observations are possible from the ground as Earth's atmosphere is mostly transparent at these wavelengths (Figure 2.2), using one or an array of antennas, i.e., through *single-dish* or *interferometric* observations.

2.3.1 *Single-dish versus interferometric observations*

The minimum angular separation between two resolvable objects in the sky, i.e. the angular resolution of an antenna θ, is related to the wavelength λ and the diameter of the antenna D by (Rayleigh, 1879):

$$\theta \approx \frac{\lambda}{D}. \tag{2.5}$$

The above formula implies that the longer the wavelength of the observations is, the larger the diameter of the antenna has to be to resolve small-scale

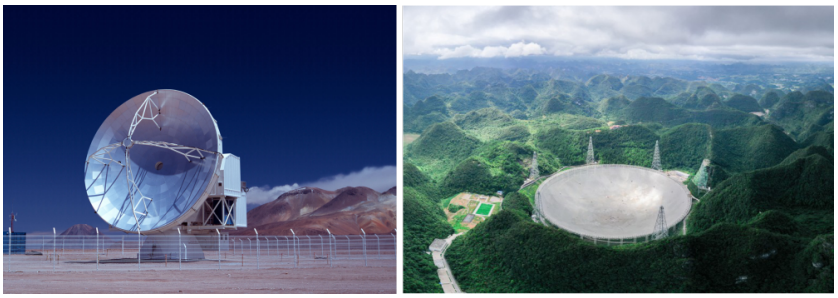

FIGURE 2.5: Examples of single-dishes. *Left:* the Atacama Pathfinder EXperiment (APEX) - Chajnantor plateau, Chile. Credit: ESO. *Right:* the Five-hundred-meter Aperture Spherical radio Telescope (FAST) - Pingtang, China. Credit: Ou Dongqu/Xinhua/ZUMA.

structures in the sky. The existing single-dish telescopes measure from a few tens to a few hundreds of meters. For instance, the Atacama Pathfinder EXperiment (APEX) telescope used in this thesis (Figure 2.5), has a main-dish diameter of 12 m and an angular resolution of $\sim 27''$ at 1.3 mm (Güsten *et al.*, 2006). The world's largest single-dish radio-observatory, the Five-hundred-meter Aperture Spherical radio Telescope (FAST) gets as far as $10''$ at centimeter wavelengths (Figure 2.5). This angular resolution is excellent to probe the large-scale cloud emission, but it is not sufficient to resolve, e.g., the inner 200 AU of protostellar envelopes, corresponding to sub-arcsecond angular sizes (Schöier *et al.*, 2002) or even smaller structures such as protoplanetary disks (Andrews *et al.*, 2018).

The angular resolution limitation of single dishes can not be overcome by simply constructing larger antennas. Despite being challenging to design from an engineering point of view, such colossal constructions would be troublesome to operate, besides requiring substantial maintenance. Additionally, to an increment in the diameter of the antenna inevitably corresponds a diminution of the surface accuracy of the dish, hampering the achievement of angular resolutions below $10''$ (Rohlfs and Wilson, 1996). Instead, higher angular resolution observations are provided by means of radio-interferometry, which consists of combining the signals collected from multiple separate antennas. The result of this powerful combination is comparable to observing with a huge telescope that has a diameter dictated by the longest distance between a pair of antennas, e.g., a *baseline* $D_{\rm int}$ up to $\sim$ 16 km in the case of the Atacama Large Millimeter/submillimeter Array (ALMA; Figure 2.6). Compared to Eq. 2.5, the angular resolution of an array of antennas is given by:

$$\theta \approx \frac{\lambda}{D_{\rm int}} \tag{2.6}$$

where $D_{\rm int}$ is the longest baseline of the interferometer. In its most extended 12-m array configuration, ALMA probes the interstellar physical and chemical conditions with an angular resolution of $\sim 0.01''$, which is commensurate to observing nearby star-forming regions down to a few AU.

The highest angular resolution is not required for all science goals. For instance, the observations presented in Chapters 5, 6 and 7 target the outer envelopes of low-mass protostars, and therefore the emission of interstellar molecules over large spatial scales. For this purpose, it is not necessary to make use of the longest baselines of the interferometer, instead, the shortest

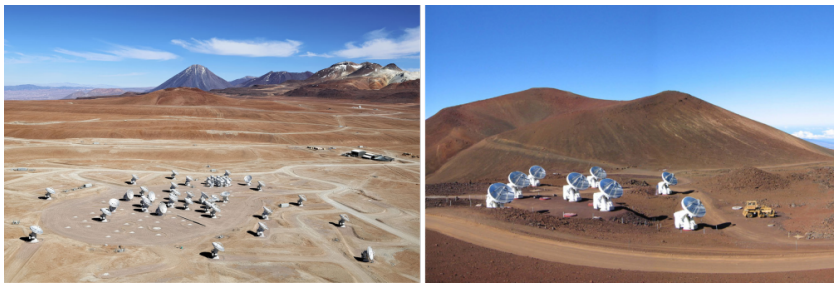

FIGURE 2.6: Examples of interferometers. *Left:* the Atacama Large Millimeter/submillimeter Array (ALMA) - Chajnantor plateau, Chile. Credit: ESO. *Right:* the Submillimeter Array (SMA) - Mauna Kea, Hawai'i, USA. Credit: CfA

baselines are most suited. Compared to the longest baselines they recover most of the extended emission and, with respect to single-dish observations they allow to reach angular resolutions sufficiently high ($3 - 4''$) to resolve compact objects (see Sect. 2.3.4). Figure 2.6 displays the interferometer used to collect the data presented in this thesis, the Submillimeter Array (SMA; Ho *et al.*, 2004). The SMA array is composed by eight 6-m diameter antennas. The shortest baseline in the sub-compact array is 9.5 m, whereas the longest baseline in the very extended configuration is 508 m.

2.3.2 *Two-antenna interferometer*

To describe the basics of interferometry, Figure 2.7 considers for simplicity an interferometer composed by only two antennas. Interferometers constituted by more elements follow the same basic principles. Each antenna receives the radiation from an astronomical source located at an angle θ in the form of plane electromagnetic waves, inducing a signal U. The incoming wave front of the plane wave reaches antennas A_1 and A_2 at different times. This time delay is called *geometric delay* τ_g and it is generated due to the orientation of the baseline described with the vector **b** with respect to the pointing direction of the antennas, i.e., the source position, indicated with the vector **s**:

$$\tau_g = \frac{\mathbf{b} \cdot \mathbf{s}}{c} \tag{2.7}$$

where c is the speed of light. The signals U_1 and U_2 received by each antenna reach the correlator where they are combined (voltage multiplication) and corrected for the time delay (time averaging). The output of this operation is called the *interferometer response* $r(\tau_g)$. The step after the correlation consists of the integration of the interferometer response over time. This operation produces the *sky visibility* $V(u, v)$, where u and v are the coordinates of the plane describing the position of the baseline, i.e., the uv plane. The visibility $V(u, v)$ is defined as the Fourier transform of the specific intensity (or brightness distribution) of the source on the sky $I(x, y)$:

$$V(u, v) = \iint A(x, y) I(x, y) e^{-2\pi i (ux+vy)} \, \mathrm{d}x\mathrm{d}y \tag{2.8}$$

where $A(x, y)$ is the effective collecting area of the antenna. In the equation above, $I(x, y)$ represents the quantity to retrieve from the interferometric observations, the intensity distribution of the astronomical source. If a

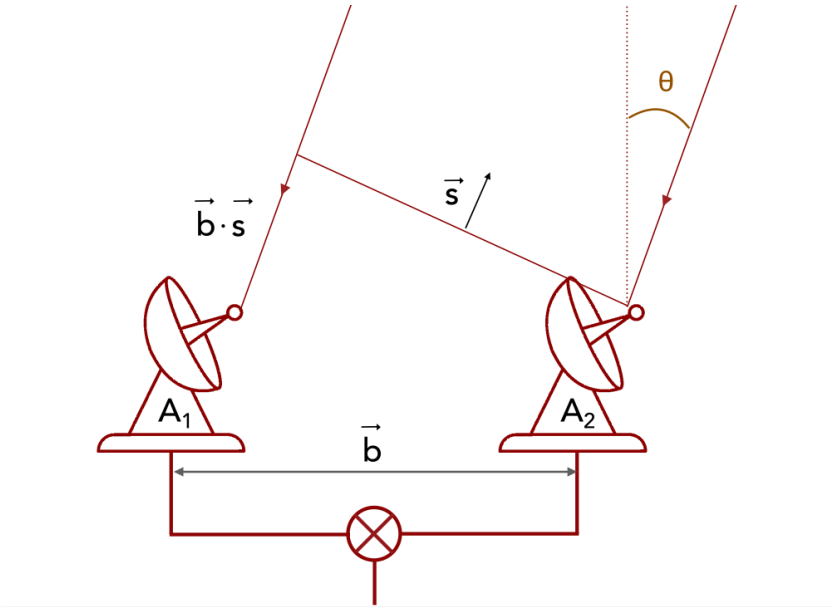

FIGURE 2.7: Schematic illustration of a two-antenna interferometer. Plane waves emitted by an astronomical source reach antennas A_1 and A_2. The source position is indicated by the vector **s**. The orientation of the baseline is described by the vector **b**.

Fourier inversion is applied to Eq. 2.8, the modified specific intensity $I'(x, y)$ is obtained:

$$I'(x,y) = A(x,y)I(x,y) = \iint V(u,v)e^{2\pi i(ux+vy)}\,dudv. \tag{2.9}$$

The two equations above, known as the van Cittert-Zernike theorem (van Cittert, 1934; Zernike, 1938), connect the visibility to the specific intensity of the source. According to the theorem, an image of the intensity of the source can be achieved by inverting the Fourier transform of the visibility. In reality, this is not possible because the antennas do not sample the entire *uv* plane. To each baseline of the interferometer corresponds one location in the *uv* plane. In the geometry depicted in Figure 2.7, there is one baseline, which collects one visibility data. Due to Earth's rotation, the position of the *u* and v coordinates changes with respect to the astronomical source, and this increases the sampling of the *uv* plane. This concept is represented in Figure 2.8. In an interferometer composed by more elements, even though the antennas are positioned to maximize the coverage of the *uv* plane, a minimum preventive separation between them is inevitably required, causing a loss of Fourier components during the imaging. Consequently, part of the intensity is unavoidably filtered out, even with the most compact array configurations. To recover part of the "missing" visibilities, in this thesis I combine interferometric and single-dish data following the procedure described in Sect. 2.3.4.

To summarize, throughout each observational run, every baseline collects visibilities, which are integrated over a few tens of seconds. This process is repeated over and over for a number of iterations for all the operative baselines until the coverage of the *uv* plane is satisfactory or, alternatively, the desired sensitivity is reached. The coverage of the *uv* plane is highly dependent on the number of operative baselines and on the integration time.

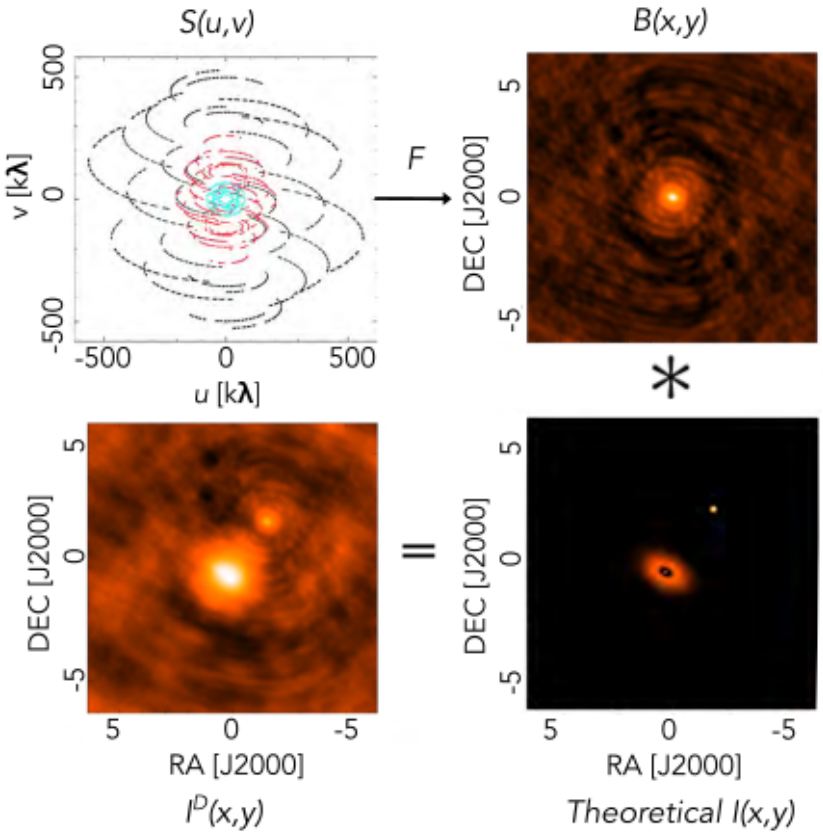

FIGURE 2.8: Relations between the sampling function $S(u,v)$, the dirty beam $B(x,y)$, the intensity distribution $I(x,y)$ and the dirty image $I^D(x,y)$. The Fourier transform of the sampling function is the dirty beam. The dirty image is the result of the convolution of the intensity distribution by the dirty beam. Credit: D. J. Wilner - 2020 SMA Interferometry School.

The higher the number of baselines, the more visibilities will be retrieved and therefore, more information on the intensity of the source will be obtained. Additionally, a longer integration time will result in a better coverage of the uv plane as a consequence of the rotation of the Earth. The totality of the baseline positions in the uv plane acquiring visibility data is defined as the *sampling* function $S(u,v)$. The Fourier transform of $S(u,v)$ is referred to as *dirty beam* $B(x,y)$:

$$B(x,y) = \iint S(u,v)e^{2\pi i(ux+vy)}\,dudv. \tag{2.10}$$

which represent the response of the interferometer to a point source (point spread function). Figure 2.8 shows an example of sampling function and dirty beam. To a better sampled uv plane (more baselines collecting visibilities) corresponds a more defined dirty beam shape.

To account for the discrepancy in the uv coverage between longer and shorter baselines, the sampled visibility is weighted according to the most appropriate *weighting* function $g(u,v)$. The application of the weighting function is a key step to reduce the imbalance between the longest baselines, which contain information on the small spatial scales, and the shortest baselines, which map the large spatial scales and carry the bulk of the flux. Natural, uniform and Briggs are the most widely used weighting functions. The natural weighting increases the signal-to-noise ratio, at the expense

of the angular resolution. This is because it gives lower weight to the long baselines, whereas the shortest baselines are enhanced. In contrast, the uniform weighting partially attenuates the short baselines, with the inevitable effect of losing some of the recorded flux at larger spatial scales. Often, the Briggs or robust weighting is adopted (Briggs *et al.*, 1999) which allows to achieve a good balance between the uniform and the natural weighting. When a Fourier transform is applied to the sampled visibility, an image of the intensity is obtained:

$$I^D(x,y) = \iint S(u,v)V(u,v)e^{2\pi i(ux+vy)} \tag{2.11}$$

I^D(x,y) is referred to as *dirty image*, and it is related to the dirty beam $B(x,y)$ and the intensity $I(x,y)$ by:

$$I^D(x,y) = I(x,y) * B(x,y), \tag{2.12}$$

the dirty image $I^D(x,y)$ is the convolution ($*$) of the intensity distribution of the source by the dirty beam. Figure 2.8 recapitulates the relations between the sampling function $S(u,v)$, the dirty beam $B(x,y)$, the intensity of the source $I(x,y)$ and the dirty image $I^D(x,y)$. The final image of the intensity distribution of the source of interest is acquired after calibrating the raw data and applying the preferred deconvolution method to erase the effects of the dirty beam from the dirty image.

2.3.3 *Interferometric data calibration and imaging*

Besides carrying the information on the source of interest, the visibilities recorded by the interferometer include "contamination" from atmospheric effects (e.g., atmospheric composition, turbulence, etc.) and from the instrumental effects (e.g., antenna position errors, receiver delays). Therefore, it is necessary to calibrate the visibilities with the outputs of selected calibrators. These are objects (typically quasars, planets, asteroids and satellites) whose positions and fluxes are well-known. Note that each calibration step requires different calibrators with specific characteristics. Each step is summarily described in the following.

1. **Bandpass calibration**
   This calibration step monitors the spectral response to ensure signal at each frequency interval. In particular, it tackles the undesired effects caused by delay offset, cable delays originated in the receiving system, as well as the repercussions due to the presence of molecular oxygen and ozone in the atmosphere. The bandpass calibrators are normally bright point-like sources akin to strong quasars (e.g, 3c84, 3c279), whose spectra are line-free over a few GHz. Quasars are particularly suited for this task as they are strong emitters at all baselines independently on the baseline length.

2. **Phase calibration**
   The second step of the calibration has the objective of removing instrumental and atmospheric phase-variability from the visibilities. Such variability takes place at different timescales in the atmosphere. There

are short-term events mostly associated with atmospheric turbulence akin to variations of water vapour in the atmosphere, and long-term events such long-lasting changes of the weather conditions throughout the observations and antenna position errors.

For the Submillimeter Array datasets, the correction for these fluctuations is carried out by observing gain calibrators. These are usually bright quasars emitting at radio wavelengths. One of the discriminators in the selection of the gain calibrators is their vicinity to the source of interest on the sky. This is because they should ideally cover the same atmospheric properties as the target. This calibration step consists of performing a linear fit or fitting with a spline function the averaged visibilities as function of time.

3. **Amplitude calibration**
   The amplitude calibration is required to eliminate instrumental variability, e.g, sub-optimal antenna pointing and focus, and to apply a residual correction for atmospheric opacity. In general, the amplitude-variability occurs at slower timescales compared to the phase-variability. The amplitude calibration step is similar to the phase calibration, but the amplitude of the visibilities is fitted instead of the phase. Normally, the phase and amplitude calibrations make use of the same calibrators. As the flux of the quasars adopted in the amplitude calibration slightly varies as function of time, their absolute flux is determined by comparison with flux calibrators in the following step.

4. **Flux calibration**
   The final step of the calibration places the visibilities on a consistent flux scale. This process can be compared with the usage of standard stars in optical observations. In this step the antenna temperature (T_A) usually in Kelvin (K) is converted into a flux in Jansky (Jy). The flux calibrators are commonly Solar System sources not heavily resolved by the interferometer such as Uranus, Callisto, and Titan. The selection of the flux calibrator depends on the targeted configuration and angular resolution.

When all the atmospheric and instrumental effects are removed and the observational data are properly calibrated, it is possible to proceed with the imaging to visualize the intensity distribution of the source of interest. The software used in this thesis to both calibrate and image, and more generally to inspect and analyse the interferometric data is the Common Astronomy Software Application (CASA)[2] package (McMullin *et al.*, 2007). The adopted deconvolution method is the CLEAN algorithm (Högbom, 1974), which assumes that the image of the intensity distribution of the source is made of point sources. The `clean` task constructs a model of the intensity distribution of the source which resembles to the dirty image $I^D(x, y)$. This is achieved through the iterations described below and illustrated in Figure 2.9:

[2] http://casa.nrao.edu/

1. Identify the peak in the dirty image $I^D(x, y)$;
2. Subtract a factor γ with the dirty beam shape from the dirty image at the peak position identified in step 1. After the first subtraction, the

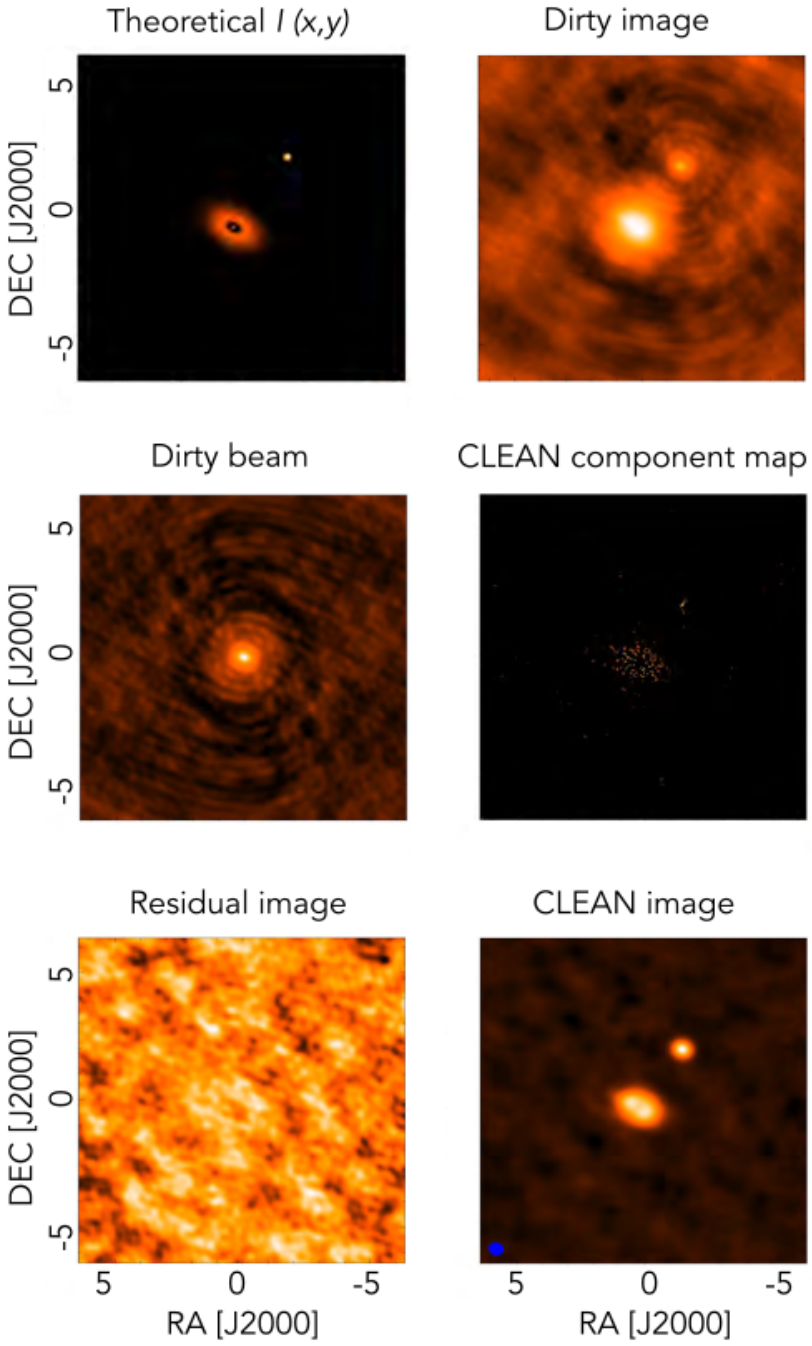

FIGURE 2.9: Simulation of the CLEAN deconvolution algorithm. The images display the theoretical model of the intensity distribution of the source $I(x, y)$, the dirty image $I^D(x, y)$, the dirty beam $B(x, y)$, the CLEAN component map, the residual image and the restored CLEAN image. Credit: D. J. Wilner - 2020 SMA Interferometry School.

dirty image is referred to as *residual image*. The factor γ is typically ~0.1.

3. Create the *CLEAN component map*, by filling the map with the point sources (i.e., intensity and position values) subtracted from step 2.

4. Iterate steps 1−3 until the peak in the residual image is smaller than a selected stopping threshold, e.g., the peak in the residual image is lower than a fraction of the theoretical rms noise.

Once the above steps are successfully completed, the point sources which are part of the CLEAN component map are convolved with the *CLEAN beam* - which is a Gaussian beam resembling the main lobe of the dirty beam - and added to the residual image (Figure 2.9). The outcome of this last operation is the *CLEAN image* which contains the information of the intensity distribution of the source of interest.

2.3.4 *Combination of interferometric and single-dish data*

When planning an observation, the characteristics of the astronomical source to be observed and the science goals to be addressed are the main factors in the selection of the most suitable radio telescope to use. Interferometers are ideal to study compact objects at high angular resolutions inaccessible with single-dishes, whereas the latter are apt to observe extended objects - since interferometers are unable to fully recover the information on the largest scales (Sect. 2.3.2). However, a number of scientific goals, akin to the projects carried out in Chapters 5, 6 and 7, require high angular resolution observations of extended objects. This implies applying the so called "short-spacing correction" to the interferometric observations, which can be achieved by:

- observing the extended object with the interferometer;
- observing the same object with the single-dish;
- calibrating both datasets to ensure they have analogous flux density scales;
- combining the interferometric and single-dish data using the preferred combination algorithm.

The following provides a description on how interferometric and single-dish data are folded together. A single-dish telescope can be described as sets of small hexagonal panels (Figure 2.10). In this definition the signal received by each hexagon is combined at the center of the dish, commensurate with the combination of the signal coming from individual antennas forming part of an inteferometer. The separation between two hexagonal panels can be referred to as the baseline d, which is equal to zero at the center of the dish. The longest baseline is dictated by the diameter of the single dish D_{sd} (Figure 2.10). This representation makes it possible to interpret a single-dish as an interferometer composed by an infinite number of antennas,

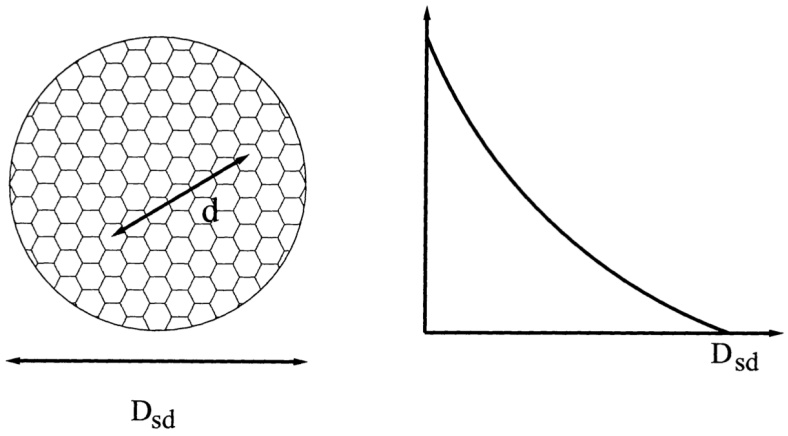

FIGURE 2.10: Schematic illustration of a single-dish represented as an interferometer. *Left:* the hexagonal panels are compared to the antennas composing the interferometer. The separation between the panels is the baseline d and the diameter of the single-dish is D_{sd}. *Right:* Graph illustrating the baseline distribution decreasing from the center of the dish to the longest baseline dictated by D_{sd}. Credit: Stanimirovic (2002)

and by inference to apply the same mathematical notation to single-dish and interferometric data. The *single-dish dirty image* is defined as:

$$I^D_{sd}(x,y) = B_{sd}(x,y) * I(x,y) \tag{2.13}$$

where $B_{sd}(x,y)$ is the *single-dish dirty beam*. When a Fourier transform is applied to Eq. 2.13, the sampled single-dish visibility $V_{sd}(u,v)$ is obtained.In contrast to the interferometric sampled visibility, $V_{sd}(u,v)$ does not require the application of a weighting function as it is a continuous function. This is due to zero spacing between the hexagonal panels of the single-dish.

The development of techniques to combine single-dish and interferometric data has been pursued since the 80's. Introductions to the subject and to different methods to perform the combination can be found in Vogel *et al.*, 1984; Weiß *et al.*, 2001; Stanimirovic, 2002; Helfer *et al.*, 2003; Kurono *et al.*, 2009; Koda *et al.*, 2011 and references therein. Throughout the years, these techniques have been tested and implemented in the most widely used astronomical data handling packages. The single-dish and interferometric data combined in this thesis employ the `feathering` algorithm, which can be executed in CASA. Figure 2.11 displays the CASA workflow for the combination of interferometric and single-dish data, which is described below:

- **Preparation of the calibrated single-dish image**
  The single-dish image is imported to CASA and it is regridded using the task `imregrid` to match the image shape, the pixel size and the coordinate system of the interferometric image. When this step is completed, the two datasets must have identically gridded spectral axes.

- **Flux conversion of single-dish image**
  Before adding the short-spacing to the interferometric data, both interferometric and single dish images are required to have the same flux density normalization scale. The single-dish image is converted from antenna units to Jy/beam using the `immath` command.

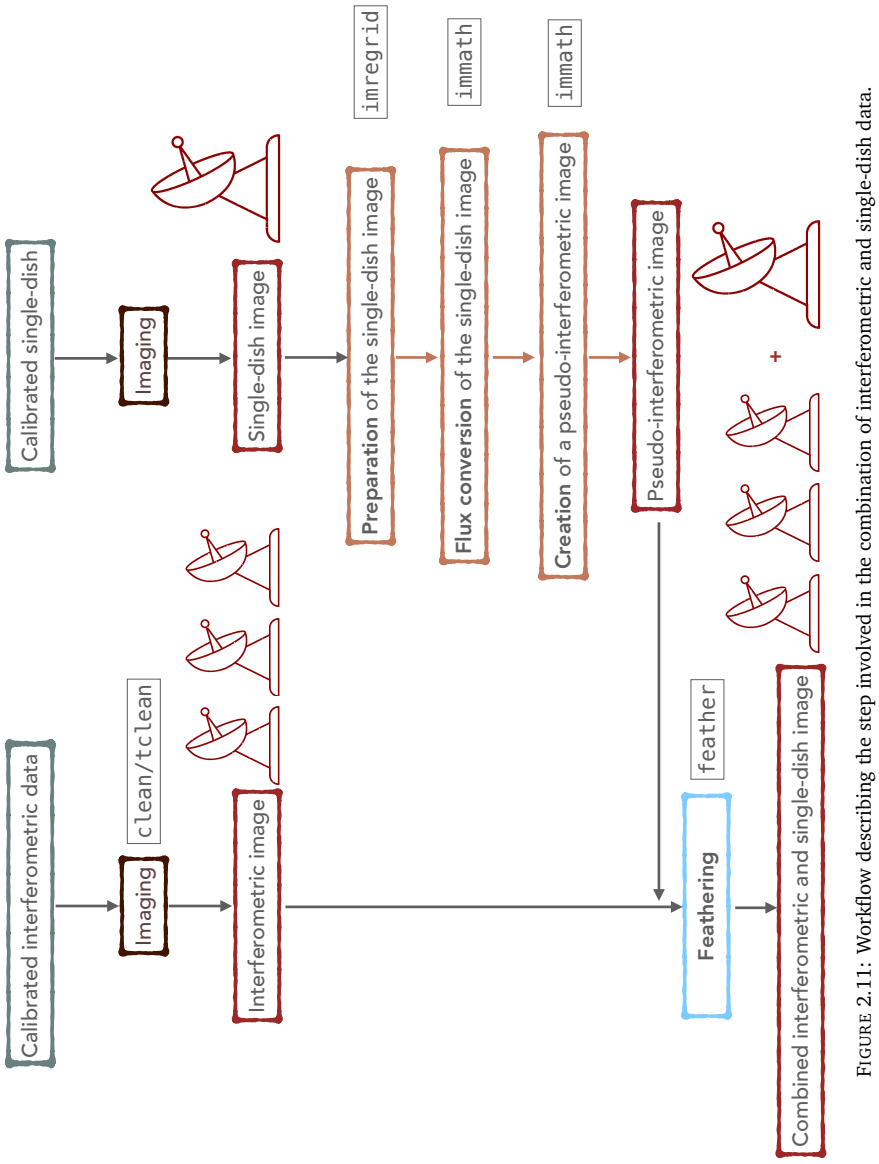

FIGURE 2.11: Workflow describing the step involved in the combination of interferometric and single-dish data.

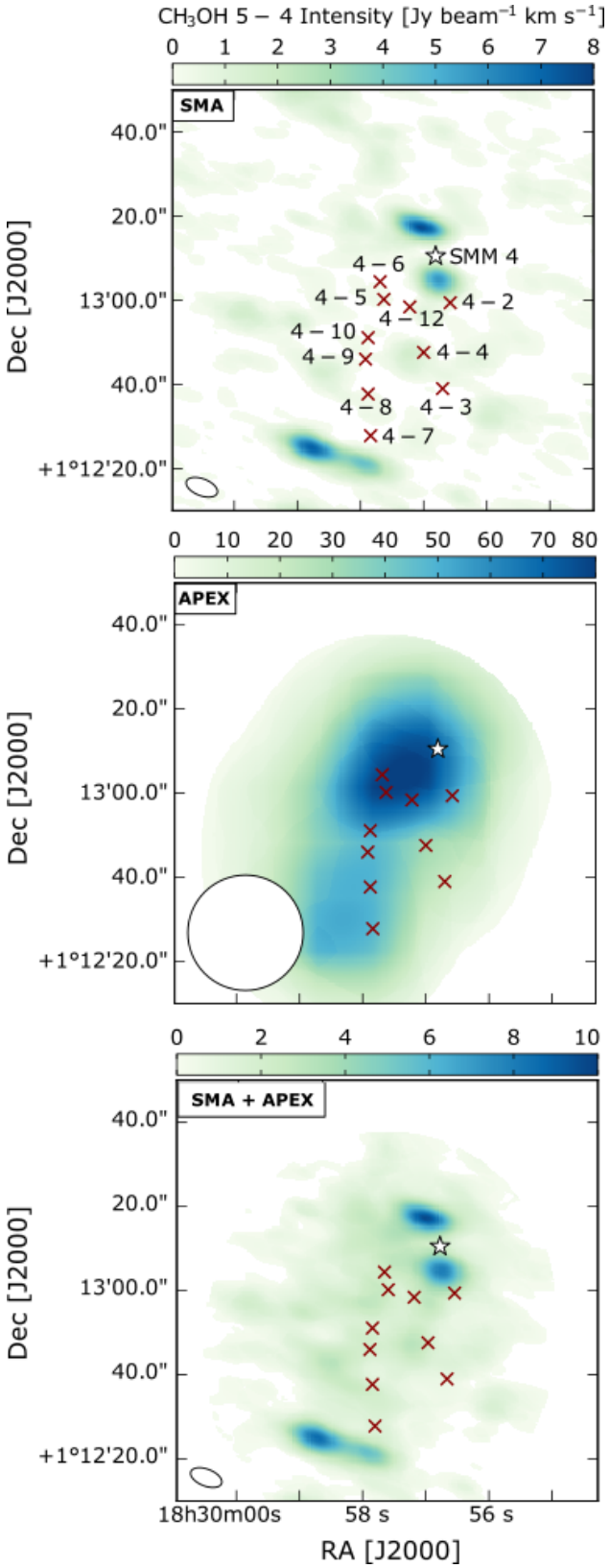

FIGURE 2.12: Example of the combination of interferometric and single dish data. The three panels display integrated intensity maps of the CH_3OH 5 − 4 A^+ line observed with the SMA (top), the APEX telescope (middle) and the combined SMA + APEX datasets (bottom). The interferometer filters out spatially extended emission. The single-dish telescope retrieves the large-scale emission. The combination of the interferometric and single-dish data recovers the spatially extended emission in the region of interest, where the sources represented by dark red crosses are located.

- **Creation of a pseudo-interferometric image**
  The single-data is multiplied by the interferometric primary beam response to assure that both datasets have the same response on the sky. This step is computed using the `immath` command. The single-dish image is thus transformed into the so-called *pseudo-interferometric* image.

- **Feathering**
  The feathering algorithm is computed using the `feather` command. This task initially scales the intensity of the pseudo-interferometric image by the ratio of the volumes of the interferometric and single dish CLEAN beams. Next, it adds the visibility of the interferometric image to the scaled pseudo-interferometric image in the *uv* plane. The outcome is Fourier-transformed to obtain the combined interferometric and single-dish image. Figure 2.12 displays an example of the combination of interferometric and single-dish using SMA and APEX datasets.

3

The star-forming regions

This thesis is driven by the observational study at infrared and millimeter wavelengths of interstellar molecules belonging to the envelopes of Class 0 and Class I young stellar objects located in three nearby star-forming regions: the Serpens SVS 4 cluster in the Serpens cloud core, the multi-protostellar system IRAS 05417+0907 in the λ Orionis Barnard 35A cloud and the Coronet cluster in Corona Australis. This chapter provides an introduction to the large-scale environments where the targeted sources of Chapters 5, 6 and 7 are currently being formed.

3.1 THE SERPENS MOLECULAR CLOUD COMPLEX

The Serpens Molecular Cloud is one of the most active sites of nearby ongoing star formation. It is located at a distance of 436 ± 9 pc (Gaia DR2;Ortiz-León *et al.*, 2018) and it harbours at least 2000 young stellar objects (Herczeg *et al.*, 2019). The star-formation activity of the cloud was discovered by Strom *et al.* (1974). Since then, the region has been at the center of an extensive multi-wavelength research (e.g. Dame and Thaddeus, 1985; Dame *et al.*, 1987; Eiroa and Casali, 1989; Eiroa *et al.*, 2008 and references therein). The cloud extends for ≈500 pc and it is part of the Serpens-Aquila complex (Figure 3.1). Compared to other nearby star-forming regions, it is particularly challenging to characterize as it is observed against the crowded Galactic Plane and it spans over a large range of extinctions.

In the Serpens-Aquila complex there are a number of individual clouds distributed within the Aquila Rift, a suite of dark clouds extending on the sky for over 25° (Cambrésy, 1999; Green *et al.*, 2015). The most studied cloud within the complex is Serpens Main (also referred to as Serpens cloud core and cluster A), where our sources of interest are located (Eiroa *et al.*, 2008) (see Chapter 5). The other star-formation sites are: Serpens Northeast, located at 1° east of Serpens Main (Dunham *et al.*, 2015); W40 and Serpens South, two dense embedded clusters located next to and along a massive filament 3° south of Serpens Main (Gutermuth *et al.*, 2008; Povich *et al.*, 2013; Dunham *et al.*, 2015; Könyves *et al.*, 2015), and Serpens far-South, situated nearby MWC 297 (Bontemps *et al.*, 2010; Dunham *et al.*, 2015; Rumble *et al.*, 2015).

The Serpens cloud core harbours a plethora of deeply embedded protostars (Eiroa *et al.*, 2008 and references therein). The principal Class 0/I

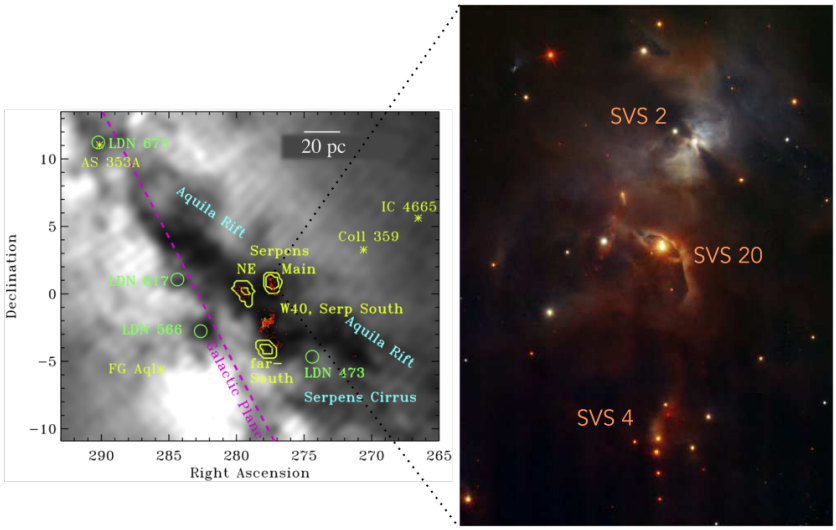

FIGURE 3.1: The Serpens Molecular Cloud Complex. *Left:* An overview of the Serpens-Aquila complex. The Serpens star-forming regions (yellow circles) are interspersed among the dark clouds belonging to the Aquila Rift. The magenta line denotes the Galactic Plane. Credit: Herczeg *et al.* (2019). *Right:* Three-colour image of the Serpens cloud core (also known as Serpens Main). The composite is made from the Very Large Telescope HAWK-I J-, H- and K-bands. The bottom of the image displays the Serpens SVS 4 cluster studied in this thesis. Credit: Eiroa *et al.* (2008).

sources in the core are ten, of which four have been securely classified as Class 0: SMM1, SMM3, SMM4 and S68N (or SMM9) (Hurt and Barsony, 1996). The dynamical structure and physical properties of these four protostars has been studied extensively (e.g., Casali *et al.*, 1993; Davis *et al.*, 1999; Larsson *et al.*, 2000; Harvey *et al.*, 2007; Evans *et al.*, 2009; Kristensen *et al.*, 2010; Tychoniec *et al.*, 2019), revealing stellar multiplicity. For instance, the brightest millimeter source in the core, the Class 0 SMM1 consists of four continuum sources (Choi, 2009; Dionatos *et al.*, 2014; Hull *et al.*, 2017), whereas SMM4 has been resolved into two components (Aso *et al.*, 2018).

The molecular transitions detected towards Serpens Main at infrared, millimeter and submillimeter wavelengths unveil a rich-chemistry in the cloud core (e.g., McMullin *et al.*, 1994; White *et al.*, 1995; McMullin *et al.*, 2000; Kristensen *et al.*, 2010; Öberg *et al.*, 2011c; Dionatos *et al.*, 2013; Martín-Doménech *et al.*, 2019; Bergner *et al.*, 2019), especially towards the innermost regions of the SMM1 envelope.

Chapter 5 of this thesis is centered on Serpens SVS 4, a dense cluster of protostars located in the south-eastern core of Serpens Main near the Class 0 binary SMM4 (Figure 3.1). The cluster counts 11 objects within a region of ≈20 000 AU across, and it is so dense that it was long thought to be a single source, until it was resolved by Eiroa and Casali (1989). The cluster members have low-to-intermediate masses (Pontoppidan *et al.*, 2004) and they have mostly been studied in the near- and mid-infrared spectral domains, especially the two most massive sources SVS 4–5 and SVS 4–9 (Chiar *et al.*, 1994; Pontoppidan *et al.*, 2003a; Boogert *et al.*, 2008; Bottinelli *et al.*, 2010). The cluster currently holds the highest solid-state methanol abundance among low- to intermediate-mass protostars, 28% with respect to water (Pontoppidan *et al.*, 2003b; Pontoppidan *et al.*, 2004), and solid CO_2 abundances $\sim 30-50\%$ relative to water (Pontoppidan *et al.*, 2008).

3.2 THE ORION MOLECULAR CLOUD COMPLEX

The Orion Molecular Cloud Complex is the closest site of high-mass star-formation and probably the most studied stellar nursery in our Galaxy and the entire Universe (Menten *et al.*, 2007; Bally, 2008). It extends for ~ 30° on the sky and it harbours a vast number of sub-clouds and stellar groups lying at different distances (Figure 3.2). In the past couple of years, *Gaia* DR2 studies provided more accurate values for the distance to individual parts of the cloud (Zucker *et al.*, 2019; Zucker *et al.*, 2020).

Ongoing star formation in the complex is predominantly concentrated in four regions: Orion A and Orion B, representing the largest sites of star-formation in the main cloud (e.g., Carpenter, 2000; Johnstone *et al.*, 2001; Megeath *et al.*, 2012; Megeath *et al.*, 2016) and home of the Orion Nebulae Cluster (ONC). The youngest populations in Orion A and B form part of the Orion OB1c and OB1d sub-associations, situated at Orion's Sword, ~4° south of Orion's Belt (Buckle *et al.*, 2012; Megeath *et al.*, 2012; Polychroni *et al.*, 2013). The third stellar nursery is the σ Orionis region positioned below the eastern side of the Orion's Belt and hosting a stellar population significantly younger compared to the majority of Orion's Belt stars (Walter *et al.*, 1997; Jeffries, 2007; Hernández *et al.*, 2007; Caballero, 2008; Hernández *et al.*, 2014). Finally, the fourth star-forming site is the λ Orionis region, which harbours the sources studied in Chapter 6. It is located in the northernmost part of the complex also known as Orion's head (e.g., Sharpless, 1959; Lada and Black, 1976; Murdin and Penston, 1977; Mathieu, 2008; Bayo *et al.*, 2011; Sahan and Haffner, 2016), at a mean distance of 410 ± 20 pc (Zucker *et al.*, 2019; Zucker *et al.*, 2020).

The λ Orionis region is seen as a ring of dust and gas surrounding a core of OB stars (Figure 3.2) (e.g., Wade, 1957; Maddalena and Morris, 1987; Lang *et al.*, 2000; Dolan and Mathieu, 2002). There are three sub-clouds within the ring: Barnard 30 (B30) and Barnard 35A (B35A) (Murdin and Penston, 1977; Barrado *et al.*, 2018) and Barnard 223 (B23) (Bayo *et al.*, 2011; Bell *et al.*, 2013). It is highly debated whether the latter cloud is associated with the λ Orionis region or only projected in the same portion of the sky, as the radial velocities of the pre-main sequence stars in B223 differ from those in B30 and B35A (Dolan and Mathieu, 2002; Yi *et al.*, 2018). The three clouds exhibit several cold cores, which compared to the cores found in Orion A and B, show the lowest median masses, sizes and gas fraction and the highest dust temperatures (Liu *et al.*, 2016). These factors suggest a negative feedback from the λ Orionis massive star on the formation and evolution of dense cores in the region (Yi *et al.*, 2018; Yi *et al.*, 2021).

Chapter 6 of this thesis studies the young protostellar population of the Barnard 35A cloud (aka B35, BRC18, SFO18, L1594). B35A displays a prominent cometary shape and a bright rim on the western edge (Lada and Black, 1976) (Figure 3.2). The morphology of the cloud, and plausibly the star-formation in its interior, are the result of the interaction between the radiation fields from the nearby OB stars and the expansion of the surrounding H II region Sh2-264 (Sharpless, 1959; Qin and Wu, 2003; Sahan and Haffner, 2016). Objects of interest within the cloud are: the embedded Class I source IRAS 05417+0907 ($L = 6L_{\odot}$; Sugitani *et al.*, 1991;

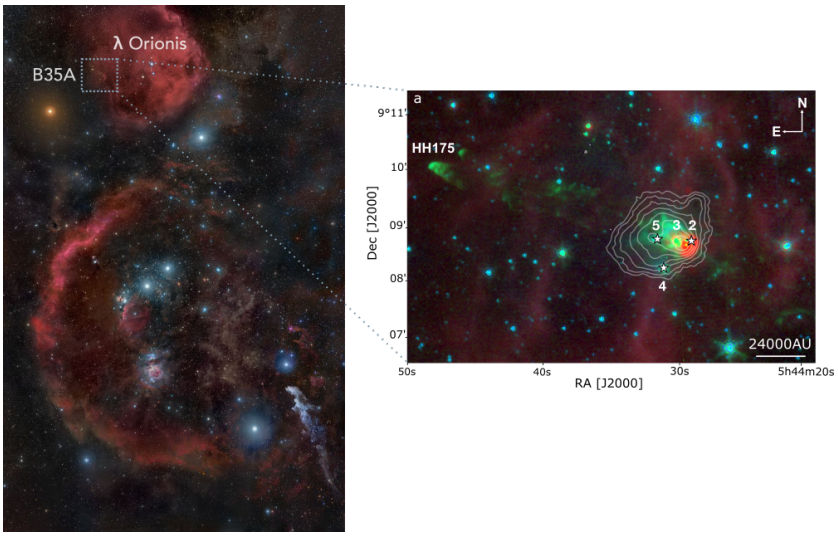

FIGURE 3.2: The Orion Molecular Cloud Complex. *Left:* An overview of the Orion Cloud Complex. The Barnard 35A cloud (dotted rectangle) is located to the east of the λ Orionis star Credit: R. B. Andreo. *Right:* Three-colour image of the Barnard 35A cloud. The composite is made from the *Spitzer* IRAC 3.6 μm (blue), 4.5 μm (green) and MIPS 24.0 μm (red) bands. A SCUBA–2 850 μm map (Reipurth and Friberg, 2021) is overlaid on the composite. For more details on this figure please refer to Chapter 6).

Morgan *et al.*, 2008) for long thought to be a single source, but forming a system composed by at least four objects (Connelley *et al.*, 2008; Reipurth and Friberg, 2021); the FU Orionis star situated to the south-eastern end of the cloud enclosed in a large reflection nebula (Herbig, 1966), and the giant Herbig-Haro object HH175 (Myers *et al.*, 1988; Qin and Wu, 2003; Craigon, 2015; Reipurth, 2000) emanated from the IRAS 05417+0907 multiple system and crossing the cloud in the eastern-western direction for ~1.6 pc at the cloud's estimated distance (Reipurth and Friberg, 2021).

The large-scale morphology and chemical inventory of B35A have been studied at millimeter and submillimeter wavelengths (De Vries *et al.*, 2002; Craigon, 2015; Kim *et al.*, 2020; Reipurth and Friberg, 2021; Yi *et al.*, 2021) and in the optical/near-infrared (Noble, 2011; Noble *et al.*, 2013; Noble *et al.*, 2017; Suutarinen, 2015a; Reipurth and Friberg, 2021).

3.3 THE CORONA AUSTRALIS MOLECULAR CLOUD COMPLEX

The Corona Australis Molecular Cloud Complex (CrA) is one of the nearest star-forming regions disclosing a wealth of young embedded objects (Peterson *et al.*, 2011). It is located at a distance of 149.4 ± 0.4 pc (*Gaia*-DR2; Galli *et al.*, 2020) and it extends for over 5° on the sky. The study of Corona Australis, and specifically of its young stellar population, was initiated by Herbig (1960) who discovered two variable young stars, R CrA and T CrA, in the most extincted region of the cloud. The follow-up works made Corona Australis one of the best targets for star-formation studies (e.g., Taylor and Storey, 1984; Knacke *et al.*, 1973; Neuhäuser *et al.*, 2000; Nutter *et al.*, 2005; Forbrich *et al.*, 2007; Peterson *et al.*, 2011).

Corona Australis possesses a characteristic elongated "head-tail" structure (Figure 3.3). The "head" region, also referred to as the "Coronet", is where

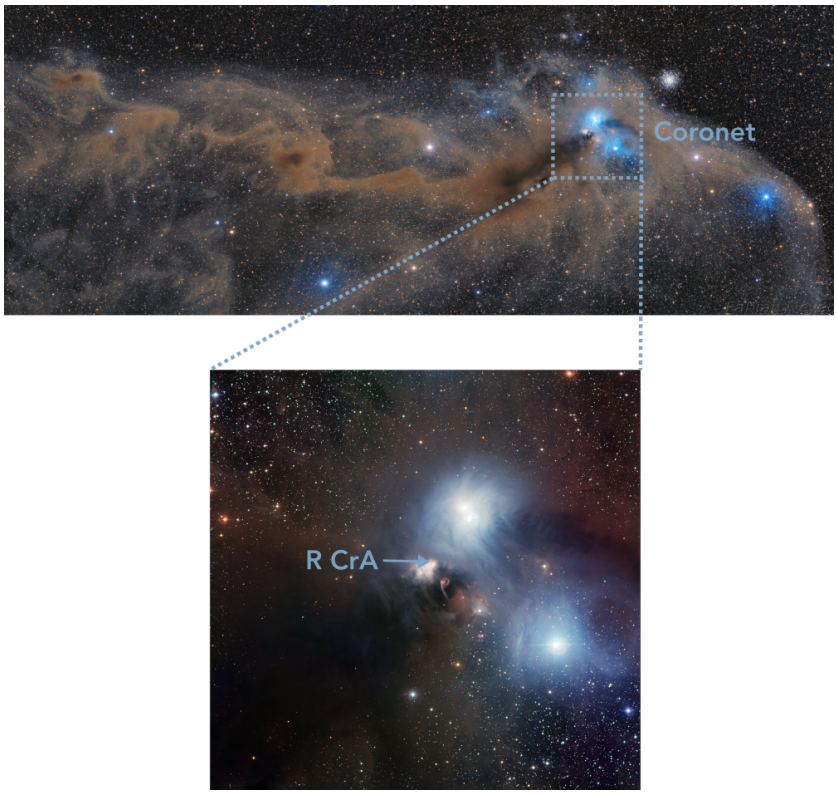

FIGURE 3.3: The Corona Australis Molecular Cloud Complex. *Top:* An overview of the Corona Australis Cloud Complex. The Coronet cluster (dotted rectangle) represents the densest region of the cloud. It harbours the Herbig Ae/Be star R CrA and several Class 0/I young stellar objects Credit: F. Neyer. *Bottom:* Three-colour image of the Coronet cluster. The composite is made from MPG/ESO telescope Wide Field Imager 456 nm (blue), 539 nm (green) and 651 nm bands. Credit: ESO.

most of the young stellar population (Class 0/I) is concentrated (Taylor and Storey, 1984; Forbrich *et al.*, 2007; Forbrich and Preibisch, 2007). The Coronet is the targeted region described in Chapter 7. The most recent membership analysis study of Corona Australis detected a total of 262 young stellar objects, of which the vast majority are Class II/III sources (Galli *et al.*, 2020). The census also reports the existence of a large population of more evolved YSOs located "off cloud", in the northern region of the complex (Galli *et al.*, 2020). The number of youngest objects (Class 0/I) is not well constrained due to the high extinction of the densest clouds and especially of the Coronet region (Alves *et al.*, 2014; Galli *et al.*, 2020).

Five dark clouds have been detected in CrA from the extinction map of Rossano (1978). These are named A to E, starting from the Coronet (CrA-A) in the eastern side of the cloud to the west-southern end (Figure 3.3). The location of the dense cores in the complex is well correlated with the spatial distribution of the filamentary structure where the clouds are (Bresnahan *et al.*, 2018). Notably, only low-mass starless cores were identified further away from filaments, whereas all the more massive cores were detected along filaments inside the clouds or in their vicinity (Bresnahan *et al.*, 2018).

Among the five dark clouds, the most studied is the Coronet which harbours the Class 0/I sources targeted in Chapter 7. This site is responsible for the majority of the dynamical activity in the entire complex. Beside

hosting the variable Herbig Ae/Be star R CrA, it is home of the T Tauri star T CrA, located to the south-east of R CrA (Taylor and Storey, 1984). The region among the two variable stars, also known as the IRS7 region, harbours a pre-stellar core, SMM1A, and a suite of Class I (or lower) young stellar objects (e.g., Brown, 1987; Nutter *et al.*, 2005; Groppi *et al.*, 2007; Chen and Arce, 2010; Peterson *et al.*, 2011). The wealth of arcs and clumps in the area, identified as Herbig-Haro objects, corroborates the presence of young stellar objects belonging to the earliest classes (Strom *et al.*, 1974; Reipurth, 2000).

A number of multi-wavelength studies has been carried out towards the Coronet, aiming at investigating the effect of external irradiation of R CrA onto the physical and chemical evolution of the protostars in the region. Most observations, including unbiased surveys, were conducted at millimeter/submillimeter wavelengths (e.g., Schöier *et al.*, 2006; Lindberg and Jørgensen, 2012; Watanabe *et al.*, 2012; Lindberg *et al.*, 2015; Lindberg *et al.*, 2017) and suggest that the Herbig Ae/Be star R CrA influences the region by increasing the temperature of the molecular gas and by favouring the formation of photon-dominated regions through irradiation. The mid-infrared spectra of a handful of objects in the Coronet present ice features attributable to H_2O, CO_2, CH_3OH, and plausibly ammonium ion (Boogert *et al.*, 2008; Pontoppidan *et al.*, 2008; Bottinelli *et al.*, 2010).

4

This thesis

"*Se non ora, quando?*"
—Primo Levi

4.1 RESEARCH CONTEXT AND DESCRIPTION

The interplay between interstellar dust, ice and gas plays a key role in the journey starting in dense molecular clouds and ending with the rise of new planetary systems. Along this path, ice mantles on dust grains can be described as open systems, in constant exchange with the surrounding gas phase through accretion and desorption processes. The outcome of this mutual ice-gas interaction are organic molecules of different levels of complexity (Jørgensen *et al.*, 2020). These can evolve into biomolecules and undergo an intricate and poorly understood cascade of biochemical reactions, which ultimately can give rise to living organisms in the Universe. In this context, a logical approach to constrain the formation of complex molecules consists of investigating the chemical processes during the formation of solar-type stars. In other words, providing constraints on the nature of the material and the relative importance of the mechanisms involved in the gas and ice interplay during stellar evolution.

At present, a lot is still unknown about the degree of chemical complexity and the relationships between the intertwined solid-state and gas-phase chemistries in stellar nurseries. The count of securely detected molecules in the ISM (> 200) increased considerably in the last decades and with it, the existence of new chemical routes in star-forming regions (McGuire, 2018). However, despite the recent advances in the field, some ultimate questions remain unanswered such as:

- What are the exact processes linking solid-state and gas-phase species in cold protostellar envelopes?
- To what degree the physical environment impacts the the solid- and gas-phase chemistries during the formation of low-mass protostars?

To address the above questions, in this thesis I carried out multi-wavelength observational studies of low-mass protostellar envelopes using a suite of millimeter and infrared facilities (e.g., the *Submillimeter Array* (SMA), *the Atacama Pathfinder EXperiment* (APEX), the *Institut de RadioAstronomie Millimétrique* (IRAM) 30m, the *James Clerk Maxwell Telescope* (JCMT), and the *Very Large Telescope* (VLT)). To access whether the physical conditions affect the gas and ice interplay, the selected sample consists of young stellar objects

located in three nearby star-forming regions, which do not share similar formation histories and are characterized by different physical structures. The targeted regions, the Serpens SVS4 cluster in Serpens Main, the multi-protostellar system IRAS 05417+0907 in the λ Orionis Barnard 35A cloud, and the Coronet cluster in Corona Australis are described in Chapter 3.

The approach followed consists of combining millimeter and near-/mid-infrared observations, and thus directly obtain and compare abundances of key astrochemical molecules, particularly of methanol, in both solid and gas phases towards the same astrophysical region. This procedure, previously adopted by Öberg *et al.* (2009a) and Noble *et al.* (2017), provides critical information tracing the solid-state and gas-phase chemistries in a complementary manner. In other words, it makes it possible to relate small-scale variations in the ice chemistry probed by infrared observations with large-scale astrophysical phenomena explored with millimeter observations.

Comparative studies similar to the ones presented in Chapters 5, 6 and 7 are relatively uncommon due to the challenges in obtaining observational constraints on solid-state chemistry. This is primarily due to the difficulties in disentangling the contribution of multiple molecules from blended absorption bands (Sect. 2.2) and to the low sensitivity of infrared observations, which hampers the detection of solid-state molecules with abundances with respect to H_2 below $\approx 10^{-6} - 10^{-7}$. In comparison, millimeter observations can detect gas-phase molecules with fractional abundances as low as $\approx 10^{-12}$. Additionally, the sample of sources for which spectroscopic infrared data exist is significantly reduced compared to the regions for which millimeter data are available (Boogert *et al.*, 2015). This reflect the fact that the observation of several ice bands is only possible from space as described in Chapter 2. As a consequence of the above, solid-state and gas-phase observations are frequently treated separately or the latter are often invoked to indirectly constrain solid-state chemistry. However, this approach leads to severe assumptions on the composition of the ice mantles, on the grain-surface chemistry and on how efficiently molecules are desorbed to the gas-phase (Noble *et al.*, 2017). One way to observationally overcome these assumptions is to compare, whenever possible, direct measurements of solid-state and gas-phase molecules.

To determine the abundances of gas-phase molecules and of their solid counterparts, and to cast light onto the poorly constrained non-thermal desorption processes described in Chapter 1, the most appropriate targets are the coldest shielded regions of protostellar envelopes, where the ice mantles are not thermally desorbed and, by consequence, non-thermal desorption processes are the most dominant (Sect. 1.3). To map the emission towards these extended regions at rather high-angular resolution ($3 - 4''$), the adopted observation strategy consisted of accompany interferometric observations with single-dish observations (Sect. 2.3.4). This procedure allows to recover the extended emission filtered out by the interferometer and to perform a quantitative analysis of the observational data.

The most suitable molecule for this type of comparative studies is methanol for multiple reasons. First, it is the only complex organic molecule unambiguously detected in both solid and gas phases. Interestingly, it is the simplest among the COMs detected in the gas-phase (McGuire, 2018), but it is the

most complex molecule securely detected in the ice mantles in interstellar and circumstellar environments (Boogert *et al.*, 2015). Second, CH_3OH is primarily formed in the solid-state (Watanabe and Kouchi, 2002; Fuchs *et al.*, 2009), as its gas-phase formation pathways are considered to be remarkably less efficient in comparison (Roberts and Millar, 2000; Garrod and Herbst, 2006). This indicates that CH_3OH is the ideal species to constrain non-thermal desorption mechanisms. Consequently, in the past years laboratory experiments and models have focused on determining non-thermal desorption rates and efficiencies principally for methanol with respect to other interstellar species (e.g., Öberg *et al.*, 2009b; Bertin *et al.*, 2016; Cruz-Diaz *et al.*, 2016; Martín-Doménech *et al.*, 2016; Minissale *et al.*, 2016a; Cazaux *et al.*, 2016). As a result, one of the aims of this thesis is to provide observational constraints to the current laboratory and computational predictions.

Finally, methanol is considered to be the "seed" molecule for the production of complex organic species both in the solid-state (e.g., Öberg *et al.*, 2009b; Chuang *et al.*, 2016; Fedoseev *et al.*, 2017) and in the gas gas-phase (e.g., Shannon *et al.*, 2014; Balucani *et al.*, 2015; Vazart *et al.*, 2020). This implies that current astrochemical models largely rely on the presence of CH_3OH ice and its efficient desorption to explain the observed abundances of complex organics in the hot-corino stage and in the cold phase. However, in some cases this can lead to overestimated gas-phase CH_3OH abundances compared to the observed values (e.g., Vasyunin and Herbst, 2013; Vasyunin *et al.*, 2017). This reflects the poorly known values for non-thermal desorption efficiencies and the overall challenges in providing observational constraints on CH_3OH ice in star-forming regions (Boogert *et al.*, 2015). Alternatively, there might be other chemical routes to unveil which link solid-state and gas-phase CH_3OH to the production of COMs in star-forming regions.

4.2 PUBLICATIONS

This section provides a summary overview of the scientific articles included in Chapters 5, 6, 7. The articles are:

1. G. Perotti, W. R. M. Rocha, J. K. Jørgensen, L. E. Kristensen, H. J. Fraser, and K. M. Pontoppidan 2020, A&A, 643, A48. "Linking ice and gas in the Serpens low-mass star-forming region";

2. G. Perotti, J. K. Jørgensen, H. J. Fraser, A.N. Suutarinen, L. E. Kristensen, W. R. M. Rocha, P. Bjerkeli, K. M. Pontoppidan, 2021, A&A, submitted. "Linking ice and gas in the λ Orionis Barnard 35A cloud";

3. G. Perotti, J. K. Jørgensen, L. E. Kristensen, W. R. M. Rocha, E. Artur de la Villarmois, H. J. Fraser, P. Bjerkeli, M. Sewilo, S. B. Charnley, in preparation. "Linking ice and gas in the Coronet cluster in Corona Australis". The inclusion of the awarded second track of SMA data is required to complete this article. This observational run has been delayed due to the shutdown of the SMA due to Covid-19.

4.2.1 *Article I: Linking ice and gas in the Serpens low-mass star-forming region*

This paper present a study the gas-ice interplay towards ten deeply embedded low-to-intermediate mass protostars constituting the Serpens SVS4 cluster in Serpens Main (Sect. 3.1). In particular, millimeter and near-infrared observations are combined to obtain direct measurements of CH_3OH and CO gas-phase and ice towards the ten young protostars. The SMA and APEX datasets are folded together to recover the spatially extended emission filtered out by the interferometer in the manner described in Sect. 2.3.4. Simultaneously, the VLT-ISAAC near-infrared data are decomposed using a combination of laboratory components and analytical functions using the OMNIFIT fitting utility (Sect. 2.2.1). Finally, the chemical behaviours of these two pivotal gas-phase species are analysed and directly compared to their ice counterparts. To maintain the ice and gas measurements in their own reference frame, two separate H_2 column density maps are derived: one from SCUBA−2 submillimeter continuum maps at 850 μm, and one from the extinction in the J-band to adopt in the abundance determination of the gas-phase and ice species, respectively.

An important conclusion of this observational study is that the gas and ice variations towards the Serpens SVS4 cluster members do not show clear trends. This lack of correlation is attributed to the complex physical structure of the SVS4 cluster, plausibly embedded in the protostellar envelope of the Class 0 protostar SMM4 and affected by the outflow associated with this young source. This indicates that care should be taken when assuming the abundance of solid-state species from known gas-phase abundances and vice versa. Another important result is that the calculated CH_3OH gas-to-ice ratios in the cluster range from 1.4×10^{-4} to 3.7×10^{-3}. The sources responsible for the lower values of the CH_3OH gas-to-ice ratio are either the most deeply embedded or the ones located further away from the main source of UV irradiation, the Class 0 SMM4, where the non-thermal desorption of CH_3OH ice is less efficient. The lower values of the CH_3OH gas-to-ice ratios are in good agreement with the observational study by Öberg *et al.* (2009a) reporting a CH_3OH gas-to-ice ratio equal to 1.2×10^{-4} and to the astrochemical predictions by Cazaux *et al.* (2016).

4.2.2 *Article II: Linking ice and gas in the λ Orionis Barnard 35A cloud*

The main focus of this article is the gas-ice interplay towards the multi-protostellar system IRAS 05417+0907 in the λ Orionis Barnard 35A (B35A) cloud. This system is composed by at least four sources: B35A−2, B35A−3, B35A−4, B35A−5. Compared to Serpens Main, this region is impacted by the stellar winds from the nearby high-mass star λ Orionis, which is thought to be responsible for the star-formation activity in B35A (Sect. 3.2). Therefore, one of the main aims of this paper is to analyse the dependencies of the gas-ice interaction of a second nearby star-forming region, characterized by a physical environment which diverges from Serpens SVS4. We adopt the same observational strategy used in *Article I*: the SMA and APEX datasets are combined to recover the extended CH_3OH emission, whereas SMA and archival IRAM 30m data are folded together to account for the missing CO isotopologues emission. Archival ice column densities determined from

AKARI observations of IRAS 05417+0907 are used to compare the gas and ice abundances.

Our observations show that CH_3OH probes the trajectory of the giant outflow emanated from IRAS 05417+0907, and that the observed CH_3OH emission is due to non-thermal desorption mechanisms, plausibly sputtering of CH_3OH ice during shock events. One important consideration is that none of the targeted species shows an expected trend in ice abundances with respect to gas-abundances, corroborating the result obtained in *Article I*, and suggesting that the interaction between ice and gas species is more complex than previously thought. A second important conclusion is that the dust column density probed by the submillimeter emission is not directly linked to the H_2O ice column density. For instance, the H_2O ice column density is higher towards the protostellar object B35A−4 compared to object B35A−5, whereas the opposite is seen for the submillimeter dust emission. Our conclusion is that this discrepancy is due to the fact that B35A−5 is located along the trajectory of the outflow terminating in the Herbig-Haro object HH 175, in a region where sputtering and heating impact the morphology of the observed submillimeter dust emission. This study shows that millimeter and near-infrared observations are complementary and indispensable to relate the small-scale variations of grain-surface and ice chemistry with large-scale astrophysical phenomena traced by millimeter observations.

4.2.3 *Article III: Linking ice and gas in the Coronet cluster in Corona Australis*

In this article, we focus on the gas-ice interplay towards a third nearby star-forming region, the Coronet situated in Corona Australis (Sect. 3.3). Although it is a deeply embedded cluster of young stellar objects resembling Serpens SVS4, the Coronet harbours a younger stellar population which is strongly irradiated by the nearby Herbig Ae/Be star R CrA. Therefore, this region is an ideal testbed to study the effects of external irradiation from Herbig Ae/Be stars onto the ice and gas chemistries in low-mass protostellar envelopes. The SMA observations are used to study the gas-phase molecular inventory, whereas archival SMA, APEX, and Spitzer Space Telescope data are used to determine the CH_3OH gas-to-ice ratios in the region.

A first important conclusion is that the gas-phase chemistry of the Coronet is affected by the high UV flux from the nearby R CrA. This is reflected in the enhanced emission of formaldehyde (H_2CO) not associated with the young stellar objects in the field of view. In contrast, the H_2CO emission is confined to two ridges which show peculiar shapes, supporting the idea of Lindberg and Jørgensen (2012) that the cluster is strongly impacted by external heating. Additionally, the detection of molecular tracers of shocks such as sulfur oxides (SO, SO_2) at the locations of IRS7A and SMM1C, and of silicon oxide (SiO) south of R CrA suggests that IRS7A, SMM1C and R CrA are likely responsible for outflows and Herbig-Haro objects in the region.

Another important consideration is obtained from the analysis of the gas and ice variations in the Coronet. The comparison reveals a negative trend between the ammonium ion (NH_4^+) and H_2CO gas abundances, with the caveat that NH_4^+ is one of the carriers of the 6.85 μm band. This result indicates that the high-temperature regions traced by the emission of H_2CO

have a lower content of NH_4^+ residing on the grains, in agreement with its desorption with increasing dust temperatures. Finally, the CH_3OH gas-to-ice ratios calculated towards the Coronet from literature data are consistent with the values obtained in *Article I*.

4.3 OVERALL CONCLUSIONS AND OUTLOOK

Taken together, the main contributions of the dissertation research to the field are:

- There is not a one-to-one correspondence between the abundance of gas-phase species and their ice counterparts. As a matter of fact, ice and gas variations towards the studied regions do not follow a predictable trend. This implies that invoking ice chemistry and grain-surface chemistry to explain the observed gas-phase abundances can lead to inaccurate results, especially without an extensive knowledge of the physical environment surrounding the sources of interest.

- The CH_3OH gas-to-ice ratios constrained from observations validate the predicted values ($\sim 10^{-3} - 10^{-4}$) proposed by laboratory experiments (e.g., Öberg *et al.*, 2009b) and models (e.g., Cazaux *et al.*, 2016), favouring an efficient non-thermal desorption of methanol in the gas-phase of cold envelopes. This observational constraint accounts for multiple non-thermal desorption mechanisms, and not for methanol photodesorption only.

- The distribution of CH_3OH gas-to-ice ratios for the Coronet, Serpens SVS4, and towards low-mass Class 0/I protostars in Öberg *et al.* (2009a) suggests that the CH_3OH chemistry at play in cold low-mass protostellar envelopes, located in different low-mass star-forming regions is rather insensitive to varying physical conditions as can be seen in Figure 4.1. However, a larger sample of CH_3OH gas-to-ice ratios is needed to provide a conclusive assessment.

- The combination of infrared and millimeter observations is fundamental to cast light onto the gas-ice interplay, and hence to link the small-scale variations in the ice chemistry with large-scale astrophysical phenomena probed by millimeter observations.

With the awareness of the importance of the gas and ice interplay in the production of complex molecules, it has become clear that gas-phase and solid-state observations are complementary and that their concurrent analysis can advance our understanding of key aspects of star- and planet formation (e.g., desorption processes and snow-lines). Future infrared facilities, most notably the *James Webb Space Telescope* (JWST), will provide high-sensitivity maps of interstellar ice molecules in a variety of astrophysical environments. Compared to its predecessor, the *Spitzer Space Telescope*, the sensitivity of JWST will be fifty times higher at 7 μm just because of its sheer collecting area. Therefore, JWST observations will make it possible to provide better constraints on the solid-state abundances of the eight species securely detected in the ice mantles (H_2O, CO, CO_2, NH_3, CH_4, CH_3OH,

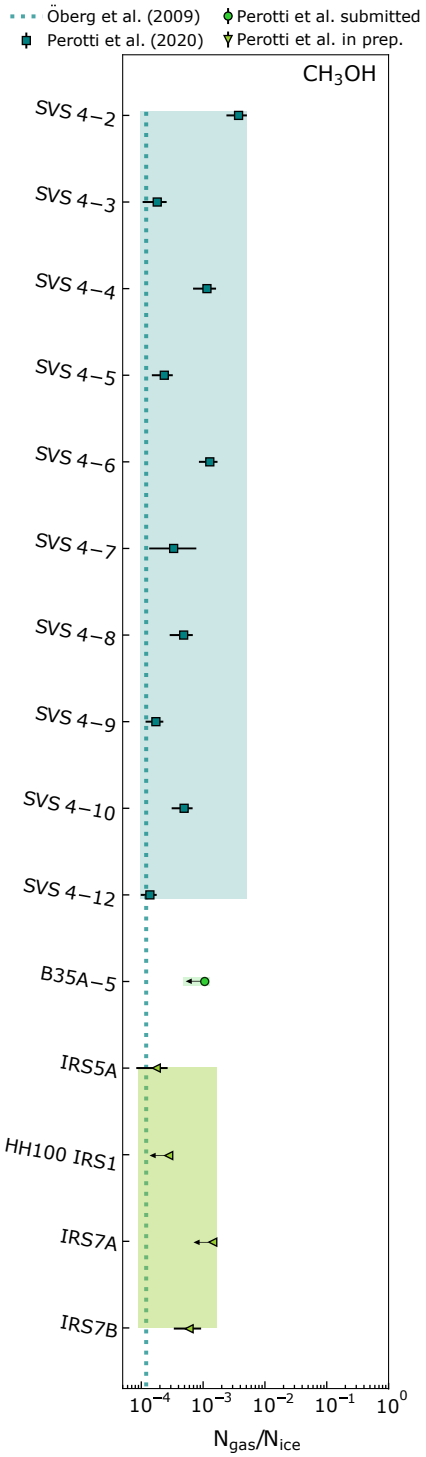

FIGURE 4.1: CH_3OH gas-to-ice ratios (N_{gas}/N_{ice}) towards low-mass protostars in Serpens SVS 4, Orion B35A and Coronet. The Serpens SVS 4 ratios (dark green squares) are from Perotti *et al.* (2020), whereas the Orion B35A upper limit (light green circle) is from Perotti et al. submitted. The light green triangles indicate the ratios estimated in Perotti et al. in preparation for the Coronet cluster in Corona Australis. The dotted light blue line marks the averaged CH_3OH gas-to-ice ratio determined for Class 0/I objects in Öberg *et al.* (2009a). The shaded areas indicate the ranges of gas-to-ice ratios towards the three molecular clouds.

^{13}CO and $^{13}CO_2$) and to confirm the tentative detections (e.g., NH_4^+, H_2CO, HCOOH, CH_3CHO, CH_3CH_2OH).

In this respect, an obvious continuation of the work presented in this thesis will be the combination of high-sensitivity ALMA and JWST data. The ice and gas interplay will be explored systematically for each evolutionary stage of the star-formation process, from cold clouds to nearby edge-on protoplanetary disks. These observational constraints will make it possible to trace the chemical journey of the material from the clouds to the planet-forming zone, and hence to understand what is the level of chemical complexity of the matter incorporated into comets and planets. The outcomes of these studies can be compared to the composition of cometary material or of the organic matter found in pristine records of the early Solar System, carbonaceous chondrites. The dependency of the gas-to-ice ratios, and therefore of the interconnected gas-phase and ice chemistries on the physical conditions will be address routinely for multiple interstellar species, eventually more complex than CH_3OH (e.g., CH_3CH_2OH). Particularly important for this purpose will be the comparison between the gas-to-ice ratios obtained towards clusters of young stellar objects versus isolated protostars, to disentangle the relative importance of different astrophysical phenomena.

The resulting observational constraints will motivate compelling laboratory experiments, especially of non-thermal desorption processes. At present, the most studied non-thermal desorption channel in the laboratory is photo-desorption, but even for this process, the rates and yields have only be determined for a handful of interstellar ice molecules. The yields of the other non-thermal desorption mechanisms described in Sect. 1.2.3 are unknown for the majority of the interstellar species. Consequently, astrochemical models often do not include non-thermal desorption processes or only for a limited number of species, which in turn affects the model results. It is therefore a priority to obtain reliable laboratory and model predictions to confront with observational results. In particular, it is of paramount importance to increment modelling efforts simulating the ice photo-chemistry of methanol and of more complex organics under laboratory conditions, to gain a better understanding of the reactions which regulate the ice chemistry prior and during the core collapse.

Another important venue for future work will be comparative studies of the observationally constrained gas-to-ice ratios with the values obtained from radiative transfer models combined with astrochemical models, specifically tuned to reproduce the physical structure of the targeted objects. These will be of uttermost importance for the study of the gas-ice interplay in protoplanetary disks, to determine at which radii from the central protostar specific molecules are thermally desorbed (i.e., the location of snow-lines) and how this affects the chemical composition of the forming planets.

4.4 OWN CONTRIBUTIONS VERSUS CONTRIBUTIONS OF COLLABORATORS

This section reports my own contributions to the articles and the contributions of my collaborators.

Article I This project is based on millimeter SMA and APEX observations

with L. E. Kristensen as principal investigator, and near-infrared VLT-ISAAC observations with K. M. Pontoppidan as principal investigator. I carried out the calibration and reduction of the raw SMA and APEX datasets. L. E. Kristensen assisted in this process. The combination of the interferometric and single-dish data was performed by myself and J. K. Jørgensen provided assistance with it. The flux calibration and the telluric absorption line removal of the near-infrared VLT data was performed by K. M. Pontoppidan. The rest of the infrared data reduction, the continuum and optical depth determination, and the spectral decomposition with OMNIFIT was carried out by myself with the assistance of W. R. M. Rocha. Guidance in the usage of OMNIFIT and in the selection of the methodology to derive the column density of the ice species was provided by H. J. Fraser and W. R. Rocha. The ice laboratory components were supplied by H. J. Fraser and prepared to be imported to OMNIFIT by W. R. Rocha. I led the analysis of the millimeter and infrared data and the final discussion. I wrote the paper on my own and made all the figures and tables, except for Figure 5.6 which was made by W. R. Rocha. All co-authors gave valuable inputs and edited the article.

Article II This study makes use of SMA and APEX observations of which I am the principal investigator, and literature ice column densities derived from data taken with the AKARI satellite provided by A. N. Suutarinen. I was actively involved in the SMA data collection. Reduced IRAM 30m maps of the CO isotopologues were obtained from H. J. Fraser group members. The calibration, reduction and combination of the interferometric and single-dish data was performed by myself. L. E. Kristensen assisted with the imaging of the SMA data and J. K. Jørgensen gave valuable inputs for the combination of SMA and APEX data. W. R. Rocha gave support with the production of the H_2 column density map from the visual extinction in the J-band. I lead the analysis of the data and the resulting discussion. I wrote the entire paper by myself and created all the tables and figures, except for Figure 1 which was made by K. M. Pontoppidan. P. Bjerkeli supplied important comments during the analysis of the data. All the co-authors made useful suggestions and edited the article.

Article III This paper is based on SMA observations of which I am the principal investigator and literature gas and ice column densities determined from data taken with SMA, APEX and *Spitzer Space telescope* observations. The raw SMA data were calibrated and imaged by myself. I wrote the paper on my own and produced all the tables and figures, except for Figure 1 which was made by W. R. Rocha. We are currently awaiting for the second awarded track of the SMA data, delayed due to the pandemic, which will target the CH_3OH $J = 5 - 4$ branch at 241.791 GHz. The SMA has resumed operations, and our track is supposed to be carried out in the current observational semester. Afterwards, we will be able to combine these SMA data with awarded APEX and ACA data, and to compare the CH_3OH gas-to-ice ratios obtained from literature data with the value calculated from the new SMA data at a higher angular resolution.

5

Linking ice and gas in the Serpens low-mass star-forming region

G. Perotti[1], W. R. M. Rocha[1], J. K. Jørgensen[1], L. E. Kristensen[1], H. J. Fraser[2], K. M. Pontoppidan[3]

[1] Niels Bohr Institute & Centre for Star and Planet Formation, University of Copenhagen, Øster Voldgade 5−7, 1350 Copenhagen K., Denmark
[2] School of Physical Sciences, The Open University, Walton Hall, Milton Keynes, MK7 6AA, United Kingdom
[3] Space Telescope Science Institute, 3700 San Martin Drive, Baltimore, MD 21218, USA

Published in Astronomy & Astrophyics, vol. 643, article no. A48, Nov 2020

Abstract

Context. The interaction between dust, ice, and gas during the formation of stars produces complex organic molecules. While observations indicate that several species are formed on ice-covered dust grains and are released into the gas phase, the exact chemical interplay between solid and gas phases and their relative importance remain unclear.

Aims. Our goal is to study the interplay between dust, ice, and gas in regions of low-mass star formation through ice- and gas-mapping and by directly measuring gas-to-ice ratios. This provides constraints on the routes that lead to the chemical complexity that is observed in solid and gas phases.

Methods. We present observations of gas-phase methanol (CH_3OH) and carbon monoxide (^{13}CO and $C^{18}O$) at 1.3 mm towards ten low-mass young protostars in the Serpens SVS 4 cluster from the SubMillimeter Array (SMA) and the Atacama Pathfinder EXperiment (APEX) telescope. We used archival data from the Very Large Telescope (VLT) to derive abundances of ice H_2O, CO, and CH_3OH towards the same

region. Finally, we constructed gas-ice maps of SVS 4 and directly measured CO and CH_3OH gas-to-ice ratios.

Results. The SVS 4 cluster is characterised by a global temperature of 15 ± 5 K. At this temperature, the chemical behaviours of CH_3OH and CO are anti-correlated: larger variations are observed for CH_3OH gas than for CH_3OH ice, whereas the opposite is seen for CO. The gas-to-ice ratios (N_{gas}/N_{ice}) range from 1 – 6 for CO and $1.4 \times 10^{-4} - 3.7 \times 10^{-3}$ for CH_3OH. The CO gas-maps trace an extended gaseous component that is not sensitive to the effect of freeze-out. Because of temperature variations and dust heating around 20 K, the frozen CO is efficiently desorbed. The CH_3OH gas-maps, in contrast, probe regions where methanol is predominantly formed and present in ices and is released into the gas phase through non-thermal desorption mechanisms.

Conclusions. Combining gas- and ice-mapping techniques, we measure gas-to-ice ratios of CO and CH_3OH in the SVS 4 cluster. The CH_3OH gas-to-ice ratio agrees with values that were previously reported for embedded Class 0/I low-mass protostars. We find that there is no straightforward correlation between CO and CH_3OH gas with their ice counterparts in the cluster. This is likely related to the complex morphology of SVS 4: the Class 0 protostar SMM 4 and its envelope lie in the vicinity, and the outflow associated with SMM 4 intersects the cluster. This study serves as a pathfinder for future observations with ALMA and the James Webb Space Telescope (JWST) that will provide high-sensitivity gas-ice maps of molecules more complex than methanol. Such comparative maps will be essential to constrain the chemical routes that regulate the chemical complexity in star-forming regions.

5.1 INTRODUCTION

The interplay between ice and gas in the Universe is an elusive relationship spanning from the formation of simple molecules to the creation of more complex organics; the building blocks of life in planetary systems like our own. In star-forming regions inside dense molecular clouds, the most likely mechanism to form complex organic molecules (COMs) is the thermal and energetic processing of ice-covered dust grains (Boogert *et al.*, 2015; Öberg, 2016). Unfortunately, detecting complex icy molecules is challenging because the vibrational modes of functional groups associated with these frozen molecules are blended in the infrared. So far, methanol (CH_3OH) is the most complex molecule that has been securely detected in the ices in the interstellar medium, although ice features of a few other species, including acetaldehyde (CH_3CHO) and ethanol (CH_3CH_2OH), have also been suggested to contribute to the infrared spectra of young protostars (Schutte *et al.*, 1999; Öberg *et al.*, 2011a; Terwisscha van Scheltinga *et al.*, 2018). Gas-phase (sub)millimeter single-dish and interferometric observations have demonstrated that a plethora of molecules more complex than methanol exist in the gas phase towards low- and high-mass star-forming regions (see e.g. reviews by Herbst and van Dishoeck, 2009 and Jørgensen

et al., 2020). One way to access the complex organic inventory of molecular ices consists of indirectly deriving ice abundances from gas-phase mapping (Whittet *et al.*, 2011) and subsequently reverse-engineering their path into the gas phase to constrain their origins in the ices. However, this method relies on assumptions about how efficiently icy molecules are released into the gas. To investigate the ice-gas interaction in star-forming regions, combined gas and ice maps are required to constrain the physical and chemical environment. In this paper, gas and ice maps of methanol (CH_3OH) and carbon monoxide (CO) are presented. The data are used to determine CH_3OH and CO gas-to-ice ratios and thus to shed light onto the chemical processes occurring in cold low-mass star-forming regions. Methanol is one of the key species in studies of the organic content of star-forming regions: it is the precursor of many complex organic molecules (Nuevo *et al.*, 2018; Rivilla *et al.*, 2019) and the ideal candidate to link gas and ice processes: at the low temperatures of cold environments, there is no efficient methanol formation path in the gas phase (Turner, 1998; Garrod *et al.*, 2007), but laboratory experiments have demonstrated that the production of methanol can successfully occur on ices at low temperatures (~10 K) through grain-surface hydrogenation reactions of CO ice (Watanabe and Kouchi, 2002; Fuchs *et al.*, 2009; Linnartz *et al.*, 2015). After it has formed in the ices, the question remains at what level it is released back into the gas phase through thermal and non-thermal processes. Bertin *et al.* (2016) and Cruz-Diaz *et al.* (2016) have experimentally shown that the methanol desorption yield is at least one order of magnitude lower than the current value that is largely used in the literature and was measured by Öberg *et al.* (2009a), which causes the methanol gas-phase abundance to be overestimated in astrochemical models. Theoretical three-phase chemical models that combine gas-phase chemistry with bulk and surface have addressed the effect of the reactive desorption (Dulieu *et al.*, 2013) on the gas-phase abundance of molecules (Cazaux *et al.*, 2016). In these models, neither photons nor cosmic rays play a role in the desorption mechanism, and the molecules are released into the gas phase upon formation on grains. Cazaux *et al.* (2016) showed that the gas-to-ice ratio for methanol is $\sim 10^{-4}$ at 10^5 years when the ice desorption is taken into account. In the opposite case, when the icy molecules are not released into the gas phase, the methanol gas-to-ice ratio is $\sim 10^{-6}$.

This prediction can be tested observationally by combining gas-phase and ice observations to directly measure the gas-to-ice ratios and desorption efficiency. Maps like this were created for carbon monoxide by Noble *et al.* (2017) for B 35A, a star-forming dense core in Orion. The authors used data from the AKARI satellite and ground-based observations from the Institut de RadioAstronomie Millimétrique (IRAM) 30 m telescope and the James Clerk Maxwell Telescope (JCMT). Noble *et al.* (2017) concluded that there is no trivial relationship between ice and gas. No obvious trends were found between CO ice and gas-phase $C^{18}O$, suggesting that the interplay between CO freeze-out and desorption is complex in this region. Because methanol is the best candidate to bridge ice and gas chemistries, we have targeted the SVS 4 cluster, which currently holds the largest reservoir of ice methanol in the nearby star-forming regions (Pontoppidan *et al.*, 2004).

SVS 4 is a small dense cluster located to the south-east of the Serpens

molecular cloud. With 11 low- to intermediate-mass young stellar objects (YSOs) within a region of 20 000 AU, it is one of the densest YSO clusters ever observed (Eiroa and Casali, 1989; Pontoppidan *et al.*, 2003a; Eiroa *et al.*, 2008). The SVS 4 young stars are all situated within ~ 20″ at most from one another, as shown in Figure 5.1 and listed in Table 5.1. Additionally, the Class 0 protostar SMM 4, which has an outflow and a large envelope, is located only 26″ (~10 000 AU) from the centre of the cluster. According to Pontoppidan *et al.* (2004), the cluster is located inside the south-eastern part of the envelope of SMM 4. As a result, lines of sight towards the SVS 4 stars probe the envelope material and the outflow of the Class 0 protostar. Among the SVS 4 cluster members, SVS 4–9 is an intermediate-mass YSO, and Preibisch (2003) found it to be the brightest X-ray source in the Serpens molecular cloud. SVS 4–3 and SVS 4–6 are also X-ray sources (Preibisch, 2004; Giardino *et al.*, 2007).

The ice content of the SVS 4 region has been investigated extensively by Pontoppidan *et al.* (2003b), Pontoppidan *et al.* (2003a), Pontoppidan *et al.* (2004), and Pontoppidan *et al.* (2008). These studies found that the SVS 4 cluster had one of the highest methanol ice abundances of low-mass stars (up to 28% relative to water ice and 3×10^{-5} compared to gas-phase H_2) reported to date (Pontoppidan *et al.*, 2003b; Pontoppidan *et al.*, 2004). The SVS 4 methanol ice abundance relative to water is comparable to the one observed towards the most methanol-rich massive stars known (Pontoppidan *et al.*, 2003b). The nature of the Class 0 protostar SMM 4 itself has been extensively studied at millimeter and sub-millimeter wavelengths. These studies have revealed that the continuum emission towards SMM 4 is spatially resolved into two Class 0 protostars, SMM 4A and SMM 4B, embedded in the same core (Lee *et al.*, 2014; Aso *et al.*, 2018; Maury *et al.*, 2019). In contrast, little has been done to investigate the gas-phase molecular content of the outer envelope of SMM 4, where the SVS 4 stars are located. Öberg *et al.* (2009a) observed methanol towards SVS 4–5 in the $2_K - 1_K$ rotational band with the IRAM 30 m telescope providing a column density of 2.7×10^{14} cm^{-2} for a rotational temperature of about 8 K. Öberg *et al.* (2009a) inferred that the spectrum of SVS 4–5 shows multiple emission components, which reflects the complexity of the cluster and also the contributions from the outflow associated with SMM 4. Kristensen *et al.* (2010) mapped the gas-phase methanol in the $7_K - 6_K$ rotational band with JCMT towards SMM 4 and two outflow positions (SMM 4–W and SMM 4–S), and found a variation between $10^{14} - 10^{15}$ cm^{-2} that was attributed to the methanol sputtering triggered by the outflow. Other than methanol, Öberg *et al.* (2011c) observed a suite of molecular transitions for the complex organic O-bearing species $HCOOCH_3$, CH_3CHO, and CH_3OCH_3 towards SMM 4 and SMM 4–W in 17″ and 28″ beams with IRAM, indicating a rich chemistry in the vicinity of SMM 4 and the low-mass outflow SMM 4–W.

In this paper we present millimeter interferometric and single-dish gas observations of methanol ($J = 5_K - 4_K$) and carbon monoxide (^{13}CO and C^{18}O, $J = 2 - 1$) towards the Serpens SVS 4 cluster. In a complementary manner, we analyse L- and M-band infrared ice spectra of ten SVS 4 stars taken from the Very Large Telescope (VLT-ISAAC) archive[1]. We combine gas- and ice-mapping techniques and directly measure CO and CH_3OH gas-to-ice

[1] http://archive.eso.org

ratios in the cluster. The resulting gas-ice maps and ratios serve to constrain the routes leading to chemical complexity in solid and gas phases of cold low-mass star-forming regions.

The paper is structured as follows. In Section 5.2 we present the ice and gas-phase observations together with the archival data. Section 5.3 summarises the method we adopted to derive the ice and gas column densities and reports the observational results. Section 5.4 interprets the gas-ice maps and analyses the gas and ice variations. Section 5.5 discusses the results and provides a comparison between observed and predicted CO and CH_3OH gas-to-ice ratios. Finally, Section 5.6 concludes the paper.

5.2 OBSERVATIONS AND ARCHIVAL DATA

5.2.1 *SMA and APEX observations*

The SVS 4 cluster was observed on May 13, 2017, using the eight-antenna SubMillimeter Array (SMA; Ho *et al.*, 2004). The array was in its sub-compact configuration, resulting in baselines between 8–45 m. The region was covered by two pointings whose dimensions are dictated by the SMA primary beam size of 50″. The first pointing was centred on the Class 0 protostar Serpens SMM 4, and the second was offset by one half SMA primary beam to the south-east. The exact coordinates of the two SMA pointings are α_{J2000} = 18$^{\rm h}$29$^{\rm m}$57$^{\rm s}$.63, δ_{J2000} = +01°13′00.″2, and α_{J2000} = 18$^{\rm h}$29$^{\rm m}$57$^{\rm s}$.88, δ_{J2000} = +01°12′37.″7. The pointings covered frequencies ranging from 214.3 to 245.6 GHz with a a spectral resolution of 0.6 MHz (0.78 km s^{-1}). Observations of the CH_3OH $J_K = 5_K - 4_K$ branch at 241.791 GHz were made, and of ^{13}CO $J = 2–1$ at 220.398 GHz and of C^{18}O $J = 2–1$ at 219.560 GHz were also made to compare methanol and CO emission.

The data were calibrated and imaged using CASA[2] (McMullin *et al.*, 2007). The complex gains were calibrated through observations of the quasars 1751+096 and 1830+063, and the bandpass and the flux calibrations through observations of the quasar 3c279 and Callisto, respectively. The resulting SMA dataset has a typical beam-size of 7.″9 × 4.″0 with a position angle of 68.8°.

[2] http://casa.nrao.edu/

Although the array was in this compact configuration, some emission is resolved out due to lack of short spacings. To map the extended emission towards the SVS 4 cluster, the SMA observations were therefore accompanied by short-spacing data obtained on May 10 – 14, 2017, with the Atacama Pathfinder EXperiment (APEX; Güsten *et al.*, 2006). The observations covered frequencies between 218.2 – 220.7 GHz and between 241.3 – 243.8 GHz, corresponding to the SMA 230 GHz receiver lower and 240 GHz receiver upper sidebands.

The frequency resolution of the APEX dataset is 0.076 MHz (0.099 km s^{-1}). The map size achieved with APEX is 75″ × 100″, and it fully covers the region mapped by the SMA primary beams. The coordinates of the APEX pointing are α_{J2000} = 18$^{\rm h}$29$^{\rm m}$57$^{\rm s}$.76, δ_{J2000} = +01°12′49.″0. A total integration time of 4.2 hours was adopted to match the sensitivity of the SMA data and to fold the datasets together. The APEX beam-size at the observed

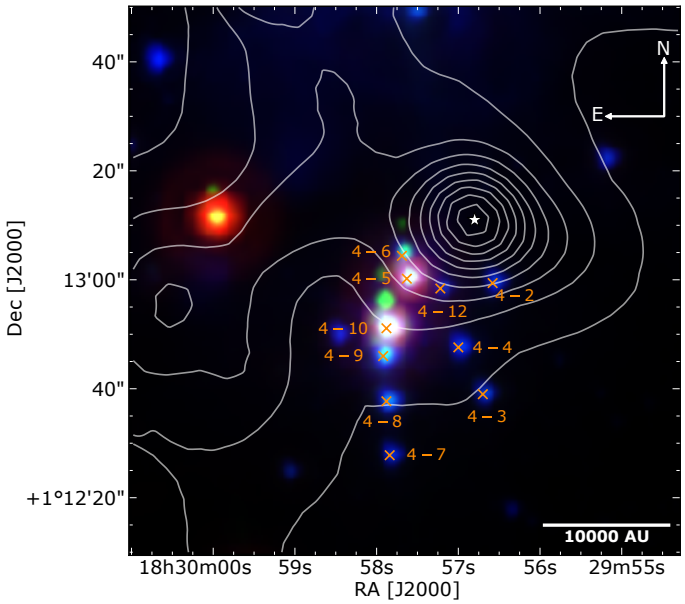

FIGURE 5.1: Three-colour image of the SVS 4 cluster overlaid with SCUBA-2 850 μm density flux in mJy beam^{-1} (Herczeg *et al.*, 2017). The contours are in decreasing steps of 10% starting at 3.12 Jy beam^{-1}. The composite is made from *Spitzer* IRAC 3.6 μm (blue), 8.0 μm (green), and MIPS 24.0 μm (red) bands (Fazio *et al.*, 2004). The dark orange crosses mark the position of the SVS 4 sources, and the white star represents SMM 4.

TABLE 5.1: Sample of sources.

Source	RA [J2000]	DEC [J2000]	A_J [mag]
SVS 4–2	18:29:56.58	+01:12:59.4	4.2
SVS 4–3	18:29:56.70	+01:12:39.0	18.0
SVS 4–4	18:29:57.00	+01:12:47.6	4.9
SVS 4–5	18:29:57.63	+01:13:00.2	21.0
SVS 4–6	18:29:57.69	+01:13:04.4	4.9
SVS 4–7	18:29:57.84	+01:12:27.8	10.5
SVS 4–8	18:29:57.88	+01:12:37.7	10.8
SVS 4–9	18:29:57.92	+01:12:46.0	10.5
SVS 4–10	18:29:57.88	+01:12:51.1	6.2
SVS 4–12	18:29:57.22	+01:12:58.4	26

Notes. The coordinates and the extinction in the J band (A_J) are from Pontoppidan *et al.* (2004). The estimated relative uncertainty on A_J is 5% (Pontoppidan *et al.*, 2004).

frequencies is 27.″4. The reduction of the APEX dataset was performed with the GILDAS package CLASS[3]. Subsequently, the reduced APEX datacube was imported to CASA to perform the combination of interferometric and single-dish data.

[3] http://www.iram.fr/IRAMFR/GILDAS

The SMA and APEX data were combined following the procedure described in Appendix 5.B.1. The species for which most of the flux is recovered in the combination is ^{13}CO, followed by C^{18}O and CH_3OH. The interferometric observations missed up to 90% of the emission, which implies that

TABLE 5.2: Spectral data of the detected molecular transitions.

Transition	Frequency[a]	A^a_{ul}	g^a_u	E^a_u	n^b_{cr}
	[GHz]	[s^{-1}]		[K]	[cm^{-3}]
$C^{18}O$ $J = 2 - 1$	219.560	6.01×10^{-7}	5	15.9	1.9×10^4
^{13}CO $J = 2 - 1$	220.398	6.04×10^{-7}	5	15.9	2.0×10^4
CH_3OH $J = 5_0 - 4_0$ E^+	241.700	6.04×10^{-5}	11	47.9	5.5×10^5
CH_3OH $J = 5_1 - 4_1$ E^-	241.767	5.81×10^{-5}	11	40.4	4.8×10^5
CH_3OH $J = 5_0 - 4_0$ A^+	241.791	6.05×10^{-5}	11	34.8	5.0×10^5
CH_3OH $J = 5_1 - 4_1$ E^+	241.879	5.96×10^{-5}	11	55.9	4.6×10^5
CH_3OH $J = 5_2 - 4_2$ E^-	241.904	5.09×10^{-5}	11	60.7	4.2×10^5

Notes.[a] From the Cologne Database for Molecular Spectroscopy (CDMS; Müller *et al.* (2001)) and the Jet Propulsion Laboratory catalog (Pickett *et al.*, 1998). [b] Calculated using a collisional temperature of 10 K and collisional rates from the Leiden Atomic and Molecular Database (LAMDA; Schöier *et al.*, 2005). The references for the collisional rates are Yang *et al.* (2010) for the CO isotopologues and Rabli and Flower (2010) for CH_3OH.

the gas column density would have been underestimated by approximately one order of magnitude. This illustrates how crucial the combination of interferometric and large-scale single-dish data is when the gas emission is extended and interferometric data have to be employed in a quantitative analysis (e.g. derivation of column densities).

5.2.2 *VLT observations*

Archival data from the Very Large Telescope (VLT) were used to constrain the CH_3OH and CO ice content of the SVS-4 region. L- and M-band spectra of ten SVS 4 sources (listed in Table 5.1) were obtained using the Infrared Spectrometer and Array Camera (ISAAC) mounted on the Unit Telescope UT1-Antu of the VLT. All the L-band data have previously been published in Pontoppidan *et al.* (2004) and were observed as part of programme 71.C-0252(A). Briefly, a low-resolution grating and 0.″6 slit were used to cover the 2.80 – 4.15 μm spectral range, which yielded a resolving power of $\lambda/\Delta\lambda \sim 600$. In the case of SVS 4–5 and SVS 4–9, the brightest sources, the 3.53 μm feature related to the methanol C-H stretching was observed with a resolving power of 3300.

For the M-band observations, two sources (SVS 4–5 and SVS 4–9) were observed on May 6, 2002, as reported by Pontoppidan *et al.* (2003a), and M-band spectra of eight other sources were obtained between May 2005 and August 2006, and are presented for the first time in this paper. The M-band spectra used the medium-resolution grating and the 0.″3 or 0.″6 slit, depending on source brightness, to yield resolving powers of $\lambda/\Delta\lambda$ 5 000 – 10 000 and a wavelength of 4.53 – 4.90 μm. Standard on-source integration times were $\sim$ 45 min per pointing. The total integration time was doubled to 90 minutes for the faintest sources. The observations were

carried out in pairs; each pointing was rotated to observe two stars at the same time. The data were reduced following the procedure described in Pontoppidan *et al.* (2003a). The spectra were flux calibrated with respect to the standard stars HR 6629 and HR 7236 and wavelength calibrated to remove telluric absorption lines.

5.3 RESULTS

This section provides a summary of the methods we used to calculate the ice and gas-phase column densities presented in Sections 5.3.1 – 5.3.2. Comprehensive descriptions of the methods applied when fitting the observational infrared data and producing the gas-phase maps are given in Appendices 5.A and 5.B.

5.3.1 *Ice column densities*

To investigate the spatial distribution of ices towards the SVS 4 cluster, accurate ice column densities must be derived. To accomplish this, the spectrum was divided by a continuum and the optical depth was derived using the formula $\tau_\lambda = -\ln(F_\lambda^{\rm obs}/F_\lambda^{\rm cont})$, where $F_\lambda^{\rm obs}$ is the observed flux and $F_\lambda^{\rm cont}$ is the continuum. A combination of blackbodies was used to determine the dust continuum for the L bands, whereas a spline function was adopted for the M bands. Table 5.A.1 in Appendix 5.A lists the photometric points used in the determination of the L-band continuum.

Following the τ calculation, the spectral decomposition of the observational data was carried out with the OMNIFIT[4] fitting utility (Suutarinen, 2015b): OMNIFIT is an open-source Python library used to fit observational data of astrophysical ices using multi-component laboratory spectra and analytical data. It makes use of the LMFIT package[5] to perform the optimisation. In the M-band fitting, the non-linear optimisation by the Levenberg-Marquardt method was adopted, whereas the simplex Nelder-Mead and Monte Carlo Markov chain were used in the L-band fitting. The selected laboratory ice data were fitted to the observational spectra by applying a scale factor k. OMNIFIT provides a specific scale factor for each laboratory ice dataset. Further details on the fitting utility can be found in Appendices 5.A.2 and 5.A.3.

[4] https://ricemunk.github.io/omnifit/

[5] https://lmfit.github.io/lmfit-py/

Table 5.3 lists the components and the fit parameters we adopted to fit the VLT-ISAAC data. OMNIFIT was applied in the same way to all the ten SVS 4 sources. To avoid fitting saturated features in the spectra, especially in the 3 μm region, only specific wavelength ranges were considered in the fits. For the L-band spectra, the 2.85 – 2.94 μm, 3.17 – 3.23 μm and 3.77 – 4.0 μm ranges were fitted. The first and second of these cover the blue wing and a portion of the red wing of the O-H stretching mode of H_2O ice, respectively. Finally, the third range was included because it was found to be a constraining factor to fit the C-H stretching mode of CH_3OH ice. It is worth noting that the typical C-H stretching region was not selected as a fitting range because of the effect of the 3.47 μm band and the scatter of the red wing of the O-H stretching mode. For the M bands, the whole spectral range, 4.62 – 4.72 μm, was fitted.

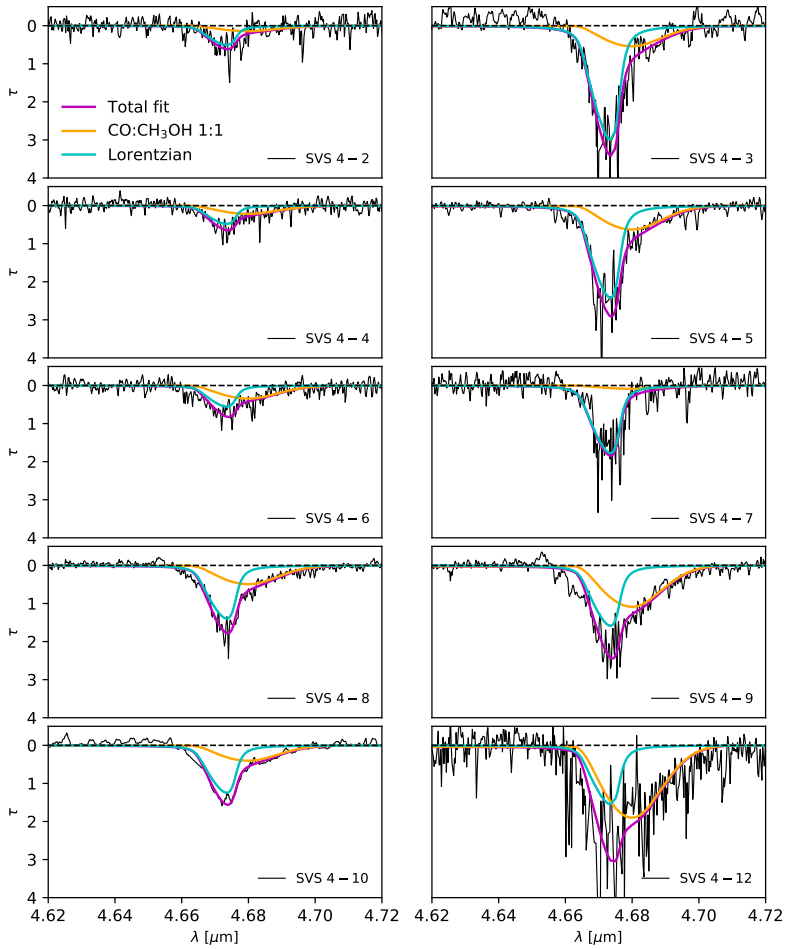

FIGURE 5.2: M-band optical depth towards the SVS 4 sources (black). The coloured lines represent the CO:CH_3OH 1:1 laboratory spectrum (orange), the CDE-corrected Lorentzian reproducing the pure CO (cyan) and the total fit (magenta). The dashed black lines are used as a reference for τ=0. The goodness of the fit χ^2_ν starting from SVS 4–2 to SVS 4–12 is 0.95, 0.22, 0.79, 0.32, 0.83, 0.74, 0.30, 0.25, 0.87, and 0.64.

The spectral fitting procedure developed by Suutarinen (2015a) and adopted in this study stands as an alternative to the commonly used method to detect molecules in interstellar ices (Grim *et al.*, 1991; Brooke *et al.*, 1999). In contrast to the latter, which consists of fitting a polynomial to the red wing of the O-H stretching mode and analysing the residual optical depth at 3.53 μm to detect CH_3OH, the fitting procedure we adopted attempts to simultaneously fit multiple ice components to the 3 μm region to find the maximum amount of CH_3OH that is hidden below the red wing. This approach makes it possible to concurrently account for both the C-H and the O-H stretches that are attributable to CH_3OH. This aspect is often overlooked, although the O-H stretching contribution of CH_3OH necessarily replaces some of the absorption of H_2O. The aim of this fitting procedure is to determine the maximum amount of CH_3OH ice that is hidden below the red wing of interstellar ices, and thus to help explain the high CH_3OH abundances that are observed in the gas-phase.

Figure 5.2 shows the optical depth of the sources listed in Table 5.1 decomposed by analytical and experimental components using the OMNIFIT fitting utility (Suutarinen, 2015b). As outlined in Pontoppidan *et al.* (2003a),

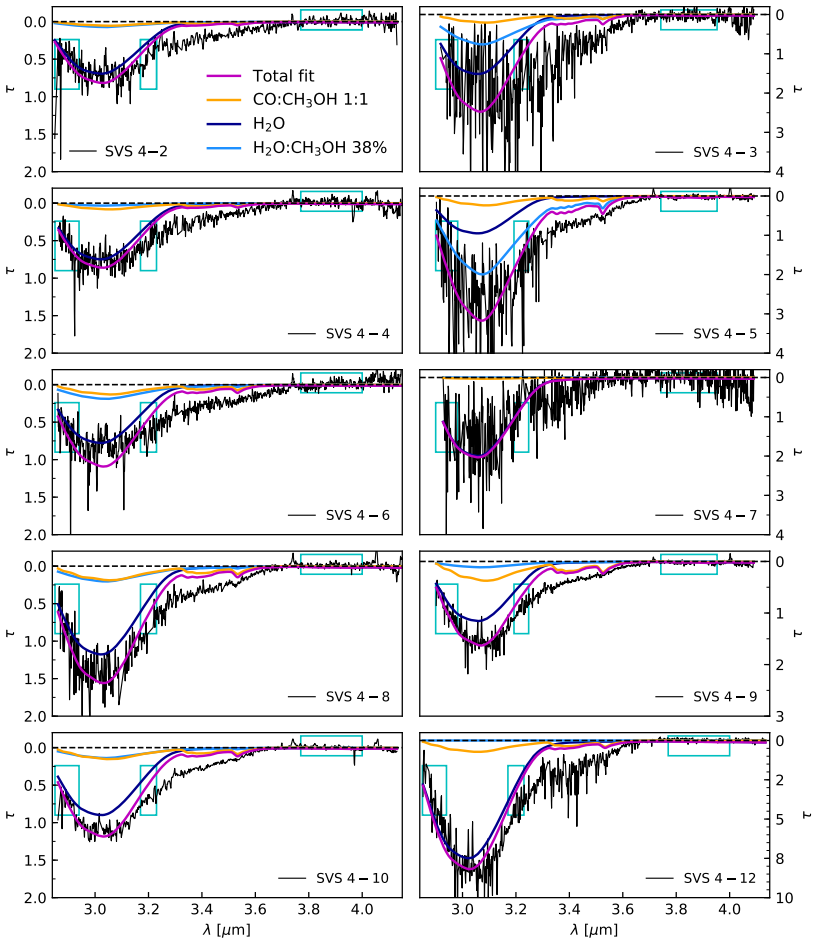

FIGURE 5.3: L-band optical depth towards the SVS 4 sources (black). The coloured lines represent the laboratory ice data employed in the fitting: the pure H_2O (dark blue), the H_2O:CH_3OH 38% (light blue), the CO:CH_3OH 1:1 (orange), and the total fit (magenta). The dashed black lines are used as a reference for $\tau = 0$. The cyan boxes illustrate the selected fitting ranges. The goodness of the fit χ^2_ν starting from SVS 4−2 to SVS 4−12 is 0.59, 7.47, 0.55, 9.15, 0.79, 4.14, 0.72, 0.43, 0.25, and 22.5.

the M-band features can be decomposed by a linear combination of three components: blue, middle, and red. We address only the middle and red components because the blue component does not constrain the methanol ice abundance, but rather that of CO_2 ice (Boogert *et al.*, 2015). The central peak (i.e. middle component) is associated with the C-O vibrational mode of pure CO ice. It was fitted using a continuous distribution of ellipsoids (CDE) corrected Lorentzian function in order to take into account irregularities in the grain shape and match the central peak of the observations (Pontoppidan *et al.*, 2003a).

The red component, on the other hand, was fitted with CO:CH_3OH laboratory data (Cuppen *et al.*, 2011) because the observed CO peak position is slightly shifted to longer wavelengths, possibly due to migration of CO in the ices observed towards the cluster sources (Devlin, 1992; Zamirri *et al.*, 2018). Although the red component can be associated with CO:H_2O ice (Thi *et al.*, 2006), the CO:CH_3OH mixture is the most likely carrier of this feature (Cuppen *et al.*, 2011), and it is assumed to trace warmer regions than pure CO. The goodness of the fit was addressed using the reduced χ^2_ν,

that is given by $\chi^2_\nu = \chi^2/\nu$, where ν is the difference between the number of data points and the number of free parameters in the fit.

The decomposition of the L-band features, between 2.80 – 4.15 μm, was carried out using three experimental components shown in Figure 5.3: pure H_2O in blue (Fraser *et al.*, 2004), H_2O:CH_3OH in cyan (Dawes *et al.*, 2016), and CO:CH_3OH in orange (Cuppen *et al.*, 2011). Pure H_2O was selected because it is the most abundant ice component. H_2O:CH_3OH was chosen because CH_3OH is the second major contributor to the O-H stretching at 3 μm, after H_2O. H_2O:CH_3OH was preferred over pure CH_3OH as the C–H stretching of the latter is too prominent and shifted in the observational data. As Dawes *et al.* (2016) showed, the O-H spectroscopic profile and exact peak position of the H_2O:CH_3OH mixture are dependent not only on the host molecule of the mixture (H_2O), but also on the minor component (CH_3OH). CH_3OH is thought to form on dust grains from hydrogenation of CO ;this may occur early, that is, during the early stages of CH_3OH formation, and involves reactions of HCO + OH, or it may occur late after critical CO freeze-out. Ice studies of binary and tertiary systems show that even if ices form in layers, the heating and processing with time and diffusion will lead to ice mixing. In addition, H_2O:CH_3OH was used because recent modelling and laboratory experiments showed evidence of the production of CH_3OH mixed in H_2O matrices upon UV and X-ray irradiation of simple ice components, for instance, H_2O:CO (Jiménez-Escobar *et al.*, 2016; Muñoz Caro *et al.*, 2019) or by interaction of CH_4, O_2 and H (Qasim *et al.*, 2018). At the same time, mixtures such as NH_3:H_2O or CO_2:H_2O were discarded because they would have very little effect on the shape and spectroscopy of the O-H stretching at 3 μm and they would reduce the contribution of CH_3OH, which would prevent us from determining the maximum amount of methanol that is

TABLE 5.3: Fit parameters used to fit the infrared spectra with OMNIFIT.

L-band fitting			
Components	Fitting range [a]	Scale factor (k) [b]	Refs. [c]
pure H_2O	1 – 3	vary	5
H_2O:CH_3OH	1 – 3	vary	6
CO:CH_3OH	1 – 3	M-band values	7
M-band fitting			
Components	Fitting range [a]	Scale factor (k) [b]	Refs. [c]
CO:CH_3OH	4	vary	7
CDE-Lorentzian	4	–	8

Notes.[a] The fitting ranges are [1] 2.85 – 2.94 μm, [2] 3.17 – 3.23 μm, [3] 3.77 – 4.0 μm, and [4] 4.62 – 4.72 μm. The goodness of the fits, χ^2_ν, was calculated for the specified fitting ranges. [b] Scale factor: multiplier of the spectrum in OMNIFIT (see Eq. 5.A.2.). [c] The references for the laboratory ice data are [5] Fraser *et al.* (2004), [6] Dawes *et al.* (2016), [7] Cuppen *et al.* (2011), and [8] Pontoppidan *et al.* (2003a).

hidden below the red wing. Finally, CO:CH_3OH was selected to ensure that the fit of the methanol band at 3.53 μm is consistent with the fit of the CO red component of the M-band spectra. To do so, the k values for CO:CH_3OH obtained in the M-band fitting were carried over in the L-band fitting. For all the other laboratory ice data, k varies. The same approach was also used by Suutarinen (2015a) to fit the L-band features of several YSOs, including SVS 4–5 and SVS 4–9. It is worth noting that the 3 μm water band of SVS 4–12 is saturated (see Figure 5.A.2), and therefore, the optical depth below λ = 3.3 μm for this source was determined by scaling the SVS 4–9 L-band features to the SVS 4–12 red wing following the procedure presented in Pontoppidan *et al.* (2004). The best scaling was found for $\tau_{\rm max}^{\rm L-band} = 9$.

Despite the degeneracies involved in the spectral fitting, Figure 3 shows that in addition to the contribution of the O-H stretching of methanol, the pure H_2O component mainly reproduces the 3 μm absorption band. This is in agreement with a scenario where the predominant ice constituent is pure water, but it also supports the hypothesis of a degree of mixing in astrophysical ices. For most of the spectra, a third component, the H_2O:CH_3OH mixture, is required to obtain a better fit constrained by the adopted fitting ranges. For some sources, for example SVS 4–2, SVS 4–4, and SVS 4–6, the selection of the fitting ranges results in an overfit of the O-H stretching mode. Given the low signal-to-noise ratio (S/N) of the observations, this study does not aim to prove that H_2O:CH_3OH models the observational spectra better than other laboratory data. It was selected to find the maximum amount of CH_3OH that is hidden in the H_2O ice, if the L band is decomposed with the laboratory data selected in this study.

It is worth noting that the CH_3OH band at 3.53 μm is not constrained by the fitting procedure itself, but rather by the methanol fraction in both CO:CH_3OH and H_2O:CH_3OH mixtures. The amount of CH_3OH estimated from the M-band fitting results in sufficient absorption to model the C–H stretching mode at 3.53 μm, and therefore the addition of H_2O:CH_3OH, aimed to fit the constrained ranges, has a minor contribution in the 3.3–3.6 μm interval. The only two exceptions are SVS 4–3 and SVS 4–5 for which a greater contribution of the H_2O:CH_3OH mixture is observed. Overall, the fit of the C–H stretching mode at 3.53 μm is satisfactory because the model is predicting an absorption lower than or equal to the observed band, as well as taking into account that other molecules and physical processes, such as scattering by large grains, contribute to this spectral range. Reproducing the full range of absorptions observed in the red wing was not part of the scope of this study, and the selected fitting ranges would indeed prevent a good quality fit of it.

The CO, H_2O, and CH_3OH ice column densities were obtained from the integrated τ of the components found by the fitting routine. The calculation of the ice column densities is described in detail in Appendices 5.A.3–5.A.4 and their values are shown in Tables 5.4 and 5.5. In these tables, the total ice column density is the sum of the pure and mixed components. SVS 4–12 shows the deepest absorptions features, thus the column densities are the highest towards this source. The uncertainties in the column density were calculated from the error in the optical depth.

Figure 5.4 compares the derived ice column densities between the SVS 4

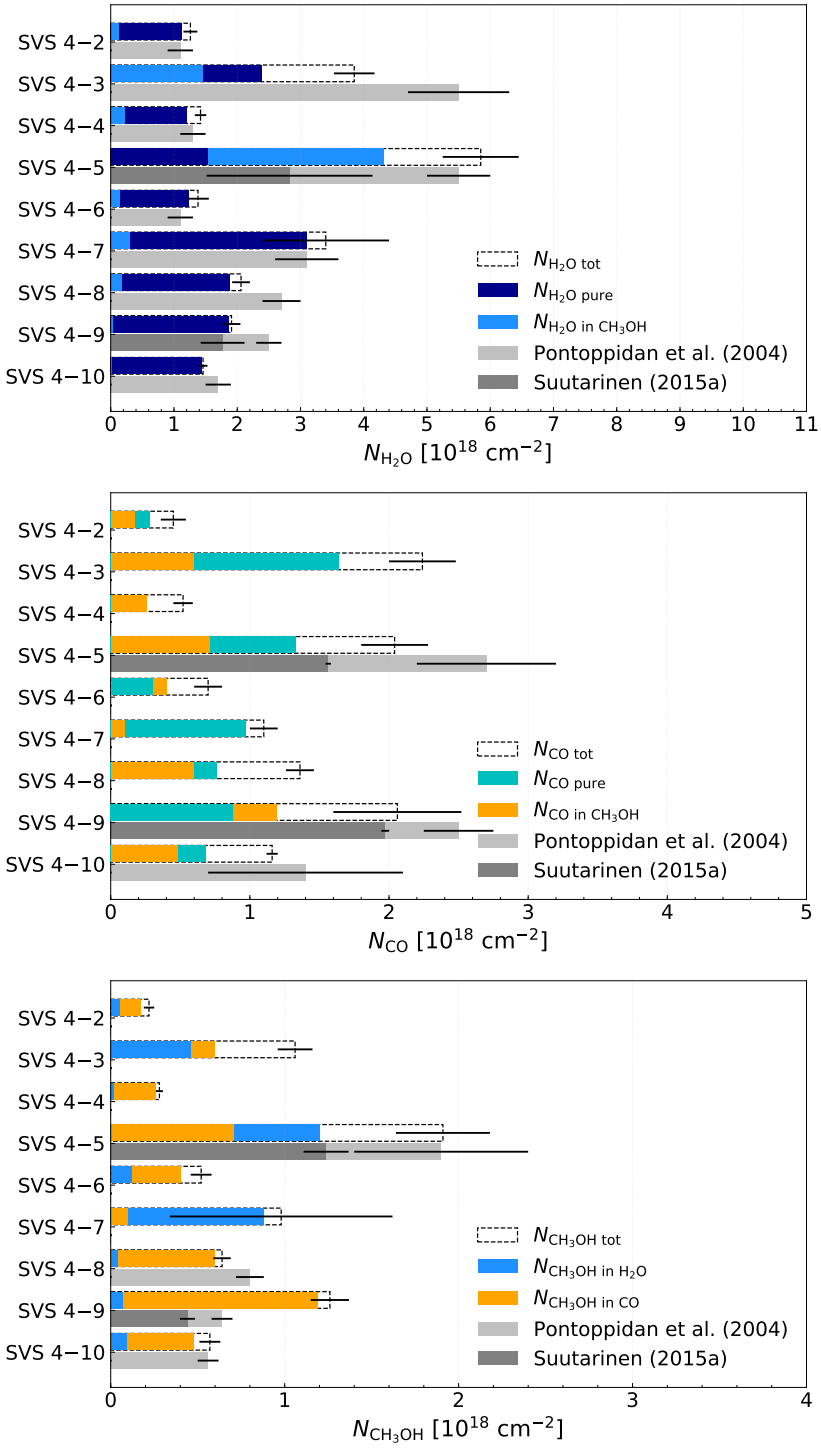

FIGURE 5.4: H_2O (top), CO (middle), and CH_3OH (bottom) ice column densities obtained in this study compared to Pontoppidan *et al.* (2004) (light grey) and Suutarinen (2015a) (dark grey). The CO column density towards SVS 4−10 is from Chiar *et al.* (1994). The coloured bars represent the ice column densities of the pure species or of the species in a mixture, and the dashed bars depict the total ice column densities obtained by summing the ice column densities of the pure species and of the species in a mixture.

TABLE 5.4: Total ice and gas column densities of the species analysed towards the SVS 4 sources.

Source	$N^{\rm ice}_{\rm H_2O\ tot}$	$N^{\rm ice}_{\rm CO\ tot}$	$N^{\rm ice}_{\rm CH_3OH\ tot}$	$N^{\rm gas}_{\rm CO\ tot}$	$N^{\rm gas}_{\rm CH_3OH\ tot}$	$N^{\rm SCUBA-2}_{\rm H_2}$	$^{*}N^{AJ}_{\rm H_2}$
	$[10^{18}{\rm cm}^{-2}]$	$[10^{18}{\rm cm}^{-2}]$	$[10^{18}{\rm cm}^{-2}]$	$[10^{18}{\rm cm}^{-2}]$	$[10^{14}{\rm cm}^{-2}]$	$[10^{23}{\rm cm}^{-2}]$	$[10^{23}{\rm cm}^{-2}]$
SVS 4–2	1.26 ± 0.11	0.45 ± 0.08	0.22 ± 0.03	$2.71\,^{+0.55}_{-0.13}$	$8.24\,^{+12.6}_{-1.70}$	$0.80\,^{+0.90}_{-0.30}$	0.14
SVS 4–3	3.85 ± 0.32	2.24 ± 0.20	1.06 ± 0.10	$2.58\,^{+0.53}_{-0.12}$	$1.92\,^{+1.53}_{-0.10}$	$0.18\,^{+0.20}_{-0.06}$	0.6
SVS 4–4	1.42 ± 0.09	0.52 ± 0.05	0.28 ± 0.02	$2.65\,^{+0.53}_{-0.13}$	$3.23\,^{+2.55}_{-0.13}$	$0.30\,^{+0.34}_{-0.11}$	0.16
SVS 4–5	5.85 ± 0.60	2.04 ± 0.19	1.91 ± 0.27	$3.70\,^{+0.75}_{-0.18}$	$4.50\,^{+6.80}_{-0.87}$	$0.65\,^{+0.73}_{-0.24}$	0.7
SVS 4–6	1.38 ± 0.17	0.70 ± 0.08	0.52 ± 0.06	$3.20\,^{+0.65}_{-0.16}$	$6.67\,^{+10.2}_{-1.29}$	$0.78\,^{+0.87}_{-0.28}$	0.16
SVS 4–7	3.40 ± 1.00	1.10 ± 0.09	0.98 ± 0.64	$2.80\,^{+0.57}_{-0.14}$	$3.27\,^{+4.98}_{-0.59}$	$0.16\,^{+0.18}_{-0.06}$	0.35
SVS 4–8	2.06 ± 0.14	1.36 ± 0.07	0.64 ± 0.05	$2.77\,^{+0.56}_{-0.14}$	$3.10\,^{+2.44}_{-0.14}$	$0.20\,^{+0.22}_{-0.07}$	0.36
SVS 4–9	1.91 ± 0.14	2.06 ± 0.37	1.26 ± 0.11	$2.35\,^{+0.48}_{-0.11}$	$2.17\,^{+2.72}_{-0.32}$	$0.28\,^{+0.32}_{-0.10}$	0.35
SVS 4–10	1.46 ± 0.07	1.16 ± 0.03	0.57 ± 0.06	$2.66\,^{+0.54}_{-0.13}$	$2.81\,^{+2.81}_{-0.27}$	$0.38\,^{+0.42}_{-0.14}$	0.2
SVS 4–12	12.4 ± 5.90	3.12 ± 0.74	2.28 ± 0.18	$3.32\,^{+0.68}_{-0.16}$	$3.14\,^{+4.77}_{-0.60}$	$0.73\,^{+0.82}_{-0.26}$	0.86

Notes. Columns 5–7 list the column densities that were calculated for $T = 15$ K. For $N^{\rm gas}_{\rm CO}$, $N^{\rm gas}_{\rm CH_3OH}$, and $N_{\rm H_2}$, the values in the superscript and subscript represent the upper and lower limits if the column densities are calculated at $T = 10$ K or $T = 20$ K, respectively. * Estimated relative uncertainty of 5%. See Sections 5.3.1–5.3.2 and Appendices 5.A, 5.B, and 5.C for a more detailed description of the determination of ice, gas, and H_2 column densities.

TABLE 5.5: Ice column densities of the pure and mixed components given as percentages of the total column densities.

Source	$\frac{N^{\rm ice}_{\rm H_2O\ pure}}{N^{\rm ice}_{\rm H_2O\ tot}}$ [%]	$\frac{N^{\rm ice}_{\rm CO\ pure}}{N^{\rm ice}_{\rm CO\ tot}}$ [%]	$\frac{N^{\rm ice}_{\rm CH_3OH\ in\ H_2O}}{N^{\rm ice}_{\rm CH_3OH\ tot}}$ [%]
SVS 4–2	89.7 ± 11.7	62.2 ± 21.7	22.7 ± 13.9
SVS 4–3	62.1 ± 8.50	73.2 ± 11.6	43.4 ± 9.43
SVS 4–4	84.5 ± 8.30	50.0 ± 11.7	7.10 ± 3.61
SVS 4–5	26.3 ± 6.56	65.2 ± 11.7	62.8 ± 16.3
SVS 4–6	89.9 ± 16.0	42.9 ± 11.7	23.1 ± 9.98
SVS 4–7	91.2 ± 39.8	88.2 ± 11.5	89.8 ± 87.8
SVS 4–8	91.3 ± 8.84	55.9 ± 5.51	6.20 ± 1.64
SVS 4–9	97.9 ± 10.3	42.2 ± 20.7	5.6 ± 3.21
SVS 4–10	98.6 ± 6.73	58.6 ± 2.65	15.8 ± 10.7
SVS 4–12	97.7 ± 66.3	27.3 ± 23.9	0.40 ± 0.44

Notes. To avoid redundancy, the percentages of ice column densities of H_2O in CH_3OH, CO in CH_3OH, and CH_3OH in CO w.r.t. the total H_2O, CO, and CH_3OH ice column densities are not tabulated. They are equal to 100 minus the value reported in the corresponding column (e.g. 10.3 cm^{-2} for H_2O in CH_3OH towards SVS 4–2). See Sections 5.3.1 and Appendix 5.A for a more detailed description of the determination of ice column densities.

sources (Table 5.4) to measurements from the literature (Pontoppidan *et al.*, 2004; Suutarinen, 2015a). Because of the low S/N, SVS 4–12 is not included in this figure. In the case of H_2O ice, shown in the upper panel, the pure water component is the most abundant compared to the mixed water, except in the case of SVS 4–7. This result indicates a negligible level of molecular migration in the ice matrix. It is also worth observing that the H_2O ice column density is diminished by the contribution of the O-H stretching associated with CH_3OH. In the case of CO ice, the pure CO column density dominates the mixed component, except in the case of SVS 4–4, SVS 4–6 and SVS 4–9, which suggests that the circumstellar environment around these three objects is warmer than in the other regions in the SVS 4 cluster. In one case, SVS 4–4, the column densities of pure CO and CO in the CO:CH_3OH mixture are the same.

For CH_3OH, the CO:CH_3OH component dominates in all the sources, except for SVS 4–5 and SVS 4–7. This indicates that the amount of methanol constrained from the M-band fitting is sufficient to reproduce the methanol absorption in the L band. SVS 4–4 shows the same behaviour as observed in the CO case because the column densities of CH_3OH in CO:CH_3OH and H_2O:CH_3OH are the same. When the values estimated in this study can be compared to the literature, the total ice methanol column densities agree well with those reported by Pontoppidan *et al.* (2004), except for SVS 4–9 because of uncertainties in the local continuum determination for

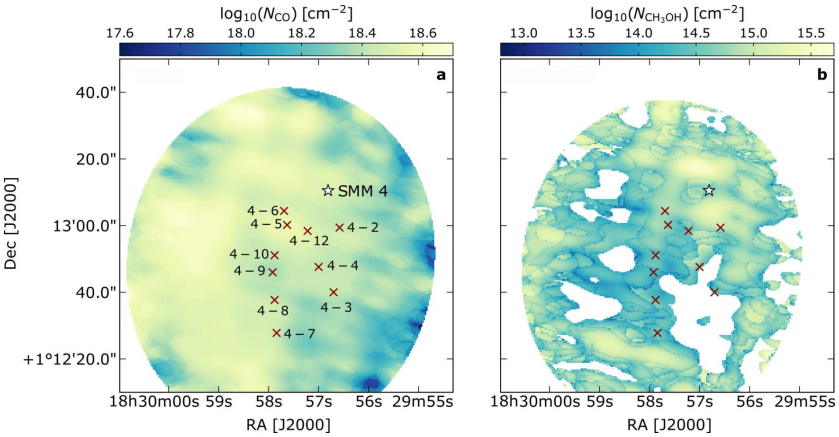

FIGURE 5.5: Gas column density maps of the SVS 4 cluster. *a:* ^{12}CO column density map. *b:* CH_3OH column density map. The white spaces within the area covered by SMA+APEX are regions where the strength of the emission drops below 5σ. The red crosses mark the position of the SVS 4 sources, and the white star represents SMM 4.

this particular source. SVS 4–5 has the highest methanol column density in both studies except for SVS 4–12. The column densities given by Suutarinen (2015a) are generally a factor of ~1–3 lower. The average total ice column densities of H_2O, CO, and CH_3OH are 2.5×10^{18} cm^{-2}, 1.3×10^{18} cm^{-2} , and 0.8×10^{18} cm^{-2}, respectively. The CO and CH_3OH average abundances with respect to H_2O are 0.52 and 0.32. The high CO fraction relative to H_2O indicates an environment for the SVS 4 cluster with a temperature below the CO desorption (~20 K), and it agrees with the average ice column densities of low-mass stars shown in Öberg *et al.* (2011a). On the other hand, the CH_3OH fraction with respect to H_2O ice is a factor of 2.6 higher than the upper quartile values calculated in Öberg *et al.* (2011a). Nevertheless, this value is consistent with the high methanol ice abundance for the SVS 4 cluster measured by Pontoppidan *et al.* (2004), namely 0.28, which suggests a peculiar efficiency of methanol ice synthesis in this region of the Serpens molecular core.

5.3.2 *Gas column densities*

The CO isotopologue and CH_3OH gas column densities were calculated from the integrated line intensities from the combined SMA + APEX maps. Table 5.2 lists the spectral line data of the detected molecular transitions. All the gas column densities derived in this section and their uncertainties are listed in Table 5.4, and the CO and CH_3OH column density maps are displayed in Figure 5.5. Towards some of the SVS 4 sources, the ^{13}CO emission is found to be moderately optically thick (see Appendix 5.B.2). As a result, the ^{13}CO column densities are underestimated towards these positions. Therefore the optically thin C^{18}O emission is used to estimate the column density of the CO gas. The C^{18}O column densities are obtained using the combined SMA + APEX integrated intensity of the C^{18}O $J = 2–1$ line at 219.560 GHz, assuming a kinetic temperature equal to 15 K and optically thin emission. The derived C^{18}O column densities are of the order of 10^{15} cm^{-2} towards all the SVS 4 star positions. The C^{18}O column densities are then converted into ^{12}CO column densities using a ^{16}O/^{18}O isotope ratio

of 557 ± 30 (Wilson, 1999). The calculated ^{12}CO column densities are of the order of 10^{18} cm^{-2} towards the SVS 4 stars (Figure 5.5).

The gas column densities of CH_3OH towards the SVS 4 sources were calculated from the combined SMA + APEX integrated intensities by assuming local thermodynamic equilibrium (LTE) and that the emission of methanol is optically thin. A kinetic temperature equal to 15 K was selected in this case as well, representing the global temperature of the cluster (see Section 5.4.1). The measured CH_3OH column densities are of the order of 10^{14} cm^{-2} towards all the SVS 4 sources (Figure 5.5). Similar column densities are also reported in Kristensen *et al.* (2010), especially towards two outflow knot positions nearby SMM 4 labelled SMM 4–S and SMM 4–W and in Öberg *et al.* (2009a) towards SVS 4–5. In case of sub-thermal excitation the methanol column density would be overestimated by up to one order of magnitude (Bachiller *et al.*, 1995; Bachiller *et al.*, 1998).

5.4 ANALYSIS

5.4.1 *H_2 column density and physical structure of the region*

The SVS 4 sources might be embedded within the envelope of SMM 4 to different degrees and not be uniformly located behind it (Pontoppidan *et al.*, 2004). As a result, the absolute ice column densities might not be the most appropriate measure to compare directly to gas-phase column densities. The gas and ice observations might be tracing different columns of material. To address this point, a search for an ice-gas correlation was conducted by comparing gas and ice abundances relative to the H_2 column density of the region. The abundances of the gas species were calculated by dividing the gas column densities by the H_2 column density estimated from the submillimeter continuum (SCUBA-2) map at 850 μm (Herczeg *et al.*, 2017), assuming that the continuum radiation comes from optically thin thermal dust emission (Appendix 5.C and Kauffmann *et al.*, 2008). Under these assumptions, the strength of the submillimeter continuum emission depends on the dust temperature, T, on the column density, and on the opacity, κ_ν.

The dust temperature for the SVS 4 region has previously been estimated to lie in the range of 10 K $\leq T \leq$ 20 K according to Schnee *et al.* (2005) and to the dust radiative transfer model presented in Kristensen *et al.* (2010). The H_2 column density is thus calculated for T = 10 K, 15 K and 20 K. We adopted the opacities corresponding to dust grains covered by a thin ice mantle (Ossenkopf and Henning, 1994) with κ_ν equal to 0.0182 cm^2 g^{-1} at 850 μm ("OH5 dust"). When a temperature of 15 K is assumed, all the sources lie in the region where the H_2 column density is of the order of 10^{22} cm^{-2} (see Figure 5.C.1 and Table 5.4). The estimated gas abundances relative to H_2 range from $10^{-5} - 10^{-4}$ for CO and $10^{-9} - 10^{-8}$ for CH_3OH at the SVS 4 source positions. The latter agree with the values measured by Kristensen *et al.* (2010) towards the Serpens molecular core.

The H_2 column densities derived from the SCUBA-2 measurements using the method above provide a good estimate of the total beam-averaged amount of gas and are therefore useful as a reference for the optically thin gas-phase tracers. However, it is not clear that they can directly be related

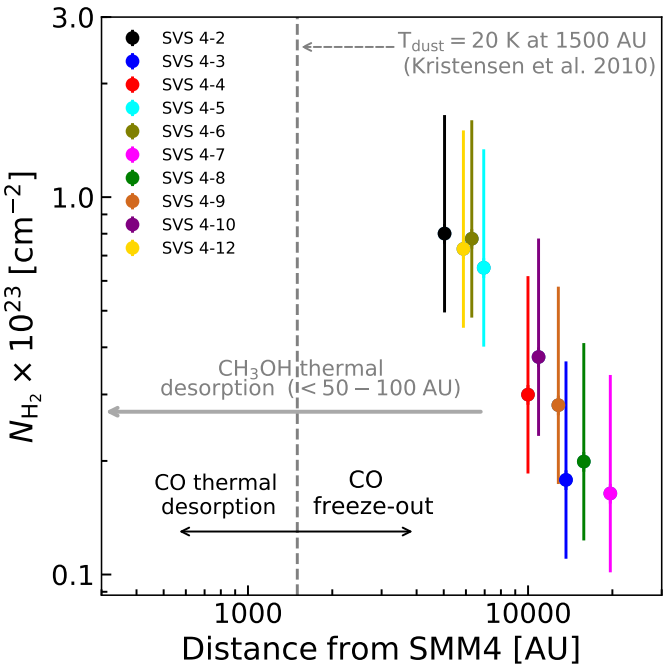

FIGURE 5.6: H_2 column density estimated from the 850 μm dust emission map (Herczeg *et al.*, 2017) as a function of the distance from SMM 4. A distance of 433 pc is assumed (Ortiz-León *et al.*, 2018) in order to show the distance in astronomical units. All the sources are located in both CO and CH_3OH freeze-out zones, as indicated by the solid arrows and the grey dashed line, as taken from the DUSTY model in Kristensen *et al.* (2010).

to the ice data that provide (pencil-beam) measurements of the column densities towards the infrared sources that may or may not be embedded within the cloud. For ice abundances we therefore adopted a slightly different method of deriving the H_2 column densities, starting from extinction in the J-band A_J (Table 5.1) and adopting the relation N_{H_2}=3.33 $\times$ $10^{21} A_J$ given in Figure 10 of Pontoppidan *et al.* (2004). At the SVS 4 source positions, the H_2 column density is of the order of 10^{22} cm^{-2} and the measured ice abundances relative to H_2 are of the order of 10^{-5} for CO and CH_3OH and 10^{-5} – 10^{-4} for H_2O ice. The ice abundances agree with the values reported by Pontoppidan *et al.* (2004) for the SVS 4 cluster. The column densities derived using the two different methods are of the same order of magnitude, but with small variations, possibly due to the assumptions about the temperature, the exact location of the infrared sources along the LoS compared to the distribution of the cloud material, and the differences in the exact column densities traced by the SCUBA-2 and A_J measurements.

Figure 5.6 shows the N_{H_2} variation as a function of the distance from the SMM 4 position for each SVS 4 source. The upper and lower error bars in this figure represent the H_2 column density calculated for T = 10 K and 20 K, respectively. The vertical dashed line indicates the dust temperature of 20 K at 1500 AU from SMM 4, calculated from Kristensen *et al.* (2010) by scaling the luminosity of the protostar according to the most updated distance measurements obtained with *Gaia-DR2* (433 pc ± 4; Ortiz-León *et al.*, 2018). The DUSTY model assumes a spherically symmetric envelope and that the central heating source is a blackbody at T = 5000 K. The

black rightward arrow indicates the distance where CO gas is expected to freeze out on dust grains, which enhances the CH_3OH formation through CO hydrogenation. Pure CO ice starts to desorb at $T > 20$ K (black leftward arrow), although some frozen CO molecules migrate to porous water ice and are only desorbed at $T > 90$ K (Collings *et al.*, 2003). According to the model, the methanol ice desorption region is located below 50 − 100 AU, as indicated by the solid grey arrow in the figure. The comparison with the model shows that the SVS 4 sources lie in a region in which both CO and CH_3OH are frozen out. The observed gas emission associated with these molecules, however, has been released to the gas-phase by non-thermal desorption mechanisms.

5.4.2 *Combined gas-ice maps*

In Figure 5.7, panels *a* and *b* compare the CO ice abundance to the gas-phase ^{13}CO 2 − 1 (panel *a*) and $C^{18}O$ 2 − 1 (panel *b*) emission. Because of optical depth effects, the $C^{18}O$ emission shows more structure than ^{13}CO and traces the densest regions of the cluster. The interplay between CO ice and CO gas in cold dark regions is mainly dominated by the freeze-out of CO gas onto the dust grains. When we assume that the overall column density of CO molecules (CO gas + CO ice) is constant, an anti-correlation is expected to be observed between CO gas and CO ice. Most of the SVS 4 sources show higher CO ice abundances (e.g. SVS 4−6, SVS 4−9, and SVS 4−10) where the ^{13}CO emission is more intense, suggesting that part of the variations are due to the overall physical structure of the region. The same relations are seen in panel *b*. Because ice absorption and gas emission might not be probing the same column of material, this preliminary conclusion has to be verified by comparing ice and gas abundances, and this is addressed in Sect. 5.4.3.

To test whether the $C^{18}O$ line emission traces the densest regions of the core, Figure 5.8 shows a comparison of the 850 μm dust continuum distribution in SVS 4 with molecular emission traced by $C^{18}O$. It can be observed that the $C^{18}O$ emission in SVS 4 does not closely follow the dust emission. However, some care has to be taken in interpreting the dust emission map of SVS 4 because embedded sources can lead to an increase in dust temperature, and consequently, in the submillimeter continuum flux, which alters the dust emission morphology (e.g. Chandler and Carlstrom, 1996). Still, the distributed $C^{18}O$ emission does indicate that CO gas is present on larger scales in the outer envelope of SMM 4.

In Figure 5.7, panels *c* and *d* compare the CH_3OH ice (panel *c*) and H_2O ice (panel *d*) abundances to the CH_3OH $5_0 - 4_0$ A^+ integrated intensity. The peak CH_3OH emission likely traces the emission of the outflow associated with SMM 4 (Kristensen *et al.*, 2010): the strongest CH_3OH emission is observed in three ridges in the NW/SE direction from the centre of the cluster and not where the majority of the SVS 4 sources are located. Two ridges are localised in the vicinity of SMM 4, and the third is observed in the southern region of the map, in the proximity of the outflow knot position SMM 4−S. No straightforward trend is observed between gas-phase methanol and water ice: generally, the H_2O ice abundances are higher

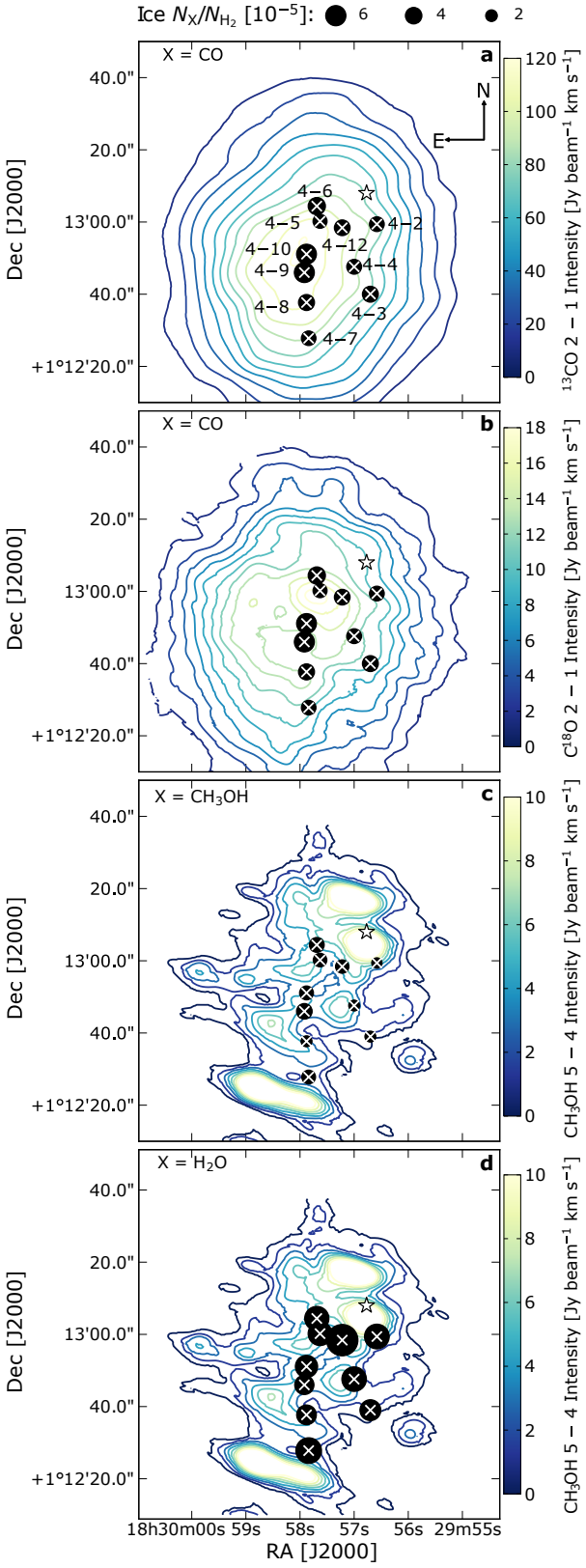

FIGURE 5.7: Gas-ice maps of the SVS 4 cluster. Ice abundances are shown as black circles. The contours at 3σ, 6σ, 9σ, etc. represent the gas-phase integrated intensities. *a:* CO abundances on gas ^{13}CO 2 − 1 ; *b:* CO abundances on gas C^{18}O 2 − 1 ; *c:* CH_3OH abundances on gas CH_3OH 5_0 − 4_0 A^+. *d:* H_2O abundances on gas CH_3OH 5_0 − 4_0 A^+. The white crosses mark the position of the SVS 4 sources, and the white star represents SMM 4.

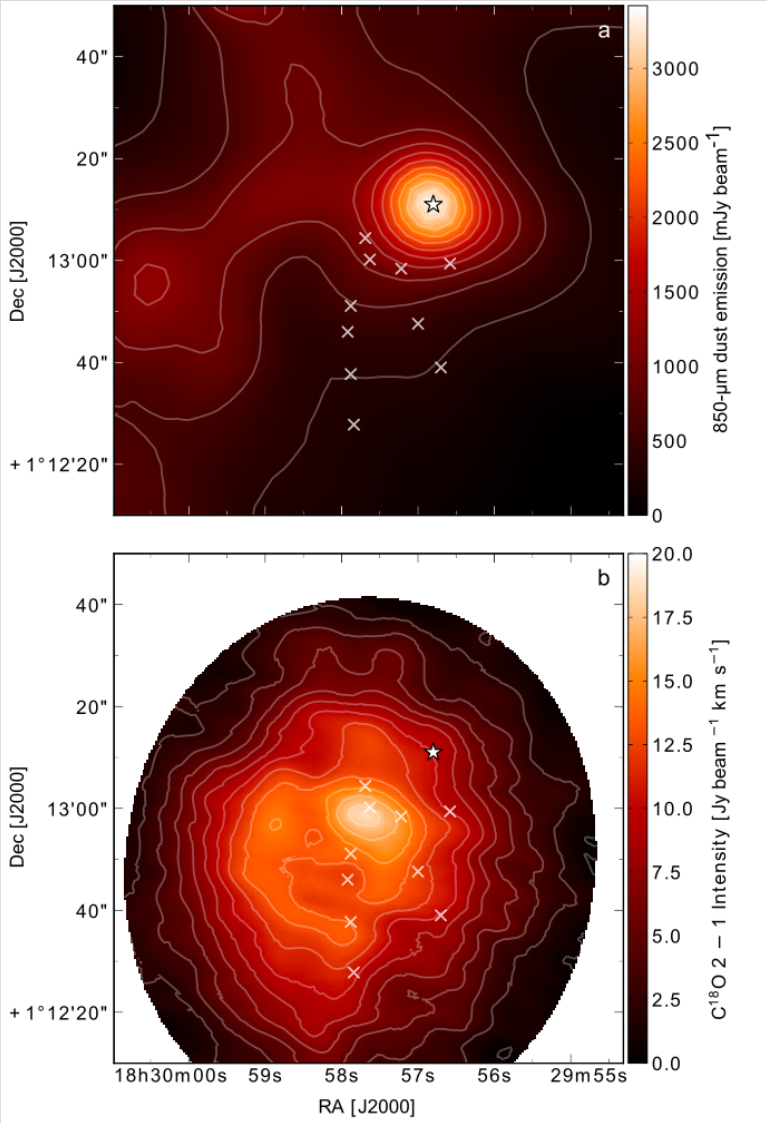

FIGURE 5.8: *a*: SCUBA-2 850 μm dust continuum emission (contours decrease in steps of 10% starting at 3.12 Jy beam^{-1}, Herczeg *et al.*, 2017). *b*: integrated intensity from the molecular emission line of C^{18}O 2–1 (contours are at 3σ, 6σ, 9σ, etc.). The white crosses mark the position of the SVS 4 sources, and the white star represents SMM 4.

where the gas-phase methanol emission is stronger (e.g. SVS 4–2, SVS 4–5, SVS 4–6, and SVS 4–12). Similarly, the methanol ice abundances are lower where the methanol emission is weaker (e.g. SVS 4–4, SVS 4–8). However, some deviations from this behaviour are seen for SVS 4–2, SVS 4–7, and SVS 4–10.

It is worth noting that the morphology of the CH_3OH emission differs from the emission of the CO isotopologues. While the CH_3OH emission is structured, the CO isotopologues show a more uniform distribution. Furthermore, the emission of each molecular tracers is very much dominated by the large-scale structure of SMM 4 and no separate peaks are seen towards any of the SVS 4 sources, suggesting that they do not strongly affect the gas locally.

5.4.3 *Gas and ice variations*

To further explore trends between ice and gas in the region, Figure 5.9 compares the inferred values towards each of the SVS 4 cluster members. Figure 5.9*a* shows that there is no clear trend between CO ice and ^{12}CO gas column densities. For instance, the CO gas column density for SVS 4−3 and SVS 4−4 changes only by 3%, whereas the ice column density for these sources changes by a factor of 4.3. The ^{12}CO gas column density is almost uniform at the SVS 4 source positions, suggesting an extended gaseous component that is not sensitive to CO freeze-out. As discussed in Section 5.4.2, an anti-correlation between CO ice and gas is expected in cold dark star-forming regions due to the effect of CO freeze-out. The absence of this trend in SVS 4 indicates that this relation is not valid in this region, which is characterised by a complex physics. The low temperatures in the cluster allow CO freeze-out to occur, but at the same time, due to temperature variations and dust heating around 20 K caused for example by SMM 4 or its outflow, the frozen CO is efficiently released into the gas phase.

Figure 5.9*b* compares the CH_3OH gas and ice column densities. The CH_3OH gas map in Figure 5.5*b* indicates that the methanol column density is higher around SMM 4 and just south of SVS 4−7; it is almost one order of magnitude higher than towards the column density at the SVS 4 source positions. Figure 5.9*b* shows that the gas column density spans from ~1.9 to 8×10^{14} cm^{-2} and the ice column density from ~0.2 to 2.3×10^{18} cm^{-2}. The dashed grey line illustrates the sources that are located within 9000 AU from SMM 4. The sources in the vicinity of SMM 4, excluding SVS 4−12, show an enhancement in the CH_3OH gas column density of a factor of 1.5−3.0, in agreement with strong methanol emission associated with the SMM 4 outflow. SVS 4−12, a particularly deeply embedded source (A_J= 26 mag), does not follow this trend. On the other hand, no clear enhancement of the methanol ice column densities is seen in the SMM 4 outflow region. It thus appears that the majority of the methanol is in solid form on the grains, even for the LoSs showing gas methanol enhancements.

Fig. 5.9, panels *a* and *b* show that the chemical behaviours of CH_3OH and CO are anti-correlated: larger variations are observed for CH_3OH gas than for CH_3OH ice, while the opposite is seen for CO. This might be partly explained by the higher volatility of CO compared to CH_3OH, especially because the temperatures in the cluster are close to the CO sublimation temperature (15−20 K).

The CO and CH_3OH gas column density are compared to the H_2O ice column density in panels *c* and *d*, although no correlation is expected between them because their formation routes are different. The column density of water ice varies from ~1.3 to 5.9×10^{18} cm^{-2} when SVS 4−12 is not taken into account. SVS 4−12 shows an additional enhancement of a factor of 2. The large error bars for this source are due to the low S/N in the L and M bands and the poor fitting in the red wing between 3.0−3.7 μm. Such a high variation indicates that this region is cold to keep water in the solid phase, and that simultaneously, the hydrogenation of atomic oxygen to form water occurs efficiently. The same trends observed in panels *a* and *b* are also

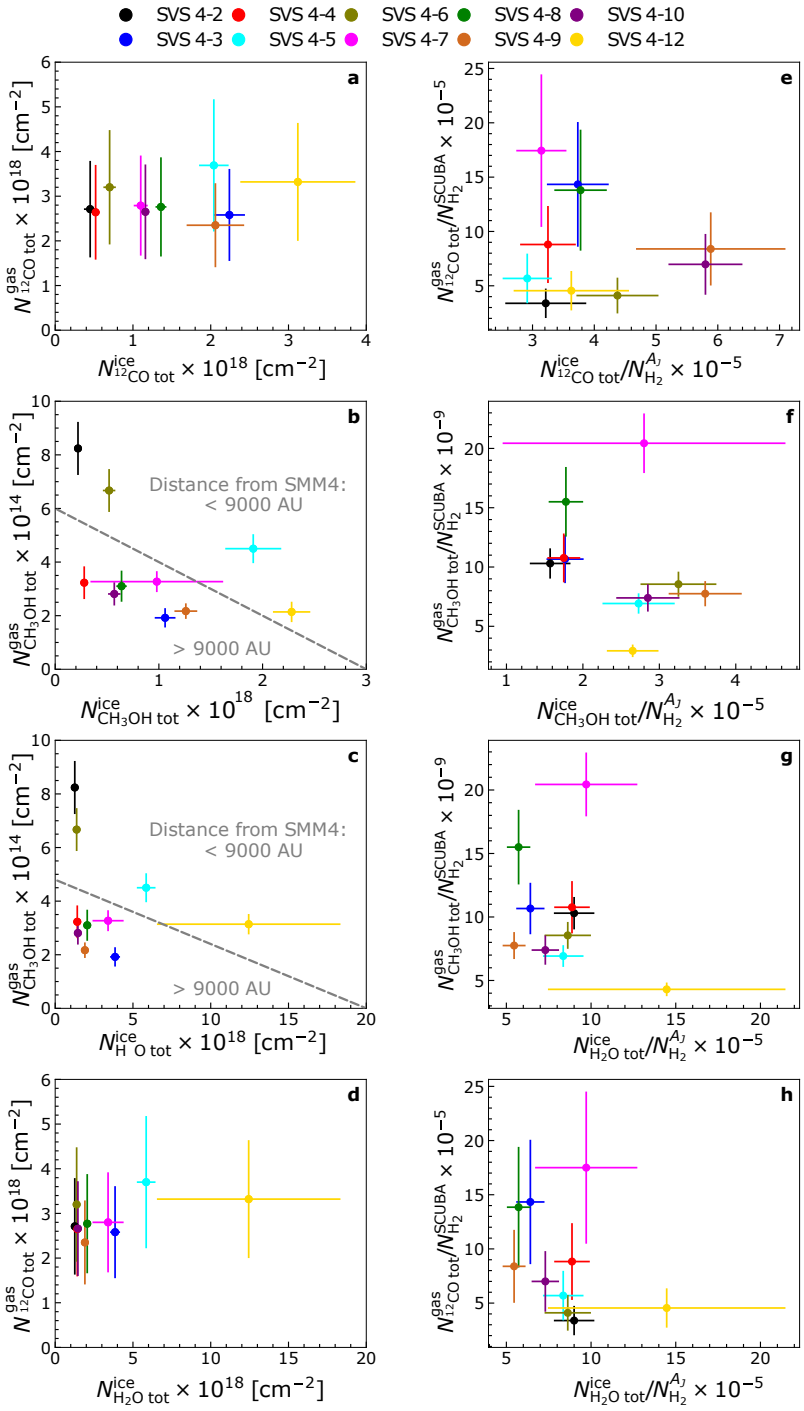

FIGURE 5.9: Gas and ice variations. Panels $a - d$: relation between CO, CH_3OH, and H_2O ice and CO and CH_3OH gas column densities. Panels $e - h$: relation between CO, CH_3OH, and H_2O ice and CO and CH_3OH gas abundances relative to H_2. The coloured filled circles identify the SVS 4 stars; the dashed grey line divides the sources into two groups: YSOs located within 9000 AU from SMM 4, and YSOs located at distances > 9000 AU from SMM 4.

seen when CO and methanol gas are compared to H_2O ice.

Figure 5.9, panels $e - h$, illustrates the gas and ice abundances towards the cluster. A lack of correlation between the ice and gas species is also observed when the relative abundances are compared. This additional result supports the conclusion that there is no straightforward correlation between CO and CH_3OH gas with their ice counterparts in the cluster. This is most likely related to the complexity of the SVS 4 morphology: the presence of the Class 0 protostar and its envelope, the outflow that intersects the cluster, and the vicinity of the SVS 4 stars. All these factors are reflected in temperature and density variations throughout the entire region.

5.5 DISCUSSION

In the previous sections, gas-ice maps have been analysed to investigate the feedback between ice and gas processes. In this section, the information contained in the maps is used to directly determine the CH_3OH and CO gas-to-ice ratios (N_{gas}/N_{ice}) shown in Figure 5.10, calculated from the column densities derived in Sections 5.3.1 and 5.3.2. The azure shaded areas in the figure indicate the estimated ranges of CH_3OH and CO gas-to-ice ratios towards the SVS 4 sources, whereas the dotted light blue line displays the CH_3OH gas-to-ice ratio estimated by Öberg *et al.* (2009a). The solid black lines show the predictions from the astrochemical model by Cazaux *et al.* (2016): the model simulates a typical molecular cloud with a three-phase chemical model that includes gas-phase chemistry that interacts with the surface and bulk chemistry. In the model, thermal desorption and non-thermal desorption of the species in the ice mantles are taken into account. More specifically, two non-thermal desorption mechanisms are included for CO and H_2O: (i) absorption of a single UV-photon or induced by H_2 ionisation by cosmic rays (i.e. photodesorption), and (ii) desorption promoted by the exothermicity of a chemical reaction (i.e. reactive desorption). The CH_3OH ice-to-gas ratio found by Cazaux *et al.* (2016) agrees very well with the lower value derived in this study. It is important to note that only one non-thermal desorption mechanism for methanol is included in the model, reactive desorption. This keeps the gas-to-ice ratio at about 10^{-4}. If additional non-thermal desorption mechanisms were considered, the methanol gas-to-ice ratio calculated by the model would be higher.

The CH_3OH gas-to-ice ratio ($N_{CH_3OH_{gas}}/N_{CH_3OH_{ice}}$) varies between 1.4×10^{-4} and 3.7×10^{-3} (Figure 5.10*a*). The higher values correspond to SVS 4–2 and SVS 4–6, which are located at the CH_3OH peak emission close to SMM 4. These two sources also show the highest CH_3OH gas column densities. Non-thermal desorption mechanisms might be more efficient in this region of the cluster because of the higher degree of UV irradiation originating from the SMM 4 protostar.

The lower values reflect the less efficient methanol non-thermal desorption of the protostars located farther away from SMM 4, and that are by inference subjected to a lower degree of UV irradiation. Simultaneously, because the SMM 4 outflow intersects the cluster, gas-phase destruction by shocks (e.g. collisional dissociation) might be responsible for low gas-to-ice ratios in the region. Our derived value is supported by previous measure-

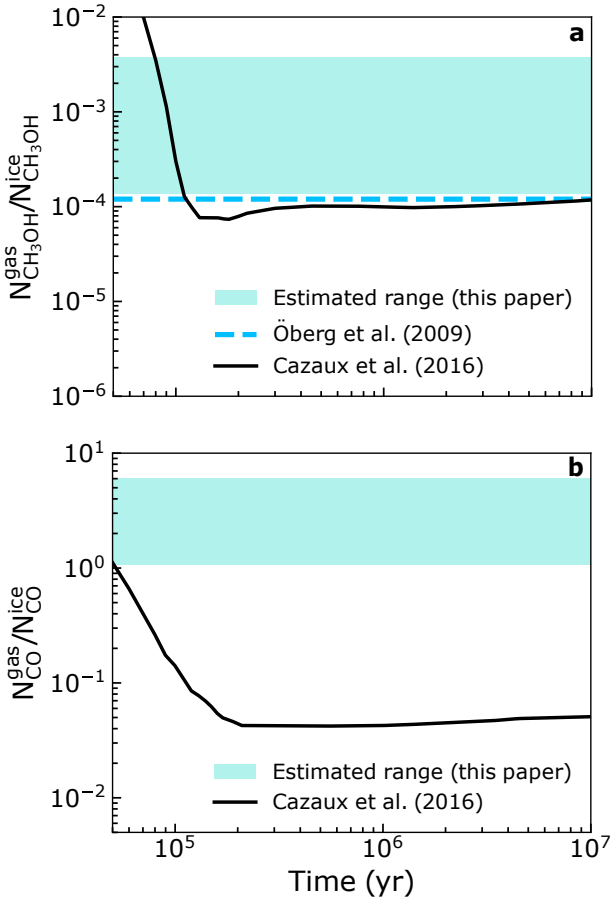

FIGURE 5.10: CH_3OH and CO gas-to-ice ratios (N_{gas}/N_{ice}) for the SVS 4 sources in the Serpens molecular core. The shaded azure areas represent the ranges estimated in this paper for both molecules. The curves represented by the solid black lines indicate the theoretical ratio estimated from the astrochemical model by Cazaux *et al.* (2016). The dashed light blue line in the left panel marks the ratio estimated by Öberg *et al.* (2009a).

ments by Öberg *et al.* (2009a) towards four embedded Class 0/I low-mass protostars.

The CO gas-to-ice ratio ($N_{CO_{gas}}/N_{CO_{ice}}$) derived in this study varies between 1 and 6 (Figure 5.10*b*). This range is significantly higher than the one predicted in the model by Cazaux *et al.* (2016). As discussed previously in Section 5.4, according to the DUSTY model calculated for SMM 4 in Kristensen *et al.* (2010), the dust temperature in the SVS 4 cluster is estimated to be below 20 K, and at these temperatures, CO is indeed expected to be frozen out on grains. The high relative abundance of gaseous CO might be attributed to the morphology of the SVS 4 cluster, and more specifically, to the extended gaseous component traced in the CO gas observations. Because this component is not included in the model by Cazaux *et al.* (2016), this explains the mismatch found in Figure 5.10*b*.

5.6 CONCLUSIONS

We presented SMA and APEX observations of Serpens SVS 4, a dense cluster of low- to intermediate-mass young stars located in the outer envelope of the Class 0 protostar SMM 4. The SMA observations were combined with APEX

single-dish maps and with data from the VLT archive to construct combined gas-ice maps of H_2O, ^{12}CO and CH_3OH of the cluster. In these maps the abundances of H_2O, ^{12}CO, and CH_3OH ices relative to H_2 are displayed with the gas-phase emissions of CH_3OH, ^{13}CO, and $C^{18}O$. These suites of maps are powerful probes of the physical and chemical history of dense cores. They allowed us to study the complex relationships between gas and ice, specifically, the processes linking ice to gas-phase density in cold dark regions: freeze-out and non-thermal desorption. Finally, gas-to-ice ratios of CO and CH_3OH were directly measured to observationally validate their theoretical predictions. The main conclusions of the paper are summarised below.

CO gas and H_2 do not follow the same density profile. The H_2 column density increases from SW towards SMM 4, whereas the CO ridge is located at the centre of SVS 4 cluster. Nevertheless, both distributions are more uniform than that of CH_3OH, which shows three strong ridges that are likely associated with the sputtering induced by the SMM 4 outflow. The methanol gas column density in these regions is around one order of magnitude higher that at the SVS 4 source positions.

There is no clear trend between CO and CH_3OH gas with their ice counterparts in the SVS 4 cluster. This result is expected based on the physical structure of the SVS 4 cluster. Temperature and density variations that affect the chemistry are present in the region, which is strongly influenced by the Class 0 protostar, its outflow, and the high YSO density. The CH_3OH and CO chemical behaviours are anti-correlated: larger variations are seen for CH_3OH gas than for CH_3OH ice, while the opposite is seen for CO.

The CO gas-mapping illustrates the existence of an extended gaseous component that does not probe the densest regions of the cluster where the ice is located. Consequently, the effect of the freeze-out on the CO gas column densities is not observed.This is reflected in higher CO gas column densities and in higher CO gas-to-ice ratios compared to the theoretical ratio estimated by Cazaux *et al.* (2016).

The higher values for the CH_3OH gas-to-ice ratio, induced by the sources located close to the SMM 4 ridges, agree well with the prediction that methanol ice can be formed on dust grains by surface chemistry and is then released into the gas phase in cold regions through non-thermal desorption. The lower values match the measurements performed by Öberg *et al.* (2009a) for embedded Class 0/I low-mass protostars. Generally, the methanol gas-to-ice ratio range found in this study promotes a scenario in which the vast majority of the methanol molecules in SVS 4 is in ice form, condensed on the surfaces of dust grains.

Similar studies of other star-forming regions will reveal how universal, for example, the gas-to-ice ratios and trends found for the Serpens SVS 4 cluster are. For example, more isolated young stellar objects are suitable to address how efficiently methanol is desorbed in absence of external irradiation. In contrast, regions dominated by strong external irradiation can constrain how efficient the methanol photodesorption is compared to the other non-thermal desorption mechanisms. Future observations with the James Webb Space Telescope (JWST) will overcome the main limitation in the detection of complex molecules in the ice phase, the low spectral resolution. For

example, medium-resolution MIRI observations of the 7−8 μm region will allow us to access the ice content of a suite of species more complex than methanol (e.g. CH_3CHO and CH_3CH_2OH). The combination of these data with high-sensitivity ALMA observations will enable us to construct accurate gas-ice maps of several complex organic molecules and to distinguish the interplay between ice and gas in low- and high-mass star-forming regions.

ACKNOWLEDGEMENTS

We thank the anonymous referee for the useful comments that improved the manuscript. This work is based on observations with the Submillimeter Array (SMA), Mauna Kea, Hawaii, program code: 2016B-S022; with the Atacama Pathfinder EXperiment (APEX), Llano Chajnantor, Chile, program code: 099.F-9316(A) and with the Very Large Telescope (VLT), Paranal, Chile, under European Southern Observatory (ESO) programmes 075.C-0384(A) and 077.C-0363(A). The SubMillimeter Array is a joint project between the Smithsonian Astrophysical Observatory and the Academia Sinica Institute of Astronomy and Astrophysics and is funded by the Smithsonian Institution and the Academia Sinica. The Atacama Pathfinder EXperiment (APEX) telescope is a collaboration between the Max Planck Institute for Radio Astronomy, the European Southern Observatory, and the Onsala Space Observatory. Swedish observations on APEX are supported through Swedish Research Council. The group of JKJ acknowledges the financial support from the European Research Council (ERC) under the European Union's Horizon 2020 research and innovation programme (grant agreement No 646908) through ERC Consolidator Grant "S4F". The research of LEK is supported by a research grant (19127) from VILLUM FONDEN. HJF gratefully acknowledges the support of STFC for Astrochemistry at the OU under grants No ST/P000584/1 and No ST/T005424/1 enabling her participation in this work. GP is grateful to EU COST Action CM1401 "Our Astro-Chemical History" for funding contributions towards the realization of this work.

Appendix

5.a FITTING OF ICE DATA

5.A.1 *Continuum determination*

In order to derive the column densities of ice water, carbon monoxide, and methanol, the L- and M-band spectra have to be converted into an optical depth scale given by

$$\tau_\lambda = -\ln\left(\frac{F_\lambda^{\rm obs}}{F_\lambda^{\rm cont}}\right), \tag{5.1}$$

where $F_\lambda^{\rm obs}$ is the observed flux and $F_\lambda^{\rm cont}$ is the continuum spectral energy distribution (SED).

Determining the continuum of embedded sources is not straightforward because several physical parameters of the disc and envelope must be known (Whitney *et al.*, 2003; Gramajo *et al.*, 2010; Robitaille, 2017), together with accurate photometric measurements. In this paper, the continuum of the L-band observations was derived by the fitting of the near-infrared photometric data in Table 5.A.1 and the spectral data above 3.6 μm. The accuracy of the 2MASS photometric data and VLT-ISAAC spectral data is about 8% and 13%, respectively. To account for the different flux accuracy, weighted fits were used to determine the continuum: less weight was given to the VLT data compared to 2MASS data. The weights are inversely proportional to the variance of the data. The fitting was performed using one or two blackbodies if A_J towards the source was higher or lower than 9.8 mag, respectively. Although a huge degeneracy involving the disc (M_{disc}) and envelope mass (M_{env}) and the inclination (i) arises in interpreting SED of YSOs, the use of one blackbody to trace the continuum of the L-band observations towards embedded sources ($M_{env} \sim 0.4 M_\odot$), as result of the re-emission of the stellar flux by the envelope, is consistent with radiative transfer models (Whitney *et al.*, 2003; Robitaille *et al.*, 2006; Robitaille *et al.*, 2007) of Class 0 and late Class 0 objects. In less embedded environments, the combination of the scattered or re-emitted photons by the disc and envelope becomes more evident, and a low-infrared excess is observed longward of 3.6 μm. In this case, a second blackbody component is required to fit the final part of the L band. Two blackbodies were adopted for SVS 4−5 because of the high mid-infrared excess, as pointed out by Pontoppidan *et al.* (2004), and because SVS 4−9 is a peculiar source due to its strong X-ray flux (Preibisch, 2003). Because the extinction law at the L bands is significantly lower than the visual extinction (Cardelli *et al.*, 1989), we decided to use reddened blackbody functions as also adopted by previous studies (Ishii *et al.*, 2002; Chiar *et al.*, 2002; Moultaka *et al.*, 2004). The good agreement between the optical depths of the SVS 4 sources obtained in this work and those derived by Pontoppidan *et al.* (2004) (see Figures 4−6 of Pontoppidan *et al.* (2004) and A.1 and A.2 of this work) contributes to the reliability of this method. The left-hand sides of Figures 5.A.1 and 5.A.2 show the observed

TABLE 5.A.1: Photometry of the SVS 4 sources.

SVS	1.235 μm^a [mJy]	1.250 μm^b [mJy]	1.635 μm^b [mJy]	1.662 μm^a [mJy]	2.159 μm^a [mJy]
4–2	1.59 ± 0.08	1.8 ± 0.2	8.5 ± 0.9	7.73 ± 0.25	16.4 ± 0.38
4–3	≤ 0.09	–	0.4 ± 0.1	≤ 0.24	1.59 ± 0.08
4–4	1.37 ± 0.06	1.50 ± 0.2	10.5 ± 1	10.5 ± 0.3	24.5 ± 0.56
4–5	≤ 0.4	–	0.03±0.01	≤ 2.34	4.0 ± 0.3
4–6	0.6 ± 0.06	0.5 ± 0.1	3 ± 0.3	3.19 ± 1.62	10.3 ± 0.49
4–7	≤ 0.08	0.015±0.005	0.6 ± 0.1	0.48 ± 0.08	4.3 ± 0.13
4–8	≤ 0.21	0.04 ± 0.01	1.8 ± 0.2	1.76 ± 0.10	14.4 ± 0.37
4–9	≤ 0.38	0.21 ± 0.05	9.7 ± 0.1	10.1 ± 0.39	68.6 ± 2.15
4–10	0.79 ± 0.07	0.6 ± 0.1	9.9 ± 1	10.7 ± 0.44	41.4 ± 1.0
4–12	–	–	–	–	0.2 ± 0.02

Notes. ^{a} from 2MASS (Skrutskie *et al.*, 2006) ^{b} from UKRIT (Pontoppidan *et al.*, 2004).

flux, the photometry data, and the synthetic continuum used in this paper. The optical depth, calculated with Equation 5.1, is shown on the right-hand side of both figures. SVS 4–12 is a saturated source, and only the red wing is shown. In order to estimate the optical depth, the SVS 4–9 curve was scaled to the red wing of SVS 4–12, as suggested by Pontoppidan *et al.* (2004). The authors stated that the optical depth profile does not change significantly if another SVS 4 source is used in the scaling because the SVS 4 spectra have similar shapes.

For the M-band observations, on the other hand, the local continuum was calculated with a spline function. In order to only take the continuum SED into account, the CO and ^{13}CO 1–0 ro-vibrational transitions were masked together with the Pfund HI line. To perform the masking, the CO and ^{13}CO ro-vibrational spectra obtained from HITRAN database[6] (Rothman *et al.*, 1987) were overlaid on the SEDs. The narrow gas-phase lines were then carefully removed from the SEDs at the designated frequencies.

[6] https://hitran.org

5.A.2 *Optical depth fitting*

The M-band optical depths were fitted using the OMNIFIT code (Suutarinen, 2015b), an open-source code that aims to fit observational data of astrophysical ices using multi-component laboratory spectra and analytical data. The LMFIT package[7] was used to perform non-linear optimisation with the Levenberg-Marquardt method. M-band optical depths were modelled by combining a CDE-corrected Lorentzian function CO:CH_3OH (1:1) laboratory data (Cuppen *et al.*, 2011) for the middle and red component, respectively. In the case of the L bands, three laboratory data were used, pure H_2O (Fraser *et al.*, 2004), CO:CH_3OH (M-band values), and H_2O:CH_3OH (Dawes *et al.*, 2016). The CO:CH_3OH optical depth was kept constant from the M-band fitting. In order to decide the best water-methanol mixing ratio (R), five variations were checked and the maximum likelihood estimation (MLE) was

[7] https://lmfit.github.io/lmfit-py/

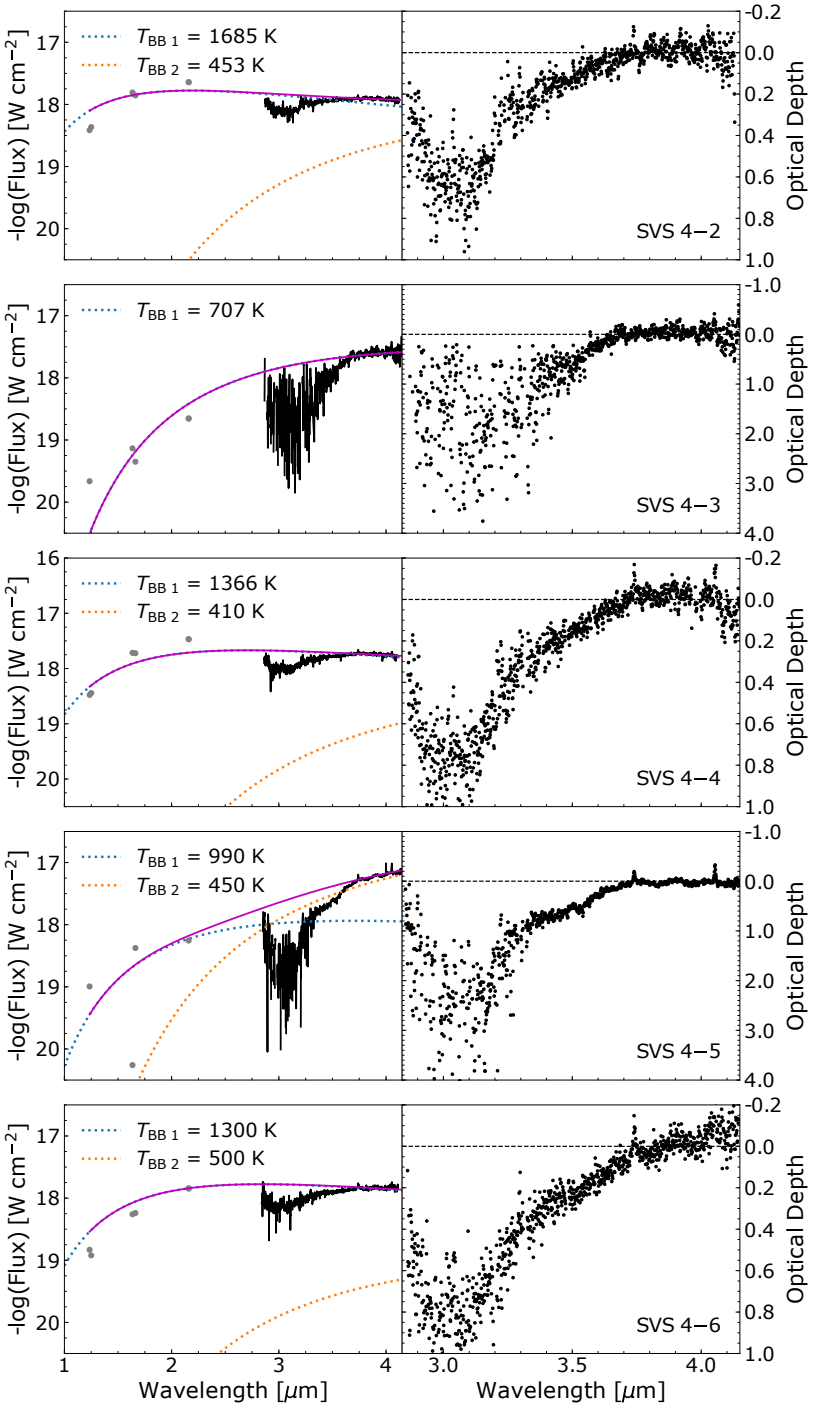

FIGURE 5.A.1: L-band SED and optical depth of the sources towards the SVS 4 cluster. *Left:* The dotted blue and orange lines show the blackbody functions we used to determine the continuum (magenta line) by fitting the dark grey photometric points. The temperature of each blackbody component is shown in the upper left corner of each panel and is given in K. *Right:* L-band observations towards the SVS 4 sources on an optical depth scale. The dashed black lines are used as a reference for τ=0.

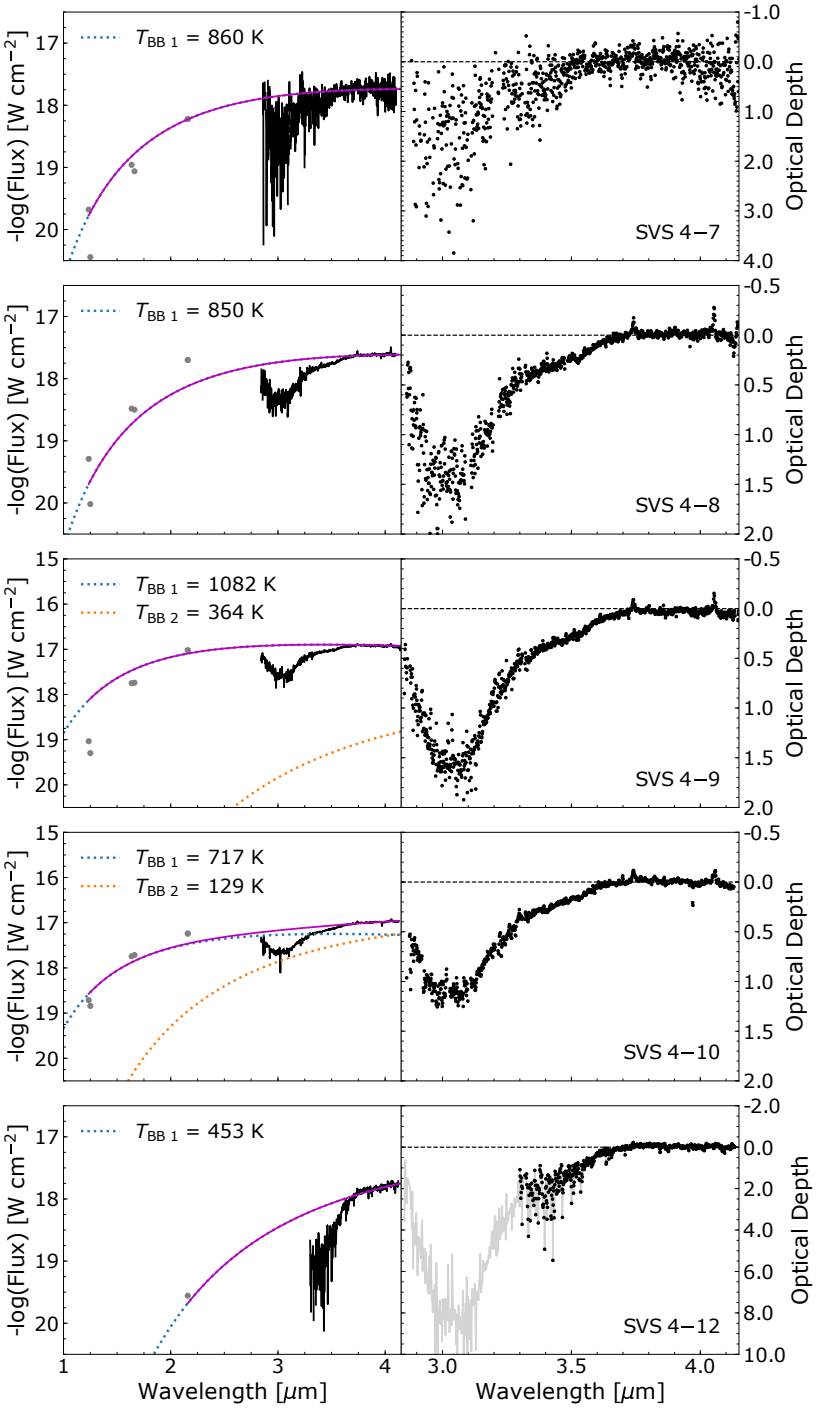

FIGURE 5.A.2: Continued from Fig.5.A.1. The light grey line represents the SVS 4−9 optical depth scaled to the red wing of SVS 4−12.

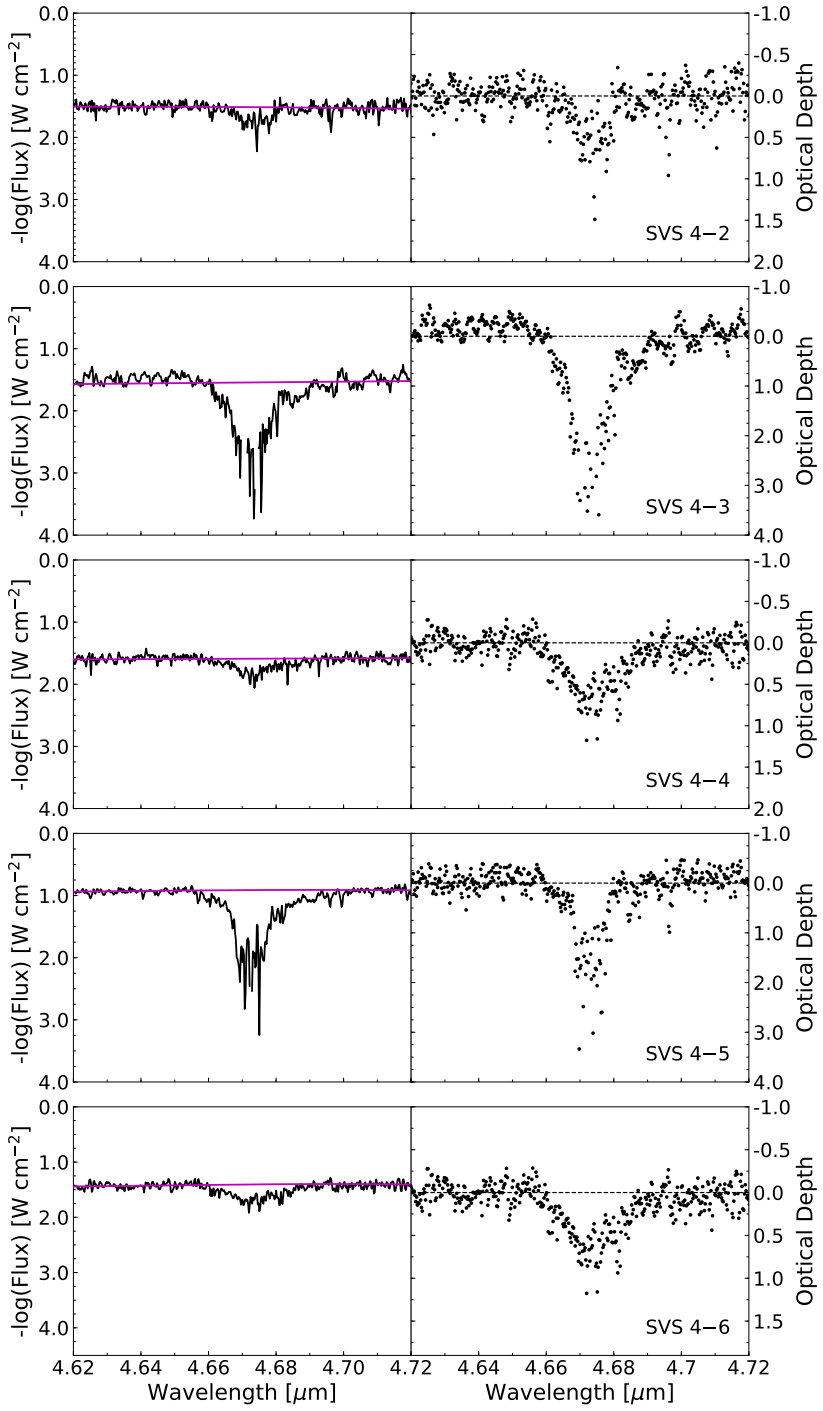

FIGURE 5.A.3: M-band SED and optical depth of the sources towards the SVS 4 cluster. *Left:* The spline function we used to determine the continuum for the M-band spectra is shown in magenta. *Right:* M-band observations towards the SVS 4 sources on an optical depth scale. The dashed black lines are used as a reference for τ=0.

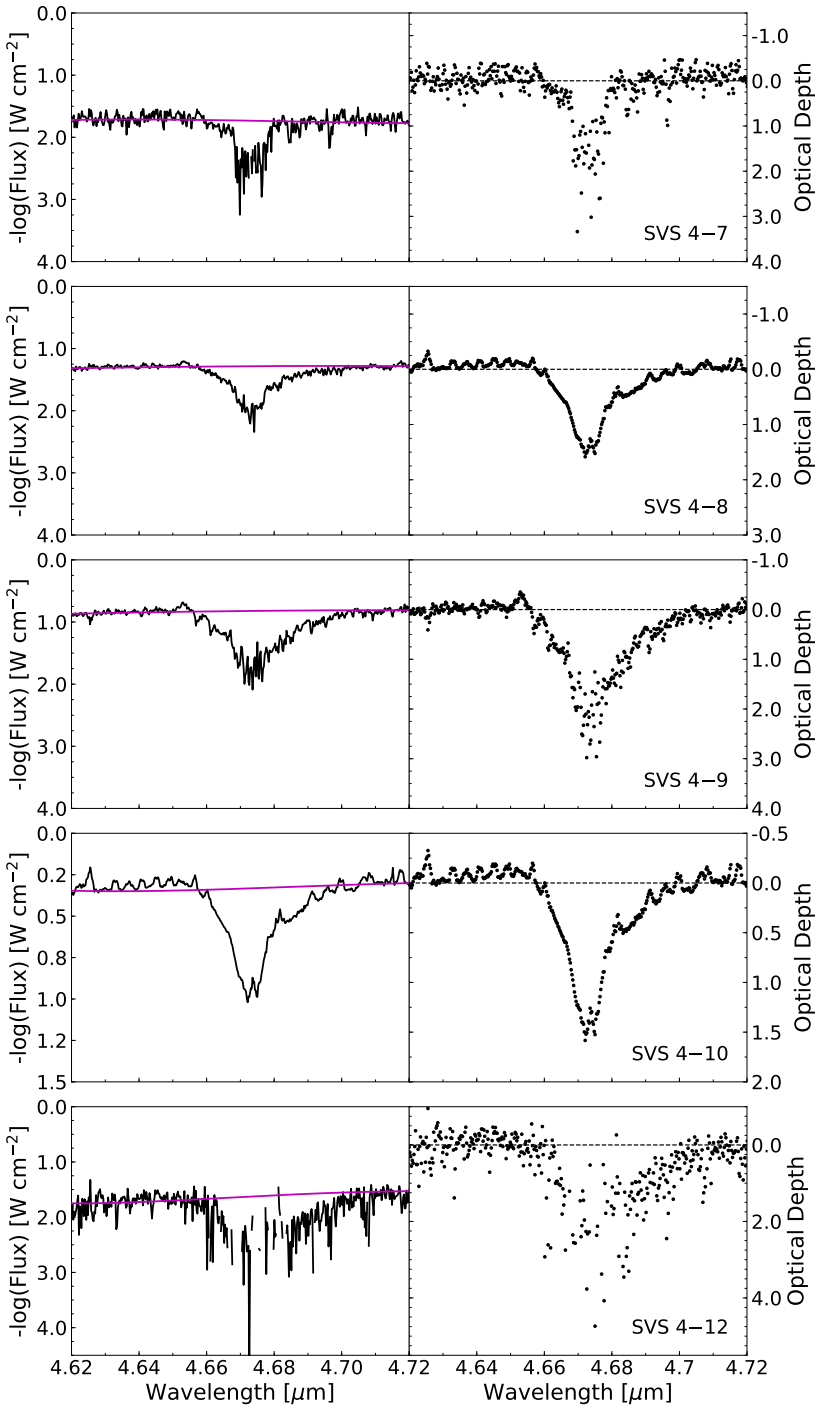

FIGURE 5.A.4: Continued from Fig.5.A.3.

used to determine the best model given the higher probability. In order to achieve this goal, the OMNIFIT code was modified and the optimisation procedure adapted to allow the Monte Carlo Markov chain (MCMC) analysis. The log-likelihood function is given by

$$\ln p(\tau_\lambda^{obs} | k \cdot \tau_{\lambda,true}^{lab}) = -\frac{1}{2} \sum_n \left[\frac{(k \cdot \tau_{\lambda,true}^{lab} - \tau_\lambda^{obs})^2}{\sigma_n^2} + \ln(2\pi\sigma_n^2) \right], \quad (5.2)$$

where $\tau_\lambda^{\rm obs}$ was defined in Equation 5.1, $\tau_{\lambda,true}^{\rm lab}$ is the optical depth of the laboratory data, k the scale factor, and σ_n^2 is the optical depth error, propagated from the flux error. The MLE was initially found using the downhill simplex method (Nelder and Mead, 1965), and the best solution used as initial point to sample the posterior distribution using the affine-invariant MCMC package `emcee` (Foreman-Mackey *et al.*, 2013). The log-likelihood comparisons are shown in Figure 5.A.5.

5.A.3 *Derivation of H_2O and CH_3OH ice column density*

The pure H_2O column density was calculated by integrating the optical depth of the O-H stretching mode at 3.0 μm of the fitted laboratory spectra, after decomposing the L-band spectra performed by OMNIFIT, using the equation below:

$$N_{\rm ice} = \frac{1}{\mathcal{A}} \int_{\nu_1}^{\nu_2} \tau_\nu d\nu, \quad (5.3)$$

where $\mathcal{A}$ is the band strength of a specific vibrational mode, and ν must be understood as the wavenumber in units of cm^{-1}. The band strength we used was 2×10^{-16} cm molecule^{-1} taken from Hudgins *et al.* (1993).

Because we lack accurate band strengths for the H_2O:CH_3OH component, mixed water and methanol column densities were derived from non-saturated and negligibly blended bands at 1660 cm^{-1} (6.0 μm) and 2827 cm^{-1} (3.57 μm), respectively, following the empirical relations found by Giuliano *et al.* (2016) for a binary mixture of H_2O:CH_3OH:

$$N_{\rm H_2O} = (29067 \times \tau_{1660\ \rm cm^{-1}} - 300) \times 10^{15}\ \text{molec cm}^{-2} \quad (5.4)$$

$$N_{\rm CH_3OH} = (3804 \times \tau_{2827\ \rm cm^{-1}} + 4) \times 10^{15}\ \text{molec cm}^{-2}, \quad (5.5)$$

where $\tau_{1660\ \rm cm^{-1}}$ and $\tau_{2827\ \rm cm^{-1}}$ are the optical depth values at this position in the spectrum.

5.A.4 *Derivation of CO ice column density*

The pure CO ice column density was calculated by the equation below, taken from Pontoppidan *et al.* (2003a):

$$N_{\rm Pure\ CO} = 6.03\ \text{cm}^{-1} \times \tau_{\rm peak} \times A_{\rm bulk}^{-1}, \quad (5.6)$$

where $A_{\rm bulk}^{-1}$ is the band strength of the bulk (1.1×10^{-17} cm molecule^{-1} – Gerakines *et al.*, 1995), and the numerical factor takes the effect of the CDE correction into account.

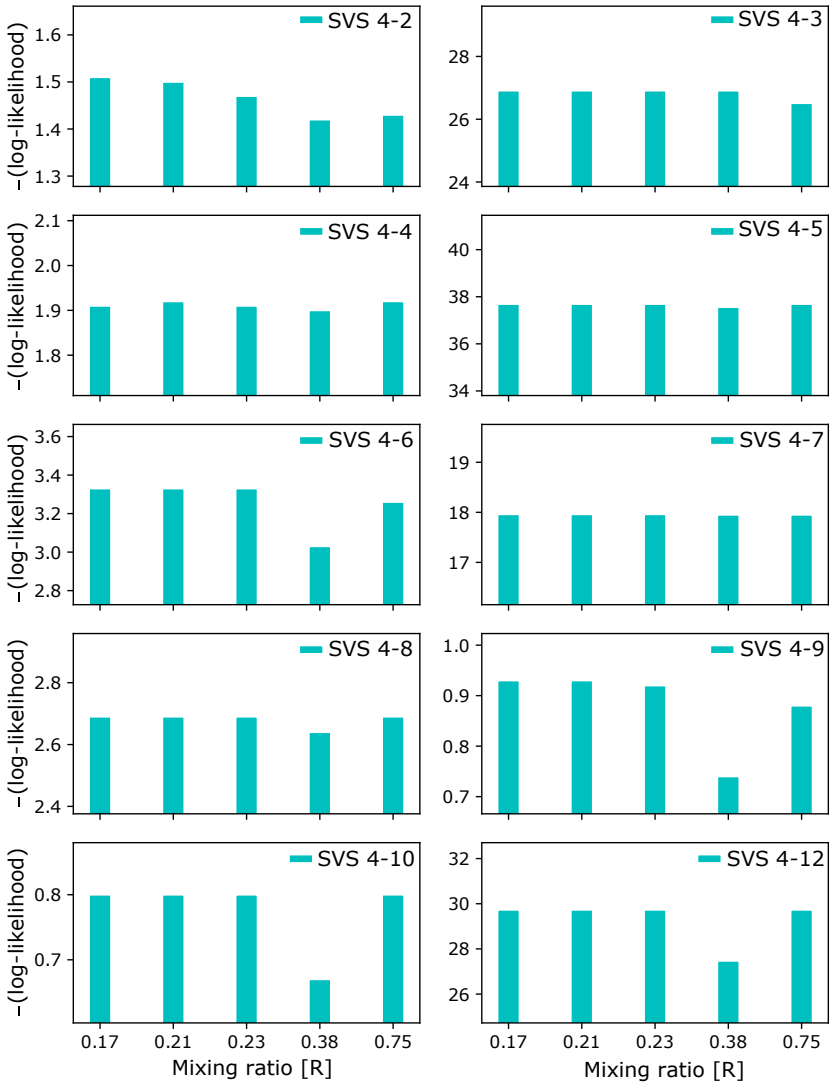

FIGURE 5.A.5: Log-likelihood bar plot of the H_2O:CH_3OH mixing ratios (R). The mixture with R=38% provides a slightly better match of observations and models for all SVS 4 sources, except for SVS 4–3.

The column density of CO trapped in the CO:CH_3OH sample was calculated from the oscillator number method, described in Suutarinen (2015a). A modified version of Equation 5.3 was used,

$$N = k \cdot \frac{1}{\mathcal{A}} \int_{\nu_1}^{\nu_2} \tau_\nu d\nu, \tag{5.7}$$

where k is a scale factor calculated by OMNIFIT (See Equation 5.A.2), and the oscillator number is the entire term given by $\frac{1}{\mathcal{A}} \int_{\nu_1}^{\nu_2} \tau_\nu d\nu$. The value used for the oscillator number of CO and CH_3OH was 5.183×10^{17} cm^{-2} taken from Suutarinen (2015a).

5.b PRODUCING GAS-PHASE MAPS

5.B.1 *Combination of interferometric and single-dish data*

The combination of interferometric and single-dish data was performed using CASA version 4.6.0 and following the CASA Guide[8] M100 Band3 Combine 4.3 (for a detailed explanation of the combination, see the CASA Guide and references therein). Initially, the APEX dataset was resampled to match the shape of the SMA datacube using the `imregrid` task in CASA. Subsequently, the two datasets were trimmed with the CASA `imsubimage` task to exclude the noisy edge regions in the single-dish data and the regions masked by the `clean` task in the interferometric data. Then the SMA non-uniform primary beam response was multiplied to the single-dish data by applying the CASA task `immath`. This step was performed to ensure that the two datasets had a common response on the sky. The SMA and APEX datasets were then combined by executing the CASA task `feather`. The `feather` algorithm applies a Fourier transform and scales the single-dish (low-resolution) data to the interferometric (high-resolution) data. Finally, it merges the two datasets with different spatial resolution, and in our case, it folds into the SMA data the short-spacing corrections of the APEX telescope.

[8] https://casaguides.nrao.edu/index.php

Figures 5.B.2-5.B.4 show the integrated intensity maps of the CH_3OH $5_0 - 4_0$ A^+ line and of the CO isotopologues (^{13}CO and $C^{18}O$) lines using the SMA data, APEX data, and the combined SMA + APEX data. The maps distinctly illustrate that the SMA data filter out spatially extended emission associated with the cloud. On the other hand, the extended emission is very well recovered in the single-dish APEX data. Therefore it is crucial to combine interferometric and large-scale single-dish data when a quantitative analysis of the datasets is performed (e.g. derivation of column densities). The species for which most of the flux is recovered in the combination is ^{13}CO, followed by $C^{18}O$ and CH_3OH.

5.B.2 *CO isotopologue optical depth*

When the gas ratio abundance ^{12}CO:^{13}CO:$C^{18}O$ is constant, the ^{13}CO optical depth can be calculated from the line intensity ratio (Myers *et al.*, 1983; Ladd *et al.*, 1998), given by

$$\frac{I(^{13}\mathrm{CO})}{I(\mathrm{C}^{18}\mathrm{O})} \approx \frac{1-\exp(-\tau^{^{13}\mathrm{CO}})}{1-\exp(-\tau^{^{13}\mathrm{CO}}/f)}, \tag{5.8}$$

where $I(^{13}CO)$ and $I(C^{18}O)$ are the line intensities of ^{13}CO and $C^{18}O$, respectively. $\tau^{^{13}CO}$ is the ^{13}CO optical depth, and f is the $^{13}CO/C^{18}O$ abundance ratio. In the literature, the intrinsic ratio for the Milky Way disc is about 7–10 (Wilson and Matteucci, 1992; Barnes *et al.*, 2015). In this paper, $f = 8$ is assumed. Figure 5.B.1 shows the $I(^{13}CO)/I(C^{18}O)$ line intensity ratio versus the $I(C^{18}O)$ line intensity, where the sources are identified by the colours. The two dashed lines indicate the line ratio associated with the $\tau^{^{13}CO}$. In the trivial case that the ^{13}CO emission is optically thick and the $C^{18}O$ emission is optically thin, $C^{18}O$ increases compared to ^{13}CO along the LoS. Consequently, the ratio between the two lines will decrease, as shown in Figure 5.B.1. Although the $\tau^{^{13}CO}$ does indicate the ^{13}CO emission is only

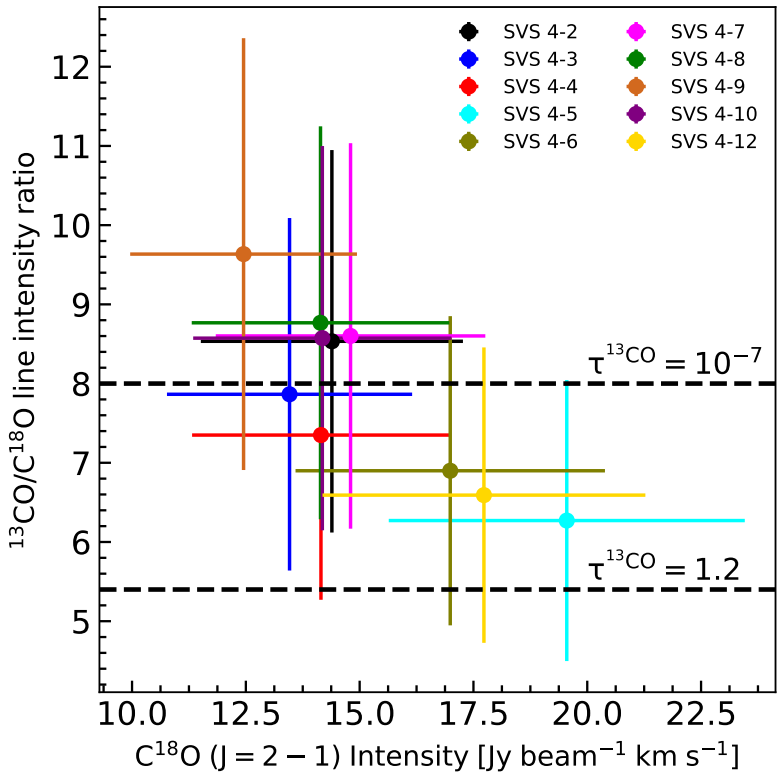

FIGURE 5.B.1: $I(^{13}CO)/I(C^{18}O)$ line intensity ratio *vs.* the $I(C^{18}O)$ line intensity. The dashed lines indicate two optical depth regimes for ^{13}CO; the sources are represented by coloured dots. The error bars assume a 20% error from the flux calibration.

moderately optically thick, the decreasing profile indicates that the $C^{18}O$ emission is optically thin and is therefore more reliable to calculate the ^{12}CO column density assuming local thermodynamic equilibrium (LTE) conditions. This result is still valid when an $^{13}CO/C^{18}O$ abundance ratio (f) equal to 7 or 10 is assumed.

TABLE 5.B.1: Integrated ^{13}CO and $C^{18}O$ line intensities in units of Jy beam^{-1} km s^{-1} over each source position.

Source	^{13}CO ($J = 2 - 1$)	$C^{18}O$ ($J = 2 - 1$)
SVS 4–2	122.80 ± 24.55	14.39 ± 2.86
SVS 4–3	105.36 ± 21.13	13.46 ± 2.73
SVS 4–4	104.00 ± 20.72	14.15 ± 2.80
SVS 4–5	122.59 ± 24.52	19.55 ± 3.91
SVS 4–6	117.22 ± 23.48	16.99 ± 3.38
SVS 4–7	127.30 ± 25.46	14.80 ± 2.96
SVS 4–8	123.97 ± 24.98	14.14 ± 2.93
SVS 4–9	119.95 ± 24.00	12.45 ± 2.50
SVS 4–10	121.57 ± 24.32	14.18 ± 2.81
SVS 4–12	116.87 ± 23.41	17.73 ± 3.51

TABLE 5.B.2: Integrated CH_3OH line intensities in units of Jy beam^{-1} km s^{-1} over each source position.

SVS	$5_0 - 4_0$ E$^+$	$5_1 - 4_1$ E$^-$	$5_0 - 4_0$ A$^+$	$5_1 - 4_1$ E$^+$	$5_2 - 4_2$ E$^-$
SVS 4–2	0.66 ± 0.13	6.23 ± 1.24	7.98 ± 1.60	0.50 ± 0.10	0.19 ± 0.10
SVS 4–3	...	0.69 ± 0.14	0.97 ± 0.20	...	...
SVS 4–4	...	1.73 ± 0.35	1.10 ± 0.22	...	...
SVS 4–5	0.63 ± 0.13	3.82 ± 0.76	1.65 ± 0.50	0.41 ± 0.13	0.12 ± 0.05
SVS 4–6	0.50 ± 0.10	3.37 ± 0.67	3.89 ± 0.78	0.85 ± 0.17	0.92 ± 0.19
SVS 4–7	0.16 ± 0.05	2.74 ± 0.60	1.26 ± 0.45	0.43 ± 0.10	0.33 ± 0.07
SVS 4–8	...	1.32 ± 0.26	1.32 ± 0.26	...	...
SVS 4–9	0.30 ± 0.07	1.48 ± 0.30	1.97 ± 0.40	0.12 ± 0.04	...
SVS 4–10	0.32 ± 0.07	1.12 ± 0.22	2.42 ± 0.48	...	...
SVS 4–12	0.11 ± 0.04	4.29 ± 0.86	4.55 ± 0.91	0.19 ± 0.05	0.25 ± 0.07

Notes. Not provided numbers mean that the integrated intensities are below 5σ of the noise level.

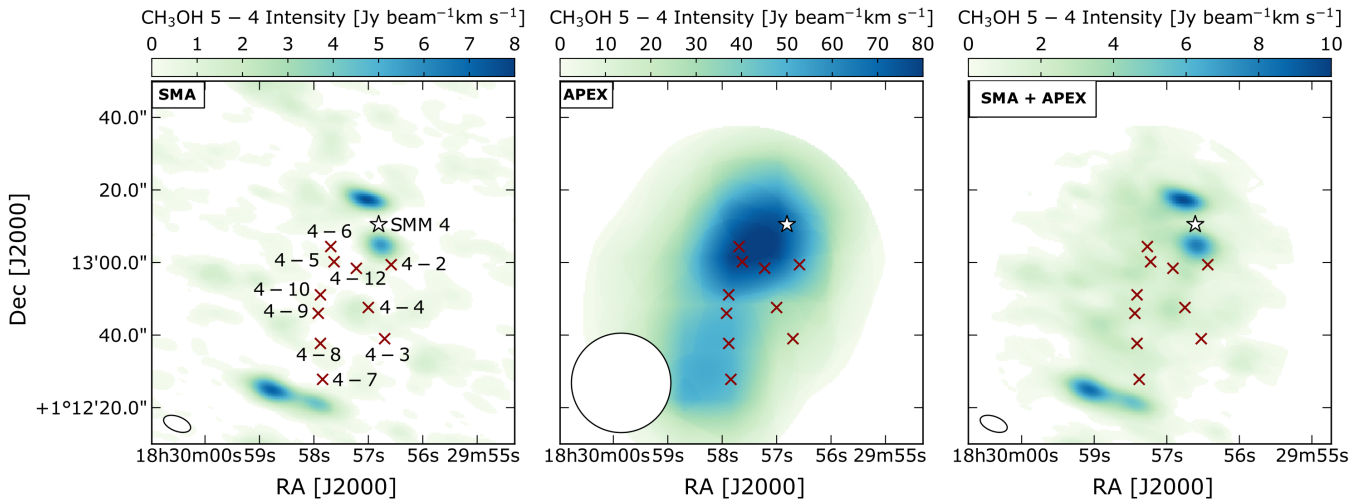

FIGURE 5.B.2: *Left:* $CH_3OH\ 5_0 - 4_0\ A^+$ line emission observed by the SMA. *Middle:* $CH_3OH\ 5_0 - 4_0\ A^+$ line emission detected by the APEX telescope. *Right:* $CH_3OH\ 5_0 - 4_0\ A^+$ line emission resulting from the SMA + APEX combination. All lines are integrated between 5 and 13 km s^{-1}. Contours are at 3σ, 6σ, 9σ, etc. The synthesised beam is shown in white in the bottom left corner of each panel. The dark red crosses and the white star illustrate the positions of the SVS 4 stars and of SMM 4, respectively.

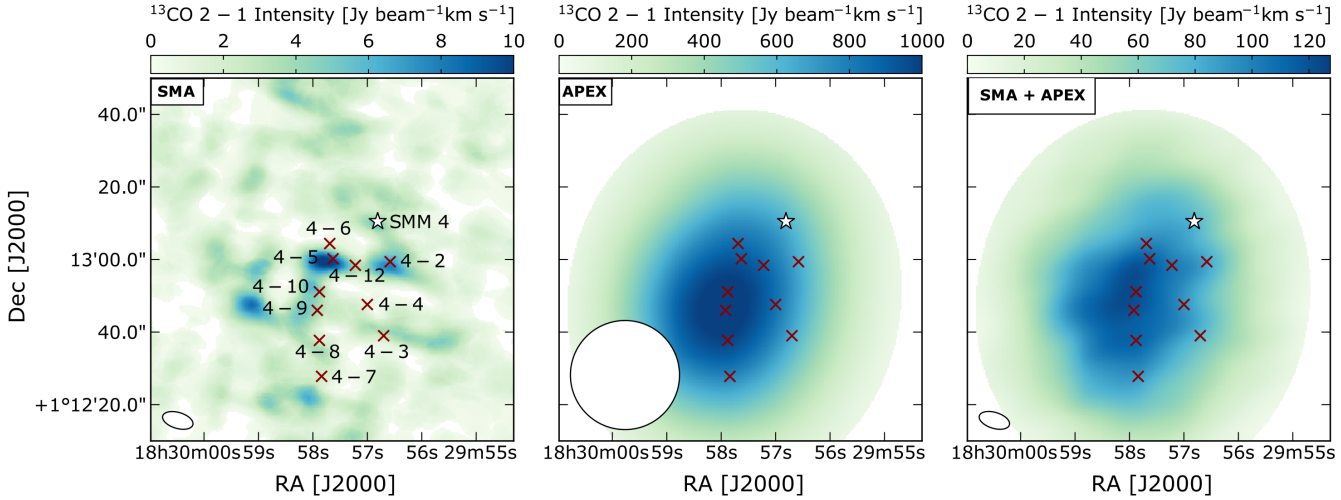

FIGURE 5.B.3: *Left:* ^{13}CO 2–1 line emission observed by the SMA. *Middle:* ^{13}CO 2–1 line emission detected by the APEX telescope integrated between 0 and 15 km s^{-1}. *Right:* ^{13}CO 2–1 line emission resulting from the SMA + APEX combination. All lines are integrated between 0 and 13 km s^{-1}. Contours are at 3σ, 6σ, 9σ, etc. The synthesised beam is shown in white in the bottom left corner of each panel. The dark red crosses and the white star illustrate the positions of the SVS 4 stars and of SMM 4, respectively.

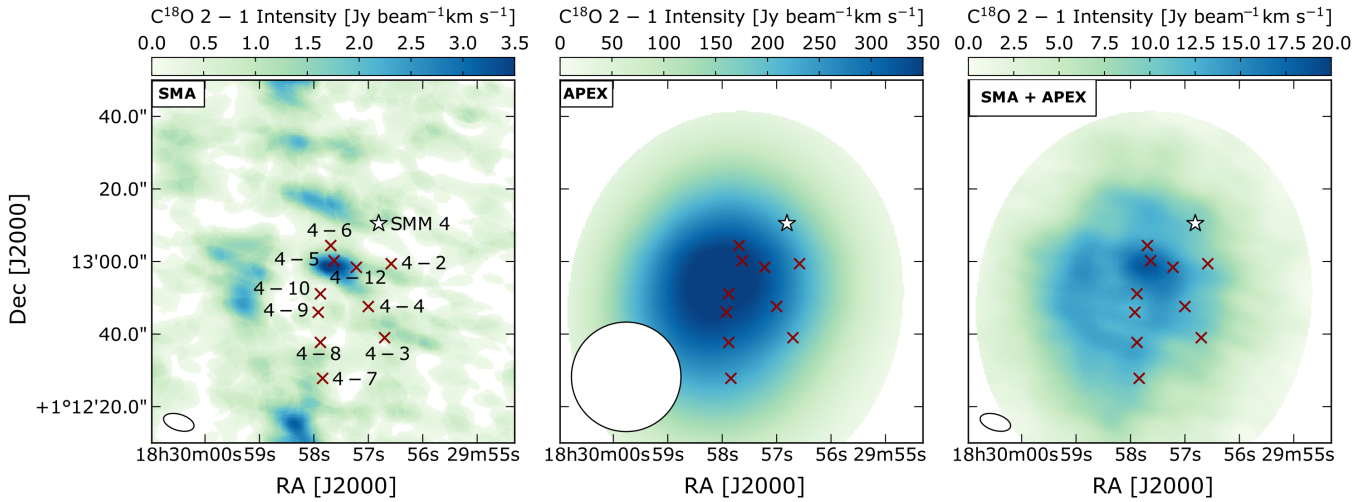

FIGURE 5.B.4: *Left:* $C^{18}O$ 2–1 line emission observed by the SMA. *Middle:* $C^{18}O$ 2–1 line emission detected by the APEX telescope. *Right:* $C^{18}O$ 2–1 line emission resulting from the SMA + APEX combination. All the lines are integrated between 4 and 11 km s^{-1}. Contours are at 3σ, 6σ, 9σ, etc. The synthesised beam is shown in white in the bottom left corner of each panel. The dark red crosses and the white star illustrate the position of the SVS 4 stars and of SMM 4, respectively.

5.c PRODUCING AN H_2 COLUMN DENSITY MAP

The production of the H_2 column density map is accomplished by making use of the submillimeter continuum (SCUBA-2) maps at 850 μm (Herczeg *et al.*, 2017). The equations and the conversion factors used here come from Kauffmann *et al.* (2008) and are briefly explained below.

The H_2 column density N_{H_2} is related to the observed flux per beam $S_\nu^{\rm beam}$, the dust opacity k_ν , and the Planck function $B_\nu(T)$ by

$$N_{H_2} = \frac{S_\nu^{\rm beam}}{\Omega_{\rm A}\ \mu_{H_2}\ m_{\rm H}\ k_\nu\ B_\nu(T)}, \tag{5.9}$$

where $\Omega_{\rm A}$ is the beam solid angle, μ_{H_2} is the molecular weight per hydrogen molecule, and $m_{\rm H}$ is the hydrogen atom mass. When rearranged in useful units, Equation 5.9 yields

$$N_{H_2} = 2.02 \times 10^{20}\ {\rm cm^{-2}} (e^{1.439\ (\lambda/{\rm mm})^{-1} (T/10\ {\rm K})^{-1}} - 1) \left(\frac{k_\nu}{0.01\ {\rm cm^2\ g^{-1}}}\right) \left(\frac{S_\nu^{\rm beam}}{\rm mJy\ beam^{-1}}\right)^{-1} \left(\frac{\theta_{\rm HPBW}}{10\ {\rm arcsec}}\right)^{-2} \left(\frac{\lambda}{\rm mm}\right)^{-3}, \tag{5.10}$$

where the dust opacity k_ν is 0.0182 cm^2 g^{-1}, the telescope beam $\theta_{\rm HPBW}$ is 15 arcsec, and the wavelength of the observations λ is 850 μm.

The dust opacity adopted in the calculation of the H_2 column density comes from Ossenkopf and Henning (1994), where an H-density of 10^6 cm^{-3} and dust with thin ice-mantles coagulating for 10^5yr were assumed. The adopted dust temperatures are 10, 15, and 20 K. The dust opacities and dust temperature comply with the standard assumptions made by the c2d collaboration. The dust emission is provided by ground-based sub-millimeter observations at 850 μm from the SCUBA-2 camera at the James Clerck Maxwell Telescope as part of the proposal ID M16AL001 (Herczeg *et al.*, 2017).

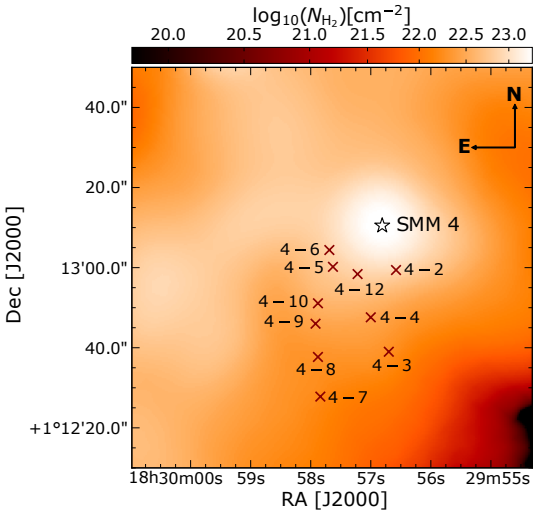

FIGURE 5.C.1: H_2 column density map of SVS 4, calculated from the SCUBA-2 dust emission map at 850 μm from Herczeg *et al.* (2017), assuming $T_{\rm dust} = 15$ K. The crosses indicate the position of the SVS 4 stars and of SMM 4.

6

Linking ice and gas in the λ Orionis Barnard 35A cloud

G. Perotti[1], J. K. Jørgensen[1], H. J. Fraser[2], A.N. Suutarinen[2], L. E. Kristensen[1], W. R. M. Rocha[1], P. Bjerkeli[3], K. M. Pontoppidan[4]

[1] Niels Bohr Institute & Centre for Star and Planet Formation, University of Copenhagen, Øster Voldgade 5−7, 1350 Copenhagen K., Denmark
[2] School of Physical Sciences, The Open University, Walton Hall, Milton Keynes, MK7 6AA, United Kingdom
[3] Department of Space, Earth, and Environment, Chalmers University of Technology, Onsala Space Observatory, 439 92 Onsala, Sweden
[4] Space Telescope Science Institute, 3700 San Martin Drive, Baltimore, MD 21218, USA

Submitted to Astronomy & Astrophysics

Abstract

Context. Dust grains play an important role in the synthesis of molecules in the interstellar medium, from the simplest species such as H_2 to complex organic molecules. How some of these solid-state molecules are converted into gas-phase species is still a matter of debate.

Aims. To directly compare ice and gas abundances of methanol (CH_3OH) and carbon monoxide (CO), obtained from near-infrared (2.5−5 μm) and millimeter (1.3 mm) observations, and to investigate the relationship between ice, dust and gas in low-mass protostellar envelopes.

Methods. We present Submillimeter Array (SMA) and Atacama Pathfinder EXperiment (APEX) observations of gas-phase CH_3OH ($J_K = 5_K - 4_K$), ^{13}CO and $C^{18}O$ ($J = 2-1$) towards the multiple protostellar system IRAS 05417+0907 located in the B35A cloud, λ Orionis region. We use archival IRAM 30 m data and AKARI H_2O, CO and CH_3OH ice observations towards the same target to compare ice

and gas abundances and directly calculate CH_3OH and CO gas-to-ice ratios.

Results. The CO isotopologues emissions are extended, whereas the CH_3OH emission is compact and traces the giant molecular outflow emanating from IRAS 05417+0907. A discrepancy between sub-millimeter dust emission and H_2O ice column density is found for B35A−4 and B35A−5, similar to what has previously been reported.

Conclusions. The difference between the submillimeter continuum emission and the infrared H_2O ice observations suggests that the distributions of dust and H_2O ice differ around the young stellar objects in this dense cloud. The reason for this may be that the two sources are located in different environments resolved by the interferometric observations: B35A−5 is located in a shocked region plausibly affected by sputtering and heating impacting the submillimeter dust emission pattern, while B35A−4 is situated in a more quiescent part of the cloud. Gas and ice maps are essential to connect small-scale variations in the ice composition with large-scale astrophysical phenomena probed by gas observations.

6.1 INTRODUCTION

The interaction between dust, ice and gas is ubiquitous in star-forming regions and it is essential for the synthesis of interstellar molecules, the main ingredients for the origin of life on Earth. In the last decades the number of detected molecules in the interstellar medium (ISM) increased considerably (McGuire, 2018) and with it, the awareness of an interplay between solid and gaseous molecules in star-forming regions (Herbst and van Dishoeck, 2009; Boogert *et al.*, 2015; Jørgensen *et al.*, 2020; Öberg and Bergin, 2021). Some of the questions remained to be answered are what is the link between the distribution of solids (dust, ices) and gaseous molecules in molecular clouds, and what does this tell us about the solid-gas intertwined chemistries (e.g., thermal and non-thermal desorption mechanisms releasing solid-state molecules into the gas-phase and vice versa).

Desorption mechanisms are of utmost importance to understand some critical aspects of star- and planet-formation (van Dishoeck and Blake, 1998). Besides enhancing the chemical complexity in the gas-phase (Cazaux *et al.*, 2003; Jørgensen *et al.*, 2016; Bergner *et al.*, 2017; Calcutt *et al.*, 2018; Manigand *et al.*, 2020; van Gelder *et al.*, 2020), the positions in protostellar disks at which they occur (i.e., snow-lines), influences the formation and evolution of planets (Öberg *et al.*, 2011b; Eistrup *et al.*, 2016; van 't Hoff *et al.*, 2017; Grassi *et al.*, 2020). Simultaneously, desorption processes can also shape the composition of grain surfaces. This is a consequence of the fact that all desorption mechanisms are much more efficient for volatile species (CO, O_2, N_2; Bisschop *et al.*, 2006; Noble *et al.*, 2012; Cazaux *et al.*, 2017) than for less volatile species (H_2O, CH_3OH; Fraser *et al.*, 2001; Bertin *et al.*, 2016; Cruz-Diaz *et al.*, 2016; Martín-Doménech *et al.*, 2016). Since thermal desorption mechanisms alone can often not account for the diversity of species observed in star-forming regions, a further question remains open as to the extent that the prevailing physical conditions might impact ice loss,

e.g. through photo-desorption, sputtering, chemical- and shock-induced processes (e.g., Kristensen *et al.*, 2010; Vasyunin and Herbst, 2013; Dulieu *et al.*, 2013; Öberg, 2016; Dartois *et al.*, 2019). Obtaining key insights on the desorption mechanisms is crucial to study the composition of ice mantles, and hence the production of complex organics, during the early phases of star-formation.

The preferred observational approach to constrain solid-state chemistry consists of inferring abundances of solid-state molecules based on their observed gas-phase emissions (Bergin and Tafalla, 2007; Öberg *et al.*, 2009a; Whittet *et al.*, 2011). Although this method of indirectly deriving ice abundances from gas-phase observations is the most used to get insights into the ice composition, it relies on major assumptions, for instance on the formation pathways and the desorption efficiency of solid-state species.

One way to test these assumptions is to combine ice and gas observations (i.e., ice- and gas-mapping techniques) and thus compare ice abundances with gas abundances towards the same region (Noble *et al.*, 2017; Perotti *et al.*, 2020). The evident advantage of combining the two techniques is that it enables us to study the distribution of gas-phase and solid-state molecules concurrently on the same lines of sight, and hence to address how solid-state processes are affected by physical conditions probed by gas phase-mapping such as density, temperature and radiation field gradients, turbulence and dust heating. However, the number of regions where such combined maps are available is still limited.

In this article we explore the interplay between ice and gas in the bright-rimmed cloud Barnard 35 (B35A; also known as BRC18, SFO18 and L1594) located in the λ Orionis star-forming region (Sharpless, 1959; Lada and Black, 1976; Murdin and Penston, 1977; Mathieu, 2008; Hernández *et al.*, 2009; Bayo *et al.*, 2011; Barrado *et al.*, 2011; Kounkel *et al.*, 2018; Ansdell *et al.*, 2020) at a distance of 410 ± 20 pc (GAIA DR2; Zucker *et al.*, 2019; Zucker *et al.*, 2020). The λ Orionis region is characterized by a core of OB stars enclosed in a ring of dust and gas (Wade, 1957; Heiles and Habing, 1974; Maddalena and Morris, 1987; Zhang *et al.*, 1989; Lang *et al.*, 2000; Dolan and Mathieu, 2002; Sahan and Haffner, 2016). The OB stars formed approximately 5 Myr ago, whereas the ring formation is less certain, occurring between 1 and 6 Myr ago due to a supernova explosion (Dolan and Mathieu, 1999; Dolan and Mathieu, 2002; Kounkel, 2020). The presence of strong stellar winds from the massive stars and ionization fronts in the region has shaped and ionized the neighboring ring of gas leading to the formation of dense molecular clouds (e.g., B35A, B30; Barrado *et al.*, 2018) and photodissociation regions (PDRs; Wolfire *et al.*, 1989; De Vries *et al.*, 2002; Lee *et al.*, 2005). For instance, the stellar wind from λ Orionis, the most massive star of the Collinder 69 cluster (an O8III star; Conti and Leep, 1974), hits the western side of B35A compressing the cloud and forming a PDR between the molecular cloud edge and the extended HII region S264 (De Vries *et al.*, 2002; Craigon, 2015).

Star formation is currently occurring in B35A: the multiple protostellar system IRAS 05417+0907 (i.e., B35A–3) lies within the western side of the cloud (Figure 6.1.1). IRAS 05417+0907 was long thought to be a single source but it is a cluster of at least four objects (B35A–2, B35A–3, B35A–4

and B35A−5) which were partially resolved by *Spitzer* IRAC observations as part of the *Spitzer* c2d Legacy survey[1] (Evans *et al.*, 2014; Table 6.2.1). B35A−3 (i.e., IRAS 05417+0907) is a Class I YSO and it is the primary of a close binary system (Connelley *et al.*, 2008); the classification of the other sources remains uncertain. B35A−3 is emanating a giant bipolar molecular outflow extending in the NE/SW direction relative to λ Orionis and terminating in the Herbig-Haro object HH 175 (Myers *et al.*, 1988; Qin and Wu, 2003; Craigon, 2015; Reipurth, 2000). A detailed multi-wavelength analysis and characterization of HH 175 and of the multiple protostellar system presented by Reipurth and Friberg (2021).

[1] https://irsa.ipac.caltech.edu/data/SPITZER/C2D/cores.html

The ice reservoir towards the YSOs in B35A has been extensively studied by Noble *et al.* (2013) and Noble *et al.* (2017) and Suutarinen (2015a). These works were based on near-infrared spectroscopic observations (2.5−5 μm) with the AKARI satellite. In Noble *et al.* (2013), H_2O, CO_2 and CO ice features were identified towards all four YSOs, whereas Suutarinen (2015a) performed a multi-component, multi-line fitting of all the ice features towards the same B35A sources identified by Noble *et al.* (2013) and Evans *et al.* (2014), and in a method similar to that employed by Perotti *et al.* (2020) were able to extract the H_2O, CO and CH_3OH ice column densities concurrently from the spectral data. It is these ice column densities that are used for comparison in the remainder of this paper.

In parallel, the morphology and kinematics of the gas in B35A has been investigated using single-dishes such as the *James Clerck Maxwell Telescope* (JCMT) and the *Institut de RadioAstronomie Millimétrique* (IRAM) 30 m telescope by Craigon (2015). The survey mapped ^{12}CO, ^{13}CO and $C^{18}O$ J=3−2 and J=2−1 over a 14.6′× 14.6′ region and confirmed the existence of a bright and dense rim along the western side of B35A, heated and compressed by the stellar wind of the nearby λ Orionis, and of a giant bipolar outflow emanating from the YSO region.

To investigate the interaction between the solid (ice) and gas phases in the region, ice maps of B35A were compared to gas-phase maps in Noble *et al.* (2017). From the combination of ice- and gas-mapping techniques, no clear correlation was found between gas or dust to ice towards B35A. The local scale variations traced by the ice-mapping were not immediately related to large scale astrophysical processes probed by the dust and gas observations.

In this paper, we present interferometric Submillimeter Array (SMA) observations of the $J_K = 5_K - 4_K$ rotational band of CH_3OH at 241.791 GHz and of the J=2−1 rotational bands of two CO isotopologues (^{13}CO and $C^{18}O$) towards the multiple protostellar system IRAS 05417+0907 in B35A. The angular resolution of the interferometric observations allows us to study the distribution of the targeted species in greater spatial detail compared to existing single-dish observations. To also recover the large-scale emission, the SMA observations are combined with single-dish data, thus resolving the protostellar system members and, concurrently probing the surrounding cloud. Furthermore, we produce ice and gas maps of a pivotal complex molecule, CH_3OH, and of one of its precursors, CO, to analyse the gas and ice interplay in the region. Lastly, we directly calculate gas-to-ice ratios of B35A to compare with ratios obtained for nearby star-forming regions.

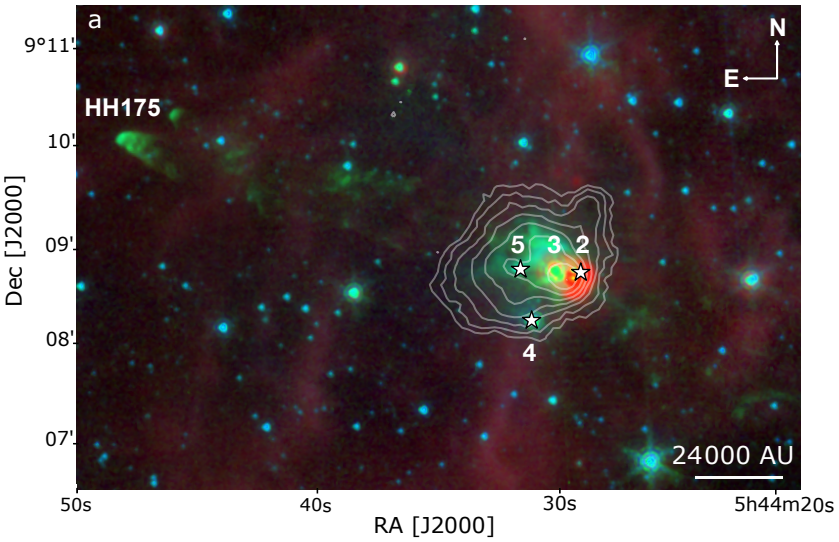

FIGURE 6.1.1: Three-color image of B35A overlaid with SCUBA−2 850 μm density flux in mJy beam^{-1} (Reipurth and Friberg, 2021; contours are in decreasing steps of 30% starting at 7.3 Jy beam^{-1}). The composite is made from *Spitzer* IRAC 3.6 μm (blue), 4.5 μm (green) and MIPS 24.0 μm (red) bands (Program ID: 139, PI: N. J. Evans II). The white stars mark the positions of the AKARI and *Spitzer* c2d identified B35A sources. Connelley *et al.* (2008) and Reipurth and Friberg (2021) show the B35A sources to be multiplet systems totalling 4 or 5 objects.

The article is organized as follows. Section 6.2 describes the gas-phase observations and the archival data used to produce the gas and ice maps. Section 6.3 presents the results of the observations. Section 6.4 analyses the variations between the gas-phase and solid-state distributions of the different molecules. Section 6.5 discusses the observational results with a particular focus on the obtained gas-to-ice ratios. Finally, Section 6.6 summarizes the main conclusions.

6.2 OBSERVATIONS AND ARCHIVAL DATA

6.2.1 *SMA and APEX observations*

The sample of sources was observed on September 19, 2018 with the *Submillimeter Array* (SMA; Ho *et al.*, 2004). The array was in its subcompact configuration with 7 operating antennas. The targeted region was covered by two overlapping pointings; the first pointing was centered on B35A−3 (i.e., IRAS 05417+0907) and the second was offset by one half primary beam to the south-east. Their exact coordinates are α_{J2000} = 05^{h}44^{m}30^{s}.00, δ_{J2000} = +09°08′57.″3 and α_{J2000} = 05^{h}44^{m}30^{s}.58, δ_{J2000} = +09°08′33.″8, respectively.

The SMA observations probed frequencies spanning from 214.3 to 245.6 GHz with a spectral resolution of 0.1 MHz (0.135 km s^{-1}). Among other species this frequency range covers the CH_3OH $J_K = 5_K - 4_K$ branch at 241.791 GHz, ^{13}CO J = 2−1 at 220.398 GHz and C^{18}O J = 2−1 at 219.560 GHz (Table 6.2.2). The observational setup consisted of a first long integration on the bandpass calibrator, the strong quasar 3c84, followed by alternated integrations on the source and on the gain calibrator, the quasar J0510+180. The absolute flux scale was obtained through observations of Uranus. The SMA data set was both calibrated and imaged using CASA[2] (McMullin *et al.*,

[2] http://casa.nrao.edu/

TABLE 6.2.1: Sample of sources.

Object[a]	RA [J2000]	DEC [J2000]	A_V [mag]
B35A–2	05:44:29.30	+09:08:57.0	52.7[b]
B35A–3	05:44:30.00	+09:08:57.3	54.9 ± 0.2[c]
B35A–4	05:44:30.85	+09:08:26.0	49.6 ± 2.3[c]
B35A–5	05:44:31.64	+09:08:57.8	19.5 ± 1.5[c]

Notes. [a] The objects are numbered according to the ID used in Noble *et al.* (2013). In Noble *et al.* (2017), objects 2, 3, 4, 5 are numbered 11, 1, 6 and 12, respectively. [b] For a detailed description of the A_V determination for B35A–2 see Section 6.3.3 and Appendix 6.B. [c] From the *Spitzer* c2d catalog[4].

TABLE 6.2.2: Spectral data of the detected molecular transitions.

Transition	Frequency[a] [GHz]	A^a_{ul} [s^{-1}]	g^a_u	E^a_u [K]	n^b_{cr} [cm^{-3}]
$C^{18}O$ $J = 2 - 1$	219.560	6.01×10^{-7}	5	15.9	9.3×10^3
^{13}CO $J = 2 - 1$	220.398	6.04×10^{-7}	5	15.9	9.4×10^3
CH_3OH $J = 5_0 - 4_0$ E^+	241.700	6.04×10^{-5}	11	47.9	5.5×10^5
CH_3OH $J = 5_1 - 4_1$ E^-	241.767	5.81×10^{-5}	11	40.4	4.8×10^5
CH_3OH $J = 5_0 - 4_0$ A^+	241.791	6.05×10^{-5}	11	34.8	5.0×10^5
CH_3OH $J = 5_1 - 4_1$ E^+	241.879	5.96×10^{-5}	11	55.9	4.9×10^5
CH_3OH $J = 5_2 - 4_2$ E^-	241.904	5.09×10^{-5}	11	60.7	4.2×10^5

Notes. [a] From the Cologne Database for Molecular Spectroscopy (CDMS; Müller *et al.* (2001)) and the Jet Propulsion Laboratory catalog (Pickett *et al.*, 1998). [b] Calculated using a collisional temperature of 20 K and collisional rates from the Leiden Atomic and Molecular Database (LAMDA; Schöier *et al.*, 2005). The references for the collisional rates are Yang *et al.* (2010) for the CO isotopologues and Rabli and Flower (2010) for CH_3OH.

2007). At these frequencies, the typical SMA beam-sizes were 7.″3 × 2.″4 with a position angle of -32.2° for CH_3OH, and 7.″9 × 2.″6 with a position angle of -31.2° for ^{13}CO and $C^{18}O$.

To trace the more extended structures in the region, the SMA data were complemented by maps obtained using the *Atacama Pathfinder EXperiment* (APEX; Güsten *et al.*, 2006) on August 20–22, 2018. The single-dish observations covered frequencies between 236–243.8 GHz, matching the SMA 240 GHz receiver upper side band. The spectral resolution of the APEX observations was 0.061 MHz (0.076 km s^{-1}). The APEX map size was 100″ × 125″ and it extended over both SMA primary beams. The coordinates of the APEX pointing are $\alpha_{J2000} = 05^h44^m30^s.00$, $\delta_{J2000} = +09°08'57.''3$. The APEX beam size was 27.″4 for the CH_3OH $J_K = 5_K - 4_K$ lines emission. The APEX data set was reduced using the GILDAS package CLASS[3]. At a later stage, the reduced APEX data cube was imported to CASA and combined with the interferometric data using the feathering technique. A description of the combination procedure is given in Appendix 6.A.1.

[3] http://www.iram.fr/IRAMFR/GILDAS

6.2.2 *JCMT/SCUBA-2, Spitzer IRAC, 2MASS, IRAM 30 m and AKARI data*

Ancillary data to the SMA and APEX observations were adopted in this study. To construct H_2 column density maps of B35A, we used submillimeter continuum maps at 850 μm obtained with the SCUBA−2 camera at the *James Clerk Maxwell Telescope* (JCMT) by Reipurth and Friberg (2021), visual extinction values from the *Spitzer* c2d catalog[4] and 2MASS and *Spitzer* IRAC photometric data (Skrutskie *et al.*, 2006; Evans *et al.*, 2014). *Institut de RadioAstronomie Millimétrique* (IRAM) 30 m telescope observations (Craigon, 2015) were used to trace the extended emission for ^{13}CO and C^{18}O $J = 2–1$. Finally, to produce gas-ice maps of B35A we made use of the ice column densities determined by Suutarinen (2015a), from *AKARI* satellite observations.

[4] https://irsa.ipac.caltech.edu/data/SPITZER/C2D/cores.html

6.3 RESULTS

This section lists the observational results, supplying a summary of the methods employed to determine CO and CH_3OH gas column densities (Section 6.3.1 and Appendix 6.A). Additionally, it presents the H_2O, CO and CH_3OH ice column densities (Section 6.3.2) and the two H_2 column density maps used in the calculation of the abundances of the ice and gas species (Sect. 6.3.3).

6.3.1 *Gas-phase species*

The spectral line data of the detected molecular transitions are listed in Table 6.2.2. Figures 6.3.1–6.3.3 display moment 0 maps of the ^{13}CO and C^{18}O J=2−1 lines and CH_3OH J=5_0-4_0 A$^+$ line, using SMA, IRAM 30 m and APEX data. Moment 0 maps of the CH_3OH J=$5_0 - 4_0$ A$^+$ line are presented in this section as this transition is the brightest of the CH_3OH J=$5_K - 4_K$ branch at 241.791 GHz. The maps show that the SMA observations filter out spatially extended emission related to the B35A cloud. The SMA data only recover ≈10% of the extended emission detected in the single-dish data. Thus, consequently we need to combine the interferometric data with the single-dish maps in order not to underestimate the column densities severely.

Panels (a) of Figures 6.3.1–6.3.2 show that the interferometric emission is predominantly compact and the peak intensity is seen, for both CO isotopologues, at the location of B35A−2. The emission observed in the IRAM 30 m data sets (panels (b) of Figures 6.3.1–6.3.2) is extended and mostly concentrated around B35A−2, B35A−3 and B35A−5. In the combined SMA + IRAM 30 m maps (panels (c) of Fig. 6.3.1–6.3.2) the peak emission is also located in the region where B35A−2, B35A−3 and B35A−5 are present.

In contrast, the observed CH_3OH peak intensity is exclusively localized at the B35A−5 position in the SMA data (panel (a) of Fig. 6.3.3). B35A−5 lies along the eastern lobe of the giant bipolar molecular outflow emanated from IRAS 05417+0907 (i.e., B35A−3) and terminating at the location of the Herbig-Haro object HH 175 (Craigon, 2015). The CH_3OH emission is extended in the APEX data (panel (b) of Fig. 6.3.3) and hence not resolved

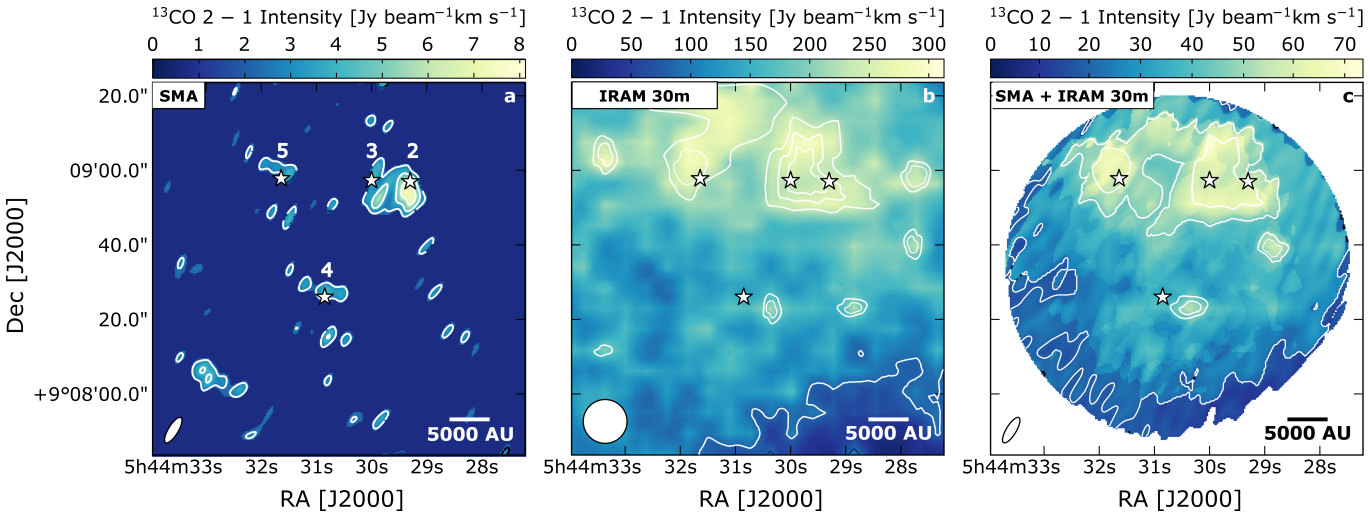

FIGURE 6.3.1: Integrated intensity maps for ^{13}CO J=2–1 detected by the SMA (a), by the IRAM 30 m telescope (b), and in the combined interferometric SMA and single-dish IRAM 30 m data (c). All lines are integrated between 7 and 16 km s^{-1}. Contours are at 5σ, 10σ, 15σ, etc. ($\sigma_{\rm SMA}$= 0.42 Jy beam^{-1}km s^{-1}, $\sigma_{\rm IRAM\ 30\ m}$= 6 Jy beam^{-1}km s^{-1}, $\sigma_{\rm SMA+IRAM\ 30\ m}$= 1.03 Jy beam^{-1}km s^{-1}). In panel (c), the white area outlines the primary beam of the SMA observations. The synthesized beams are displayed in white in the bottom left corner of each panel. The white stars mark the position of the targeted B35A sources.

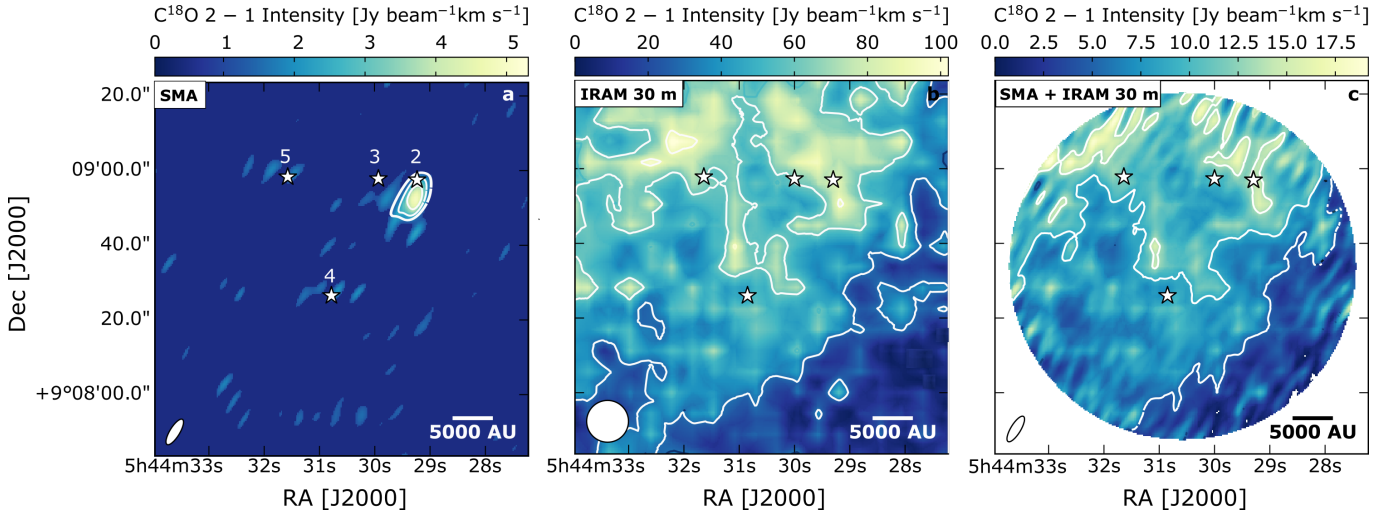

FIGURE 6.3.2: Integrated intensity maps for $C^{18}O$ J=2 – detected by the SMA (a), by the IRAM 30 m telescope (b), and in the combined interferometric SMA and single-dish IRAM 30 m data (c). All lines are integrated between 10 and 15 km s^{-1}. Contours are at 5σ, 10σ, 15σ ($\sigma_{\rm SMA}$= 0.37 Jy beam^{-1}km s^{-1}, $\sigma_{\rm IRAM\ 30\ m}$= 5 Jy beam^{-1}km s^{-1}, $\sigma_{\rm SMA+IRAM\ 30\ m}$= 0.40 Jy beam^{-1}km s^{-1}). In panel (c), the white area outlines the primary beam of the SMA observations. The synthesized beams are displayed in white in the bottom left corner of each panel. The white stars mark the position of the targeted B35A sources.

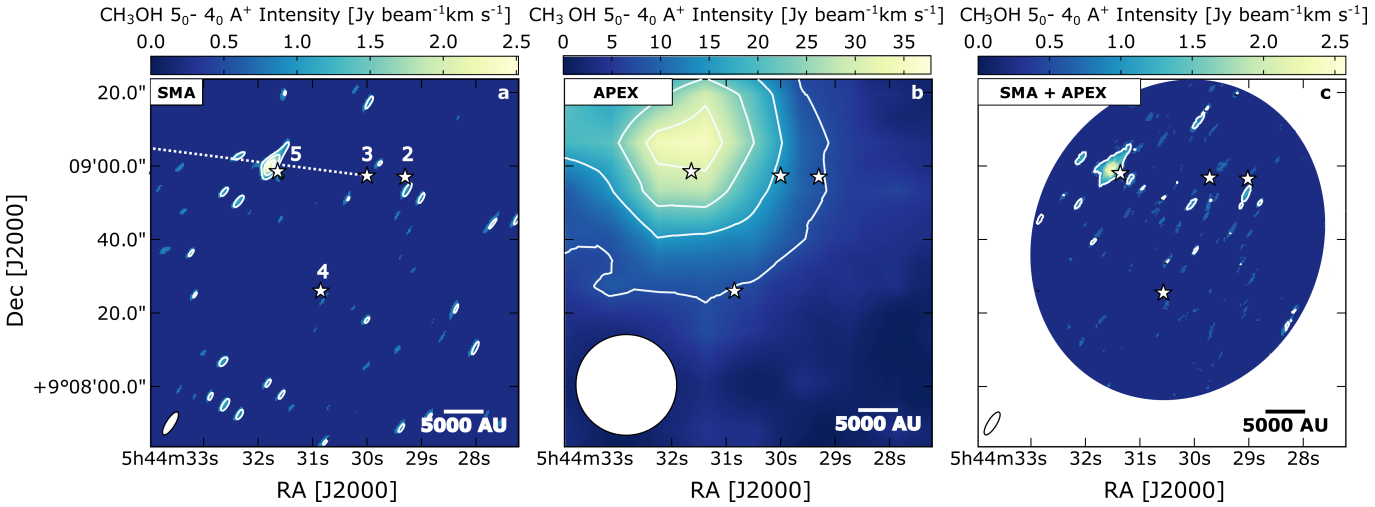

FIGURE 6.3.3: Integrated intensity maps for CH_3OH J=5_0 – 4_0 A^+ detected by the SMA (a), by the APEX telescope (b), and in the combined interferometric SMA and single-dish APEX data (c). All lines are integrated between 6 and 12.5 km s^{-1}. Contours start at 5σ (σ_{SMA}= 0.04 Jy $beam^{-1}$km s^{-1}, σ_{APEX}= 4 Jy $beam^{-1}$km s^{-1}, $\sigma_{SMA+APEX}$= 0.04 Jy $beam^{-1}$km s^{-1}) and follow a step of 5σ. In panel (c), the white area outlines the primary beam of the SMA observations. The synthesized beams are displayed in white in the bottom left corner of each panel. The white stars mark the position of the targeted B35A sources and the blue dotted line indicates the direction of the giant outflow terminating in HH 175.

TABLE 6.3.1: Total ice and gas column densities towards the B35A sources.

Object	$N^{\rm ice}_{\rm H_2O\ tot}$	$N^{\rm ice}_{\rm CO\ tot}$	$N^{\rm ice}_{\rm CH_3OH\ tot}$	$N^{\rm gas}_{\rm C^{18}O\ tot}$	$N^{\rm gas}_{\rm ^{12}CO\ tot}$	$N^{\rm gas}_{\rm CH_3OH\ tot}$	$^{\dagger}N^{\rm SCUBA-2}_{\rm H_2}$	$N^{A_V}_{\rm H_2}$
	$[10^{18}{\rm cm}^{-2}]$	$[10^{18}{\rm cm}^{-2}]$	$[10^{18}{\rm cm}^{-2}]$	$[10^{15}{\rm cm}^{-2}]$	$[10^{18}{\rm cm}^{-2}]$	$[10^{14}{\rm cm}^{-2}]$	$[10^{22}{\rm cm}^{-2}]$	$[10^{22}{\rm cm}^{-2}]$
B35A–2	2.96 ± 0.13	0.34 ± 0.03	0.26 ± 0.03	9.38 ± 1.92	5.22 ± 1.07	...	1.76 ± 0.09	7.22*
B35A–3	2.96 ± 0.12	0.32 ± 0.03	0.16 ± 0.03	7.02 ± 1.44	3.91 ± 0.80	...	1.69 ± 0.08	7.52 ± 0.02
B35A–4	3.35 ± 0.11	0.28 ± 0.06	0.10 ± 0.06	4.99 ± 1.03	2.78 ± 0.57	...	0.39 ± 0.02	6.79 ± 0.68
B35A–5	0.78 ± 0.12	< 0.18	< 0.18	7.11 ± 1.46	3.96 ± 0.81	1.91 ± 0.24	1.09 ± 0.05	2.66 ± 0.20

Notes. Columns 2–4 display the ice column densities from Suutarinen (2015a). Columns 5–7 list the gas column densities for $T_{\rm rot}$= 25 K. The errors are estimated based on the rms noise of the spectra and on the ~20% calibration uncertainty. Non-detections are indicated by "...". † $N^{\rm SCUBA-2}_{\rm H_2}$ is calculated using $T_{\rm dust}$= 25 K. The errors are calculated from the 5% flux calibration uncertainty. * The uncertainty on the A_V and consequently on the $N^{A_V}_{\rm H_2}$ for B35–2 is not estimated because this object is not detected in the J, H and K bands.

at one particular source position. The emission in the SMA + APEX moment 0 map (panel (c) of Fig. 6.3.3) is compact and concentrated in one ridge in the proximity of B35A–5. The channel maps (Figures 6.A.3–6.A.5) and the spectra (Figure 6.A.1) extracted from the combined interferometric and single-dish data sets show predominantly blue-shifted components (Appendix 6.A.3). Blue- and red-shifted components are seen for the CO isotopologues, which were previously observed by De Vries *et al.* (2002), Craigon (2015) and Reipurth and Friberg (2021) and attributed to outflowing gas.

The ^{13}CO emission is optically thick towards the B35A sources, therefore the ^{13}CO column densities are underestimated towards the targeted region (Appendix 6.A.2). Consequently, the optically thin C^{18}O emission is adopted to estimate the column density of ^{12}CO in B35A. First, C^{18}O column densities towards the protostellar system members are obtained from the integrated line intensities of the combined SMA + IRAM 30 m maps (panels (c) of Figure 6.3.2), assuming optically thin emission and a kinetic temperature for the YSO region equal to 25 K (Craigon, 2015). The formalism adopted in the column density calculation is presented in Appendix 6.A.4, whereas the calculated C^{18}O column densities and their uncertainties are listed in Table 6.3.1. The C^{18}O column densities are converted to ^{12}CO column densities assuming a ^{16}O/^{18}O isotope ratio of 557 ± 30 (Wilson, 1999). The resulting ^{12}CO column densities (Table 6.3.1) are in good agreement with the values reported in Craigon (2015).

The CH_3OH column density towards B35A–5 is estimated from the integrated line intensities of the combined SMA + APEX maps for the five CH_3OH lines (Table 6.A.2), assuming optically thin CH_3OH emission, a kinetic temperature of 25 K (Craigon, 2015) and local thermodynamic equilibrium (LTE) conditions. The CH_3OH column density and its uncertainty is reported in Table 6.3.1. For all the gas-phase species, the uncertainty on the column densities is estimated based on the spectral rms noise and on the ~20% calibration uncertainty.

6.3.2 *Ice column densities*

The ice column densities of H_2O, CO and CH_3OH made use of in this paper were originally derived by Suutarinen (2015a) from the AKARI (2.5–5 μm) NIR spectra of the targeted B35A sources. Suutarinen (2015a) adopted a non-heuristic approach, employing ice laboratory data and analytical functions to concurrently account for the contribution of a number of molecules to the observed ice band features. A detailed description of the AKARI observations is given in Noble *et al.* (2013) and the methodology adopted to derive the column densities of the major ice species can be found in Suutarinen (2015a).

The total ice column densities from Suutarinen (2015a) are listed in Table 6.3.1. Among the three molecules, H_2O ice is the most abundant in the ices of B35A, with column densities up to 3.35×10^{18} cm^{-2}, followed by CO and CH_3OH (Table 6.3.1). The column densities of the latter two molecules are comparatively one order of magnitude less abundant than H_2O ice. Upper limits are given for the CO and CH_3OH column densities

towards B35A–5 because of difficulties in distinguishing the absorption features in the spectrum of this YSO (Noble *et al.*, 2013; Suutarinen, 2015a). A trend is observed for the CO and CH_3OH values: the column densities towards B35A–2 are the highest reported, followed by B35A–3, B35A–4 and B35A–5. The CO and CH_3OH ice column densities appear to follow the visual extinction with B35A–2 and B35A–3 being the most extincted sources and showing the highest CO and CH_3OH column densities (Tables 6.2.1 & 6.3.1). In this regard, it is important to recall that B35A–2 is not detected in the J, H and K bands, making the determination of its visual extinction uncertain (Section 6.3.3 and Appendix 6.B).

6.3.3 H_2 column densities

An important factor to consider when combining ice- and gas-mapping techniques is that ice absorption and dust and gas emissions may probe different spatial scales (Noble *et al.*, 2017). As a matter of fact, the targeted sources may be embedded to different depths in the B35A cloud and consequently, the gas and ice observations may not be tracing the same columns of material. Therefore, the search for gas-ice correlations towards B35A has to be performed by comparing gas and ice abundances relative to H_2, following the approach adopted in Perotti *et al.* (2020).

To keep the gas and ice observations in their own reference frame, two H_2 column density maps are produced: one to derive gas abundances and one to determine ice abundances (Figure 6.3.4). For the gas observations, estimates of the H_2 column density are made using submillimeter continuum maps of B35A at 850μm (SCUBA–2; Reipurth and Friberg, 2021), under the assumption that the continuum emission is originated from optically thin thermal dust radiation (Kauffmann *et al.*, 2008). In this regime, the strength of the submillimeter radiation is dependent on the column density (N), the opacity (κ_ν) and the dust temperature (T). The adopted value for the opacity per unit dust+gas mass at 850 μm is 0.0182 cm^2 g^{-1} ("OH5 dust"; Ossenkopf and Henning, 1994). The temperature of B35A has been estimated by Morgan *et al.* (2008) and Craigon (2015). Both studies found two distinct regimes within the cloud: a cold region ($T_{\rm gas}$ = 10 – 20 K, $T_{\rm dust}$ = 18 K) in the shielded cloud interior to the east of the YSOs and a warm region ($T_{\rm gas}$ = 20 – 30 K) to the west of the YSOs. Since the region where the YSOs are located lies close to the warm cloud western edge, a $T_{\rm dust}$ = 25 K is adopted to estimate the H_2 column density map illustrated in Figure 6.3.4 (a) based on Craigon (2015) and Reipurth and Friberg (2021). The H_2 column density towards the B35A sources is reported in Table 6.3.1. The error on the H_2 column density was estimated according to the 5% flux calibration uncertainty (Dempsey *et al.*, 2013). Increasing the dust temperature to 30 K would lower the H_2 column density by 22% and consequently increase the abundance of the gas-phase species by the same amount – while lowering the dust temperature to 18 K would increase the H_2 column density by 61% and consequently lowering the gas abundance likewise.

The above estimates assume an excitation temperature equal to 25 K for CO and CH_3OH. Increasing both the excitation temperature and the dust temperature to 30 K would result in gas abundances increasing by 24%.

Conversely, lowering both temperatures to 18 K, would lower the abundances by 33%. A comprehensive description of the production of the H_2 column density map from SCUBA−2 measurements is given in Appendix C of Perotti *et al.* (2020).

The H_2 column density map calculated from the SCUBA−2 measurements supplies an accurate estimate of the total beam-averaged amount of gas towards B35A, and therefore provides a useful reference for the optically thin gas-phase tracers. However, the derived H_2 column density map can not directly be related to the AKARI data that supply (pencil-beam) measurements of the column densities towards the infrared sources that may or may not be embedded within the B35A cloud.

For the ice observations, the H_2 column density map is therefore obtained by performing a linear interpolation of the tabulated visual extinction (A_V) values for B35A taken from the *Spitzer* c2d catalog[5] (see Appendix 6.B). Since no calculated A_V values are reported for B35A−2 and B35A−3, the A_V for B35A−3 is acquired by de-reddening the spectral energy distribution (SED) at the 2MASS J, H, K photometric points to fit a blackbody and using a second blackbody to model the infrared excess at longer wavelengths. A detailed description of the fitting procedure adopted for B35A−3 is given in

[5] https://irsa.ipac.caltech.edu/data/SPITZER/C2D/cores.html

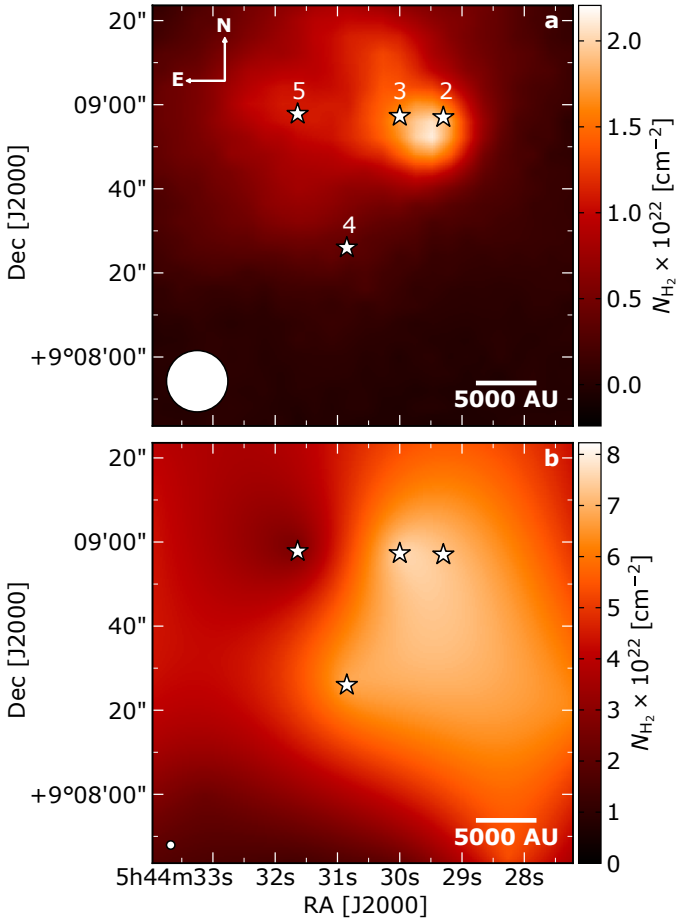

FIGURE 6.3.4: H_2 column density maps of B35A. *a*: N_{H_2} map calculated from SCUBA−2 dust emission at 850 μm (Reipurth and Friberg, 2021). *b*: N_{H_2} map calculated from the visual extinction. The synthesized beams are displayed in white in the bottom left corner of each panel. The white stars mark the positions of the targeted B35A sources.

Appendix 6.B. Following Evans *et al.* (2009) and Chapman *et al.* (2009) we adopt an extinction law for dense interstellar medium gas with $R_V = 5.5$ from Weingartner and Draine (2001) to calculate A_V. The visual extinction for B35A–2 could not be estimated through a similar procedure due to the lack of near-IR photometry data available for this object, thus the A_V for this source is obtained through the interpolation of the available visual extinction measurements for B35A. The final A_V values of the four sources are listed in Table 6.2.1. Finally, the visual extinction is converted to H_2 column density using the relation: $N_{\mathrm{H_2}} = 1.37 \times 10^{21}$ cm^{-2} (A_V/mag) established for dense interstellar medium gas (Evans *et al.*, 2009). The H_2 column density calculated from the A_V map is shown in Figure 6.3.4 (b).

The H_2 column densities calculated from both methods are of the same order of magnitude, 10^{22} cm^{-2} (Table 6.3.1). The column densities differ by approximately a factor of 4 possibly due to variations in the exact column densities traced by SCUBA–2 and A_V measurements and assumptions on the dust temperature. In both H_2 column density maps (Fig. 6.3.4 a and b), it is seen that the four sources lie in the densest region of the cloud, confirming the results previously presented in Craigon (2015) and Reipurth and Friberg (2021). Although the two maps were calculated using two different methods, they reproduce the same trend: B35A–2 and B35A–3 are located where the H_2 column density peaks, whereas B35A–4 and B35A–5 are situated in less dense regions. However, in the H_2 column density map calculated from the visual extinction (Fig. 6.3.4 b), lower $N_{\mathrm{H_2}}$ values are reported for B35A–5 with respect to the other YSOs, whereas this is not the case in the H_2 column density map calculated from the SCUBA–2 map (Fig. 6.3.4 a) where lower $N_{\mathrm{H_2}}$ values are observed for B35A–4. This difference can be explained by recalling that B35A–5 is the less extincted YSO ($A_V = 19.5$ mag) and it is located along the trajectory of the giant outflow launched by B35A–3. Consequently, the SCUBA–2 observations (14.6″ beam) are likely tracing the more extended structure of the dust emission in the region and not resolving the more compact emission towards each individual objects. It is worth observing that embedded protostars and Herbig-Haro objects can substantially affect the dust emission morphology (Chandler and Carlstrom, 1996), hence, the $N_{\mathrm{H_2}}$ enhancement seen in Figure 6.3.4 (a) likely reflects dust heating by the embedded protostars and by HH175 resulting in an increase of the submillimeter continuum flux, rather than in an higher column density.

6.4 ANALYSIS

6.4.1 *Gas-ice maps*

In Figure 6.4.1, the distributions of gas-phase ^{13}CO 2–1 (panel a) and C^{18}O 2–1 (panel b) emissions are compared to CO ice abundances. Both CO isotopologue emissions are concentrated at the B35A–2, B35A–3, B35A–5 source positions. The emission towards these three sources is of comparable intensity but it drops in the surroundings of B35A–4 and especially towards the southern edge of the cloud. The CO ice abundances with respect to H_2 are not characterized by large variations, instead, they are quite uniform

TABLE 6.4.1: Ice and gas abundances relative to H_2 towards the B35A sources.

Object	$X^{ice}_{H_2O}$	X^{ice}_{CO}	$X^{ice}_{CH_3OH}$	$X^{gas}_{^{12}CO}$	$X^{gas}_{CH_3OH}$
	$[10^{-5}]$	$[10^{-5}]$	$[10^{-5}]$	$[10^{-4}]$	$[10^{-8}]$
B35A–2	4.10 ± 0.18	0.47 ± 0.04	0.36 ± 0.04	2.97 ± 0.63	...
B35A–3	3.99 ± 0.16	0.43 ± 0.04	0.21 ± 0.04	2.31 ± 0.49	...
B35A–4	4.93 ± 0.52	0.41 ± 0.50	0.15 ± 0.09	7.13 ± 1.50	...
B35A–5	2.93 ± 0.50	< 0.68	< 0.68	3.63 ± 0.76	1.75 ± 0.24

Notes. The column densities employed in the determination of the ice and gas abundances of H_2O, CO and CH_3OH are listed in Table 6.3.1. The abundances of the gaseous species are obtained using $N^{SCUBA-2}_{H_2}$, whereas the abundances of the ice species are relative to $N^{A_V}_{H_2}$ (Table 6.3.1). "..." mark the non-detections of gas-phase CH_3OH.

and consistent within the uncertainties (Table 6.4.1). Only an upper limit could be determined for the CO ice column density towards B35A–5, due to the uncertainty in distinguishing the absorption feature at 3.53 μm in the spectrum of this object.

In Figure 6.4.1 (c), the distribution of gas-phase CH_3OH 5_0–4_0 A^+ emission is compared to CH_3OH ice abundances. As described in Section 6.3.1, the CH_3OH emission is concentrated solely in one ridge, located in proximity of the B35A–5 position. At this location only an upper limit on the CH_3OH ice abundance could be determined. The morphology of the CH_3OH emission suggests that while B35A–5 is situated in a shocked region, sitting along the trajectory of the giant outflow, B35A–4 lies in a more quiescent area, less influenced by high-velocity flows of matter. The CH_3OH ice abundances with respect to H_2 are characterized by slightly larger variations compared to CO ice (Table 6.4.1).

Finally, in Figure 6.4.1 (d), the distribution of gas-phase CH_3OH 5_0–4_0 A^+ emission is compared to H_2O ice abundances. The H_2O ice abundances are approximately one order of magnitude higher than the CO and CH_3OH ice abundances (Table 6.4.1). The lowest H_2O ice abundance is reported towards B35A–5 where the CH_3OH peak emission is observed. In contrast, the highest H_2O ice abundance is obtained towards B35A–4, where CH_3OH emission is not detected.

6.4.2 *Gas and ice variations*

In Figure 6.4.2, the search for gas-ice correlations towards B35A is addressed by analysing gas and ice abundances relative to H_2 (Table 6.4.1). The y-axes of all three panels display CO gas abundances, which are compared to abundances of CO ice (panel a), CH_3OH ice (panel b) and H_2O ice (panel c). To maintain gas and ice observations in their own reference frame, the CO gas abundances have been estimated using N_{H_2} calculated from SCUBA–2 850 μm maps, whereas the ice abundances have been calculated using N_{H_2} obtained from the visual extinction map (see Section 6.3.3 and Appendix 6.B). The formalism adopted to propagate the uncertainty from

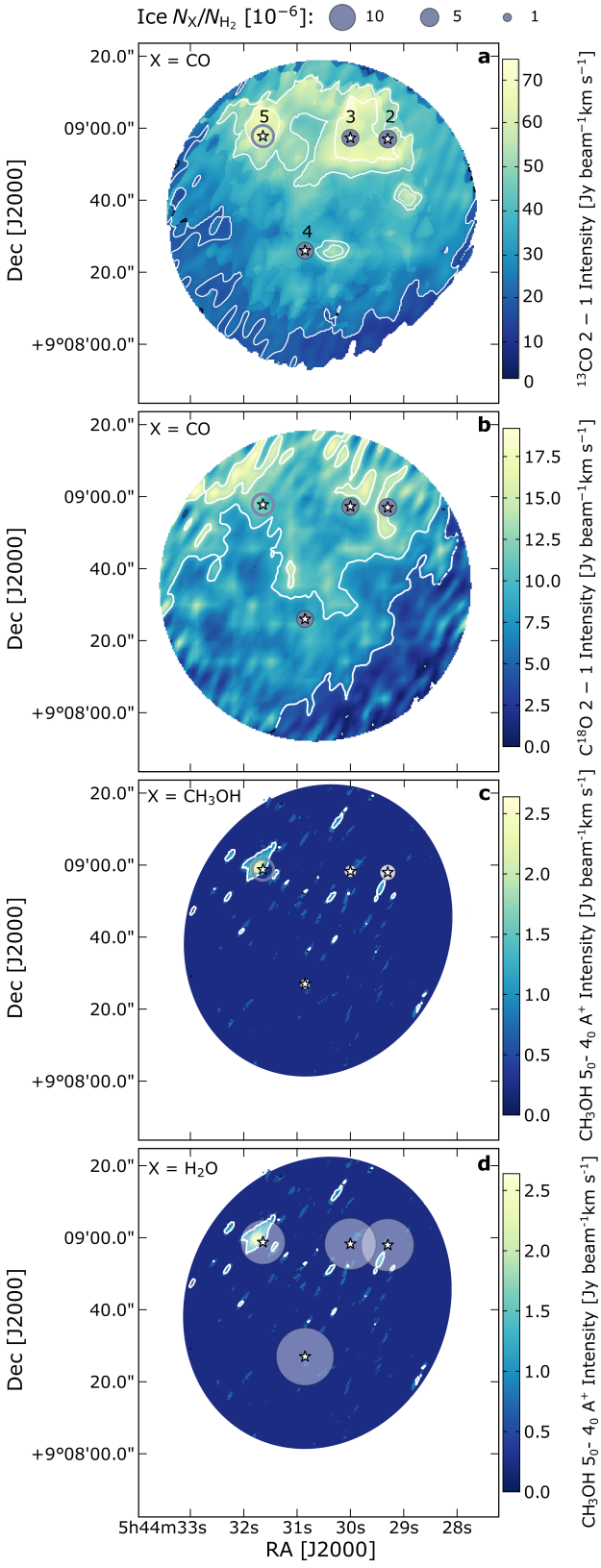

FIGURE 6.4.1: Gas-ice maps of B35A. Ice abundances are indicated as filled grey (panels a,b) or white circles (panels c and d), upper limits are displayed as empty circles. Contour levels are 5σ, 10σ, 15σ. *a:* CO ice abundances on gas ^{13}CO 2–1; *b:* CO ice abundances on gas C^{18}O 2–1 ; *c:* CH_3OH ice abundances on gas CH_3OH $5_0 - 4_0$ A^+. *d:* H_2O ice abundances on gas CH_3OH $5_0 - 4_0$ A^+. The white area outlines the primary beam of the SMA observations. The white stars mark the position of the targeted B35A sources.

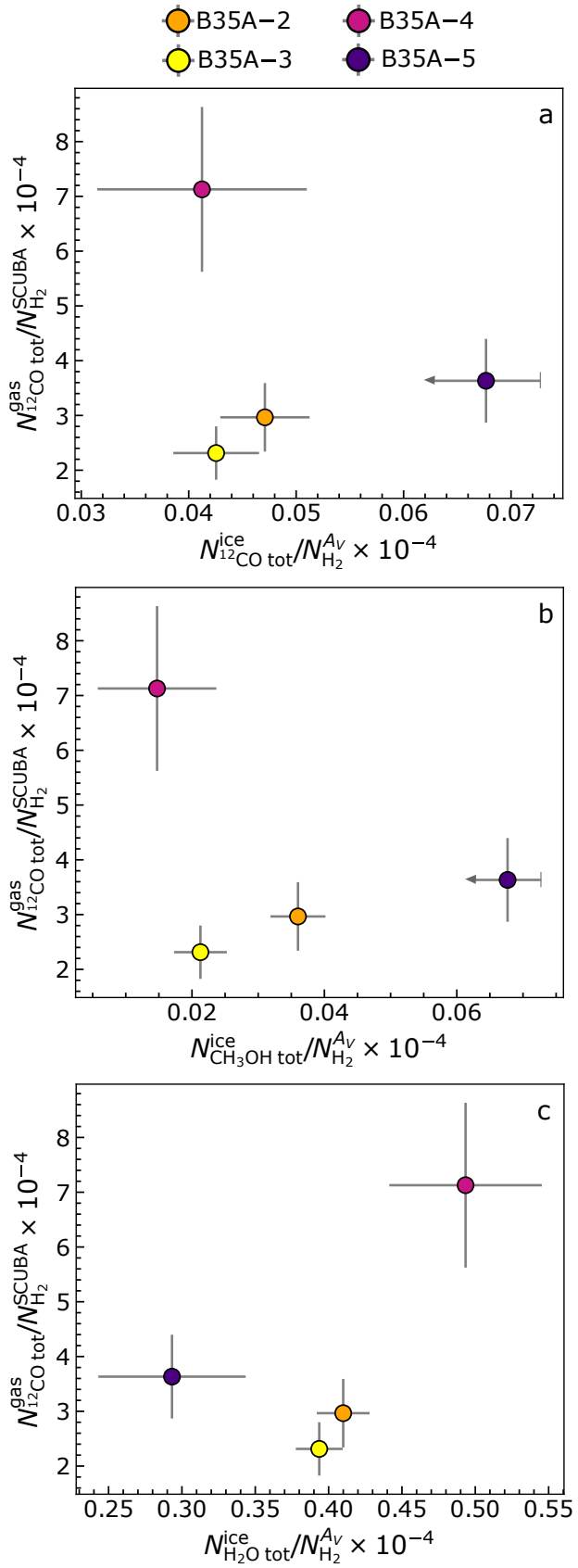

FIGURE 6.4.2: Gas and ice variations in B35A. The circles represent the targeted B35A sources. Panels (a) – (c) show the relation between CO, CH_3OH, and H_2O ice and CO gas abundances relative to H_2.

the column densities to the abundances is reported in Appendix 6.A.4.

It can be immediately noted that none of the ice species exhibits a predictable trend in ice abundance with gas abundance. Panels (a) and (b) show a similar behaviour since they are comparing molecules chemically linked - CO gas versus CO ice and CO gas vs CH_3OH ice being CO the precursor of CH_3OH. At the same time, panel (c) does not display the same relationships seen in the previous two panels. The latter observation is not surprising since there are no reasons for CO and H_2O to be directly linked from a purely chemical perspective.

In both panels (a) and (b) of Figure 6.4.2, B35A−4 displays the highest CO gas and the lowest CO and CH_3OH ice abundances. When the uncertainties are taken into account, the CO ice abundances towards B35A−2, B35A−3 and B35A−4 are alike (Table 6.4.1). For the CH_3OH ice abundances, B35A−3 and B35A−4 are consistent within the error bars, only towards B35A−2 a significant difference is found. Both CO and CH_3OH ice abundances towards B35A−5 are upper limits (Table 6.4.1). The similarity between CO and CH_3OH ice trends and the fact that the CH_3OH/CO ice ratios are > 0.3 indicates an efficient CH_3OH formation through CO hydrogenation (Watanabe and Kouchi, 2002) on the grain surfaces of B35A. The CO gas abundances towards B35A−2, B35A−3 and B35A−5 are in agreement within the uncertainties (Table 6.4.1).

In panels (c) some of the gas-ice variations differ with respect to panels (a) and (b): B35A−4 is characterized by the highest H_2O ice abundance, whereas B35A−5 shows the lowest H_2O ice abundance. This result corroborates the prediction that the ices of B35A−5 are the most depleted of volatile molecules among the B35A sources. The behaviours of B35A−2 and B35A−3 are similar if the uncertainties are considered (Table 6.4.1). The observed ice and gas variations between CO gas, CH_3OH gas and H_2O ice towards B35A−4 and B35A−5 favour a scenario in which H_2O ice is formed and predominantly resides on the ices of B35A−4, likely located in the most "quiescent" area of the targeted region, whereas in the proximity of a shocked region (B35A−5), H_2O ice mantles are partially desorbed. This result is discussed further in Sect. 6.5.1. Although the gas and ice variations analysed in this Section and in Sect. 6.4.1 are based on a small sample, they still highlight interesting trends in accordance to what we would expect from our knowledge of the physical structure of the targeted region.

6.4.3 *Comparison with previous gas-ice maps of B35A*

Noble *et al.* (2017) produced the first gas-ice maps of B35A. They compared AKARI ice abundances from Noble *et al.* (2013) with single-dish (JCMT/HARP and IRAM 30 m/HERA) gas-phase maps of $C^{18}O$ (Buckle *et al.*, 2009; Craigon, 2015; J=3−2 and 2−1), submillimeter continuum SCUBA maps at 850 μm, 450 μm/850 μm (Di Francesco *et al.*, 2008) and Herschel/SPIRE maps at 250 μm (Griffin *et al.*, 2010). The H_2 gas-phase map adopted to calculate ice abundances was determined from CO observations (Craigon, 2015).

Noble *et al.* (2013) and Noble *et al.* (2017) derived their ice column densities without considering the presence of CH_3OH, thus the H_2O ice

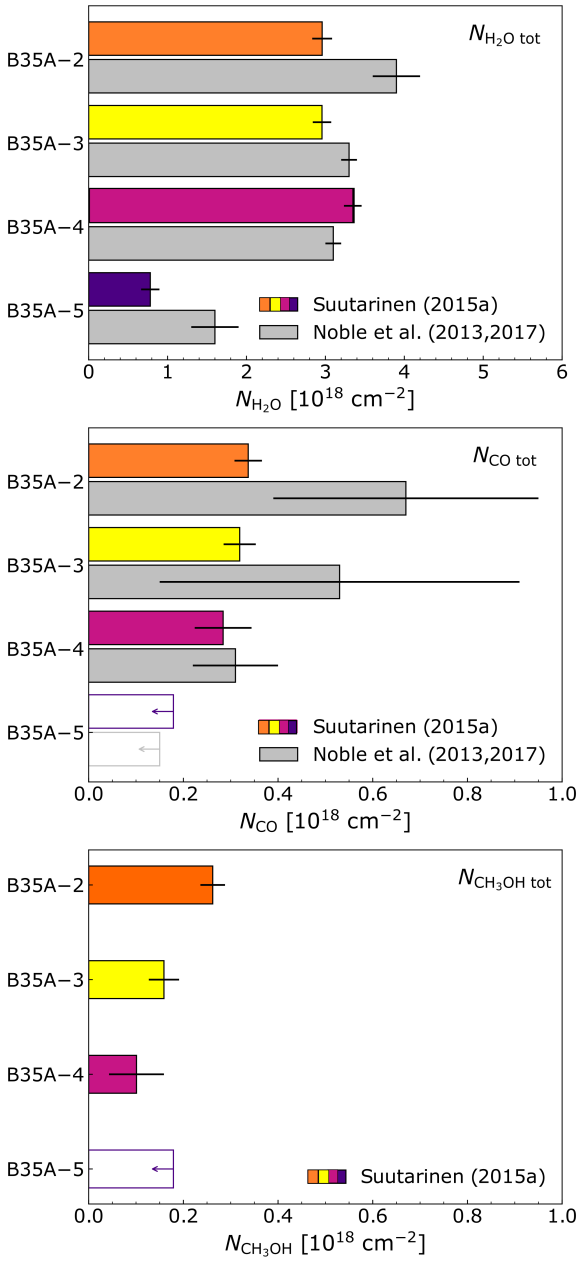

FIGURE 6.4.3: H_2O (top), CO (middle) and CH_3OH (bottom) total ice column densities obtained in Suutarinen (2015a) (the sources are colour-coded) compared to Noble *et al.* (2017) (light grey). The empty bars represent upper limits on the column densities.

column densities were routinely higher than those used here from Suutarinen (2015a) (Figure 6.4.3). Simultaneously, the CO ice column densities were calculated using different laboratory data (e.g., the CO-ice red component was fitted using a CO:H_2O (Fraser and van Dishoeck, 2004) laboratory spectrum as opposite to the CO:CH_3OH mixture (Cuppen *et al.*, 2011), resulting in higher CO-ice column density compared to Suutarinen (2015a).

The combination of gas, dust and ice observations proposed in Noble *et al.* (2017) is characterized by a number of limitations which are taken into account in the presented work. The lower angular resolution of the adopted single-dish observations, the analysis of the chemical behaviours of simple molecules only (e.g., H_2O, CO and CO_2) and the avoidance to consider that

the ice and gas observations might probe different depths are some of them. The presented work overcomes these limitations by making use of higher angular resolution interferometric observations, studying the ice and gas variations of both simple (H_2O, CO) and complex molecules (CH_3OH) and lastly, by comparing ice and gas abundances derived using two different H_2 column density maps (to keep the ice and gas observations in their own reference frame).

From the analysis of the gas-ice maps, Noble *et al.* (2017) inferred that the dust in B35A is mainly localized around B35A−2 and B35A−3, in agreement with the higher ice column densities of H_2O and CO towards these two sources (Figure 6.4.3). However, they observed that the H_2O ice column densities are lower towards B35A−5 compared to B35A−4, even though the dust emission is higher towards B35A−5. The authors concluded that no clear trend is seen between ice, dust and gas in B35A and that more knowledge of the local-scale astrophysical environment is needed to disentangle the exact interplay between ice and gas in the region. The findings of Noble *et al.* (2017) are in agreement with the observational results and the gas-ice maps of B35A presented here (with the caveat that both CO ice abundances towards B35A−5 in Noble *et al.* (2017) and in this work are upper limits). However, the gas-ice maps produced in this study allow to explain that the lower H_2O ice abundance towards B35A−5 compared to B35A−4 is plausibly caused by the influence of shocks on the ice chemistry. CH_3OH is a tracer of energetic inputs in the form of outflows (Kristensen *et al.*, 2010; Suutarinen *et al.*, 2014), and it traces the trajectory of the bipolar outflow in B35A. As a result, lower H_2O ice abundances towards B35A−5 are likely the result of sputtering effects in the outflow shocks (e.g., Suutarinen *et al.*, 2014 and references therein). Simultaneously, the fact that the submillimeter dust emission towards B35A−5 is high where the H_2O ice abundances are lower can also be explained by the presence of the outflow terminating in the HH object 175. In fact, UV radiation generated in the Herbig-Haro object itself may locally heat the dust, enhancing the sub-millimeter continuum flux of the region (Chandler and Carlstrom, 1996; Kristensen *et al.*, 2010; Figure 6.3.4 *a*).

6.5 DISCUSSION

The CH_3OH gas abundances in B35A (10^{-8}) are greater than what could be inferred by pure gas-phase synthesis (e.g., Garrod and Herbst, 2006). Hence, the observed CH_3OH gas must be produced on the grain surfaces and be desorbed afterwards. In the following, the preferred scenario for CH_3OH desorption in B35A is discussed. Additionally, the observational results presented in Sections 6.3.1–6.3.2 are employed to determine CH_3OH and CO gas-to-ice ratios (N_{gas}/N_{ice}) towards the multiple protostellar system in B35A. Finally, a comparison between the gas-to-ice ratios directly determined towards B35A and the gas-to-ice ratios of nearby star-forming regions is proposed.

6.5.1 *Sputtering of CH_3OH in B35A*

In Sections 6.3.1 and 6.4.1, it is seen that the CH_3OH emission is concentrated almost exclusively in one ridge, which coincides with the B35A–5 position. B35A–5 sits along the eastern lobe of a large collimated outflow emanated from the binary Class I IRAS 05417+0907 (i.e, B35A–3). The eastern lobe has a total extent of 0.6 pc and it terminates into the Herbig-Haro object HH 175 (Craigon, 2015). The total extent of the outflow is 1.65 pc (Reipurth and Friberg, 2021), which places HH 175 among the several dozens HH objects with parsec dimensions (Reipurth and Bally, 2001). Herbig-Haro objects are omnipresent in star-forming regions, but it is still not clear how exactly they are tied into the global star-formation process, e.g., how do they alter the morphology and kinematics of the gas in which they originate. These are highly energetic phenomena which are believed to form when high-velocity protostellar jets collide with the surrounding molecular cloud, inducing shocks. Such shocks compress and heat the gas, generating UV radiation (Neufeld and Dalgarno, 1989). The activity of Herbig-Haro objects can dramatically change the chemical composition of the gas in their vicinity, mutating the chemistry of the region during so-called sputtering processes (Neufeld and Dalgarno, 1989; Hollenbach and McKee, 1989).

Sputtering takes place in shocks when neutral species (e.g., H_2, H or He) collide with the surface of ice-covered dust grains with sufficient kinetic energy to expel ice species (e.g., CH_3OH, NH_3, H_2O) into the gas phase (Jørgensen *et al.*, 2004; Jiménez-Serra *et al.*, 2008; Kristensen *et al.*, 2010; Suutarinen *et al.*, 2014; Allen *et al.*, 2020). During a sputtering event, the ice molecules can desorb intact or be destroyed (e.g., via dissociative desorption) either due to the high kinetic energy or by reactions with H atoms (Blanksby and Ellison, 2003; Dartois *et al.*, 2019; Dartois *et al.*, 2020). The fragments of dissociated molecules can then readily recombine in the gas-phase (Suutarinen *et al.*, 2014 and references therein).

The inferred dust temperatures in the B35A region (20–30 K) are remarkably lower than the CH_3OH sublimation temperature (~128 K; Penteado *et al.*, 2017), excluding thermal desorption as potential mechanism triggering the observed CH_3OH emission. This consideration, together with the observation of the CH_3OH emission along the HH 175 flow direction and the anticorrelation between CH_3OH emission and the lower H_2O ice abundances towards B35A–5 suggests that ice sputtering in shock waves is a viable mechanism to desorb ice molecules in B35A. Simultaneously, the absence of shocks towards B35A–4 likely explains the highest abundance of H_2O ice observed in this more quiescent region (Figure 6.4.1 d). Higher angular resolution observations of CH_3OH in the region are required to provide quantitative measurements of the amount of CH_3OH desorbed via sputtering compared to other non-thermal desorption mechanisms. Additional gas-phase observations of H_2O towards the B35A sources are needed to constrain further the processes linking H_2O ice and H_2O gas in this shocked region (e.g., sputtering of H_2O ice mantles versus direct H_2O gas-phase synthesis) and, in a broader context to contribute explaining the high abundances of H_2O observed in molecular outflows (Nisini *et al.*, 2010; Bjerkeli *et al.*, 2012; Bjerkeli *et al.*, 2016; Santangelo *et al.*, 2012; Vasta *et al.*, 2012; Dionatos

et al., 2013).

6.5.2 *Gas-to-ice ratios*

Figure 6.5.1 displays the CH_3OH (panel a) and CO (panel b) gas-to-ice ratios towards ten sources constituting the SVS 4 cluster located in the Serpens molecular cloud (Perotti *et al.*, 2020) and towards the B35A sources in the Orion molecular cloud. The shaded areas indicate the estimated ranges of gas-to-ice ratios towards both molecular clouds, providing complementary information of the gas-to-ice ratios of both regions compared to the value calculated towards each individual source.

Figure 6.5.1 (a) shows the CH_3OH gas-to-ice ratios ($N_{CH_3OH_{gas}}/N_{CH_3OH_{ice}}$) towards the SVS 4 sources and B35A–5. Only an upper limit for the CH_3OH gas-to-ice towards B35A–5 is obtained (i.e, 1.1×10^{-3}) due to the uncertainty on the CH_3OH ice column density determination towards this source (Suutarinen, 2015a). Therefore, only limited information is available on the CH_3OH chemistry in B35A. Figure 6.5.1 (a) also displays the averaged CH_3OH gas-to-ice ratio towards four low-mass embedded protostars located in nearby star-forming regions from Öberg *et al.* (2009a). A detailed comparison between the CH_3OH gas-to-ice ratios for the SVS 4 cluster members and the value estimated by Öberg *et al.* (2009a) is given in Perotti *et al.* (2020), and therefore not repeated here.

The observations of B35A address cold quiescent CH_3OH emission (J= 5_K-4_K transitions at 241.7 GHz and E_u from 34.8 to 60.7 K, see Table 6.2.2) and presumably quiescent gas not affected by outflow shocks and/or thermally desorbed in the vicinity of the protostar. The same applies to the observations presented in Öberg *et al.* (2009a) (J= 2–1 transitions at 96.7 GHz and E_u in the range 14.4–35.4 K). However, B35A–5 and the SVS 4 sources reporting the highest gas-to-ice ratios are likely affected to some extent by outflow shocks (i.e., B35A–5 by the giant outflow terminating in HH 175 and the SVS 4 sources by the outflow notoriously associated to SMM 4). This might justify the mismatch between Öberg *et al.* (2009a) value and the higher values of the gas-to-ice ratios. In the case of the B35A cloud, high-sensitivity infrared observations of B35A are required to constrain further this observation.

CO gas-to-ice ratios ($N_{CO_{gas}}/N_{CO_{ice}}$) towards the SVS 4 and B35A sources are illustrated in Figure 6.5.1 (b). As discussed previously in Perotti *et al.* (2020), the range of gas-to-ice ratios for SVS 4 extends between 1 and 6 and it is significantly higher than the predicted value (~4×10^{-2}; Cazaux *et al.*, 2016). This theoretical prediction is estimated from the three-phase astrochemical model by Cazaux *et al.* (2016) which includes thermal and non-thermal desorption processes of the species constituting the ice mantles. This comparison with the theoretical prediction has to be taken with care, since the physical model is not specifically tuned to reproduce the structures of the SVS 4 cluster or the B35A cloud. The estimated dust temperature towards the SVS 4 cluster is below 20 K (Kristensen *et al.*, 2010), indicating that CO is likely frozen out on the grain surfaces in this temperature range. We concluded from the high relative CO gas abundances that the gas-mapping is not tracing the densest regions of the SVS 4 cluster but an extended

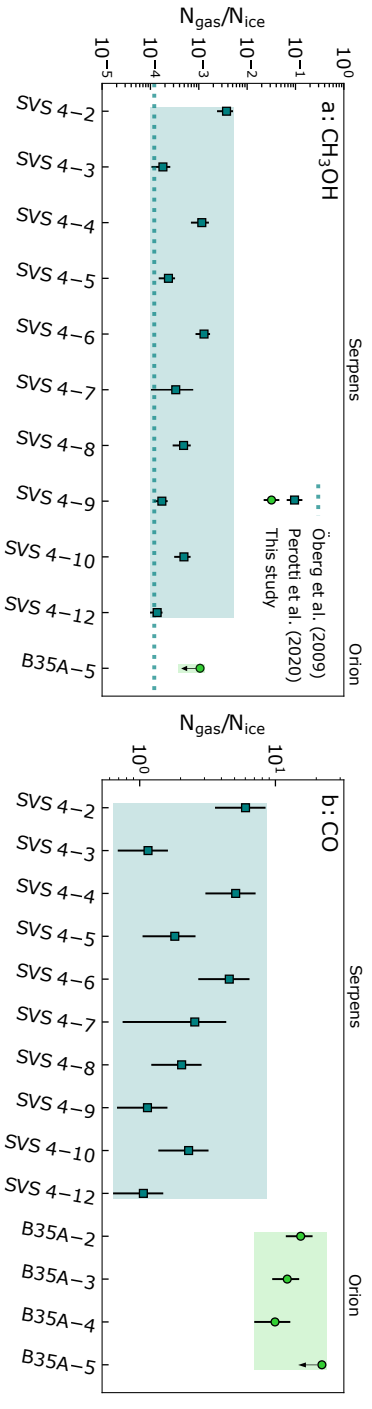

FIGURE 6.5.1: CH_3OH (panel a) and CO (panel b) gas-to-ice ratios (N_{gas}/N_{ice}) for the multiple protostellar system in Orion B35A and Serpens SVS 4. The dark green squares indicate the gas-to-ice ratios estimated by Perotti *et al.* (2020) for the Serpens SVS 4 cluster. The light green circles mark the ratios calculated in this study. The dotted light blue line in panel (a) represents the ratio estimated by Öberg *et al.* (2009a) towards Class 0/1 objects. The shaded areas indicate the estimated ranges of the gas-to-ice ratios.

component that is not sensitive to the effect of freeze-out (Figure 8 of Perotti *et al.*, 2020).

High CO gas-to-ice ratios are also observed for B35A, but in this case they are mainly attributable to CO thermally desorbed in the region. The physical conditions of B35A and SVS 4 differ significantly, for example, the western side of B35A is highly influenced by the ionization-shock front driven by the λ Orionis OB stars and the dust temperature in the YSOs region of B35A has been estimated to be at least 25–30 K (Craigon, 2015; Morgan *et al.*, 2008). Therefore, at these temperatures, above the CO sublimation temperature (~20 K; Bisschop *et al.*, 2006; Collings *et al.*, 2004; Acharyya *et al.*, 2007), CO is efficiently thermally desorbed from the grain surfaces and it is expected to primarily reside in the gas-phase. According to this result, the observed CH_3OH ice might have formed at earlier stages, prior to the warm-up of the dust grains or alternatively, from CO molecules trapped in porous H_2O matrices, and therefore not sublimated at these temperatures. Additionally, higher abundances of CO might reflect an active CO gas-phase synthesis in the region. Follow-up observations of higher J transitions of CO isotopologues are required to provide a conclusive assessment.

6.6 CONCLUSIONS

Millimetric (SMA, APEX, IRAM 30 m) and infrared (AKARI) observations are used to investigate the relationships between ice, dust and gas in the B35A cloud, associated with the λ Orionis region. Gas and ice maps are produced to compare the distribution of solid (H_2O, CO and CH_3OH) and gaseous (^{13}CO, $C^{18}O$ and CH_3OH) molecules and to link the small-scale variations traced by ice observations with larger-scale astrophysical phenomena probed by gas observations. The main conclusions are:

- The CO isotopologues emission is extended in B35A, whereas the observed CH_3OH emission is compact and centered in the vicinity of B35A–5. B35A–5 sits along the trajectory of the outflow emanated from IRAS 05417+0907 (i.e., B35A–3), thus the observed gas-phase CH_3OH may be plausibly explained by sputtering of ice CH_3OH in the outflow shocks.
- The dust column density traced by the submillimeter emission is not directly related to the ice column inferred from the infrared observations. The submillimeter dust emission is stronger towards B35A–5 compared to B35A–4, however the H_2O ice column density is higher for B35A–4. This discrepancy is understood by taking into account that B35A–5 is situated in a shocked region affected by the presence of the Herbig-Haro object HH175 – and thus likely influenced by sputtering and heating affecting the observed submillimeter dust emission pattern.
- None of the ice species shows a predictable trend in ice abundance with gas-phase abundance. This implies that inferring ice abundances from known gas-phase abundances and vice versa is inaccurate without an extensive knowledge of the physical environment of the targeted region.
- The high CO gas-to-ice ratios suggest that the CO molecules are efficiently thermally desorbed in B35A. This is supported by dust temper-

ature estimates (25−30 K) towards the B35A sources above the CO sublimation temperature (~20 K).

- Simultaneously, the dust temperatures in the region are significantly lower than the CH_3OH sublimation temperature (128 K), excluding thermal desorption as the mechanism responsible for the observed CH_3OH emission.
- The combination of gas- and ice observations is essential to comprehend the relationships at the interface between solid and gas phases, and hence to link the small-scale variations detected in the ice observations with large-scale phenomena revealed by gas-phase observations.

The presented work is a preparatory study for future JWST + ALMA observations, which will shed further light on the dependencies of gas-to-ice ratios on the physical conditions of star-forming regions. In fact, future mid-infrared facilities, among all JWST, will considerably increase the number of regions for which ice maps are available. Such high-sensitivity ice maps can be then combined with ALMA observations, to provide better constraints on the complex interplay between ice, dust and gas during the earliest phases of star-formation. The present study already shows that such gas-ice maps will be valuable, given that they probe ice- and gas-phase chemistries to a greater extent than by ice- or gas-maps alone.

ACKNOWLEDGEMENTS

The authors wish to thank Bo Reipurth for fruitful discussions on HH 175 and Alison Craigon, Zak Smith, Jennifer Noble for providing the reduced IRAM 30 m data. The authors also wish to acknowledge the anonymous reviewer for the careful reading of the manuscript and the useful comments. This work is based on observations with the Submillimeter Array, Mauna Kea, Hawaii, program code: 2018A-S033, with the Atacama Pathfinder Experiment, Llano Chajnantor, Chile, program code: 0102.F-9304. The Submillimeter Array is a joint project between the Smithsonian Astrophysical Observatory and the Academia Sinica Institute of Astronomy and Astrophysics and is funded by the Smithsonian Institution and the Academia Sinica. The Atacama Pathfinder EXperiment (APEX) telescope is a collaboration between the Max Planck Institute for Radio Astronomy, the European Southern Observatory, and the Onsala Space Observatory. Swedish observations on APEX are supported through Swedish Research Council grant No 2017-00648. The study is also based on data from the IRAM Science Data Archive, obtained by H.J.Fraser with the IRAM 30 m telescope under project ID 088-07. Finally, this work is based on archival data from the AKARI satellite, a JAXA project with the participation of the European Space Agency (ESA). The group of JKJ acknowledges the financial support from the European Research Council (ERC) under the European Union's Horizon 2020 research and innovation programme (grant agreement No 646908) through ERC Consolidator Grant "S4F". The research of LEK is supported by research grant (19127) from VILLUM FONDEN. HJF gratefully acknowledges the support of STFC for Astrochemistry at the OU under grant Nos ST/P000584/1 and ST/T005424/1 enabling her participation in this work.

Appendix

6.a PRODUCTION OF GAS-PHASE MAPS

6.A.1 *Interferometric and single-dish data combination*

The combined interferometric (SMA) and single-dish (APEX/IRAM 30 m) data were obtained using CASA version 5.6.1 by executing the CASA task `feather`. The `feathering` algorithm consists of Fourier transforming and scaling the single-dish (lower resolution) data to the interferometric (higher resolution) data. In a second step, the two datasets with different spatial resolution are merged. In this work, APEX short-spacing are used to correct the CH_3OH emission detected by SMA observations, whereas the IRAM 30 m short-spacing are folded into the CO isotopologue emissions observed with the SMA. The combination of the interferometric and single-dish datasets was carried out following the procedure described in Appendix B.1 of Perotti *et al.* (2020) and references therein.

Artefacts might arise when combining interferometric and single dish data. To benchmark our results we have been varying the arguments of the feathering algorithm (e.g., `sdfactor` (scale factor to apply to single dish image), `effdishdiam` (new effective single dish diameter) and `lowpassfiltersd` (filtering out the high spatial frequencies of the single dish image) from the default values. The variations of the above parameters resulted in amplifying the signal close to the primary beam edges by approximately 15%, therefore the default values were chosen.

6.A.2 *Optical depth of the CO isotopologues*

If the emission of the ^{13}CO and C^{18}O isotopologues is co-spatial, the line profiles are similar and the gas ratio abundance ^{12}CO:^{13}CO:C^{18}O is constant, the ^{13}CO optical depth can be assessed from the ^{13}CO and C^{18}O integrated intensity ratio $I(^{13}\mathrm{CO})/I(\mathrm{C}^{18}\mathrm{O})$ using the formalism firstly described by Myers *et al.* (1983) and Ladd *et al.* (1998). The treatment employed here is adapted from Myers *et al.* (1983) and uses formula 6.1 given by e.g., Carlhoff *et al.* (2013) and Zhang *et al.* (2018), relating the integrated intensity ratio of the two isotopologues (Table 6.A.1) and the optical depth τ:

$$\frac{I(^{13}\mathrm{CO})}{I(\mathrm{C}^{18}\mathrm{O})} \approx \frac{1-\exp(-\tau^{^{13}\mathrm{CO}})}{1-\exp(-\tau^{^{13}\mathrm{CO}}/f)}. \tag{6.1}$$

In the above equation $\tau^{^{13}\mathrm{CO}}$ is the ^{13}CO optical depth, and f is the intrinsic ^{13}CO/C^{18}O abundance ratio, which is equal to 7–10 for the Milky Way (Wilson and Matteucci, 1992; Barnes *et al.*, 2015). If f=8 is assumed, to be consistent with the approach adopted in Perotti *et al.* (2020), $\tau^{^{13}\mathrm{CO}}$ is equal to 1.22 for B35A–2, 0.39 for B35–3, 0.47 for B35A–5, and 0.03 for B35–4, indicating ^{13}CO optically thick emission towards three (B35A–2, B35–3 and B35A–5) out of four sources in the B35A cloud as $I(^{13}\mathrm{CO})/I(\mathrm{C}^{18}\mathrm{O})$ is below the intrinsic ratio f for these three sources. The same conclusion is obtained

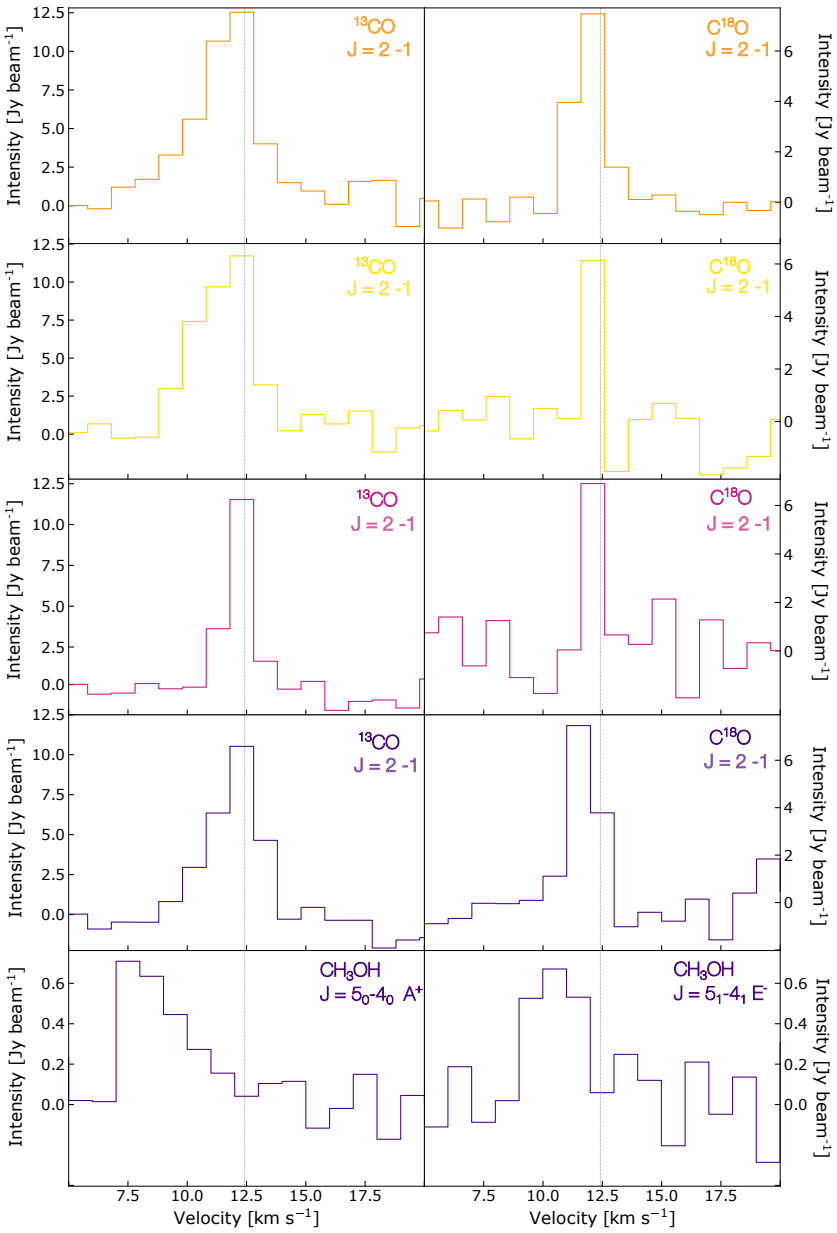

FIGURE 6.A.1: ^{13}CO J=2–1, C^{18}O J=2–1, CH_3OH J=5$_0$–4$_0$ A$^+$ and CH_3OH J=5$_1$–4$_1$ E$^-$ spectra towards the B35A sources detected in the combined interferometric and single-dish data sets. The spectra are colour-coded according to Figure 6.4.2. The cloud velocity (12.42 km s^{-1}) is shown in all spectra with a vertical gray line.

if f=7 or f=10 are assumed. Based on this result, the C^{18}O emission is used to estimate the column densities of ^{12}CO under local thermodynamic equilibrium (LTE) conditions.

6.A.3 *Channel maps and spectra of individual transitions*

Channel maps and spectra for the ^{13}CO J=2–1, C^{18}O J=2–1 and CH_3OH J=5$_0$–4$_0$ A$^+$ detected in the combined interferometric (SMA) and single-dish (IRAM 30m/APEX) data are displayed in Figures 6.A.1, 6.A.3, 6.A.4 and 6.A.5. The CO isotopologue emission is predominantly concentrated towards B35A–2 and B35A–3, whereas the CH_3OH emission is uniquely localized in the vicinity of B35A–5. Blue-shifted components are observed

TABLE 6.A.1: Integrated ^{13}CO and $C^{18}O$ line intensities in units of Jy beam^{-1} km s^{-1} over each source position.

Source	^{13}CO ($J = 2 - 1$)	$C^{18}O$ ($J = 2 - 1$)
B35A–2	70.64 ± 10.59	14.18 ± 2.86
B35A–3	72.36 ± 10.85	10.66 ± 2.17
B35A–4	59.63 ± 8.95	7.55 ± 1.56
B35A–5	70.74 ± 10.61	10.75 ± 2.19

TABLE 6.A.2: Integrated CH_3OH line intensities in units of Jy beam^{-1} km s^{-1} towards B35A–5.

Source	$5_0 - 4_0$ E$^+$	$5_1 - 4_1$ E$^-$	$5_0 - 4_0$ A$^+$	$5_1 - 4_1$ E$^+$	$5_2 - 4_2$ E$^-$
B35A–5	0.27 ± 0.10	0.77 ± 0.18	1.03 ± 0.22	0.29 ± 0.11	0.20 ± 0.09

in combination with broad spectral profiles and wings which deviate from the cloud velocity (12.42 km s^{-1}).

6.A.4 *Derivation of gas-phase column densities*

The column densities of gas-phase species towards the B35A sources were calculated using the integrated intensities of the combined interferometric (SMA) and single-dish (IRAM 30 m/APEX) data (Tables 6.A.1 and 6.A.2). The values inserted in the equations below are listed in Table 6.2.2 and have been taken from the CDMS (Müller *et al.*, 2001), JPL (Pickett *et al.*, 1998) and LAMDA (Schöier *et al.*, 2005) spectral databases. The adopted formalism assumes local thermodynamic equilibrium (LTE) conditions and more specifically, optically thin line emission, homogeneous source filling the telescope beam and that level populations can be described by a single excitation temperature. According to the treatment by Goldsmith and Langer (1999), under the aforementioned conditions, the integrated main-beam temperature $\int T_{\rm MB}\, dv$ and the column density N_u in the upper energy level u are related by:

$$N_u = \frac{8\,\pi\,k_{\rm B}\nu^2}{h\,c^3\,A_{\rm ul}} \int T_{\rm MB}\, dv \tag{6.2}$$

where $k_{\rm B}$ is the Boltzmann's constant, ν is the transition frequency, h is the Planck's constant, c is the speed of light and $A_{\rm ul}$ is the spontaneous Einstein coefficient of the transition. The total column density $N_{\rm tot}$ and the rotational temperature $T_{\rm rot}$ are related to the column density N_u in the upper energy level u (Goldsmith and Langer, 1999) by:

$$\frac{N_u}{g_u} = \frac{N_{\rm tot}}{Q(T_{\rm rot})} e^{-E_u/k_{\rm B}T_{\rm rot}} \tag{6.3}$$

where g_u is the upper level degeneracy, $Q(T_{\rm rot})$ is the rotational partition function, $k_{\rm B}$ is the Boltzmann's constant and E_u is the energy of the upper level u. In summary, the column densities have been calculated using the formalism of Goldsmith and Langer (1999), but assuming a fixed rotational

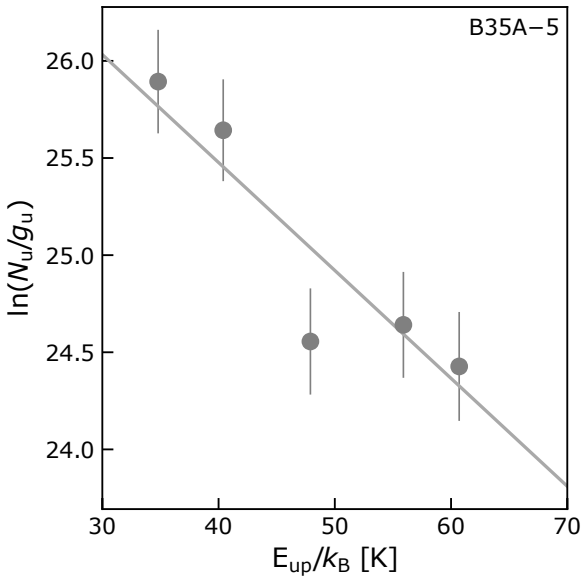

FIGURE 6.A.2: Rotational diagram of CH_3OH for B35A−5. The solid line displays the fixed slope for T_{rot} = 25 K. Error bars are for 1σ uncertainties. The derived column density is shown in Table 6.3.1.

temperature equal to 25 K (Craigon, 2015; Reipurth and Friberg, 2021). Figure 6.A.2 displays the rotational diagram of CH_3OH for B35A−5. Only CH_3OH transitions above 5σ were considered.

The uncertainties on the gas column densities were estimated based on the rms noise of the spectra and on the ∼20% calibration uncertainty. The error propagation from the column densities of the gas-phase species to the abundances was calculated as follows. For instance, if X_{CO} is the abundance of gas-phase CO, the uncertainty $\sigma(X_{CO})$ is equal to:

$$\sigma(X_{CO}) = \frac{N_{CO}}{N_{H_2}} \sqrt{\left[\frac{\sigma\left(N_{CO}\right)}{N_{CO}}\right]^2 + \left[\frac{\sigma\left(N_{H_2}\right)}{N_{H_2}}\right]^2} \tag{6.4}$$

where N is the column density of the different species (CO and H_2 from SCUBA−2 measurements in this case), $\sigma\left(N_{CO}\right)$ is the uncertainty on the CO gas column density estimated from the rms noise and the calibration uncertainty, and $\sigma\left(N_{H_2}\right)$ is the uncertainty on the H_2 column density determined from the flux calibration uncertainty. The same treatment was adopted for the ice species but using the H_2 column density and uncertainty derived from the visual extinction.

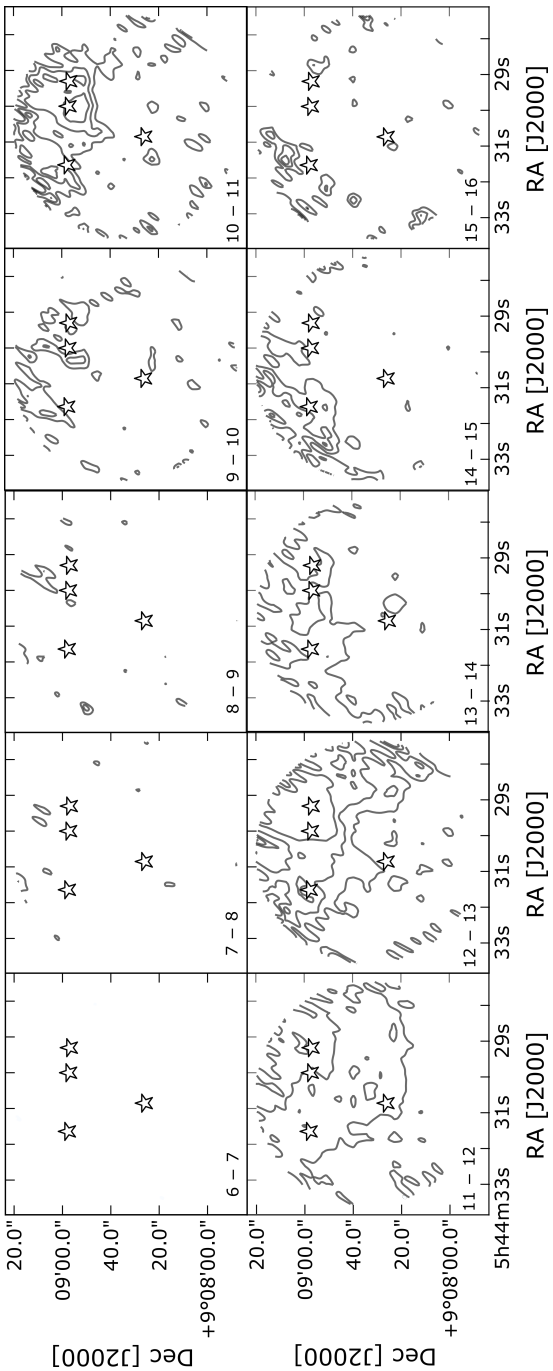

FIGURE 6.A.3: Channel maps for ^{13}CO $J = 2 - 1$ with velocity range 6 to 16 km s^{-1} in channels of 1 km s^{-1}. Contours starts at 5σ and follow a step of 5σ.

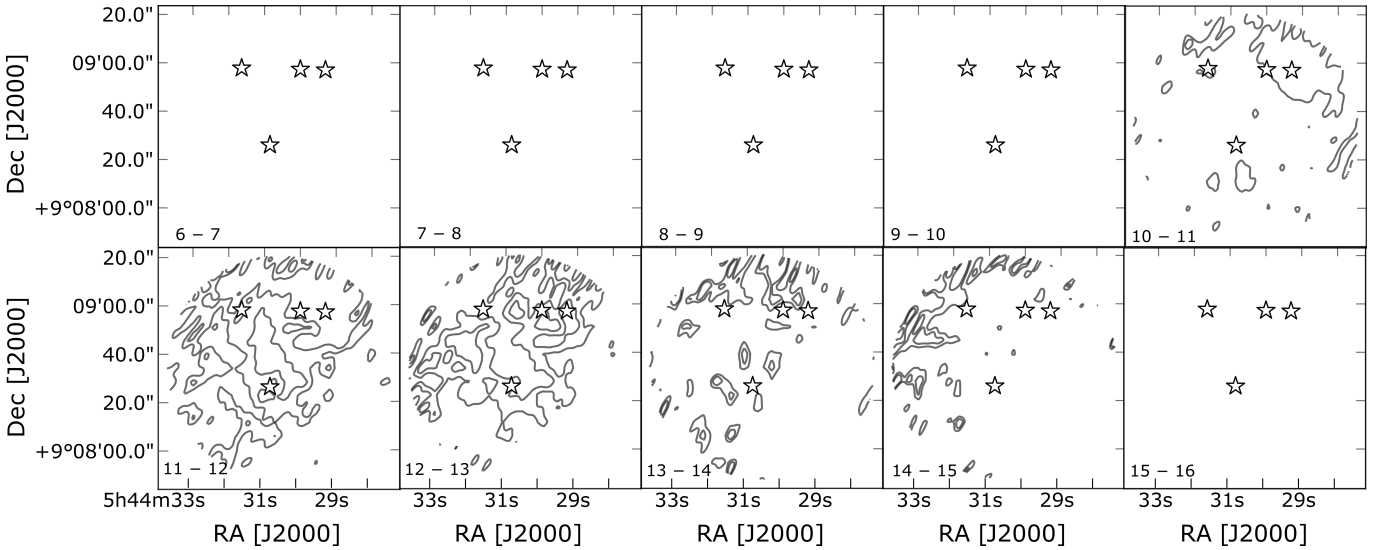

FIGURE 6.A.4: Channel maps for $C^{18}O$ $J = 2 - 1$ with velocity range 6 to 16 km s^{-1} in channels of 1 km s^{-1}. Contours starts at 5σ and follow a step of 5σ.

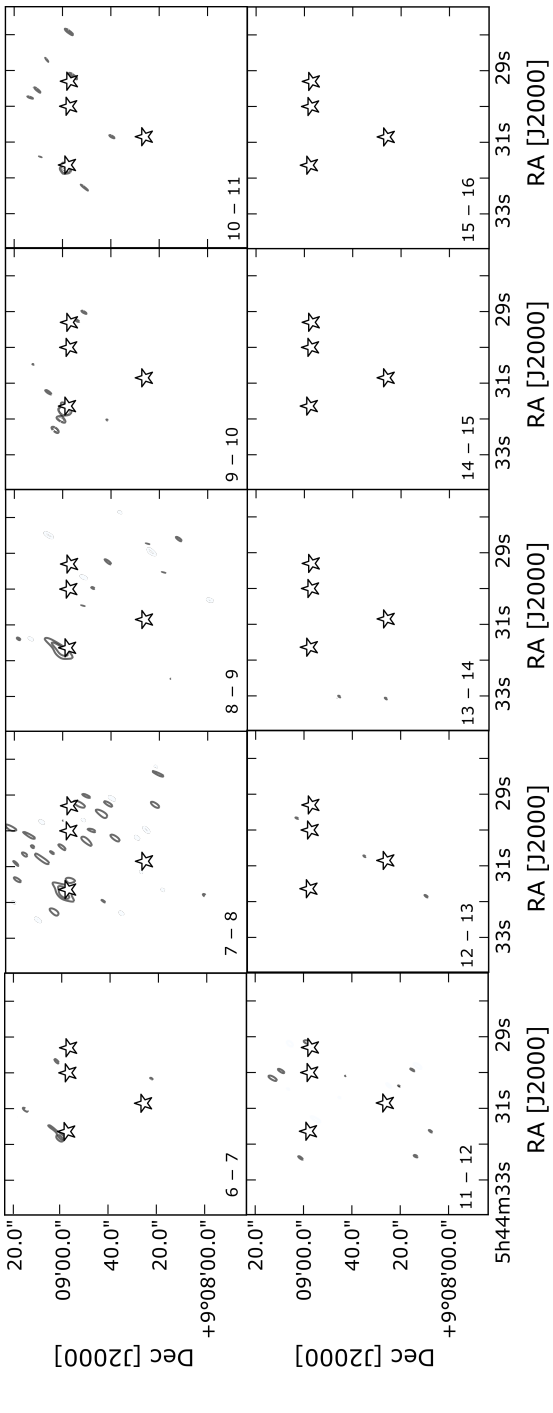

FIGURE 6.A.5: Channel maps for CH_3OH $J = 5_0 - 4_0$ A^+ with velocity range 6 to 16 km s^{-1} in channels of 1 km s^{-1}. Contours starts at 5σ and follow a step of 5σ.

6.b H_2 COLUMN DENSITY FROM VISUAL EXTINCTION

[6] https://irsa.ipac.caltech.edu/data/SPITZER/C2D/cores.html

The production of the H_2 column density map is accomplished by using the visual extinction (A_V) values for B35A tabulated in the c2d catalog[6]. No A_V values are reported for B35A−2 and B35A−3 in the catalog. As a result, the visual extinction for B35A−3 is retrieved by de-reddening its spectral energy distribution (SED) at the J, H, K 2MASS photometric points of Table 6.B.1 to fit a first blackbody and fit a second blackbody to model the infrared excess at the IRAC photometric points (see Figure 6.B.1). The extinction in the H-band (A_H) is then calculated using the following equation (Chapman *et al.*, 2009):

$$A_\lambda = -2.5 \log \left[\left(\frac{F_\lambda}{B_\lambda} \right) \left(\frac{1}{\mathrm{k}} \right) \right] \tag{6.5}$$

where λ is the wavelength corresponding in this case to the H-band (1.662 μm), F_λ is the observed flux at the selected λ, k is a scaling factor and B_λ is the blackbody function. The extinction in the H-band is then converted to visual extinction using the equation below:

$$A_V = 5.55 A_H \, (\mathrm{mag}) \tag{6.6}$$

where the conversion factor is taken from Weingartner and Draine (2001). The adopted extinction law takes into account the dust model from Weingartner and Draine (2001) for $R_V = 5.5$ designed for the dense interstellar medium and used by the c2d collaboration (Chapman *et al.*, 2009; Evans *et al.*, 2009). No near-IR photometry data are available for B35A−2, thus the A_V for this source is obtained by interpolating all the tabulated visual

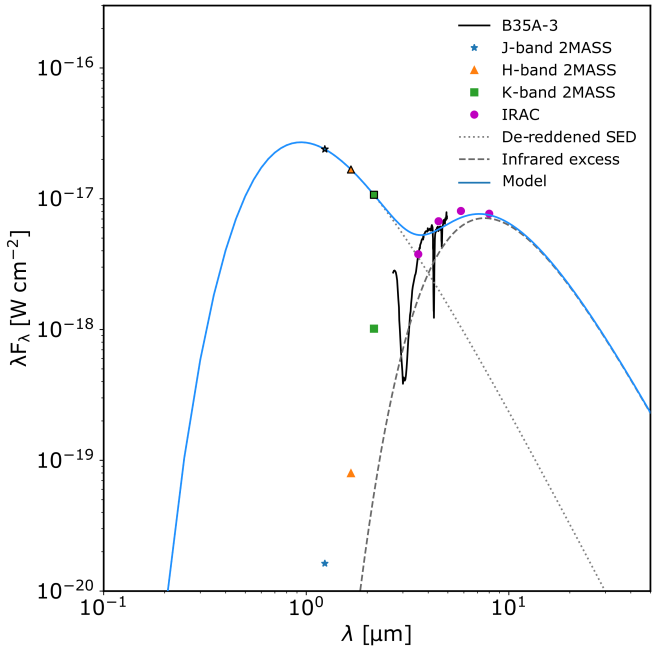

FIGURE 6.B.1: The spectral energy distribution (SED) of B35A−3, which was modeled to determine its visual extinction. The dotted and dashed lines represent the black body functions used to model the stellar component and the infrared excess, respectively. The solid line is the sum of the two contributions.

TABLE 6.B.1: Photometry of B35A–3.

Object	1.235 μm[a] [mJy]	1.662 μm[a] [mJy]	2.159 μm[a] [mJy]	3.6 μm[b] [mJy]
B35A–3	0.067	0.442 ± 0.0871	7.31 ± 0.229	44.59 ± 2.6
	4.5 μm[b] [mJy]	5.8 μm[b] [mJy]	8.0 μm[b] [mJy]	
B35A–3	101 ± 6.9	156 ± 8.09	205 ± 9.97	

Notes. [a] from 2MASS (Skrutskie *et al.*, 2006) [b] from IRAC (Evans *et al.*, 2014).

extinction values for B35A taken from the c2d catalog including the A_V value for B35A–3. The obtained visual extinction map of B35A is then converted to a H_2 column density map using the relation:

$$N_{\mathrm{H_2}} = 1.37 \times 10^{21} \mathrm{cm}^{-2} (A_V / \mathrm{mag}) \tag{6.7}$$

established for dense interstellar medium gas (Evans *et al.*, 2009).

7

Linking ice and gas in the Coronet cluster in Corona Australis

G. Perotti[1], J. K. Jørgensen[1], L. E. Kristensen[1], W. R. M. Rocha[1], E. Artur de la Villarmois[2], H. J. Fraser[3], P. Bjerkeli[4], M. Sewilo[5], S. B. Charnley[5]

[1] Niels Bohr Institute & Centre for Star and Planet Formation, University of Copenhagen, Øster Voldgade 5−7, 1350 Copenhagen K., Denmark
[2] Instituto de Astrofísica, Ponticia Universidad Católica de Chile, Av. Vicuña Mackenna 4860, 7820436 Macul, Santiago, Chile
[3] School of Physical Sciences, The Open University, Walton Hall, Milton Keynes, MK7 6AA, United Kingdom
[4] Department of Space, Earth, and Environment, Chalmers University of Technology, Onsala Space Observatory, 439 92 Onsala, Sweden
[5] NASA Goddard Space Flight Center, 8800 Greenbelt Road, Greenbelt, MD 20771, USA

In preparation

Abstract

Context. The planet-forming material is inherited from the molecular cloud via an infalling protostellar envelope. During its journey from the cloud to the disk, the chemical composition of the protostellar envelope matter is preserved or processed to various degrees based on the surrounding physical environment.

Aims. We constrain the interplay of the gas and ice in the envelopes surrounding protostars in the Coronet cluster in Corona Australis, and assess the importance of irradiation by the nearby Herbig Ae/Be star R CrA.

Methods. We present 1.3 mm Submillimeter Array (SMA) observations towards the envelopes of low-mass protostars (Class I or younger) in the Coronet cluster. Additionally, we make use of archival SMA, APEX and Spitzer IRS observations to analyse the relationships between ice and gas species in this strongly irradiated region. Finally,

we calculate methanol (CH_3OH) gas-to-ice ratios and compare them with ratios determined towards protostars located in Serpens Main and in the λ Orionis Barnard 35A cloud.

Results. In the SMA data we identify eighteen molecular transitions and a total of nine species which include molecular ions, deuterated species and isotopologues. The high UV flux appears to impact the gas-phase chemistry in the Coronet by enhancing the emission of molecular tracers such as H_2CO, SO, SO_2 and SiO. The distribution of CH_3OH gas-to-ice ratios covers one order of magnitude (1.9×10^{-4} to 1.5×10^{-3}) and validates previous laboratory predictions. The CH_3OH gas-to-ice ratios estimated in different star-forming regions are similar, indicating that the overall CH_3OH chemistry of cold low-mass envelopes is relatively independent of variations in the physical conditions. A larger sample is however required to constrain further this result and the impact of the environment on the physico-chemical evolution of protostellar envelope material.

7.1 INTRODUCTION

Sun-type stars and planets form inside molecular clouds, when dense cores undergo gravitational collapse. While collapsing, the gas and dust constituting the clouds is assembled into infalling envelopes, streamers and circumstellar disks, which supply the fundamental ingredients for planet formation. Recent observations (e.g., Andrews *et al.*, 2018; Keppler *et al.*, 2018; Segura-Cox *et al.*, 2020) suggest that planets form earlier than previously thought (a few $\times10^5$yr; Tychoniec *et al.*, 2020) and in tandem with their host star (Alves *et al.*, 2020). In this context, it is still unclear whether the cloud material is preserved when becoming part of planets or, instead, entirely thermally processed losing the cloud chemical fingerprint (see reviews, e.g., Jørgensen *et al.*, 2020; Öberg and Bergin, 2021; van Dishoeck and Bergin, 2020). If the planet-building material is preserved, a key question yet to be answered is to what extent the composition of the gas and ice material is altered during its journey from the cloud to the disk.

To address this query it is necessary to study how the environment impacts the physical and chemical properties of embedded protostars and disks. For instance, external irradiation (Winter *et al.*, 2020) and cosmic ray ionization (Kuffmeier *et al.*, 2020) might shape the chemical and physical evolution of forming low-mass stars by e.g., photoevaporating their disks (van Terwisga *et al.*, 2020; Haworth *et al.*, 2021 and references therein) or leading to less massive disks (Cazzoletti *et al.*, 2019). In this paper we investigate the variations of the gas and ice composition towards deeply embedded sources in Corona Australis, to study the effects of external irradiation on the gas-to-ice ratios.

Corona Australis (CrA) is one of the nearest regions with ongoing star-formation, located at a distance of 149.4±0.4 pc as estimated from *Gaia*-DR2 measurements (Galli *et al.*, 2020). The most updated census of the cloud counts 262 young stellar object (YSO) candidates, mostly Class II or III, predominantly concentrated in the most extincted region, the "head"

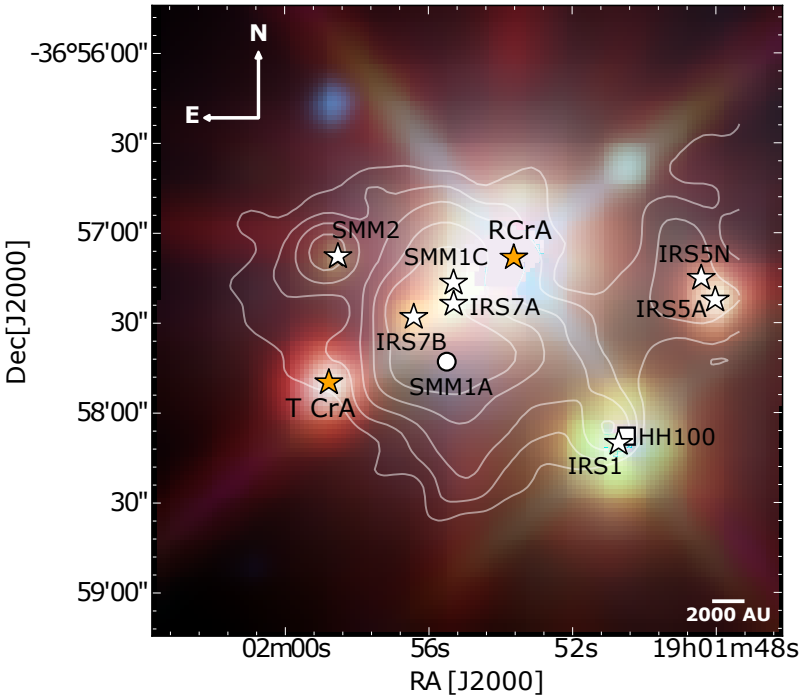

FIGURE 7.1.1: Three-color image of the Coronet cluster overlaid with SCUBA 850 μm density flux (Nutter *et al.*, 2005); contours are in decreasing steps starting at the peak flux (3.7 Jy beam^{-1}) and subtracting 30% from the previous level. The composite is made from *WISE* 3.4 μm (blue), 4.6 μm (green) and 12 μm (red) bands (Wright *et al.*, 2010). The white stars mark the positions of Class 0/I YSOs in the R CrA/Coronet region (Peterson *et al.*, 2011; Nutter *et al.*, 2005), whereas the orange stars indicate the Herbig Ae/Be star R CrA and the T Tauri star T CrA. The pre-stellar core candidate SMM1A is indicated with a white circle and the white square represents the Herbig Haro object HH100. These symbols will be adopted throughout the paper.

(Peterson *et al.*, 2011; Alves *et al.*, 2014). The correlation between the star formation activity and the head-tail structure of Corona Australis has been investigated by Dib and Henning (2019), who found that the spatial distribution of dense cores is a consequence of the physical conditions of the large scale environment present at the time the cloud assembled. The youngest population of YSO (Class 0/I) is situated in the Coronet cluster (Taylor and Storey, 1984; Forbrich *et al.*, 2007; Forbrich and Preibisch, 2007), also associated with the luminous Herbig Ae/Be star R CrA (Peterson *et al.*, 2011).

Figure 7.1.1 displays a section of the Coronet cluster and a summary of the principal cluster members is provided in Table 7.1.1. The Herbig Ae/Be R CrA (spectral type B5–B8; Gray *et al.*, 2006; Bibo *et al.*, 1992) is the brightest star in this very young cluster. Due to its variable nature (Herbig, 1960), its stellar mass and luminosity are uncertain (Mesa *et al.*, 2019). Recent *Very Large Telescope*/SPHERE observations of R CrA resolved a companion at a separation of ~0.156″–0.184″ and complex extended jet-like structures around the star (Mesa *et al.*, 2019). A second variable star, the T Tauri star T CrA is present in the Coronet cluster, approximately 30″ to the south-east of R CrA (Herbig, 1960; Taylor and Storey, 1984). The region between the two variable stars harbours a wealth of Class 0/I YSOs (Table 7.1.1).

The Coronet cluster members have been at the center of active multi-

TABLE 7.1.1: Overview of the Coronet cluster objects.

Object	RA [J2000]	DEC [J2000]	Designation[a]	Other names[b]
IRS5A	19:01:48.03	-36:57:22.2	Class I YSO	CrA-19
IRS5N	19:01:48.46	-36:57:14.7	Class I YSO	CrA-20
HH100 IRS1	19:01:50.56	-36:58:08.9	Herbig-Haro object	–
IRS1	19:01:50.68	-36:58:09.7	Class I YSO	VSSt 15, TS 2.6
R CrA	19:01:53.67	-36:57:08.0	Herbig Ae/Be star	–
SMM1C	19:01:55.29	-36:57:17.0	Class I YSO	B9, Brown 9
IRS7A	19:01:55.32	-36:57:21.9	Class I YSO	IRS7W, IRS7
SMM1A	19:01:55.60	-36:57:43.0	Pre-stellar core	–
IRS7B	19:01:56.40	-36:57:28.3	Class I YSO	SMM1B, IRS7E
SMM2	19:01:58.54	-36:57:08.5	Class I YSO	CrA-43, WMB55
T CrA	19:01:58.78	-36:57:49.9	T Tauri star	–

Notes. All the coordinates are taken from Peterson *et al.* (2011), except for SMM1A which comes from Nutter *et al.* (2005) and HH100 IRS1 from Boogert *et al.* (2008). [a] The YSO class is assigned from the spectral index α reported in Peterson *et al.* (2011); the objects designated as "Class I YSO" are Class I or younger. [b] From Peterson *et al.* (2011) and Lindberg and Jørgensen (2012).

wavelength research, mostly aimed at the characterization of the properties of YSOs at very early stages of stellar evolution. Some of the most studied objects are IRS7B and IRS7A, identified with the *Very Large Array* at 6 cm by Brown (1987). Submillimeter and millimeter studies detected three additional continuum point sources in the region: SMM1A, SMM1C and SMM2 (Nutter *et al.*, 2005; Groppi *et al.*, 2007; Miettinen *et al.*, 2008; Chen and Arce, 2010; Peterson *et al.*, 2011). The spectral energy distributions (SEDs) of the cluster members have been investigated by Groppi *et al.* (2007), suggesting that SMM1C is a Class 0 YSO and IRS7B is a transitional Class 0/I object. IRS7A and SMM2 are likely Class I sources (Peterson *et al.*, 2011) and SMM1A is classified as a pre-stellar core candidate (Nutter *et al.*, 2005; Chen and Arce, 2010). IRS1, IRS5N and IRS5A are suggested as Class I YSO based on submillimeter and infrared observations (Peterson *et al.*, 2011).

Along with the identification and the age estimation of the YSOs in the Coronet, their chemical evolution has been monitored in the past decades. The line-rich spectra of IRS7B and IRS7A has been investigated using the *Atacama Pathfinder EXperiment* (APEX) single-dish telescope by Schöier *et al.* (2006), who reported diverging kinetic temperatures for formaldehyde (H_2CO) and methanol (CH_3OH) (>30 K for H_2CO and ≈20 K for CH_3OH). Lindberg and Jørgensen (2012) suggested that the high temperatures in the region (>30 K) traced by the emission of formaldehyde (H_2CO), are caused by external irradiation from the Herbig Ae/Be star R CrA. With the purpose of analyzing the impact of external irradiation on the molecular inventory of low-mass protostars, systematic unbiased line surveys have been carried out firstly towards IRS7B using the *Atacama Submillimeter Telescope Experiment* (ASTE) by Watanabe *et al.* (2012), and extended to other Coronet cluster members using APEX by Lindberg *et al.* (2015).

These systematic surveys confirmed that external irradiation can affect the chemical nature of protostars, particularly by enhancing the abundances of Photon-Dominated Regions (PDRs) tracers (e.g., C_2H, CN, H_2CO; Watanabe *et al.*, 2012; Lindberg and Jørgensen, 2012). High-resolution *Atacama Large Millimeter/submillimeter Array* (ALMA) observations towards IR7B by Lindberg *et al.* (2014) revealed a possible additional effect of external irradiation on the chemistry of protostars: the low abundance of complex organic molecules such as CH_3OH in the inner hot regions of protostellar envelopes (<100 AU). However, the authors also suggest that the faint CH_3OH emission might be due to a flat density profile of the inner envelope due to the presence of a disc.

The composition of interstellar ices towards a few objects in Corona Australis (IRS5A, IRS5B, HH100 IRS1, IRS7A, IRS7B, IRAS32) has been investigated in the near-infrared (3−5 μm) with the *Very Large Telescope* (VLT; Pontoppidan *et al.*, 2003a, in the mid-infrared (5−8 μm) using the *Infrared Space Observatory* (ISO; Keane *et al.*, 2001) and as part of the *Spitzer* c2d Legacy Program (5−8 μm by Boogert *et al.*, 2008; 8−10 μm by Bottinelli *et al.*, 2010 and 14.5−16.5 μm by Pontoppidan *et al.*, 2008). Ice features attributed to H_2O, CO, CO_2, NH_3, CH_3OH were securely identified in the astronomical spectra of the targeted sources. Upper limits on formic acid (HCOOH) and abundances of ammonium ion (NH_4^+) relative to H_2O ice were presented by Boogert *et al.* (2008), with the caveat that the feature at 6.85 μm has not been unequivocally attributed to NH_4^+.

This paper explores the variations of the gas and ice composition in the Coronet, investigating the effects of external irradiation on the intertwined gas-phase and solid-state chemistries of the youngest objects in the Corona Australis star-forming region. We present SMA observations towards five Coronet cluster members, complementing previous SMA observations by Lindberg and Jørgensen (2012) at 1.3 mm, thus increasing the number of detected chemical species towards the YSOs lying in this region. Furthermore, the dependencies of gas-to-ice ratios on the physical conditions are addressed, by determining gas-to-ice ratios of CH_3OH in this strongly irradiated cluster and comparing them with ratios obtained towards less irradiated low-mass star-forming regions.

The paper organized is as follows. We begin in Section 7.2 by describing the observational setups, the data reduction strategy and the ancillary data to the SMA observations. In Section 7.3 we present our key observational results, while the variations on the ice and gas composition are analysed in Section 7.4. Section 7.5 discusses the determined CH_3OH gas-to-ice ratios and Section 7.6 summarises our conclusions and lists avenues for future studies.

7.2 OBSERVATIONS AND ARCHIVAL DATA

7.2.1 *SMA observations*

The Coronet cluster was observed with the *Submillimeter Array* (SMA; Ho *et al.*, 2004) on February 25, 2020 using 7 antennas in the compact configuration. The region was covered by one pointing ~ 10″ south of

R CrA (Fig. 7.3.1) with coordinates α_{J2000} = $19^{h}01^{m}53^{s}.30$, δ_{J2000} = −36°57′21.″00. The SWARM correlator provided a total frequency coverage of 16 GHz, with the lower sideband covering frequencies from 213.3 to 221.3 GHz and upper sideband 229.3 to 237.3 GHz. The spectral resolution was 0.6 MHz corresponding to 0.7 km s^{-1}.

[1] http://casa.nrao.edu/

Data calibration and imaging were performed with the CASA package[1] (McMullin *et al.*, 2007). The complex gains were calibrated through observations of the quasars 1924-292 and 1957-387 and the bandpass through observations of the bright quasar 3c279. The overall flux calibration was done through observations of Callisto. Imaging was done using the `tclean` algorithm and a Briggs weighting with robustness parameter of 1. The resulting synthetic beam size of the SMA observations was 4.″9 × 2.″6 with a position angle of -8.2°.

7.2.2 *Ancillary data*

This study made use of ancillary data to the SMA observations, primarily to compare the gas and ice molecular inventory in the Coronet. Ice column densities were adopted from *Spitzer* InfraRed Spectrograph (IRS) observations presented by Boogert *et al.* (2008) and the H_2CO and CH_3OH gas-phase column densities were taken from Lindberg and Jørgensen (2012) and Lindberg *et al.* (2015). A map of the H_2 column density towards the R CrA region was constructed using submillimeter continuum maps at 850 μm obtained with the SCUBA camera at the *James Clerk Maxwell Telescope* (JCMT; Nutter *et al.*, 2005). The H_2 column density map was used in the calculation of the abundances of the gas-phase and ice species.

7.3 RESULTS

7.3.1 *Gas-phase detections*

Figure 7.3.1 displays the SMA 1.3 mm continuum emission towards the Coronet cluster. The morphology of the continuum coincides with the position of the targeted young stellar objects in the region. The faint emission of one of the condensations associated with the pre-stellar core candidate SMM1A, SMM1A-c, Chen and Arce (2010) is also seen. The peak emission is observed towards the two Class 0 sources SMM1C and IRS7B, followed by the Class I object IRS7A and the Herbig Ae/Be star R CrA.

Eighteen molecular transitions and a total of nine species were identified in the SMA data set, in two 8 GHz frequency ranges (213.3−221.3 GHz and 229.3−237.3 GHz). The detected inventory includes molecular ions, deuterated species and isotopologues: CO (^{13}CO and $C^{18}O$), H_2CO (D_2CO), CH_3OH, DCO^+, SO, SO_2, c-C_3H_2, HC_3N, SiO (Table 7.3.1). The line emission is predominantly extended and it does not necessarily coincide with the position of the compact continuum sources in the Coronet cluster (Figures 7.3.1 −7.3.4). In contrast, it is mostly localized to the east of the Herbig Ae/Be star R CrA and to the south of the young stellar objects IRS7A and IRS7B, at the pre-stellar core SMM1A position. This statement applies especially to H_2CO and CH_3OH, and is consistent with previous 1.3 mm SMA observations of the region by Lindberg and Jørgensen (2012) covering frequencies in the

TABLE 7.3.1: Identified molecular transitions in the SMA data.

Species	Transition	Frequency[a] [GHz]	$A^a_{\rm ul}$ [s^{-1}]	$E^a_{\rm u}$ [K]
CO-species				
CO	$J = 2 - 1$	230.538	6.92×10^{-7}	17
$C^{18}O$	$J = 2 - 1$	219.560	6.01×10^{-7}	16
^{13}CO	$J = 2 - 1$	220.398	6.04×10^{-7}	16
H_2CO	$3_{0,3} - 2_{0,2}$	218.222	2.82×10^{-4}	21
H_2CO	$3_{2,2} - 2_{2,1}$	218.476	1.58×10^{-4}	68
H_2CO	$3_{2,1} - 2_{2,0}$	218.760	1.58×10^{-4}	68
CH_3OH	$4_2 - 3_1$, E	218.440	4.68×10^{-5}	46
CH_3OH	$8_{-1} - 7_0$, E	229.758	4.19×10^{-5}	89
Deuterated-species				
D_2CO	$4_{0,4} - 3_{0,3}$	231.410	3.47×10^{-4}	28
DCO^+	$J = 3 - 2$	216.112	2.57×10^{-4}	21
S-species				
SO	$5_5 - 4_4$	215.220	1.20×10^{-4}	44
SO	$6_5 - 5_4$	219.949	1.35×10^{-4}	35
SO_2	$4_{2,2} - 3_{1,3}$	235.151	7.69×10^{-5}	19
Carbon-chain species				
c-C_3H_2	$3_{3,0} - 2_{2,1}$	216.278	2.57×10^{-4}	19
c-C_3H_2	$6_{0,6} - 5_{1,5}$	217.822	5.37×10^{-4}	39
c-C_3H_2	$5_{1,4} - 4_{2,3}$	217.940	3.98×10^{-4}	35
HC_3N	$J = 24 - 23$	218.324	8.32×10^{-4}	131
Other species				
SiO	$J = 5 - 4$	217.104	5.25×10^{-4}	31

Notes.[a] From the Cologne Database for Molecular Spectroscopy (CDMS; Müller *et al.* (2001)) and the Jet Propulsion Laboratory catalog (Pickett *et al.*, 1998).

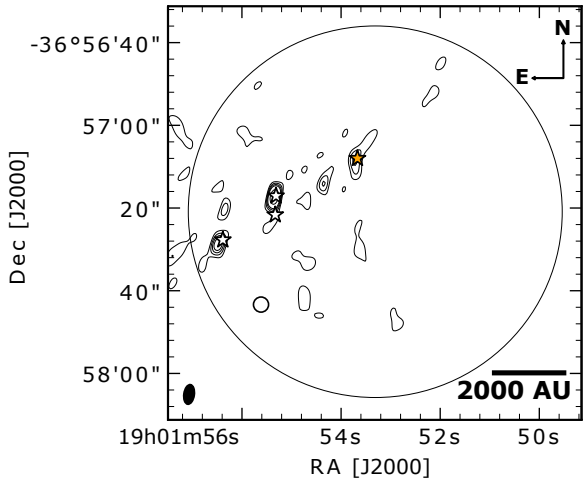

FIGURE 7.3.1: SMA continuum at 1.3 mm. The contours are at 3σ, 6σ, 9σ, 12σ, and continue in steps of 10σ (σ = 4.3 mJy). The circle indicates the SMA primary beam size, whereas the synthetic beam is represented with a black ellipse in the bottom left corner. The stars mark the position of the objects located in the Coronet cluster, refer to Fig. 7.1.1 for their identification.

ranges 216.849–218.831 GHz and 226.849–228.831 GHz. In contrast, no line emission was detected towards SMM1A in the SMA data set presented by Chen and Arce (2010), although the SMA correlator covered the same spectral ranges analysed by Lindberg and Jørgensen (2012).

The detected species can be divided into four groups based on their distribution (Table 7.3.1): (I) CO species, (II) S-species, (III) carbon-chain species, and (IV) SiO. The distribution of the emission of the deuterated species does not show peculiar patterns, instead it presents common features to the CO-species and therefore it will be discussed with group (I). A list of non-detected molecular transitions is given in Appendix 7.A, Table 7.A.1.

CO-species

Figures 7.3.2 and 7.3.3 display integrated intensity maps for CO, ^{13}CO, C^{18}O, H_2CO and its deuterated form (D_2CO) and CH_3OH. The distribution of the CO-species emission is extended, especially for CO and its isotopologues, CH_3OH and D_2CO. The three transitions of H_2CO show the same emission pattern (Figure 7.3.2, panels $d - f$). The emission is localized in two ridges: the northern ridge between R CrA and SMM1C, and the southern ridge to the south of IRS7B, at the SMM1A position. No bright line emission is observed towards the young stellar objects SMM1C, IRS7A and IRS7B. The emission offset from the YSOs positions and the elongated shape of the ridges are indicators of external heating. The emission localized in the southern ridge traces the three condensations within the pre-stellar core SMM1A (SMM1A-a, SMM1A-b, and SMM1A-c), observed in the SMA dust continuum by Chen and Arce (2010).

The strength of the H_2CO emission, for the three detected H_2CO lines is comparable in both ridges. A different morphology pattern is observed for the other CO-species, especially for CO, its isotopologues and DCO^+ (Figure 7.3.3, panel j) which do not show bright line emission towards SMM1A, and for CH_3OH, for which the emission peak is located within the SMM1A core and it does not show a northern ridge (Figure 7.3.3, panels

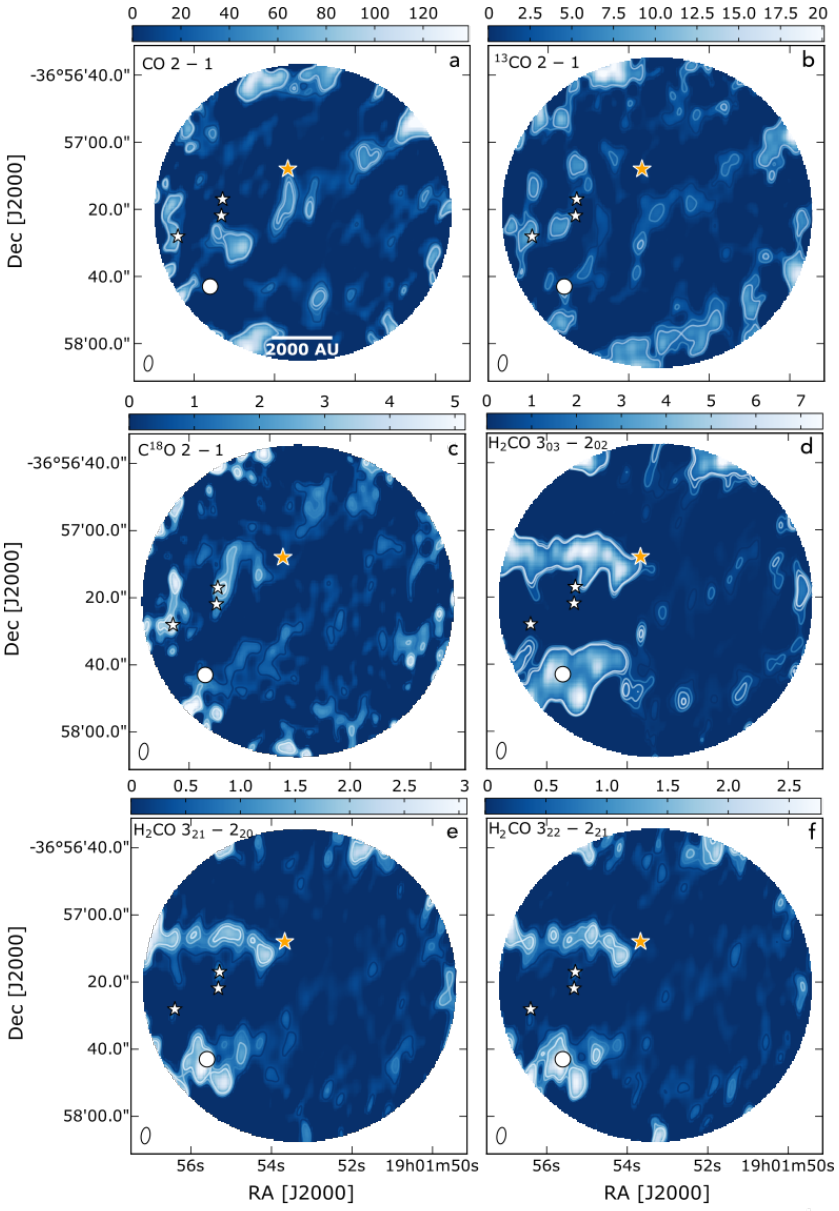

FIGURE 7.3.2: Primary beam corrected Integrated intensity maps for the different species observed with the SMA. In each plot contours start at 5σ and continue in intervals of 5σ. Shown are (a) CO $J = 2 - 1$ (σ= 0.24 Jy beam^{-1}km s^{-1}), (b) ^{13}CO $J = 2 - 1$ (σ= 0.17 Jy beam^{-1}km s^{-1}), (b) C^{18}O $J = 2 - 1$ (σ= 0.15 Jy beam^{-1}km s^{-1}), (d) H$_2$CO 3$_{03}$–2$_{02}$ (σ= 69 mJy beam^{-1}km s^{-1}), (e) H$_2$CO 3$_{21}$–2$_{20}$ (σ= 71 mJy beam^{-1}km s^{-1}), (f) H$_2$CO 3$_{22}$–2$_{21}$ (σ= 65 mJy beam^{-1}km s^{-1}). The circles outline the SMA primary beam. The synthesized beams are shown in white in the bottom left corner of each panel. The stars and the dots mark the position of the Coronet cluster objects as in Fig. 7.1.1.

$g - h$). In contrast to the other CO-species, the line emission of C^{18}O and DCO$^+$ is also observed at the SMM1C and IRS7B positions (Figures 7.3.2 and 7.3.3, panels c, i and j).

S-species

The SO and SO$_2$ line emissions appear relatively bright and compact (Figures 7.3.3 and 7.3.4, panels $k - m$), compared to the CO-species. The distribution of the emission is identical for the three transitions, and it peaks

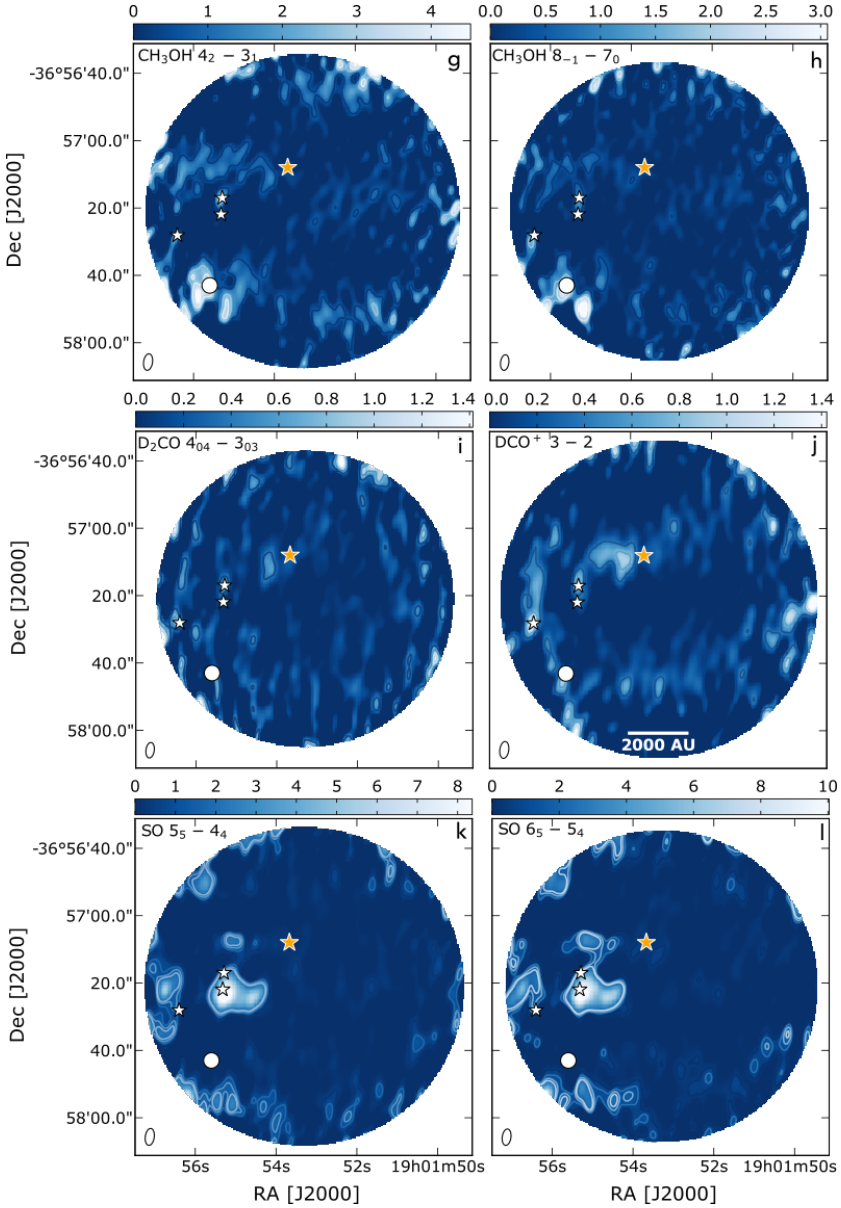

FIGURE 7.3.3: Continued from Figure 7.3.2. Primary beam corrected integrated intensity (Jy beam km s^{-1}) maps for: g) CH_3OH 4_2–3_1 (σ= 0.15 Jy beam^{-1}km s^{-1}), (h) CH_3OH 8_{-1}–7_0 (σ= 88 mJy beam^{-1}km s^{-1}) and (i) D_2CO 4_{04}–3_{03} (σ= 81 mJy beam^{-1}km s^{-1}), (j) DCO^+ J = 3 – 2 (σ= 81 mJy beam^{-1}km s^{-1}), (k) SO 5_5 – 4_4 (σ= 88 mJy beam^{-1}km s^{-1}), (l) SO 6_5 – 5_4 (σ= 95 mJy beam^{-1}km s^{-1}) detected with the SMA.

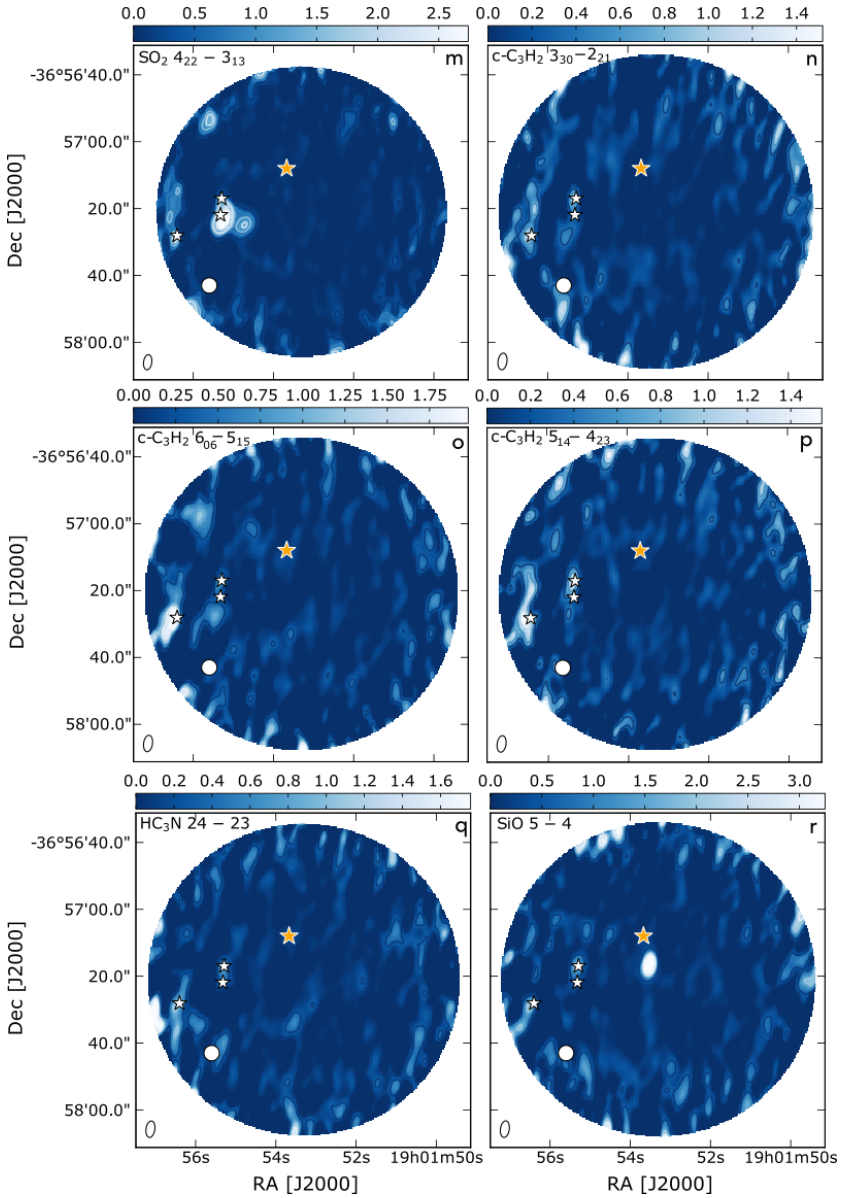

FIGURE 7.3.4: Continued from Figure 7.3.3. Primary beam corrected integrated intensity (Jy beam km s^{-1}) maps for: (m) SO_2 4_{22} – 3_{13} (σ= 61 mJy beam^{-1}km s^{-1}), (n) c-C_3H_2 3_{30}–2_{21} (σ= 76 mJy beam^{-1}km s^{-1}), (o) c-C_3H_2 6_{06}–5_{15} (σ= 74 mJy beam^{-1}km s^{-1}), (p) c-C_3H_2 5_{14}–4_{23} (σ= 85 mJy beam^{-1}km s^{-1}), (q) HC_3N J = 24 – 23 (σ= 64 mJy beam^{-1}km s^{-1}) and (r) SiO J = 5 – 4 (σ= 0.12 mJy beam^{-1}km s^{-1}) detected with the SMA.

towards IRS7A and SMM1C. The strength of the emission among the SO transitions is similar (7–10 Jy beam km s^{-1}; Figure 7.3.3, panels $k - l$). The SO_2 emission is approximately a factor of four lower (Figure 7.3.4, panels m). SO and SO_2 are molecular tracers of energetic inputs in the form of outflows and jets. The luminous SO and SO_2 emissions indicate that high-velocity flows of matter are present in the field-of-view of the observations, associated with IRS7A and SMM1C. This result is in agreement with studies of the Herbig-Haro objects in the Coronet attributed to SMM1C (Wang *et al.*, 2004; Peterson *et al.*, 2011).

Carbon-chain species

The third group of lines corresponds to carbon-chain species like c-C_3H_2 and HC_3N which show a fairly weak emission (1.4–1.75 Jy beam km s^{-1}) compared to the previous two groups (CO- and S-species). Their emission is diffuse and characterized by a fairly low S/N. In contrast to the majority of the CO-species, the carbon-chain and the S-species have their strongest emission associated with the YSOs position: for instance the the c-C_3H_2 transitions peak at the IRS7B location (Figure 7.3.4, panels o, p).

SiO

The SiO emission shows an interesting and distinct feature compared to the other three groups (Figure 7.3.4, panel r), as it appears as a bright point source just south of R CrA, to the west of SMM1C and IRS7A at velocities remarkably higher (9–12 km s^{-1}) than the R CrA velocity (5 km s^{-1}). The emission is aligned with R CrA. The same compact structure for the SiO emission has been observed previously by Lindberg and Jørgensen (2012), who concluded that it might be associated with Herbig-Haro (HH) objects in the Coronet. This result is based on observations of multiple HH objects extending south of R CrA coinciding with the location of the SiO emission detected in the SMA data. It has been suggested that HH objects in the region are emanated from the infrared source IRS1 (e.g. HH100, HH101; Hartigan and Graham, 1987), however more recent studies (Wang *et al.*, 2004; Peterson *et al.*, 2011) infer that both R CrA and SMM1C could be plausible driving sources.

In general, the emission reported in the SMA data sets is dominated by molecular tracers such as H_2CO SO, SO_2, SiO. The enhanced emission of H_2CO is consistent with temperature variations in the field of view of the observations, and particularly with the external irradiation from the variable stars in the region (R CrA and T CrA). In contrast, the shock tracers (SO, SO_2, SiO) probe the numerous outflows and Herbig-Haro objects in the region, which are indicators of a young stellar population in the earliest evolutionary stages.

TABLE 7.3.2: Total ice and gas column densities towards the Coronet cluster members.

Object	$N^{ice}_{H_2O}$	$N^{ice}_{CH_3OH}$	$N^{ice}_{NH_4^+}$	$^{\dagger}N^{gas}_{H_2CO}$	$^{\dagger}N^{gas}_{CH_3OH}$	$N^{SCUBA}_{H_2}$
	$[10^{18}cm^{-2}]$	$[10^{17}cm^{-2}]$	$[10^{17}cm^{-2}]$	$[10^{13}cm^{-2}]$	$[10^{13}cm^{-2}]$	$[10^{23}cm^{-2}]$
IRS5A	3.58 ± 0.26	2.36 ± 0.57	1.83 ± 0.14	3.7±0.74	4.5 ± 2.1	$0.55^{+0.44}_{-0.26}$
HH100 IRS1*	2.45 ± 0.24	< 2.38	2.84 ± 0.51	2.8±0.56	6.7 ± 2.6	$0.67^{+0.51}_{-0.31}$
IRS7A	10.89 ± 1.92	< 4.14	7.62 ± 0.44	4.1±0.82	64 ± 30	$1.48^{+1.12}_{-0.69}$
IRS7B	11.01 ± 1.97	7.49 ± 0.33	6.39 ± 0.22	10±1.0	45 ± 10	$1.92^{+1.45}_{-0.90}$

Notes. Columns 2–4 list the ice column densities from Boogert *et al.* (2008), and assume that NH_4^+ is the carrier of the 6.85 μm feature. † Columns 5 and 6 display the gas column densities from Lindberg and Jørgensen (2012) and Lindberg *et al.* (2015). * The single-dish observations are unable to resolve the emission towards IRS1 and HH100, the value obtained towards IRS1 is adopted here. Columns 7 shows the H_2 column densities using T_{dust}= 30 K. The values in the superscripts and subscripts represent the upper and lower limits if T_{dust}= 20 K or T_{dust}= 50 K are adopted.

7.4 ANALYSIS

In the this section, the gas and ice species detected towards the Coronet cluster members are analysed. The ice column densities of H_2O, NH_4^+ and CH_3OH adopted in this paper were determined by Boogert *et al.* (2008) from *Spitzer* IRS mid-infrared spectra (5–20 μm) as part of the *Spitzer* Legacy Program "From Molecular Cores to Planet-Forming Disks" (c2d). Infrared spectra of IRS5A, HH100 IRS1, IRS7A and IRS7B were decomposed.

For the gas-phase counterpart, we made use of H_2CO and CH_3OH gas column densities from the combination of Submillimeter Array and APEX 1.3 mm observations by Lindberg and Jørgensen (2012) and Lindberg *et al.* (2015). The adopted ice and gas column densities are reported in Table 7.3.2.

7.4.1 *H_2 column densities*

Prior to searching for gas-ice correlations, the physical structure of the Coronet cluster is investigated by producing an H_2 column density map of the targeted region. This step is required as relative abundances instead of absolute column densities need to be compared when studying gas-ice variations. This is due to the fact that gas and ice observations, by their very nature, are tracing different spatial scales (e.g., Noble *et al.*, 2017), therefore, a comparison between absolute values can lead to misinterpretations.

Figure 7.4.1 shows the H_2 column density map of the Coronet cluster obtained by making use of submillimeter continuum maps at 850 μm (SCUBA; Nutter *et al.*, 2005). A detailed description of the formalism adopted to obtain the H_2 column density from SCUBA maps is provided in Appendix C of Perotti *et al.* (2020). Briefly, in an optically thin thermal dust emission regime, the strength of the submillimeter radiation depends on the column density (N), the dust temperature (T) and the opacity (κ_ν) (Kauffmann *et al.*, 2008). The inserted value for the opacity per unit dust+gas mass is 0.0182 $cm^2\ g^{-1}$ ("OH5 dust"; Ossenkopf and Henning, 1994). The adopted values for the dust temperatures are 20, 30 and 50 K, based on previous observational studies and radiative transfer models by Lindberg and Jørgensen (2012) and Lindberg *et al.* (2015).

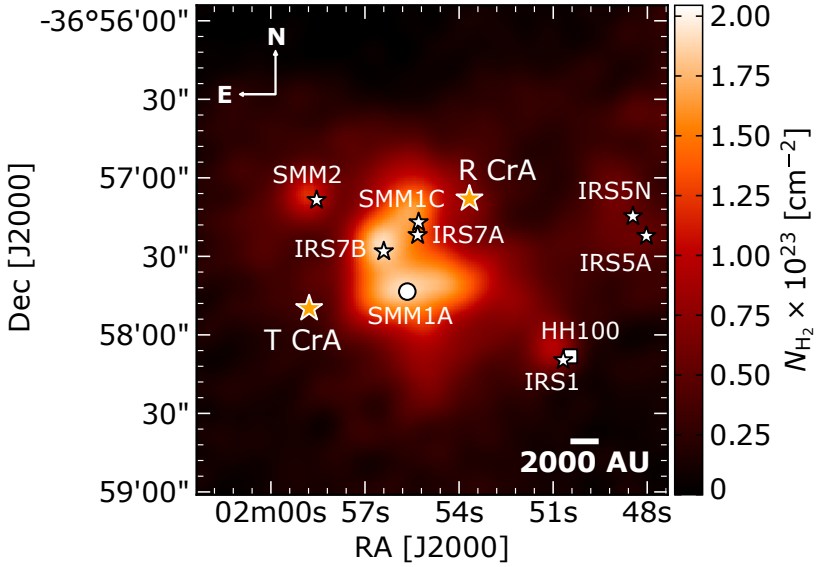

FIGURE 7.4.1: H_2 column density map of the R CrA region calculated from SCUBA dust emission maps at 850 μm (Nutter *et al.*, 2005). Refer to Fig. 7.1.1 for a guide to the symbols of the Coronet cluster objects.

TABLE 7.4.1: Ice and gas abundances relative to H_2 towards the Coronet cluster objects.

Object	$X^{ice}_{H_2O}$	$X^{ice}_{CH_3OH}$	$^*X^{ice}_{NH_4^+}$	$X^{gas}_{H_2CO}$	$X^{gas}_{CH_3OH}$
	[10^{-5}]	[10^{-6}]	[10^{-6}]	[10^{-10}]	[10^{-9}]
IRS5A	6.51 ± 0.51	4.29 ± 1.04	3.33 ± 0.27	6.73 ± 1.36	0.82 ± 0.38
HH100 IRS1	3.66 ± 0.37	< 3.55	4.24 ± 0.77	4.18 ± 0.85	1.0 ± 0.39
IRS7A	7.36 ± 1.32	< 2.98	5.15 ± 0.34	2.77 ± 0.56	4.32 ± 2.03
IRS7B	5.73 ± 1.04	3.90 ± 0.19	3.33 ± 0.15	5.21 ± 0.54	2.34 ± 0.53

Notes. The abundances are relative to $N^{SCUBA}_{H_2}$ (Table 7.3.2). * Assuming that NH_4^+ is the carrier of the 6.85 μm feature (Boogert *et al.*, 2008).

The youngest cluster members are all situated in the densest areas of the targeted region (Fig. 7.4.1); offsets from the dust continuum emission peaks are not observed. The apex of the estimated H_2 column density lies to the south-east of R CrA, and in particular at the IRS7B, SMM1A, SMM1C and IRS7A positions ($N_{H_2} > 1.45{\times}10^{23}$ cm^{-2}). SMM2, IRS1, IRS5N and IRS5A are located in slightly less dense regions ($0.5{\times}10^{23}$ cm$^{-2} < N_{H_2} < 1.25{\times}10^{23}$ cm^{-2}). The exact values of the H_2 column density are reported in Table 7.3.2.

7.4.2 *Gas and ice variations in the Coronet*

The analysis of the gas-ice variations in the Coronet is addressed in Fig. 7.4.2 by comparing ice and gas fractional abundances (X) relative to H_2 (Table 7.4.1). Panels (a)−(c) report the H_2CO gas abundances as function of H_2O (a), CH_3OH (b) and NH_4^+ (c) ice abundances, whereas panels (d)−(f) display CH_3OH gas abundances with the abundances of the aforementioned

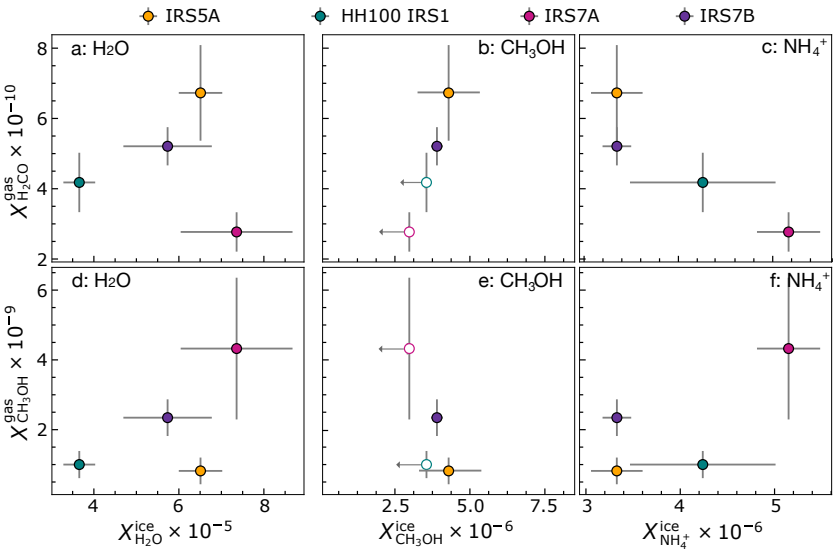

FIGURE 7.4.2: Gas and ice variations in the Coronet cluster. The circles represent the sources listed in Table 7.4.1 for which both gas and ice measurements are available. Panels (a)–(c) display the relations between H_2O, CH_3OH and NH_4^+ ice and H_2CO gas abundances relative to H_2. Panels (d)–(f) compare H_2O, CH_3OH and NH_4^+ ice and CH_3OH gas abundances relative to H_2. Upper limits are marked as empty circles.

ice species.

The H_2O ice abundances in Fig. 7.4.2 panels (a) and (d) show the largest spread among all the analysed ice species, with values ranging from 3.7 to 7.4×10^{-5} with respect to H_2 (Table 7.4.1). The lowest H_2O ice abundance is reported towards HH100 IRS1, whereas the highest is found towards IRS7A (Fig. 7.4.2 panel a). The H_2O ice abundances towards IRS5A, IRS7A and IRS7B are consistent within the uncertainty, only HH100 IRS1 deviates significantly. When H_2O ice and H_2CO gas abundances are compared, no clear correlation is seen. In contrast, a tentative correlation is observed between H_2O ice and CH_3OH gas abundances (Fig. 7.4.2 panel d). IRS5A shows the highest H_2CO gas abundance, whereas IRS7A reports the lowest. The opposite is seen for the CH_3OH gas abundances.

Figure 7.4.2 panels (b) and (e) compare CH_3OH ice abundances versus H_2O and CH_3OH gas abundances. The distribution of the data points in panel (b) hints to a positive trend between CH_3OH ice and H_2CO gas abundances, plausibly indicating a relationship between these two species in the cluster. However, firm conclusions cannot be drawn as the CH_3OH ice abundances towards HH100 IRS1 and IRS7A are upper limits. The same applies to panel (e), where a negative trend is suggested for CH_3OH ice and gas abundances. Finally, Figure 7.4.2 panels (c) and (f) analyse the chemical behaviours of NH_4^+ ice and H_2CO and CH_3OH gas, respectively. The NH_4^+ ice abundances show a minor variation and they are consistent within the error bars. An anti-correlation is observed among the NH_4^+ and H_2CO, indicating that in the regions where H_2CO gas is more abundant (IRS5A and IRS7B), a lower percentage of NH_4^+ resides on the surfaces of the dust grains. In panel (f) no straightforward trend is found among NH_4^+ ice and CH_3OH gas abundances.

The analysis of the gas-ice interplay presented in this section has to be taken with care, as it is based on a small sample. Future high-sensitivity infrared observations will constrain further the abundances of the ice species

and confirm the tentative correlations and anti-correlations observed in Fig. 7.4.2. Additionally, they will allow to carry out statistical studies of the ice variations in the Coronet.

7.4.3 *IRS7A and IRS7B*

Two of the Coronet cluster members for which ice measurements exist are part of the sample observed in this study: IRS7A and IRS7B. It is therefore possible to compare the morphology of the observed emission towards these sources (Figs. 7.3.2 – 7.3.4) with the spatial distribution of the ice species. From Table 7.4.1, the Class I IRS7A reports the highest abundances of H_2O and NH_4^+ compared to the transitional Class 0/I IRS7B. For CH_3OH the comparison is not possible as an upper limit is given for IRS7A.

Among the gas-phase detections reported towards the Coronet, only the emission of the S-bearing and carbon-chain species is compact and localized at the YSOs position. For the S-bearing species, the peak emission is reported towards IRS7A and extends to the west of this source, whereas the emission is faint towards IRS7B. For the carbon-chain species, the situation is reversed. However, the emission of carbon-chain species is weaker and affected by a low-signal to noise. We can conclude that, if the two sources are compared, IRS7A is the source reporting the highest observed emission of S-bearing species and abundance of ice species.

Future observations of the Coronet with the SMA could target the cluster members for which ice data exist. These observations could then be combined to single-dish data to recover the spatially extended emission filtered out by the interferometer, a strategy we adopted previously in e.g., Perotti *et al.* (2020). This will allow to include higher resolution data points for H_2CO and CH_3OH gas abundances in Table 7.4.1 and Figures 7.4.2 and 7.5.1. Finally, this observational strategy will make it possible to extend the analysis of the gas morphology and ice abundances presented in this section.

7.5 DISCUSSION

Laboratory experiments predict that CH_3OH ice in cold dark clouds and in the coldest regions of protostellar envelopes is desorbed with an efficiency spanning over approximately three orders of magnitude ($10^{-6} - 10^{-3}$ molecules/photon; Öberg *et al.*, 2009b; Bertin *et al.*, 2016; Cruz-Diaz *et al.*, 2016; Martín-Doménech *et al.*, 2016). This range is expected to increase up to $\sim 10^{-2}$ molecules/photon in the disk, as X-rays emitted from the central YSO are likely able to eject CH_3OH molecules from the mid-plane ices (Basalgète *et al.*, 2021a; Basalgète *et al.*, 2021b). The CH_3OH desorption efficiency and by inference the gas-to-ice ratio is highly dependent on the ice structure (crystalline or amorphous) and composition (pure CH_3OH versus CH_3OH mixed with CO molecules), as well as on the temperature, photon energy and flux (e.g., Öberg, 2016). In this study, the laboratory predictions for the CH_3OH gas-to-ice ratio have been tested observationally using literature data. This provides direct observational constraints on the gas-to-ice ratio of CH_3OH in protostellar envelopes, and its dependency on the physical conditions of star-forming regions.

Figure 7.5.1 illustrates the distribution of the CH_3OH gas-to-ice ratios (N_{gas}/N_{ice}) towards low-mass protostars located in three different molecular clouds: Serpens (Perotti *et al.*, 2020), Orion (Perotti et al. submitted) and Corona Australis. The averaged CH_3OH gas-to-ice ratio (1.2×10^{-4}) determined from millimetric and infrared measurements by Öberg *et al.* (2009a) for Class 0/I sources is over-plotted on this figure as a reference. A detailed comparison between the gas-to-ice ratio determined by Öberg *et al.* (2009a) and the ratios calculated for the sources in the Serpens SVS 4 and the Orion B35A cloud is provided in Perotti et al. submitted. In this section we focus on the ratios obtained for Corona Australis and their comparison with the values determined for the two other star-forming regions.

The distribution of CH_3OH gas-to-ice ratios towards the Coronet cluster covers approximately one order of magnitude (i.e. from 1.9×10^{-4} to 1.5×10^{-3}). The uncertainty on the determination of the CH_3OH ice column densities for HH100 IRS1 and IRS7A (Boogert *et al.*, 2008) results in upper limits for their gas-to-ice ratios, consequently we can not provide solid comparisons for these two sources. In contrast, the values obtained for IRS5A and IRS7B fall in the range of gas-to-ice ratios previously obtained for the protostars located in the Serpens SVS 4 cluster.

The CH_3OH gas-to-ice ratios constrained from gas and ice observations of protostellar envelopes (Figure 7.5.1) do not point to one value but, instead, to a distribution ($\sim10^{-4} - 10^{-3}$) which validates previous laboratory predictions (Öberg *et al.*, 2009b). This distribution agrees with a more complex scenario for the CH_3OH desorption elucidated in the laboratory in which photodissociation (i.e., photo-fragmentation) and recombination processes are triggered during and after the desorption, respectively (e.g., Bertin *et al.*, 2016).

A second interesting observation is that, the CH_3OH gas-to-ice ratios are similar, which suggest that the CH_3OH chemistry at play in cold protostellar envelopes belonging to different low-mass star-forming regions is relatively independent of variations in the physical conditions. A related result came to light when comparing abundances of complex organic molecules observed in distinct star-forming environments (e.g., Galactic disk versus Galactic center, high-mass versus low-mass star-forming region; Jørgensen *et al.*, 2020). A larger sample is however necessary to prove this statement, and additional observations, laboratory experiments and modelling efforts are required to elucidate further the impact of the physical evolution of protostars on their chemical signatures and vice versa.

Our targeted regions (Serpens SVS 4, Orion B35A and Corona Australis Coronet) share a number of similarities: e.g. they are low-mass star forming regions, they are clustered and finally, they are affected by the presence of outflows and/or Herbig-Haro objects. However, they show distinct physical conditions for instance, the Serpens SVS 4 cluster is influenced by the presence of the Class 0 binary SMM4 (Pontoppidan *et al.*, 2004), whereas B35A is affected by the nearby high-mass star λ Orionis (Reipurth and Friberg, 2021) and the Coronet is strongly irradiated by the Herbig Ae/Be star R CrA (Lindberg and Jørgensen, 2012). B35A is exposed to an interstellar radiation field χ_{ISRF} of 34 (Wolfire *et al.*, 1989)[2] enhanced by the neighbouring λ Orionis (Dolan and Mathieu, 2002), whereas the radiation field in the

[2]Note that Wolfire *et al.* (1989) report a $\log(G_0)$ of 1.3 which is here converted to χ_{ISRF} by applying the formalism described by Draine and Bertoldi (1996).

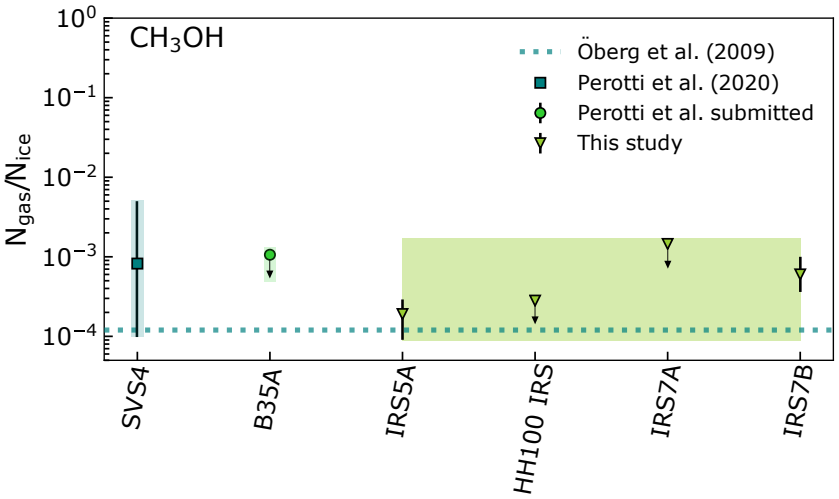

FIGURE 7.5.1: CH_3OH gas-to-ice ratios (N_{gas}/N_{ice}) towards low-mass protostars in the Corona Australis Coronet cluster (triangles). The square and the circle symbolize the averaged CH_3OH gas-to-ice ratios for Serpens SVS 4 and Orion B35A, respectively. The dotted line indicates the reference value by Öberg *et al.* (2009a). The shaded areas indicate the ranges of gas-to-ice ratios towards the three molecular clouds.

Coronet cluster has been estimated to approximately χ_{ISRF} ~750 to account for the high fluxes at millimeter wavelengths (Lindberg and Jørgensen, 2012).

In addition, the molecular clouds in which our targeted regions are located do not share a common formation history. The ongoing low-mass star formation in Serpens Main is a controversial topic in the literature. It might have been triggered by external forcing, possibly cloud-cloud collisions (Duarte-Cabral *et al.*, 2010; Nakamura *et al.*, 2017) or compression from a shock wave from a supernova. However, there is no clear evidence that a nearby supernova ever occurred (Herczeg *et al.*, 2019). Concurrently, it is challenging to explain how cloud–cloud collisions happening at certain locations could propagate over considerable distances without promoting subsequent star-forming collisions ubiquitously in the clouds (Herczeg *et al.*, 2019).

The population of young protostars in the Orion B35A cloud is located in the λ Orionis star-forming region, constituted by a group of massive OB stars surrounded by a ring of dust and gas (Wade, 1957; Murdin and Penston, 1977; Heiles and Habing, 1974; Maddalena and Morris, 1987; Zhang *et al.*, 1989; Lang *et al.*, 2000; Dolan and Mathieu, 2002; Sahan and Haffner, 2016). In contrast to Serpens, the formation of the ring constituting the λ Orionis region is attributed to a supernova explosion occurred roughly 1–6 Myr ago (Dolan and Mathieu, 1999; Dolan and Mathieu, 2002; Kounkel, 2020). The low-mass star formation in B35A was likely triggered by the presence of neighboring massive stars and their stellar winds (Barrado *et al.*, 2018).

Finally, star-formation in Corona Australis has been supposedly promoted by a high-velocity cloud impact onto the Galactic plane (Neuhäuser and Forbrich, 2008). This scenario is based on the study of the three-dimensional motion of the T Tauri stars located in CrA (Neuhäuser *et al.*, 2000). Another possible trigger is the expansion of the UpperCenLupus (UCL) superbubble.

This hypothesis is based on the finding that CrA is moving away from UCL with 7 km s^{-1} and therefore it was located close to its center about 14 Myr ago (Mamajek *et al.*, 2002).

7.6 CONCLUSIONS

We present 1.3 mm SMA observations towards the Coronet cluster in Corona Australis, a unique astrochemical laboratory to study the effect of external irradiation on the chemical and physical evolution of young protostars. In addition, we make use of multi-wavelengths archival observations (SMA, APEX, Spitzer) to test laboratory predictions for the CH_3OH gas-to-ice ratio in cold protostellar envelopes. Our key findings are:

- In the SMA data we identify eighteen molecular transitions and a total of nine species which include ions (DCO^+), deuterated species (D_2CO) and isotopologues (^{13}CO and $C^{18}O$). The strong UV flux in the region affects the gas-phase chemistry by enhancing the abundance of shocks and photon-dominated regions molecular tracers.

- Luminous H_2CO emission is confined to two bright ridges not associated with the YSOs, in agreement with studies suggesting that the cluster is significantly impacted by external irradiation, plausibly from the Herbig Ae/Be star R CrA.

- Bright and compact SO, SO_2 and SiO emission is observed in the cluster. The SO and SO_2 emissions peak at the IRS7A and SMM1C positions, whereas the SiO feature is located south of R CrA. The distribution of the emission of these tracers suggest that IRS7A, SMM1C and R CrA are possible driving sources of outflows, jets and Herbig-Haro objects in the region.

- We find a tentative correlation between H_2O ice and CH_3OH gas abundances pointing to a linked chemical behaviour of these two species. We also note a negative trend between NH_4^+ and H_2CO gas abundances, suggesting that the higher temperature regions harbour a lower content of NH_4^+ on the grain surfaces.

- The distribution of CH_3OH gas-to-ice ratios in the Coronet cluster constrained from millimetric and ice observations spans over one order of magnitude (1.9×10^{-4} to 1.5×10^{-3}) and validates previous laboratory predictions by Öberg *et al.* (2009b).

- Similarities are found between CH_3OH gas-to-ice ratios determined in different low-mass star forming regions (Serpens SVS 4 cluster, Orion B35A cloud and Coronet cluster), characterized by distinct physical conditions and formation histories. This result suggests that the CH_3OH chemistry occurring in cold low-mass envelopes is relatively independent of variations in the physical conditions.

Multiple avenues for future studies can be pursued. Comparisons of gas and ice abundances of key species are currently limited by the low number of infrared surveys. Future infrared facilities such as VLTI-GRAVITY

and JWST will routinely probe pre-stellar cores, proto-stellar envelopes and near edge-on disks, thus significantly increase the number of studied regions. Therefore, it will be feasible to search for gas-ice trends found in other regions, improve our constrains on the CH_3OH gas-to-ice ratios, and ultimately determine ratios for a larger set of interstellar molecules. This approach will provide important feedback on the interactions between ice and gas material during its journey from the molecular cloud to the disk and on the impact of the physical conditions on the physico-chemical evolution of protostars. In this context, the Corona Australis molecular cloud still has much to teach us, hosting one of the youngest population of protostars observed so far.

ACKNOWLEDGEMENTS

This work is based on observations with the Submillimeter Array, Mauna Kea, Hawaii, program code: 2019B-S014. The Submillimeter Array is a joint project between the Smithsonian Astrophysical Observatory and the Academia Sinica Institute of Astronomy and Astrophysics and is funded by the Smithsonian Institution and the Academia Sinica. This publication also makes use of data products from the Wide-field Infrared Survey Explorer, which is a joint project of the University of California, Los Angeles, and the Jet Propulsion Laboratory/California Institute of Technology, funded by the National Aeronautics and Space Administration. JKJ acknowledges the financial support from the European Research Council (ERC) under the European Union's Horizon 2020 research and innovation programme (grant agreement No 646908) through ERC Consolidator Grant "S4F".

Appendix

7.a NON-DETECTIONS

Non-detected transitions in the covered spectral range at the 3σ level are listed in Table 7.A.1, together with their spectroscopic parameters.

TABLE 7.A.1: Non-detected molecular transitions in the SMA data.

Species	Transition	Frequency^a [GHz]	A^a_{ul} [s^{-1}]	E^a_u [K]
CO-species				
p-H_2CO	$11_{2,9}$ – $12_{0,9}$	215.976	3.16×10^{-7}	280
o-H_2CO	$9_{1,8}$ – $9_{1,9}$	216.569	7.24×10^{-6}	68
Deuterated-species				
C_2D^a	$N = 3 - 2$	216.373	3.01×10^{-5}	21
C_2D^b	$N = 3 - 2$	216.428	2.78×10^{-5}	21
HDO	$3_{1,2}$ – $2_{2,1}$	225.897	1.32×10^{-5}	167
N_2D^+	$J = 3 - 2$	231.321	7.08×10^{-4}	22
S-species				
SO	1_2 – 2_1	236.452	1.41×10^{-6}	16
SO_2	$11_{1,11}$ – $10_{0,10}$	221.965	1.15×10^{-4}	60
SO_2	$12_{3,9}$ – $12_{2,10}$	237.069	1.15×10^{-4}	60
^{13}CS	5_5 – 4_4	231.220	2.51×10^{-4}	33
OCS	$J = 18 - 17$	218.903	3.02×10^{-5}	100
OCS	$J = 19 - 18$	231.061	3.55×10^{-5}	111
p-H_2S	$2_{2,0}$ – $2_{1,1}$	216.710	4.90×10^{-4}	84
H_2CS	$7_{1,7}$ – $6_{1,6}$	236.727	1.91×10^{-4}	59
Carbon-chain species				
$^{13}CN^c$	N=2–1	217.265	1.01×10^{-4}	16
$^{13}CN^d$	N=2–1	217.467	1.01×10^{-4}	16
H_2CN	$3_{0,3}$ – $2_{0,2}$	219.852	3.39×10^{-4}	21
HC_3N	$J = 26 - 25$	236.513	1.05×10^{-4}	153
c-C_3H_2	$8_{2,6}$ – $7_{1,7}$	218.448	1.48×10^{-4}	87
c-C_3H_2	$8_{3,6}$ – $7_{2,7}$	218.449	1.48×10^{-4}	87
Other species				
HNCO	$10_{0,10}$ – $9_{0,9}$	219.798	1.48×10^{-4}	58

Notes.^{a} From the Cologne Database for Molecular Spectroscopy (CDMS; Müller *et al.* (2001)) and the Jet Propulsion Laboratory catalog (Pickett *et al.*, 1998). ^{a} $N = 3 - 2$, $J = 7/2 - 5/2$, $F = 5/2 - 3/2$. ^{b} $N = 3 - 2$, $J = 5/2 - 3/2$, $F = 7/2 - 5/2$. ^{c} J=3/2 –1/2. ^{d} J=5/2 –3/2.

Bibliography

1. ALMA Partnership *et al.*, *ApJ* **808**, L3 (2015).
2. K. Acharyya *et al.*, *A&A* **466**, 1005–1012 (2007).
3. C. M. O. D. Alexander *et al.*, *Geochim. Cosmochim. Acta* **71**, 4380–4403 (2007).
4. V. Allen, M. Cordiner, S. Charnley, *arXiv e-prints* (2020).
5. K. Altwegg *et al.*, *Science Advances* **2**, e1600285–e1600285 (2016).
6. F. O. Alves *et al.*, *ApJ* **904**, L6 (2020).
7. J. Alves, M. Lombardi, C. J. Lada, *A&A* **565**, A18 (2014).
8. S. Andersson, E. F. van Dishoeck, *A&A* **491**, 907–916 (2008).
9. S. Andersson *et al.*, *J. Chem. Phys.* **124**, 064715–064715 (2006).
10. D. P. P. Andrade, M. L. M. Rocco, H. M. Boechat-Roberty, *MNRAS* **409**, 1289–1296 (2010).
11. P. André *et al.*, in *Protostars and Planets VI* (Beuther, Henrik et al., 2014), p. 27.
12. P. André *et al.*, *A&A* **518**, L102 (2010).
13. P. André, *Comptes Rendus Geoscience* **349**, 187–197 (2017).
14. P. Andre, D. Ward-Thompson, M. Barsony, *ApJ* **406**, 122 (1993).
15. S. M. Andrews *et al.*, *ApJ* **869**, L41 (2018).
16. M. Ansdell *et al.*, *AJ* **160**, 248 (Dec. 2020).
17. M. Antiñolo *et al.*, *ApJ* **823**, 25 (2016).
18. E. Artur de la Villarmois *et al.*, *A&A* **626**, A71 (2019).
19. Y. Aso *et al.*, *ApJ* **863**, 19 (2018).
20. R. Bachiller *et al.*, *A&A* **295**, L51 (1995).
21. R. Bachiller *et al.*, *A&A* **335**, 266–276 (1998).
22. J. Bally, in *Handbook of Star Forming Regions, Volume I* (Reipurth, B., 2008), vol. 4, p. 459.
23. N. Balucani, C. Ceccarelli, V. Taquet, *MNRAS* **449**, L16–L20 (2015).
24. P. J. Barnes *et al.*, *ApJ* **812**, 6 (2015).
25. D. Barrado *et al.*, *A&A* **526**, A21 (2011).
26. D. Barrado *et al.*, *A&A* **612**, A79 (2018).
27. R. Basalgète *et al.*, *A&A* **647**, A35 (2021).
28. R. Basalgète *et al.*, *A&A* **647**, A36 (2021).
29. M. R. Bate, *MNRAS* **475**, 5618–5658 (2018).
30. A. Bayo *et al.*, *A&A* **536**, A63 (2011).
31. C. P. M. Bell *et al.*, *MNRAS* **434**, 806–831 (2013).
32. C. J. Bennett *et al.*, *ApJ* **660**, 1588–1608 (2007).
33. P. J. Benson, P. C. Myers, *ApJS* **71**, 89 (1989).
34. E. A. Bergin, M. Tafalla, *ARA&A* **45**, 339–396 (2007).
35. J. B. Bergner *et al.*, *ApJ* **841**, 120 (2017).
36. J. B. Bergner *et al.*, *ACS Earth and Space Chemistry* **3**, 1564–1575 (2019).
37. M. Bertin *et al.*, *ApJ* **817**, L12 (2016).
38. E. A. Bibo, P. S. The, D. N. Dawanas, *A&A* **260**, 293–302 (1992).
39. S. E. Bisschop *et al.*, *A&A* **449**, 1297–1309 (2006).
40. L. Bizzocchi *et al.*, *A&A* **569**, A27 (2014).
41. P. Bjerkeli *et al.*, *A&A* **546**, A29 (2012).

42. P. Bjerkeli *et al.*, *A&A* **595**, A39 (2016).
43. R. D. Blandford, D. G. Payne, *MNRAS* **199**, 883–903 (1982).
44. S Blanksby, G Ellison, *Accounts of Chemical Research* **36**, 255–263 (2003).
45. J. Blum, G. Wurm, *ARA&A* **46**, 21–56 (2008).
46. D. Bockelee-Morvan *et al.*, *A&A* **287**, 647–665 (1994).
47. C. F. Bohren, D. R. Huffman, *Absorption and scattering of light by small particles* (New York: Wiley, 1983).
48. A. S. Bolina, W. A. Brown, *Surface Science* **598**, 45–56 (2005).
49. W. B. Bonnor, *ZAp* **39**, 143 (1956).
50. S. Bontemps *et al.*, *A&A* **518**, L85 (2010).
51. A. C. A. Boogert, P. A. Gerakines, D. C. B. Whittet, *ARA&A* **53**, 541–581 (2015).
52. A. C. A. Boogert *et al.*, *A&A* **360**, 683–698 (2000).
53. A. C. A. Boogert *et al.*, *ApJ* **678**, 985–1004 (2008).
54. A. C. A. Boogert *et al.*, *ApJ* **729**, 92 (2011).
55. A. C. A. Boogert *et al.*, *ApJ* **777**, 73 (2013).
56. S. Bottinelli *et al.*, *ApJ* **718**, 1100–1117 (2010).
57. F. Brauer, T. Henning, C. P. Dullemond, *A&A* **487**, L1–L4 (2008).
58. D. Bresnahan *et al.*, *A&A* **615**, A125 (2018).
59. D. S. Briggs, F. R. Schwab, R. A. Sramek, in *Synthesis Imaging in Radio Astronomy II* (Taylor, G. B., Carilli, C. L., and Perley, R. A., 1999), vol. 180, p. 127.
60. T. Y. Brooke, K. Sellgren, T. R. Geballe, *ApJ* **517**, 883–900 (1999).
61. A. Brown, *ApJ* **322**, L31 (1987).
62. V. Buch, R. Czerminski, *J. Chem. Phys.* **95**, 6026–6038 (1991).
63. J. V. Buckle *et al.*, *MNRAS* **399**, 1026–1043 (2009).
64. J. V. Buckle *et al.*, *MNRAS* **422**, 521–541 (2012).
65. J. A. Caballero, *A&A* **478**, 667–674 (2008).
66. H. Calcutt *et al.*, *A&A* **616**, A90 (2018).
67. L. Cambrésy, *A&A* **345**, 965–976 (1999).
68. J. A. Cardelli, G. C. Clayton, J. S. Mathis, *ApJ* **345**, 245 (1989).
69. P. Carlhoff *et al.*, *A&A* **560**, A24 (2013).
70. J. M. Carpenter, *AJ* **120**, 3139–3161 (2000).
71. M. M. Casali, C. Eiroa, W. D. Duncan, *A&A* **275**, 195–200 (1993).
72. S. Cazaux *et al.*, *ApJ* **593**, L51–L55 (2003).
73. S. Cazaux *et al.*, *A&A* **585**, A55 (2016).
74. S. Cazaux *et al.*, *ApJ* **849**, 80 (2017).
75. P. Cazzoletti *et al.*, *A&A* **626**, A11 (2019).
76. C. J. Chandler, J. E. Carlstrom, *ApJ* **466**, 338 (1996).
77. N. L. Chapman *et al.*, *ApJ* **690**, 496–511 (2009).
78. S. B. Charnley, A. G. G. M. Tielens, S. D. Rodgers, *ApJ* **482**, L203–L206 (1997).
79. S. B. Charnley, in *IAU Colloq. 161: Astronomical and Biochemical Origins and the Search for Life in the Universe* (Batalli Cosmovici, Cristiano, Bowyer, Stuart, and Werthimer, Dan, 1997), p. 89.
80. H. Chen *et al.*, *ApJ* **445**, 377 (1995).
81. X. Chen, H. G. Arce, *ApJ* **720**, L169–L173 (2010).
82. J. E. Chiar *et al.*, *ApJ* **426**, 240 (1994).
83. J. E. Chiar *et al.*, *ApJ* **570**, 198–209 (2002).
84. J. E. Chiar *et al.*, *ApJ* **731**, 9 (2011).
85. M. Choi, *ApJ* **705**, 1730–1734 (2009).

86. L. E. U. Chu, K. Hodapp, A. Boogert, *ApJ* **904**, 86 (2020).
87. K. J. Chuang *et al.*, *MNRAS* **455**, 1702–1712 (2016).
88. K. J. Chuang *et al.*, *MNRAS* **467**, 2552–2565 (2017).
89. A. Ciaravella *et al.*, *Proceedings of the National Academy of Science* **117**, 16149–16153 (2020).
90. M. P. Collings *et al.*, *ApJ* **583**, 1058–1062 (2003).
91. M. P. Collings *et al.*, *MNRAS* **354**, 1133–1140 (2004).
92. M. S. Connelley, B. Reipurth, A. T. Tokunaga, *AJ* **135**, 2496–2525 (2008).
93. P. S. Conti, E. M. Leep, *ApJ* **193**, 113–124 (1974).
94. A. M. Craigon, http://digitool.lib.strath.ac.uk/R/?func=dbin-jump-full&object_id=27550, PhD thesis, Dept. of Physics, Univ. of Strathclyde, 2015.
95. G. A. Cruz-Diaz *et al.*, *A&A* **592**, A68 (2016).
96. H. M. Cuppen, E. Herbst, *ApJ* **668**, 294–309 (2007).
97. H. M. Cuppen *et al.*, *MNRAS* **417**, 2809–2816 (2011).
98. H. M. Cuppen *et al.*, *Space Sci. Rev.* **212**, 1–58 (2017).
99. A. Dalgarno, in, ed. by B. Bederson, A. Dalgarno (Academic Press, 1994), vol. 32, pp. 57–68.
100. T. M. Dame, P. Thaddeus, *ApJ* **297**, 751–765 (1985).
101. T. M. Dame *et al.*, *ApJ* **322**, 706 (1987).
102. E. Dartois *et al.*, *A&A* **618**, A173 (2018).
103. E. Dartois *et al.*, *Astronomy and Astrophysics* **627**, A55 (2019).
104. E. Dartois *et al.*, *A&A* **634**, A103 (2020).
105. A. Das *et al.*, *ApJS* **237**, 9 (2018).
106. C. J. Davis *et al.*, *MNRAS* **309**, 141–152 (1999).
107. A. Dawes, N. J. Mason, H. J. Fraser, *Phys. Chem. Chem. Phys.* **18**, 1245–1257 (2 2016).
108. C. H. De Vries, G. Narayanan, R. L. Snell, *ApJ* **577**, 798–825 (2002).
109. J. T. Dempsey *et al.*, *MNRAS* **430**, 2534–2544 (2013).
110. J. P. Devlin, *J. Chem. Phys* **96**, 6185–6188 (1992).
111. J. Di Francesco *et al.*, *ApJS* **175**, 277–295 (2008).
112. S. Dib, T. Henning, *A&A* **629**, A135 (2019).
113. O. Dionatos *et al.*, *A&A* **558**, A88 (2013).
114. O. Dionatos *et al.*, *A&A* **563**, A28 (2014).
115. C. J. Dolan, R. D. Mathieu, *AJ* **118**, 2409–2423 (1999).
116. C. J. Dolan, R. D. Mathieu, *AJ* **123**, 387–403 (2002).
117. B. T. Draine, *ARA&A* **41**, 241–289 (2003).
118. B. T. Draine, F. Bertoldi, *ApJ* **468**, 269 (1996).
119. M. N. Drozdovskaya *et al.*, *MNRAS* **490**, 50–79 (2019).
120. A. Duarte-Cabral *et al.*, *A&A* **519**, A27 (2010).
121. F. Dulieu *et al.*, *Scientific Reports* **3**, 1338 (2013).
122. M. M. Dunham *et al.*, in *Protostars and Planets VI* (Beuther, Henrik et al., 2014), p. 195.
123. M. M. Dunham *et al.*, *ApJS* **220**, 11 (2015).
124. R. Dupuy *et al.*, *Nature Astronomy* **2**, 796–801 (2018).
125. A. Duquennoy, M. Mayor, *A&A* **500**, 337–376 (1991).
126. R. Ebert, *ZAp* **37**, 217 (1955).
127. P. Ehrenfreund, S. B. Charnley, *ARA&A* **38**, 427–483 (2000).
128. C. Eiroa, M. M. Casali, *A&A* **223**, L17–L19 (1989).
129. C. Eiroa, A. A. Djupvik, M. M. Casali, in *Handbook of Star Forming Regions, Volume II: The Southern Sky ASP Monograph Publications* (Reipurth, B. ed, 2008), vol. 5, p. 693.

130. C. Eistrup, C. Walsh, E. F. van Dishoeck, *A&A* **595**, A83 (2016).
131. D. D. Eley, E. K. Rideal, *Nature* **146**, 401–402 (1940).
132. I. Evans Neal J. *et al.*, *ApJS* **181**, 321–350 (2009).
133. N. J. Evans II *et al.*, *VizieR Online Data Catalog* **2332** (2014).
134. E. C. Fayolle *et al.*, *ApJ* **739**, L36 (2011).
135. E. C. Fayolle *et al.*, *ApJ* **816**, L28 (2016).
136. G. G. Fazio *et al.*, *ApJS* **154**, 10–17 (2004).
137. G. Fedoseev *et al.*, *MNRAS* **448**, 1288–1297 (2015).
138. G. Fedoseev *et al.*, *ApJ* **842**, 52 (2017).
139. S. Ferrero *et al.*, *ApJ* **904**, 11 (2020).
140. J. Forbrich, T. Preibisch, *A&A* **475**, 959–972 (2007).
141. J. Forbrich *et al.*, *A&A* **464**, 1003–1013 (2007).
142. D. Foreman-Mackey *et al.*, *PASP* **125**, 306 (2013).
143. H. J. Fraser, E. F. van Dishoeck, *Advances in Space Research* **33**, 14–22 (2004).
144. H. J. Fraser *et al.*, *MNRAS* **327**, 1165–1172 (2001).
145. H. J. Fraser *et al.*, *MNRAS* **353**, 59–68 (2004).
146. S. Frimann, J. K. Jørgensen, T. Haugbølle, *A&A* **587**, A59 (2016).
147. G. W. Fuchs *et al.*, *A&A* **505**, 629–639 (2009).
148. P. A. B. Galli *et al.*, *A&A* **634**, A98 (2020).
149. R. T. Garrod, E. Herbst, *A&A* **457**, 927–936 (2006).
150. R. T. Garrod, V. Wakelam, E. Herbst, *A&A* **467**, 1103–1115 (2007).
151. R. T. Garrod, S. L. Widicus Weaver, E. Herbst, *ApJ* **682**, 283–302 (2008).
152. P. A. Gerakines *et al.*, *A&A* **296**, 810 (1995).
153. G. Giardino *et al.*, *A&A* **463**, 275–288 (2007).
154. E. L. Gibb *et al.*, *ApJS* **151**, 35–73 (2004).
155. B. M. Giuliano *et al.*, *A&A* **592**, A81 (2016).
156. P. F. Goldsmith, W. D. Langer, *ApJ* **517**, 209–225 (1999).
157. M. Goto *et al.*, *arXiv e-prints* (2020).
158. R. J. Gould, E. E. Salpeter, *ApJ* **138**, 393 (1963).
159. L. V. Gramajo *et al.*, *AJ* **139**, 2504–2524 (2010).
160. T. Grassi *et al.*, *A&A* **643**, A155 (Nov. 2020).
161. R. O. Gray *et al.*, *AJ* **132**, 161–170 (2006).
162. G. M. Green *et al.*, *ApJ* **810**, 25 (2015).
163. M. J. Griffin *et al.*, *A&A* **518**, L3 (2010).
164. R. J. A. Grim *et al.*, *A&A* **243**, 473 (1991).
165. C. E. Groppi *et al.*, *ApJ* **670**, 489–498 (2007).
166. W. M. Grundy *et al.*, *Science* **367**, aay3705 (2020).
167. R. Güsten *et al.*, *A&A* **454**, L13–L16 (2006).
168. R. A. Gutermuth *et al.*, *ApJ* **673**, L151 (2008).
169. W. Hagen, L. J. Allamandola, J. M. Greenberg, *A&A* **86**, L3–L6 (1980).
170. G. Haro, *ApJ* **115**, 572 (1952).
171. J. Harris, B. Kasemo, *Surface Science* **105**, L281–L287 (1981).
172. D. Harsono *et al.*, *A&A* **562**, A77 (2014).
173. D. Harsono *et al.*, *Nature Astronomy* **2**, 646–651 (2018).
174. P. Hartigan, J. A. Graham, *AJ* **93**, 913 (1987).

175. P. Harvey *et al.*, *ApJ* **663**, 1149–1173 (2007).
176. T. I. Hasegawa, E. Herbst, *MNRAS* **263**, 589 (1993).
177. T. I. Hasegawa, E. Herbst, C. M. Leung, *ApJS* **82**, 167 (1992).
178. T. Hassenkam *et al.*, *Nature* **548**, 78–81 (2017).
179. T. J. Haworth *et al.*, *MNRAS* **501**, 3502–3514 (2021).
180. C. Heiles, H. J. Habing, *A&AS* **14**, 1 (1974).
181. T. T. Helfer *et al.*, *ApJS* **145**, 259–327 (2003).
182. T. Henning, *ARA&A* **48**, 21–46 (2010).
183. T. Henning, G. Meeus, in *Physical Processes in Circumstellar Disks around Young Stars* (Garcia, Paulo J. V., 2011), pp. 114–148.
184. G. H. Herbig, *Vistas in Astronomy* **8**, 109–125 (1966).
185. G. H. Herbig, *ApJ* **111**, 11 (1950).
186. G. H. Herbig, *ApJS* **4**, 337 (1960).
187. E. Herbst, W. Klemperer, *ApJ* **185**, 505–534 (1973).
188. E. Herbst, C. M. Leung, *ApJS* **69**, 271 (1989).
189. E. Herbst, E. F. van Dishoeck, *ARA&A* **47**, 427–480 (2009).
190. G. J. Herczeg *et al.*, *ApJ* **849**, 43 (2017).
191. G. J. Herczeg *et al.*, *ApJ* **878**, 111 (2019).
192. J. Hernández *et al.*, *ApJ* **662**, 1067–1081 (2007).
193. J. Hernández *et al.*, *ApJ* **707**, 705–715 (2009).
194. J. Hernández *et al.*, *ApJ* **794**, 36 (2014).
195. M. Heyer, T. M. Dame, *ARA&A* **53**, 583–629 (2015).
196. C. N. Hinshelwood, in (Oxford University Press, 1940), pp. 36–39.
197. P. T. P. Ho, J. M. Moran, K. Y. Lo, *ApJ* **616**, L1–L6 (2004).
198. S. Hoban *et al.*, *Icarus* **105**, 548–556 (1993).
199. J. A. Högbom, *A&AS* **15**, 417 (1974).
200. D. J. Hollenbach, A. G. G. M. Tielens, *Reviews of Modern Physics* **71**, 173–230 (1999).
201. D. Hollenbach, C. F. McKee, *ApJ* **342**, 306 (1989).
202. D. Hollenbach, E. E. Salpeter, *ApJ* **163**, 155 (1971).
203. M. Honda *et al.*, *ApJ* **690**, L110–L113 (2009).
204. D. M. Hudgins *et al.*, *ApJS* **86**, 713–870 (1993).
205. C. L. H. Hull *et al.*, *ApJ* **847**, 92 (2017).
206. R. L. Hurt, M. Barsony, *ApJ* **460**, L45 (1996).
207. S. Ioppolo *et al.*, in *Molecules in Space and Laboratory* (Lemaire, J. L. and Combes, F., 2007), p. 73.
208. S. Ioppolo *et al.*, *ApJ* **686**, 1474–1479 (2008).
209. S. Ioppolo *et al.*, *A&A* **493**, 1017–1028 (2009).
210. S. Ioppolo *et al.*, *A&A* **646**, A172 (2021).
211. M. Ishii *et al.*, *AJ* **124**, 2790–2798 (2002).
212. J. H. Jeans, *Philosophical Transactions of the Royal Society of London Series A* **199**, 1–53 (1902).
213. R. D. Jeffries, *MNRAS* **376**, 1109–1119 (2007).
214. A. Jiménez-Escobar *et al.*, *ApJ* **820**, 25 (2016).
215. A. Jiménez-Escobar *et al.*, *ApJ* **868**, 73 (2018).
216. I. Jiménez-Serra *et al.*, *A&A* **482**, 549–559 (2008).
217. I. Jiménez-Serra *et al.*, *Astrobiology* **20**, 1048–1066 (2020).
218. D. Johnstone *et al.*, *ApJ* **559**, 307–317 (2001).

219. J. K. Jørgensen *et al.*, *A&A* **415**, 1021–1037 (2004).
220. J. K. Jørgensen *et al.*, *A&A* **595**, A117 (2016).
221. J. K. Jørgensen, A. Belloche, R. T. Garrod, *ARA&A* **58**, 727–778 (2020).
222. G. Jungclaus *et al.*, *Meteoritics* **11**, 231–237 (1976).
223. J. Kauffmann *et al.*, *A&A* **487**, 993–1017 (2008).
224. J. V. Keane *et al.*, *A&A* **376**, 254–270 (2001).
225. M. Keppler *et al.*, *A&A* **617**, A44 (2018).
226. G. Kim *et al.*, *ApJS* **249**, 33 (2020).
227. R. F. Knacke *et al.*, *ApJ* **179**, 847–854 (1973).
228. C. Knez *et al.*, *ApJ* **635**, L145–L148 (2005).
229. J. Koda *et al.*, *ApJS* **193**, 19 (2011).
230. K. W. Kolasinski, in (Wiley, J. & Sons Ltd., Chichester, England, 1st Ed., 2002).
231. V. Könyves *et al.*, *A&A* **584**, A91 (2015).
232. M. Kounkel, *ApJ* **902**, 122 (2020).
233. M. Kounkel *et al.*, *AJ* **156**, 84 (2018).
234. L. E. Kristensen, M. M. Dunham, *A&A* **618**, A158 (2018).
235. L. E. Kristensen *et al.*, *A&A* **516**, A57 (2010).
236. M. Kuffmeier, B. Zhao, P. Caselli, *A&A* **639**, A86 (2020).
237. M. Kuffmeier, T. Haugbølle, Å. Nordlund, *ApJ* **846**, 7 (2017).
238. Y. Kurono, K.-I. Morita, T. Kamazaki, *PASJ* **61**, 873 (2009).
239. C. J. Lada, J. H. Black, *ApJ* **203**, L75–L79 (1976).
240. C. J. Lada, in *Star Forming Regions* (Peimbert, Manuel and Jugaku, Jun, 1987), vol. 115, p. 1.
241. E. F. Ladd, G. A. Fuller, J. R. Deane, *ApJ* **495**, 871–890 (1998).
242. W. J. Lang *et al.*, *A&A* **357**, 1001–1012 (2000).
243. P. Langevin, *J. Phys. Theor. Appl.* **4**, 678 (1905).
244. I. Langmuir, *Trans. Faraday Soc.* **17**, 607–620 (1922).
245. B. Larsson *et al.*, *A&A* **363**, 253–268 (2000).
246. L. Le Roy *et al.*, *A&A* **583**, A1 (2015).
247. H. H. Lee *et al.*, *A&A* **311**, 690–707 (1996).
248. H.-T. Lee *et al.*, *ApJ* **624**, 808–820 (2005).
249. K. I. Lee *et al.*, *ApJ* **797**, 76 (2014).
250. K. Levenberg, *Quart. Appl. Math.* **2**, 164–168 (1944).
251. Y. Lin *et al.*, *ApJ* **840**, 22 (2017).
252. J. E. Lindberg, J. K. Jørgensen, *A&A* **548**, A24 (2012).
253. J. E. Lindberg *et al.*, *A&A* **584**, A28 (2015).
254. J. E. Lindberg *et al.*, *A&A* **566**, A74 (2014).
255. J. E. Lindberg *et al.*, *ApJ* **835**, 3 (2017).
256. H. Linnartz, S. Ioppolo, G. Fedoseev, *International Reviews in Physical Chemistry* **34**, 205–237 (2015).
257. T. Liu *et al.*, *ApJS* **222**, 7 (2016).
258. R. Lüst, A. Schlüter, *ZAp* **38**, 190 (1955).
259. M.-M. Mac Low, R. S. Klessen, *Reviews of Modern Physics* **76**, 125–194 (2004).
260. R. J. Maddalena, M. Morris, *ApJ* **323**, 179 (1987).
261. E. E. Mamajek, in *Exoplanets and Disks: Their Formation and Diversity* (Usuda, Tomonori, Tamura, Motohide, and Ishii, Miki, 2009), vol. 1158, pp. 3–10.
262. E. E. Mamajek, M. R. Meyer, J. Liebert, *AJ* **124**, 1670–1694 (2002).

263. S. Manigand *et al.*, *A&A* **635**, A48 (2020).
264. D. Marquardt, *J. Soc. Indust. Appl. Math.* **11**, 431–441 (1963).
265. R. Martín-Doménech, G. M. Muñoz Caro, G. A. Cruz-Díaz, *A&A* **589**, A107 (2016).
266. R. Martín-Doménech *et al.*, *ApJ* **880**, 130 (2019).
267. R. D. Mathieu, in *in Handbook of Star Forming Regions, Volume I. The Northern Sky* (Reipurth, B. ed, 2008), vol. 4, ASP Monographs, p. 757.
268. A. J. Maury *et al.*, *A&A* **621**, A76 (2019).
269. B. A. McGuire, *ApJS* **239**, 17 (2018).
270. J. P. McMullin *et al.*, in *Astronomical Data Analysis Software and Systems XVI* (Shaw, R. A., Hill, F., and Bell, D. J., 2007), vol. 376, p. 127.
271. J. P. McMullin *et al.*, *ApJ* **424**, 222 (1994).
272. J. P. McMullin *et al.*, *ApJ* **536**, 845–856 (2000).
273. S. T. Megeath *et al.*, *AJ* **144**, 192 (2012).
274. S. T. Megeath *et al.*, *AJ* **151**, 5 (2016).
275. C. Meinert *et al.*, *Science* **352**, 208–212 (2016).
276. K. M. Menten *et al.*, *A&A* **474**, 515–520 (2007).
277. D. Mesa *et al.*, *A&A* **624**, A4 (2019).
278. L. Mestel, *MNRAS* **138**, 359 (1968).
279. O. Miettinen *et al.*, *A&A* **486**, 799–806 (2008).
280. M. Minissale *et al.*, *A&A* **585**, A24 (2016).
281. M. Minissale *et al.*, *MNRAS* **458**, 2953–2961 (2016).
282. N. Miyauchi *et al.*, *Chemical Physics Letters* **456**, 27–30 (2008).
283. S. J. Mojzsis *et al.*, *Nature* **384**, 55–59 (1996).
284. L. K. Morgan *et al.*, *A&A* **477**, 557–571 (2008).
285. J. C. Mottram *et al.*, *A&A* **600**, A99 (2017).
286. J. Moultaka *et al.*, *A&A* **425**, 529–542 (2004).
287. G. M. Muñoz Caro *et al.*, *ACS Earth and Space Chemistry* **3**, 2138–2157 (2019).
288. H. S. P. Müller *et al.*, *A&A* **370**, L49–L52 (2001).
289. M. J. Mumma, S. B. Charnley, *ARA&A* **49**, 471–524 (2011).
290. K. Murakawa, M. Tamura, T. Nagata, *ApJS* **128**, 603–613 (2000).
291. P. Murdin, M. V. Penston, *MNRAS* **181**, 657 (1977).
292. N. M. Murillo *et al.*, *A&A* **592**, A56 (2016).
293. P. C. Myers, E. F. Ladd, *ApJ* **413**, L47 (1993).
294. P. C. Myers, R. A. Linke, P. J. Benson, *ApJ* **264**, 517–537 (1983).
295. P. C. Myers *et al.*, *ApJ* **324**, 907 (1988).
296. P. C. Myers, *ApJ* **700**, 1609–1625 (2009).
297. F. Nakamura *et al.*, *ApJ* **837**, 154 (2017).
298. J. Nelder, R. Mead, *The Computer Journal* **7**, 308 (1965).
299. D. A. Neufeld, A. Dalgarno, *ApJ* **340**, 869 (1989).
300. R. Neuhäuser, J. Forbrich, in *Handbook of Star Forming Regions, Volume II* (Reipurth, B., 2008), vol. 5, p. 735.
301. R. Neuhäuser *et al.*, *A&AS* **146**, 323–347 (2000).
302. B. Nisini *et al.*, *A&A* **518**, L120 (2010).
303. J. A. Noble *et al.*, *MNRAS* **421**, 768–779 (2012).
304. J. A. Noble *et al.*, *ApJ* **775**, 85 (2013).
305. J. A. Noble *et al.*, *Monthly Notices of the Royal Astronomical Society* **467**, 4753–4762 (2017).
306. J. A. Noble, PhD thesis, Dept. of Physics, Univ. of Strathclyde, 2011.

307. M. Nuevo, G. Cooper, S. A. Sandford, *Nature Communications* **9**, 5276 (2018).
308. D. J. Nutter, D. Ward-Thompson, P. André, *MNRAS* **357**, 975–982 (2005).
309. K. I. Öberg, S. Bottinelli, E. F. van Dishoeck, *A&A* **494**, L13–L16 (2009).
310. K. I. Öberg *et al.*, *ApJ* **621**, L33–L36 (2005).
311. K. I. Öberg *et al.*, *A&A* **504**, 891–913 (2009).
312. K. I. Öberg *et al.*, *ApJ* **740**, 109 (2011).
313. K. I. Öberg, *Chemical Reviews* **116**, 9631–9663 (2016).
314. K. I. Öberg, E. A. Bergin, *Phys. Rep.* **893**, 1–48 (2021).
315. K. I. Öberg, R. Murray-Clay, E. A. Bergin, *ApJ* **743**, L16 (2011).
316. K. I. Öberg *et al.*, *ApJ* **740**, 14 (2011).
317. T. Oka, *Proceedings of the National Academy of Science* **103**, 12235–12242 (2006).
318. G. N. Ortiz-León *et al.*, *ApJ* **869**, L33 (2018).
319. V. Ossenkopf, T. Henning, *A&A* **291**, 943–959 (1994).
320. P. Padoan, Å. Nordlund, *ApJ* **576**, 870–879 (2002).
321. Y. J. Pendleton, A. G. G. M. Tielens, M. W. Werner, *ApJ* **349**, 107 (1990).
322. E. M. Penteado, C. Walsh, H. M. Cuppen, *ApJ* **844**, 71 (2017).
323. G. Perotti *et al.*, *A&A* **643**, A48 (2020).
324. D. E. Peterson *et al.*, *ApJS* **194**, 43 (2011).
325. H. M. Pickett *et al.*, *J. Quant. Spectr. Rad. Transf.* **60**, 883–890 (1998).
326. J. B. Pickles, D. A. Williams, *Ap&SS* **52**, 443–452 (1977).
327. M. Planck, *Verhandl. Dtsch. phys. Ges.* **2**, 202 (1900).
328. D. Polychroni *et al.*, *ApJ* **777**, L33 (2013).
329. K. M. Pontoppidan, *A&A* **453**, L47–L50 (2006).
330. K. M. Pontoppidan, S. M. Blevins, *Faraday Discussions* **168**, 49–60 (2014).
331. K. M. Pontoppidan, E. F. van Dishoeck, E. Dartois, *A&A* **426**, 925–940 (2004).
332. K. M. Pontoppidan *et al.*, *A&A* **408**, 981–1007 (2003).
333. K. M. Pontoppidan *et al.*, *A&A* **404**, L17–L20 (2003).
334. K. M. Pontoppidan *et al.*, *ApJ* **678**, 1005–1031 (2008).
335. K. M. Pontoppidan *et al.*, in *Protostars and Planets VI* (Beuther, Henrik et al., 2014), p. 363.
336. K. M. Pontoppidan *et al.*, *ApJ* **874**, 92 (2019).
337. M. S. Povich *et al.*, *ApJS* **209**, 31 (2013).
338. T. Preibisch, *A&A* **410**, 951–959 (2003).
339. T. Preibisch, *A&A* **428**, 569–577 (2004).
340. R. E. Pudritz, T. P. Ray, *Frontiers in Astronomy and Space Sciences* **6**, 54 (2019).
341. D. Qasim *et al.*, *A&A* **612**, A83 (2018).
342. D. Qasim *et al.*, *Nature Astronomy* **4**, 781–785 (2020).
343. S.-L. Qin, Y.-F. Wu, *Chinese J. Astron. Astrophys.* **3**, 69–74 (2003).
344. D. Rabli, D. R. Flower, *MNRAS* **406**, 95–101 (2010).
345. F. R. S. Rayleigh, *XXXI. Investigations in optics, with special reference to the spectroscope*, 1879.
346. P. Redondo, C. Barrientos, A. Largo, *ApJ* **836**, 240 (2017).
347. P. Redondo *et al.*, *A&A* **603**, A139 (2017).
348. B. Reipurth, *VizieR Online Data Catalog*, V/104 (2000).
349. B. Reipurth, J. Bally, *ARA&A* **39**, 403–455 (2001).
350. B. Reipurth, P. Friberg, *MNRAS* **501**, 5938–5947 (2021).
351. V. M. Rivilla *et al.*, *MNRAS* **483**, L114–L119 (2019).

352. H. Roberts, T. J. Millar, *A&A* **361**, 388–398 (2000).
353. T. P. Robitaille, *A&A* **600**, A11 (2017).
354. T. P. Robitaille *et al.*, *ApJS* **169**, 328–352 (2007).
355. T. P. Robitaille *et al.*, *ApJS* **167**, 256–285 (2006).
356. W. R. M. Rocha, S. Pilling, *ApJ* **803**, 18 (2015).
357. K. Rohlfs, T. L. Wilson, *Tools of Radio Astronomy* (Springer Verlag, 1996).
358. G. S. Rossano, *AJ* **83**, 234–240 (1978).
359. L. S. Rothman *et al.*, *Appl. Opt.* **26**, 4058–4097 (1987).
360. M. Rubin *et al.*, *MNRAS* **489**, 594–607 (2019).
361. D. P. Ruffle, E. Herbst, *MNRAS* **322**, 770–778 (2001).
362. D. P. Ruffle, E. Herbst, *MNRAS* **324**, 1054–1062 (2001).
363. D. Rumble *et al.*, *MNRAS* **448**, 1551–1573 (2015).
364. M. Sahan, L. M. Haffner, *AJ* **151**, 147 (2016).
365. G. Santangelo *et al.*, *A&A* **538**, A45 (2012).
366. S. L. Schnee *et al.*, *ApJ* **634**, 442–450 (2005).
367. S. Schneider, B. G. Elmegreen, *ApJS* **41**, 87–95 (1979).
368. F. L. Schöier *et al.*, *A&A* **390**, 1001–1021 (2002).
369. F. L. Schöier *et al.*, *A&A* **432**, 369–379 (2005).
370. F. L. Schöier *et al.*, *A&A* **454**, L67–L70 (2006).
371. W. A. Schutte *et al.*, *A&A* **343**, 966–976 (1999).
372. D. M. Segura-Cox *et al.*, *ApJ* **866**, 161 (2018).
373. D. M. Segura-Cox *et al.*, *Nature* **586**, 228–231 (2020).
374. R. J. Shannon *et al.*, *Nature Chemistry* **5**, 745–749 (2013).
375. R. J. Shannon *et al.*, *RSC Advances* **4**, 26342–26353 (2014).
376. S. Sharpless, *ApJS* **4**, 257 (1959).
377. T. Shimonishi *et al.*, *ApJ* **855**, 27 (2018).
378. F. H. Shu, *ApJ* **214**, 488–497 (1977).
379. D. Skouteris *et al.*, *ApJ* **854**, 135 (2018).
380. M. F. Skrutskie *et al.*, *AJ* **131**, 1163–1183 (2006).
381. L. Song, J. Kästner, *ApJ* **850**, 118 (2017).
382. S. Spezzano *et al.*, *A&A* **643**, A60 (2020).
383. F. Stahler, S. W. Palla, in *The Formation of Stars* (Wiley-VCH Verlag GmbG & Co, 2004).
384. S. Stanimirovic, in *Single-Dish Radio Astronomy: Techniques and Applications* (Stanimirovic, Snezana et al., 2002), vol. 278, pp. 375–396.
385. T. P. Stecher, D. A. Williams, *Astrophys. Lett.* **4**, 99 (1969).
386. D. P. Stevenson, D. O. Schissler, *J. Chem. Phys.* **29**, 282 (1958).
387. S. E. Strom, G. L. Grasdalen, K. M. Strom, *ApJ* **191**, 111–142 (1974).
388. K. Sugitani, Y. Fukui, K. Ogura, *ApJS* **77**, 59 (1991).
389. A. N. Suutarinen *et al.*, *MNRAS* **440**, 1844–1855 (2014).
390. A. Suutarinen, http://oro.open.ac.uk/61309/, PhD thesis, Dept. of Physics, The Open University, 2015.
391. A. Suutarinen, *omnifit v0.1*, https://doi.org/10.5281/zenodo.29354, 2015.
392. K. N. R. Taylor, J. W. V. Storey, *MNRAS* **209**, 5P–10 (1984).
393. S. Terebey, F. H. Shu, P. Cassen, *ApJ* **286**, 529–551 (1984).
394. J. Terwisscha van Scheltinga *et al.*, *A&A* **611**, A35 (2018).
395. W.-F. Thi *et al.*, *A&A* **449**, 251–265 (2006).

396. A. G. G. M. Tielens, W. Hagen, *A&A* **114**, 245–260 (1982).
397. J. J. Tobin *et al.*, *Nature* **492**, 83–85 (2012).
398. J. J. Tobin *et al.*, *ApJ* **805**, 125 (2015).
399. W. Tscharnuter, *A&A* **39**, 207 (1975).
400. B. E. Turner, *ApJ* **501**, 731–748 (1998).
401. Ł. Tychoniec *et al.*, *A&A* **632**, A101 (2019).
402. Ł. Tychoniec *et al.*, *A&A* **640**, A19 (2020).
403. M. Vasta *et al.*, *A&A* **537**, A98 (2012).
404. A. I. Vasyunin, E. Herbst, *ApJ* **769**, 34 (2013).
405. A. I. Vasyunin *et al.*, *ApJ* **842**, 33 (2017).
406. F. Vazart *et al.*, *MNRAS* **499**, 5547–5561 (2020).
407. R. Visser, S. D. Doty, E. F. van Dishoeck, *A&A* **534**, A132 (2011).
408. R. Visser *et al.*, *A&A* **495**, 881–897 (2009).
409. S. N. Vogel *et al.*, *ApJ* **283**, 655–667 (1984).
410. C. M. Wade, *AJ* **62**, 148 (1957).
411. A. F. Wagner, M. M. Graff, *ApJ* **317**, 423 (1987).
412. V. Wakelam *et al.*, *Molecular Astrophysics* **9**, 1–36 (2017).
413. C. Walsh *et al.*, *ApJ* **823**, L10 (2016).
414. F. M. Walter *et al.*, *Mem. Soc. Astron. Italiana* **68**, 1081–1088 (1997).
415. H. Wang *et al.*, *ApJ* **617**, 1191–1203 (2004).
416. N. Watanabe, A. Kouchi, *ApJ* **571**, L173–L176 (2002).
417. Y. Watanabe *et al.*, *ApJ* **745**, 126 (2012).
418. W. D. Watson, E. E. Salpeter, *ApJ* **174**, 321 (1972).
419. W. D. Watson, *ApJ* **183**, L17 (1973).
420. J. C. Weingartner, B. T. Draine, *ApJ* **548**, 296–309 (2001).
421. A. Weiß *et al.*, *A&A* **365**, 571–587 (2001).
422. M. S. Westley *et al.*, *Nature* **373**, 405–407 (1995).
423. G. J. White, M. M. Casali, C. Eiroa, *A&A* **298**, 594 (1995).
424. B. A. Whitney *et al.*, *ApJ* **598**, 1079–1099 (2003).
425. D. C. B. Whittet *et al.*, *ApJ* **742**, 28 (2011).
426. D. A. Williams, S. Viti, *Observational Molecular Astronomy: Exploring the Universe Using Molecular Line Emissions* (Cambridge University Press, 2013).
427. J. P. Williams, W. M. J. Best, *ApJ* **788**, 59 (2014).
428. J. P. Williams, L. A. Cieza, *ARA&A* **49**, 67–117 (2011).
429. T. L. Wilson, *Reports on Progress in Physics* **62**, 143–185 (1999).
430. T. L. Wilson, F. Matteucci, *A&A Rev.* **4**, 1–33 (1992).
431. A. J. Winter *et al.*, *MNRAS* **491**, 903–922 (2020).
432. M. G. Wolfire, D. Hollenbach, A. G. G. M. Tielens, *ApJ* **344**, 770 (1989).
433. E. L. Wright *et al.*, *AJ* **140**, 1868–1881 (2010).
434. B. Yang *et al.*, *ApJ* **718**, 1062–1069 (2010).
435. H.-W. Yi *et al.*, *ApJS* **236**, 51 (2018).
436. H.-W. Yi *et al.*, *arXiv e-prints*, arXiv:2103.03499 (2021).
437. L. Zamirri *et al.*, *MNRAS* **480**, 1427–1444 (2018).
438. G. Zasowski *et al.*, *ApJ* **694**, 459–478 (2009).
439. F. Zernike, *Physica* **5**, 785–795 (1938).

440. C. Y. Zhang *et al.*, *A&A* **218**, 231–240 (1989).

441. C. Zhang *et al.*, *MNRAS* **497**, 793–808 (2020).

442. Z.-Y. Zhang *et al.*, *Nature* **558**, 260–263 (2018).

443. C. Zucker *et al.*, *ApJ* **879**, 125 (2019).

444. C. Zucker *et al.*, *A&A* **633**, A51 (2020).

445. P. H. van Cittert, *Physica* **1**, 201–210 (1934).

446. E. F. van Dishoeck, in *Millimetre and Submillimetre Astronomy* (Wolstencroft, R. D. and Burton, W. B., 1988), vol. 147, p. 117.

447. E. F. van Dishoeck, J. H. Black, *ApJS* **62**, 109 (1986).

448. E. F. van Dishoeck, E. A. Bergin, *arXiv e-prints* (2020).

449. E. F. van Dishoeck, J. H. Black, *ApJ* **334**, 771 (1988).

450. E. F. van Dishoeck, G. A. Blake, *ARA&A* **36**, 317–368 (1998).

451. M. L. van Gelder *et al.*, *A&A* **639**, A87 (2020).

452. S. E. van Terwisga *et al.*, *A&A* **640**, A27 (2020).

453. H. C. van de Hulst, *Recherches Astronomiques de l'Observatoire d'Utrecht* **11**, 2.i–2 (1946).

454. M. L. R. van 't Hoff *et al.*, *A&A* **599**, A101 (2017).

455. M. L. R. van 't Hoff *et al.*, *ApJ* **864**, L23 (2018).